DISSERTATION

DESIGN, OPTIMZIATION AND FABRICATION OF AN INTEGRATED OPTOELECTRONIC SENSING CHIP WITH APPLICATIONS IN GROUNDWATER CONTAMINANT DETECTION AND BIOSENSING

Submitted by

Timothy Erickson

Department of Electrical and Computer Engineering

In partial fulfillment of the requirements

For the Degree of Doctor of Philosophy

Colorado State University

Fort Collins, CO

Summer 2014

Doctoral Committee:

Advisor: Kevin L. Lear

Jacob Roberts
Branislav Notaros
George Collins

ABSTRACT

DESIGN, OPTIMZIATION AND FABRICATION OF AN INTEGRATED OPTOELECTRONIC SENSING CHIP WITH APPLICATIONS IN GROUNDWATER CONTAMINANT DETECTION AND BIOSENSING

The LEAC (Local Evanescent Array Coupled) chip is a CMOS-compatible, waveguide-based, label-free, optoelectronic sensor, which can function as a biosensor or environmental sensor. Unique among optoelectronic sensors, the ~1 cm^2 LEAC chip features an integrated photodetector array, which increases device portability, enables multi-analyte detection on a single waveguide, and simplifies system instrumentation. At its core, the LEAC chip is simply a precision refractometer, which can sense very small changes in refractive index (~$5x10^{-6}$) in its multiple upper cladding sensing regions. The chip can be functionalized for detection of biomarkers or groundwater contaminants, which bind or diffuse into the waveguide's upper cladding sensing region, thereby producing a measurable change in refractive index.

The research conducted during my doctoral studies has addressed two important goals. The first was to optimize the chip's sensing performance. The second goal was to run proof of concept experiments, in order to demonstrate its utility in practical sensing applications.

By incorporating multiple engineering improvements, the sensing performance of the LEAC chip has been improved to the point where it may be competitive with low-end surface plasmon resonance (SPR) systems for bulk refractive index sensing. We have demonstrated the LEAC sensing platform for both environmental and biosensing applications. These include sensing aromatic hydrocarbons such as benzene, toluene and xylenes in groundwater at sub-ppm concentrations and detection of the cardiac infarction biomarker TroponinI. Research results have been communicated in peer-reviewed journals and presented at conferences, as summarized in Appendix J. Additionally, the intellectual property that was developed during the course of research activities has served as the basis for several patent filings.

This dissertation provides a comprehensive account of research conducted on the LEAC sensing platform, while working as a graduate student in Dr. Kevin Lear's laboratory. It is structured in the following manner.

In Chapter 1, the basic functionality of LEAC chip is introduced, while providing the necessary background to motivate its development.

Chapter 2 provides a comprehensive and comparative overview of other label-free biosensors and groundwater aromatic hydrocarbon contaminant sensors. It reviews the requirements of other sensing systems and demonstrates the uniquely portable aspects of LEAC chip technology. It is provided for completeness, in order to summarize the state-of-the-art in the field of portable sensing and highlight some of the unique advantages of the LEAC sensor.

In Chapter 3, the engineering aspects of performance optimization over prior art are described in detail. Whereas the 1st generation LEAC chip was fabricated at Avago Technologies, all 2nd generation LEAC chips have been fabricated by myself in the CSU cleanroom or at the Colorado Nanofabrication Lab in Boulder. The development of 2nd generation LEAC chips, including device physics, modeling, and fabrication is rigorously described.

In Chapter 4, the bulk refractive index sensing capabilities of the chip are demonstrated as well as the chip's capacity to perform multi-analyte dry sensing assays . Through design improvements, it is quantitatively shown that the 2nd generation chip is over two orders of magnitude more sensitive than the 1st generation chip.

In **Chapter 5**, the environmental sensing capabilities of the LEAC chip are presented. Teflon AF is first characterized as a unique film for sensing BTX (benzene, toluene, and xylene) contaminants in water using near-IR surface plasmon resonance. Then LEAC chips functionalized with Teflon AF are demonstrated for BTX sensing in water at sub-ppm concentrations. Interference from potential matrix interfering contaminants is evaluated.

In **Chapter 6**, the biosensing capabilities of the LEAC chip are discussed. The LEAC chip is validated for detection of Troponin I.

In **Chapter 7**, areas for future improvements to the LEAC sensing platform are briefly touched upon along with concluding remarks.

A number of appendices related to very specific technical aspects of my work have been included as helpful documentation. These appendices include fabrication process flows, the data acquisition system, transimpedance amplifier design, grating coupler designs, mask designs (including testing structures), and other protocols. A list of publications and conferences is provided at the end of this report in Appendix I.

ACKNOWLEDGEMENTS

I am profoundly thankful for the opportunity I have had to pursue graduate studies at Colorado State University. I have had the privilege or meeting and being advised by a number of stellar people who I must thank, as I am immensely grateful for their help. I would like to thank my advisor Dr. Kevin Lear who has been a steadfast guide on this four year journey. I also owe him a huge debt of gratitude for being an advisor and friend. Nobody has shaped my development as an engineer and scientist more than him. Together, we were able to push the envelope of a particular technology, which has been a truly rewarding experience. I would like to thank my parents and siblings for their unconditional support in and out of the lab for almost three decades! I would especially like to thank my brother Jon for the countless valuable research insights he has provided during my graduate years. I owe a big thank you to a number of professors who have taken time out of their busy schedules to advise my research and grant me access to some high-end research equipment. I owe a huge thanks to Dr. Kipper in CBE for letting me use his SPR instrument and providing assistance with data analysis. I would also like to thank the members of my committee for taking the time to meet with me and teach relevant courses. I am humbled by the fact that I have had the privilege of accessing some highly specialized (and expensive) research equipment during my time as a graduate student. In addition to the relevant funding agencies, I must thank the folks who have trained me how to properly use the equipment. In no particular order, these include Pat McCurdy, Dinesh Patel, and Joe Gamble, Tomoko Borsa, Ryan Brow and Jan Van Zeghbroeck. Without them, I never would have been able to make a single LEAC chip! I would also like to thank the senior design teams that I helped to co-advise. Their creativity and alacrity to solve engineering problems in the face of adversity always seemed to put me in a good mood. I am sure that I learned just as much from them as they did from me. Lastly, I need to acknowledge some fellow grad students who have made my time outside of the lab interesting and memorable over the years. Jason Cook, Ryan Nagao, Prinda Wanakule, Varun Pattani, Sheldon Bish, and Andy Bzdok, it has been a privilege getting to know you. I hope we can catch up in the not-too-distance future.

TABLE OF CONTENTS

Chapter 1: Introduction

1.0 Motivation

In recent years, there has been a major international research effort to leverage micro and nanofabrication technologies, in order to develop portable total analytical devices that can detect and quantify chemical or biological analytes. The small footprint of these devices brings the possibility of sensitive, rapid, "in-the-field" or "point-of-care" testing. The potential uses for such devices are diverse and compelling. A patient with a life-threatening condition could be rapidly screened for a myriad of diseases and diagnosed by simply supplying a drop of blood. An oil-pipeline leak could be detected in real-time by a dime-sized sensor, thereby preventing a large-scale pollution event. A graduate student could quantify a vaccine's effectiveness by using a simple and inexpensive device, which measures the avidity of elicited antibodies for a target virus.

We live in a complex world where real-time information is becoming increasingly valuable. Engineering a device to deliver low-cost access to that information has been the central purpose of my doctoral studies. To that end, I have optimized the performance of a uniquely portable optoelectronic sensing platform and validated its use for both biomedical and environmental sensing applications. Our research group refers to this sensor as the "LEAC chip."

1.1 What is a LEAC Chip? Device Layout and Sensing Mechanism

The **L**ocal **E**vanescent **A**rray **C**oupled (LEAC) chip is an optoelectronic sensor, which can be functionalized to detect biomarkers or environmental contaminants using the *local evanescent field shift principle*. As a result of my research efforts, the chip has been demonstrated for a variety of sensing applications. These include real-time refractive index measurement of oils, environmental sensing of

aromatic hydrocarbon contaminants in groundwater, and cardiac biomarker detection. Fig. 1.1 is an SEM image of a part of the chip at 300x magnification, which shows the chip's waveguide and metal photodetector contacts.

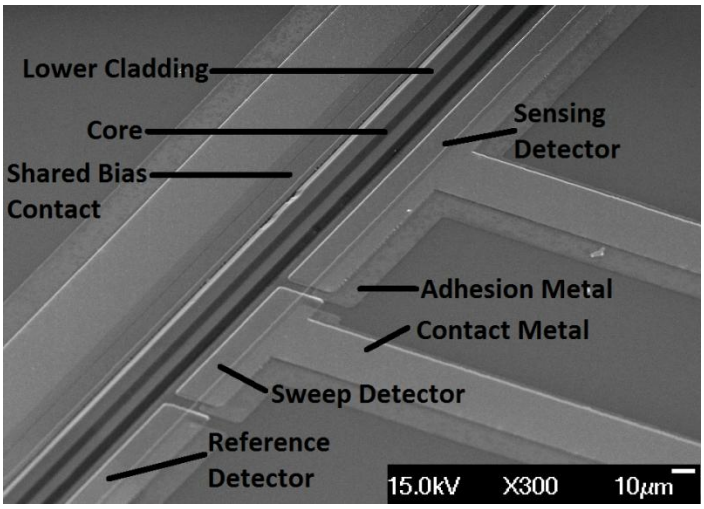

Figure 1.1: SEM image of device structure

LEAC chips are fabricated from a silicon wafer starting substrate. Portions of the Si wafer are metalized to form an integrated photodetector array. A dielectric optical waveguide is formed between the metal contacts (Fig. 1.2, left). The image on the right shows red light being coupled into the chip's waveguide from a single-mode fiber, which is excited by a 660 nm laser diode.

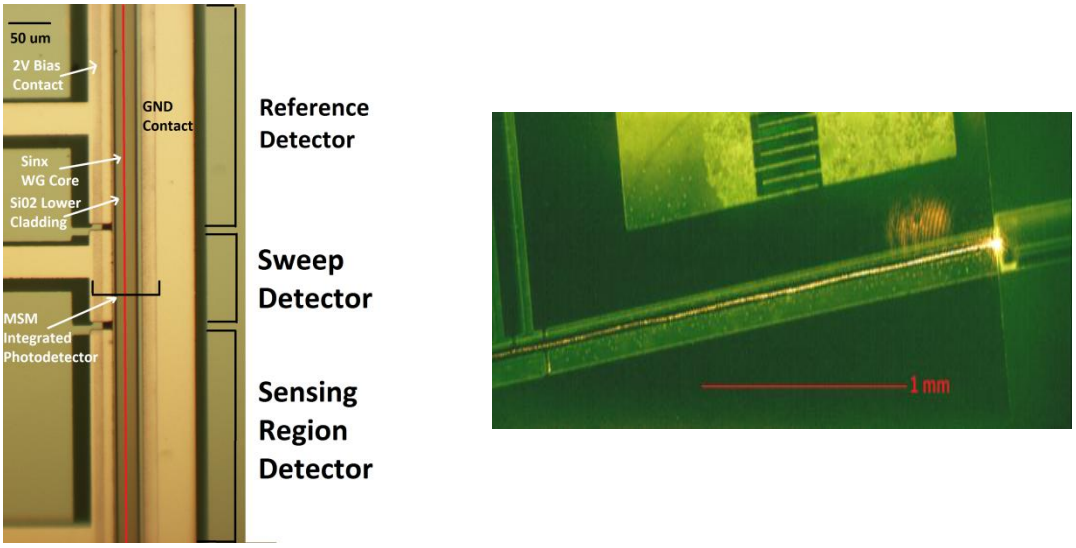

Figure 1.2: Microscope images of LEAC waveguide/photodetector structure (left) and light coupled into the chip's waveguide with an optical fiber (right)

The chip works by measuring changes in evanescent photodetector coupling induced by analyte binding or partitioning into the waveguide's *functionalized* upper cladding sensing region. Due to the nanoscale dimensions of the waveguide core in the vertical direction, coupled light is weakly confined, so there is a strong interaction between the guided mode's evanescent tail and the structure's upper cladding. In response to an increase in upper cladding refractive index, the evanescent field shifts up and away from the photodetector, resulting in less photodetector coupling loss and a corresponding decrease in the measured photocurrent in the underlying metal-semiconductor metal (MSM) photodetector. To correct for fluctuations in coupled light intensity, a fixed index photocurrent reference region is incorporated on-chip, enabling precise measurements of intensity-normalized photocurrent.

This local evanescent field shift effect is illustrated in Fig. 1.3, which is a cross-sectional view of the waveguide structure used for oil sensing.

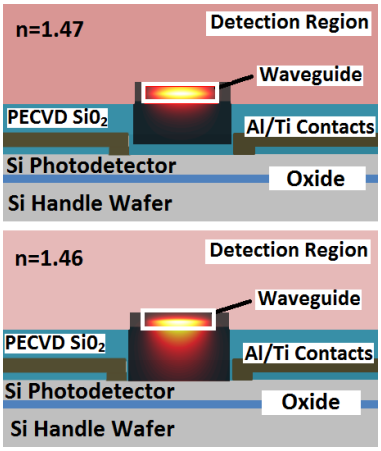

Figure 1.3: Cross sectional view of LEAC structure

Notice that the field is shifted upward and that there is minimal interaction of the evanescent field with the underlying Si when the upper cladding has an index of n=1.47; however there is significant interaction when n=1.46. As such, photodetector coupling is significantly higher for n=1.46.

For sensing applications, analyte binding or partitioning into the upper cladding sensing region causes an increase in refractive index, and therefore a decrease in the measured photocurrent. To further clarify this concept, Fig.1.4 shows the evanescent field effect for various upper cladding indices (n=1.33-1.49). The fields are calculated using a 2-d mode solver [1] and designate the field intensity in the middle of the waveguide structure (marked by the vertical stripe) for the TE_{oo} mode. The waveguide has a semi-infinite SiO_2 lower cladding (n=1.46) and a 70 nm x 7 µm SiNx core (n=1.8). Note that since the core is only 70 nm thick, more than 90% of the guided mode power resides outside the core region.

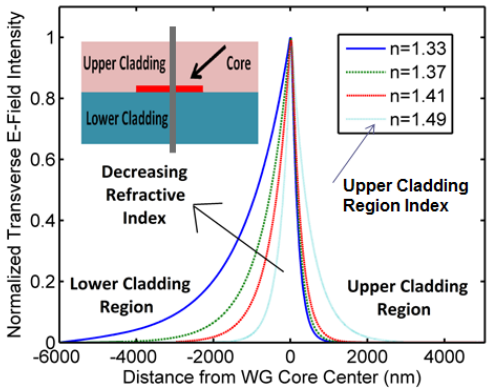

Figure 1.4: Evanescent field profiles in center of structure for various upper cladding indices

1.2 Prior Work on the LEAC Chip

Prior to my research on the LEAC project, the novel LEAC sensing concept had already been validated with a number of papers published on the sensor [2-4]. Much experimental was performed on a 1st generation LEAC chip fabricated at Avago Technologies in Fort Collins (Fig. 1.5). The Avago chip was demonstrated to statically detect dried antibody thin films, including bovine serum albumin (BSA), C-reactive protein (CRP), and a tuberculosis antigen (HspX). Detection was demonstrated at concentrations of 1 mg/mL for BSA, 0.6 mg/L for CRP and 200 µg/mL of HspX. The chip was also demonstrated to detect virus-sized, polystyrene nanospheres with diameters of 40 nm and 200 nm [5]. Fig. 1.5 is an SEM image of the 1st generation chip.

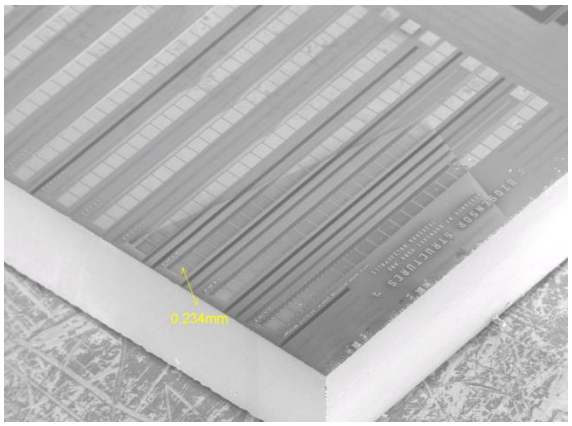

Figure 1.5: SEM image of 1st generation LEAC chip

While the 1st generation chip successfully validated the LEAC sensing concept, multiple issues needed to be addressed in order to realize the full potential of the LEAC chip as a competitive sensing platform.

Despite being made at commercial fab, the 1st generation chip exhibited excessively high scattering losses of roughly 90 dB/cm (Fig. 1.6), which reduced sensitivity by confounding measurement of the evanescent coupling signal which had a maximum photodetector coupling signal of approximately 15 dB/cm. Such high scattering losses inhibited multi-analyte detection as there was little optical power left in the guided mode after passing through the first analyte region to probe more regions along the waveguide. Furthermore, the chip exhibited low photocurrents in the range of 10-100 nA, which required amplification by factor up to 500 million (V/A), resulting in both increased shot noise and amplifier noise. The photodetector also displayed a relatively low SNR of ~100, which further limited sensitivity.

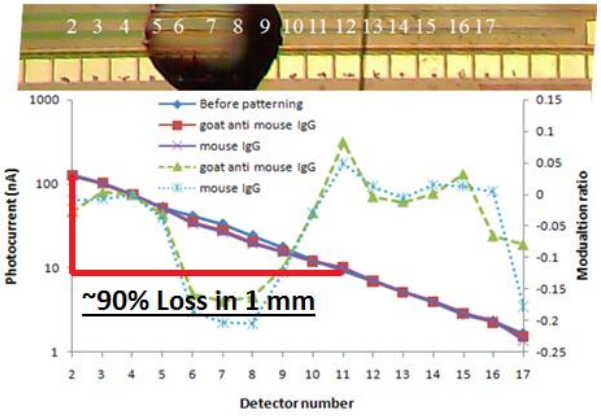

Figure 1.6: Rapid Decay of Guided Mode on 1st Gen Chip. Figure provided by Rongjin Yan.

Aside from low sensitivity and a severely limited multi-analyte detection capability, the 1st generation chip could not perform real-time sensing and lacked fluidic compatibility. These last two features are highly desirable and standard on commercial SPR systems, as they allow real-time binding measurements for characterizing reaction kinetics and performing avidity assays. Fluid compatibility would also be useful for point-of-care devices as well. The need to perform sensitive, real-time assays motivated the design of a 2nd generation LEAC chip to overcome these limitations.

1.3 PhD Project Goals

The focus of my PhD project has been to address these shortcomings and dramatically extend the capabilities of the sensor to the realm where the LEAC technology may be commercially competitive for specific sensing applications. During my time as a graduate student, three distinct PhD project goals have emerged:

1) Optimize the sensing performance of the chip through multiple engineering approaches, including rigorous device modeling, carrying out experiments to optimize photodetector SNR, and reducing waveguide scattering loss through improved fabrication techniques.

2) With the improved chip, experimentally demonstrate real-time detection of biomarkers in a fluid environment. Build a data acquisition system capable of such real-time measurements.

3) Demonstrate the LEAC chip for an environmental sensing application. Specifically, show that the LEAC chip can perform exclusionary detection of aromatic hydrocarbon contaminants, such as benzene, toluene and xylene (BTX) in groundwater.

Taken together, these goals represent a significant advance for the LEAC technology platform. An overarching goal has been to achieve SPR-like sensing performance on a 1 cm^2 CMOS chip (with an associated photocurrent current readout board). The ensuing research effort to successfully design, model, fabricate, and validate the 2^{nd} generation LEAC chip is fully documented in this dissertation.

Chapter 1 References

[1] A. Fallahkhair, K. Li and T. Murphy, "Vector finite difference modesolver for anisotropic dielectric waveguides," *J. Lightwave Technol*., 2008, 26, 1423-1431.

[2] G. Yuan; K. Lear, M. Stephens, and D. Dandy, "Initial demonstration of a local, evanescent, array coupled biosensor concept," *Sensors*, 2005 IEEE, Oct. 30 2005-Nov. 3 2005.

[3] R. Yan, N. Lynn, L. Kingry, Z. Yi, R. Slayden, D. Dandy, and K. Lear, "Waveguide biosensor with integrated detector array for tuberculosis sensing," *Appl. Phys. Letters*, 2011, 98, 013702.

[4] R. Yan, G. Yuan, M. Stephens, X. He, C. Henry, D. Dandy and K. Lear, "Evanescent field response to immunoassay layer thickness on planar waveguides," *Appl. Phys. Letters*, 2008, 93, 101110.

[5] Yan, Rongjin, et al. "Detection of virus-like nanoparticles via scattering using a chip-scale optical biosensor." *Applied Physics Letters* 101.16 (2012): 161111-161111

Chapter 2: Literature Review of Label-Free Biosensors and Aromatic Hydrocarbon Groundwater Contaminant Sensors

2.0 Overview of Sensing Systems

To provide a framework for understanding, it is worth mentioning that many electronic sensing systems employ a common measurement paradigm. In response to the presence of an analyte *A*, a transducer produces an output signal *X*, which corresponds to a physical measurand, such as wavelength, frequency, voltage, current or optical intensity. The sensitivity *S* of the transducer to a particular analyte *A* is given by the derivative $S=\Delta X/\Delta A$. A sensor's limit of detection (LOD) is a function of both sensitivity and how accurately the output signal can be measured, which depends on the level of noise in the sensor characterized by the signal standard deviation over a given measurement period δX for constant A. Provided that the signal change must be greater than or equal to the system noise, the LOD is given by

$$\text{LOD}= \delta X/S \quad \text{(Eq. 2.1)}$$

The above definition implies a one standard deviation confidence interval, corresponding to a normal confidence interval of 68.2%. A 99.7% confidence interval for LOD would require a factor of 3 in front Eq. 2.1. Thus, to achieve a low limit of detection, a system must simultaneously have a high sensitivity and low signal noise. LOD is an important figure of merit for any sensor. In addition to LOD, there are two other key figures of merit. These include the specificity of the sensor, which is the ability of the sensor to only respond to the target analyte *A*, the ability to quantify the concentration of the analyte of interest, and the dynamic range of detection for the analyte of interest. Thus, an ideally performing sensor would be simultaneously capable of single molecule detection, quantification up to 100% analyte concentration, while exhibiting zero response to non-target analytes.

As the LEAC chip is demonstrated for both label-free biosensing and sensing aromatic hydrocarbon contaminants in groundwater, this chapter reviews the state of the art in sensing systems for both of these applications. As the LEAC chip is a lab-on-a-chip sensor, the majority of this chapter discusses other lab-on-a-chip sensing platforms, while bulky and expensive systems are mentioned briefly for completeness. Label-free biosensing systems are described first followed by groundwater contaminant sensing systems.

2.1 Biosensors

The term biosensor is a broadly encompassing and meant to designate any system, which measures a biological signal or quantity. According to definition, this includes a mother's hand, placed on her child's forehead for fever sensing or an integrated microchip inside a pacemaker used to sense a cardiac rhythm. A major focus of my research has been on the development of a type of biosensor known as a label-free sensor, which measures the binding of target analytes to probe molecules in real-time. Label-free biosensors have applications ranging from diagnostic assays to drug and vaccine development, enabling real-time measurement of molecular interactions and quantification of binding kinetics. This contrasts with standard immunoassay formats, such as ELISA or lateral flow immunoassays, which require fluorescent or colorimetric labels and washing steps, and therefore cannot be used for kinetics.

In this chapter, the three predominant types of label-free biosensors are discussed, including optoelectronic biosensors, fully-electronic (FET) sensors, and mechanical sensors. As the LEAC chip is an optoelectronic biosensor, a fairly comprehensive discussion is devoted to optoelectronic sensors. For completeness, FET sensors and mechanical sensors are also discussed. As the LEAC has shown some promise as a portable sensing platform, later flow immunoassays, which are the most portable of immunoassay platforms are also discussed. Traditional, resource-intensive, label-based assay methods such as ELISA and real-time PCR are not discussed, but the reader should be aware that they often serve as gold standard diagnostic assays [1].

2.2 Label-Free Optoelectronic Sensors

While the LEAC chip's integrated photodetectors and sensing mechanism are unique, there are a number of other label-free, optoelectronic biosensing platforms, such as ring resonators [2-4], surface plasmon resonance (SPR) sensors [5-7], interferometric sensors [8-13], photonic crystal sensors [14-15], fiber optic sensors [16-17], whispering gallery mode (WGM) resonators [18] and slot waveguide sensors [19-26]. Each of these sensing platforms can provide reasonably good sensitivity, at the expense of requiring significant external hardware, including tunable lasers, optical spectrum analyzers (OSA), precise temperature control, separate optical detectors, and/or bulky external optical components, which increase system complexity and costs. These hardware requirements reduce access in resource poor settings and confine testing to well-equipped laboratories. Furthermore, the inherent bulkiness of these other platforms is problematic for certain real-time monitoring and defense applications, where it may be necessary to have a small device which can be placed inside a vent, well or process line.

In contrast to other optoelectronic sensing platforms, the LEAC platform has shown promise as a fully-integrated, standalone sensor. The LEAC chip features an integrated photodetector, exhibits minimal temperature dependence and requires only a 1 mW of optical power for waveguide excitation [27]. By incorporating a grating coupler, a low power bonded laser diode, and mixed signal electronics, a fully-integrated LEAC chip could be readily mass-produced using CMOS technology. For comparison, Table 1 references sensors described in recent literature. It includes the sensing modality, demonstrated sensitivity (static and/or real-time) in refractive index units (RIU), as well as required major external components. Sensitivities typically range from 10^{-4} to 10^{-7} RIU. Sensors with the best sensitivity performance often require significant external hardware, as indicated. As described in Chapter 3, the 2nd generation LEAC chip has an experimentally tested sensitivity of 4×10^{-6} RIU. This is competitive with the more complex systems listed below, including commercial SPR systems [28].

Table 2.1: Evanescent Wave Based Optical Sensors

Sensing Modality	Static Sensitivity (RIU)	Real-Time Sensitivity (RIU)	External Components
LEAC biosensor [28]	$4.6x10^{-6}$	$4.1x10^{-5}$	Laser diode, 4x4 inch PCB board for photocurrent readout
Ring Resonator [2]	no data	$\sim10^{-5}$	Temperature-stabilized chuck, Ge photodetector
Ring Resonator [3]	$7.6x10^{-7}$	no data	Tunable laser, OSA (0.22 pm precision), focusing optics
Fiber-based SPR [5]	$7x10^{-7}$	no data	Broadband light source, OSA (1 pm precision)
Long Range SPR [6]	$3x10^{-8}$	no data	Superluminescent diode, OSA, collimating optics
Cell Phone SPR [7]	$2.1x10^{-6}$	no data	Cell phone with front facing camera, PDMS-based optics
Mach-Zehnder Int.[8]	$6x10^{-5}$	no data	Broadband light source, OSA (1 pm precision)
Michelson Int. [9]	$5x10^{-4}$	no data	Broadband light source, OSA (1 pm precision)
Mach-Zehnder Int. [10]	no data	$5x10^{-6}$	Laser diode, lock-in amplifier, Si photodetector
3D Mach-Zehnder Int. [11]	10^{-4}	no data	Tunable laser, optical power meter
Mach-Zehnder Int. [12]	$2.5x10^{-6}$	no data	External CCD, phase-stabilized laser
Young Int. [13]	8.5×10^{-8}	no data	Monochromatic Laser, collimating optics, CCD
Photonic Crystal [14]	7×10^{-5}	no data	Tunable laser, optical power meter
Photonic Crystal Fiber [15]	$4.6x10^{-7}$	no data	Supercontinuum laser, OSA (1 pm precision)
Fiber Bragg Grating [16]	$4x10^{-5}$	no data	Tunable laser (1 pm resolution), optical power meter
Fabry-Perot Fiber [17]	$4x10^{-5}$	no data	Broadband IR light source, OSA (1 pm precision)
Microtoroid Resonator [18]	no data	no data	Tunable Laser, optical sprectrum analyzer
Slot Waveguide [21]	$2x10^{-4}$	no data	Tunable Laser, optical sprectrum analyzer
Slot Waveguide [24]	$1.3x10^{-5}$	no data	Tunable Laser, optical sprectrum analyzer

2.2a Ring Resonators

In ring resonator sensors, a bus waveguide is used to excite the resonance mode of a ring-shaped resonator cavity, as displayed in Figure 2.1 from ref. [3]

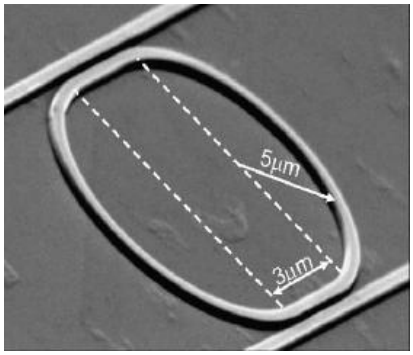

Figure 2.1: SEM image of ring resonator. Light is resonantly coupled from the bus waveguide into the ring structure and circulates multiple times before attenuation due to absorption, scattering and/or out-coupling.

The bus waveguide is typically excited with a tunable laser by grating coupler excitation. The resonance wavelength, $\lambda_{resonance}$ is given by the following condition, where L is the cavity length and m is the mode order.

$$\lambda_{resonance} = \frac{L}{m} n_{eff}$$

Thus, the resonance wavelength (scanned by the tunable laser) is highly sensitive to changes in n_{eff}, the effective index of the ring resonator. N_{eff} is highly sensitive to changes in refractive index in the medium probed by the guided mode's evanescent tail. As a result, the resonance wavelength shifts due to analyte binding or diffusion into ring's evanescent tail region. The change in resonance peak position is typically observed by either scanning a tunable laser or by using a broadband source and optical spectrum analyzer. For rings with large Q factors there can be an intense buildup of optical power in the cavity. Q characterizes the energy stored per optical cycle dived by the power loss, and the intensity buildup factor B for a ring with circumference L is given by

$$B = \frac{\lambda_{resonance} Q}{n_{eff} L \pi}$$

Thus, a ring resonator with $\lambda_{resonance}$=1550 nm, n_{eff}=2, with a Q=20,000 and a 10 μm diameter would have a buildup factor of B=152. The evanescent field of the ring's resonant mode would probe the analyte medium with an effective optical pathlength of (152)(31.4 um)= 4.7 mm. The advantage of ring resonators is that they permit perturbations (analyte binding) in the cladding medium to be sensed by the optical evanescent field multiple times, creating a longer effective sampling pathlength, and improved sensitivity despite having a form factor of just 100 um^2 (excluding the excitation bus waveguide). High Q resonators exhibit a very narrow resonance linewidth, which greatly enhances sensitivity by enabling precise measurement of small shifts in resonance position.

In 2007, Baets *et al.* demonstrated a ring resonator with a Q-factor of 20,000, a sensitivity of 70 nm/RIU and an avidin-biotin detection limit of 10 ng/mL. As resonant devices, ring resonators are typically very sensitive to temperature fluctuations and methods are required to minimize temperature fluctuations in the sample medium, including using Peltier cooled stages. Over the years, the performance metrics for ring resonator systems have improved. A cavity with a Q-factor of 1.2×10^5 and a sensitivity of 570 nm/RIU has been reported [2]. Assuming a spectrometer with a resolution of 1 pm, such a ring resonator has a bulk index resolution of 1.75×10^{-6}.

While ring resonators require significantly more external hardware than the LEAC chip (temperature stabilization, tunable lasers, optical spectrum analyzer), their chief advantage is in terms of sensitivity, resulting from the resonant optical intensity buildup. Typically sensitivity is reported in units of nm/RIU. In order to make a valid comparison the LEAC chip, the units must be converted into % change in optical intensity/RIU. The sensitivity can be inferred from Fig. 2.2, as found in reference [2], which shows the change in optical intensity as a function of NaCl concentration by mass.

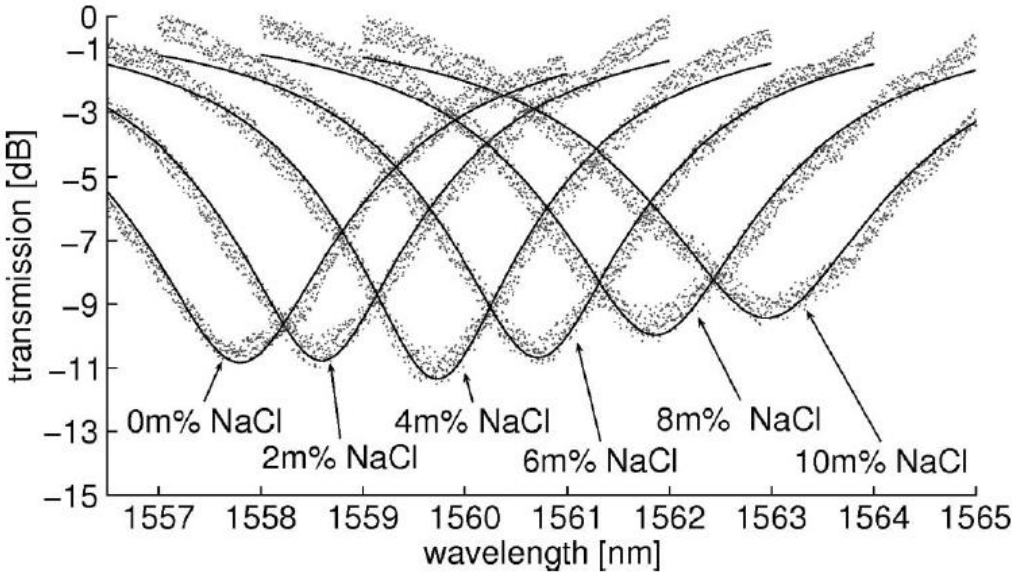

Figure 2.2: Ring resonator intensity and wavelength shift vs. change in refractive index.

For NaCl in water, the change in refractive index is given by: Δn=0.1715c, where c is the mass concentration of. A 2% NaCl concentration by mass results in an index change of 0.0036 RIU. Note that the intensity transmission for 0% to 2% solutions is given by -10.8 to -6.8 dB, respectively, corresponding to transmission of 0.083 and 0.208. Thus, the signal modulation is (0.208-0.083)/0.083=150.6%. The corresponding sensitivity is 150.6%/.0036= 41,800 %/RIU. This is approximately 23 times greater than the LEAC chip's measured sensitivity, as reported in Chapter 4. A close inspection of the plot reveals a significant amount of optical intensity noise, corresponding to about 0.4 dB. At 10 dB, this is about 1% of the intensity signal. Thus, the ring resonator chip's limit of detection (LOD) for an intensity based measurement is about 2.4×10^{-5}, which is inferior to the LEAC chip's LOD. As additional advantage of the LEAC chip is the ability to incorporate an on-chip intensity reference region integrated along the waveguide, which corrects for temperature fluctuations and increases the precision of intensity-based measurement.

2.2b Microtoroid and Microsphere Resonator Sensors

Microtoroid and microsphere resonator sensors, sometimes called whispering gallery mode sensors, are capable of exquisite sensitivity, including single molecule detection. A microtoroid is illustrated in Fig. 2.3 as found in reference [18b].

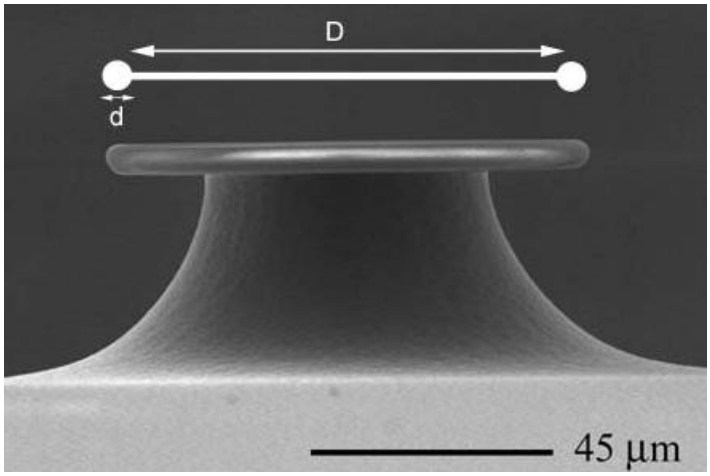

Figure 2.3: SEM of microtoroid resonator

They employ the same general sensing mechanism as ring resonators and typically require the same hardware, including tunable lasers, temperature stabilization equipment and optical spectrum analyzers. However, they employ serial fabrication methods, which permit atomic-level smoothness. Indeed, Q-factors as high as $3x10^8$ have been reported, enabling an intensity 100W to build up in a microtoroid resonator with a 1 mW laser [18]. At such high intensities, the resonance wavelength begins to shift due to the thermo-optic effect, which can interfere with the observation of binding events. Despite this apparent challenge, single molecule detection of IL-2 in serum using a microtoriod was reported in 2007 by Armani *et al.* The signal became apparent at a concentration of just $5x10^{-18}$ M.

In general, microtoroid resonators demonstrate the best limit of detection for biosensing of all optoelectronic sensors. One drawback appears to be the difficulty in coupling light into the toroid as the toroid is far above the wafer surface. Furthermore, mass-producing toroids may prove challenging, as each toroid must be serially heated with a CO_2 laser for reflow. Like ring resonators, microtoroids are incapable of simultaneous multi-analyte detection using a single light source, which is unique advantage of the LEAC chip.

2.2c Surface Plasmon Resonance (SPR)

Surface plasmon resonance has become the effective gold standard for label-free, real-time sensing and molecular binding kinetics. In surface plasmon resonance, a surface wave is excited in a thin layer of gold evaporated onto a glass substrate. Gold is selected due to both its chemical robustness and dielectric value, which permits resonant coupling at optical wavelengths. The surface plasmon is typically excited in the Kretchsmann configuration, which employs a high-index prism for momentum matching as indicated by Fig. 2.4 from ref. [6].

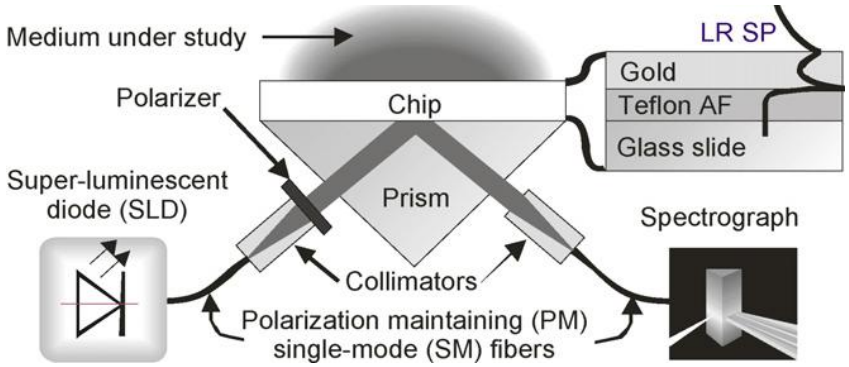

Figure 2.4: Excitation of surface plasmon surface wave in Kretchmann configration

The resonance condition is highly dependent on refractive index changes in the analyte medium, as the evanescent tail of the excited surface wave probes the dielectric medium. The resonance condition is given by [6],

$$k_x = k_0 n_p \sin(\theta) = k_0 \sqrt{\frac{\varepsilon_{mr} n_a^2}{\varepsilon_{mr} + n_a^2}}$$

where k_x is the propagation constant of the excited plasmon, k_o the free space propagation constant of the excitation light, ε_m the real dielectric constant of the metal and n_a, the effective dielectric constant of the analyte medium. From the resonance condition, for a given ε_m which is fixed at a given wavelength and temperature, variations in analyte medium index, will cause the resonant coupling angle to vary. For a fixed coupling angle, analyte binding is transduced as a change in intensity. Analyte binding causes less light to be coupled into the lossy-metal, resulting in increased reflectively from the surface. Alternately, the coupling angle can be scanned or the multiple wavelengths can be employed. As gold's dielectric is highly sensitive to wavelength, the condition resonance condition can be satisfied for a given wavelength at a fixed coupling angle. Thus, analyte binding produces a shift in the wavelength resonance peak.

Compared to optical waveguide sensors, the surface plasmon's evanescent field power is much more concentrated in the analyte medium (~94% at 580 nm vs ~10% for a LEAC chip). However this apparent

advantage is mitigated by the relatively short (24 μm for gold) propagation length due to optical losses in the metal. Thus the net interaction with the analyte medium (distance multiplied by the fraction of field in analyte medium) is very comparable to a LEAC chip with 300 μm long detectors. Silver, which exhibits less optical attenuation than gold can be used to increase SPR performance, but as silver readily oxidizes, it does not form a highly stable surface for monitoring biomolecular interactions.

Due in part to its ease of use and early adoption, SPR is a gold standard technique for kinetics. However, SPR systems have several drawbacks including cost and bulkiness. It is worthwhile to mention the best reported performance for an SPR system. By employing Teflon AF to increase the evanescent field intensity in the analyte medium, Slavik and Homola have reported a sensitivity of $3x10^{-8}$ RIU, which is the best reported sensitivity of any SPR device in the literature to date [6].

2.2d Interferometric Sensors

Analyte binding in the sensing region of an optical waveguide produces an increase in the waveguide's effective index, and therefore, an increase in optical path length. Interferometric sensors work by measuring the phase change induced by analyte binding in the sensing region of a dielectric waveguide. Interferometric sensors come in a variety of geometries, which mirror standard optical interferometers, including Young and Mach-Zehnder interferometers. The key difference is that light is confined to optical waveguides, rather than propagating in free space. The signal is produced by combining light from reference and sensing waveguides either on chip or through measurement of off-chip interference patterns. Analyte binding results in a phase shift, which is either measured by fluctuations in output intensity in the case of Mach-Zehnder Interferometers or as a change in the interference patterns for Young interferometers. The topology of a Mach-Zehnder Interferometer (MZI) with separate reference and sensing arms is shown in Fig. 2.5 from ref. [10].

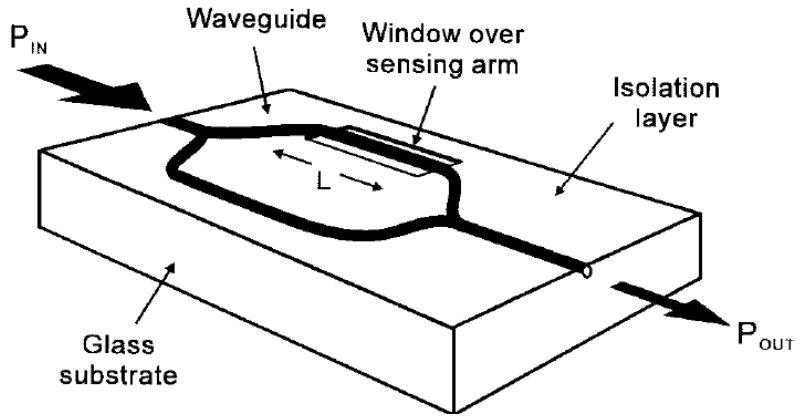

Figure 2.5: Mach-Zehnder Interferometer

Luff *et al.* have demonstrated a bulk refractive index resolution of $5x10^{-6}$ with a MZI [10], and Crespi *et al.* have demonstrated a 10^{-4} RIU limit of detection for a laser-written MZI [11]. Ymeti *et al.* have demonstrated a $8.5x10^{-8}$ RIU limit of detection by measuring the interference pattern produced by a Young Interferometer with an external CCD camera [13].

Interferometric sensors have much in common with the LEAC structure, as both measures the change in effective index induced by analyte binding to a single-mode dielectric waveguide. Interferometric sensors make a purely phase-based measurement, whereas the LEAC chip measures the resultant evanescent field shift. The LEAC chip sensor has several unique advantages over waveguide-based interferometric sensors. These include multi-analyte capability on a single-waveguide, on-chip photodetectors, and ability to use non-phase stabilized, inexpensive semiconductor lasers for waveguide excitation. Mach-Zehnder interferometers are highly sensitive to fluctuations in light source intensity, as they lack an on-chip reference sensor that can correct for fluctuations in coupled light intensity. Young interferometers are also highly susceptible to mechanical vibrations, as the interference pattern must be focused onto an off-chip CCD. Young Interferometer experiments require an air-suspended optical table to deal with mechanical vibrations. This is standard procedure for optical interference measurements and severely restricts the device's utility for inexpensive point-of-care diagnostics.

2.2e Photonic Crystal Sensors

Photonic crystal sensors rely on the unique scattering properties of period structures, which can guide and confine light at resonance wavelengths by taking advantage of optical interference phenemona. When a perturbation to the structure arises due to analyte binding to probe molecules a resonance shift can be readily observed. An introduction to the mathematics and theory behind phototonic crystal cavities and waveguides is beyond the scope of this dissertation, so it suffices to mention several concrete examples, which represent some of the best work in the field.

Photonic crystal sensors come in two varieties, 2D photonic crystals, typically fabricated in silicon using e-beam lithography [14] and photonic crystal fibers [15]. Mandal *et al.* have demonstrated a photonic crystal sensor, which has multiple sensing regions, similar to the LEAC chip. Each photonic bandgap sensor is excited by a single bus waveguide and is tuned to have a distinct resonance position. As indicated by Figure 2.6. from ref. [14], each photonic crystal produces a distinct dip in the transmission spectrum. A peak shift sensitivity of 142 nm/RIU and a $7x10^{-5}$ limit of detection were demonstrated. The system requires either a tunable laser or a broadband source and optical spectrum analyzer.

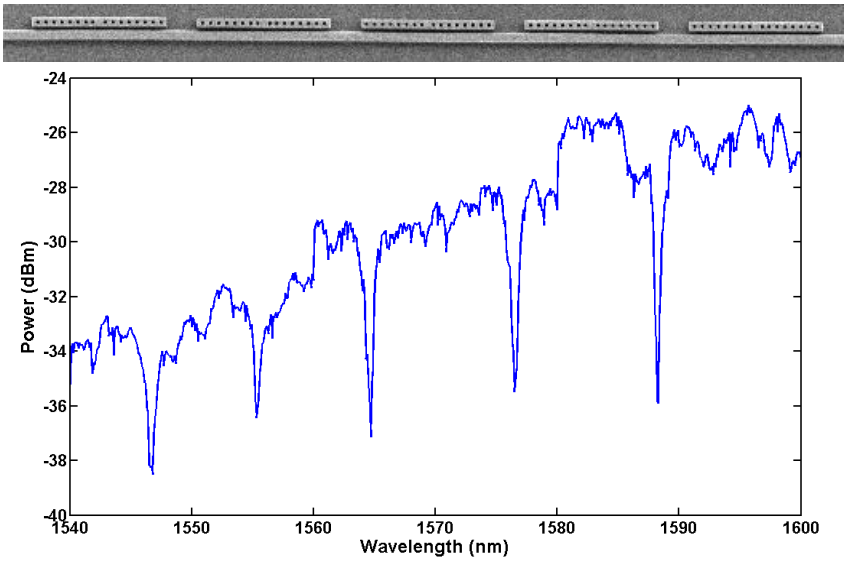

Figure 2.6: Transmssion spectrum of mutli-element photonic crystal sensor

Photonic crystal fibers can provide ultra-sensitive refractive index resolution due to having exceptionally low loss (several dB/km) and direct sampling of a very long optical pathength (several cm). By employing a photonic crystal fiber and a single hollow core of the fiber with high index fluid, Wu *et al.* demonstrated an unparalleled refractive index sensitivity of 38,000 nm/RIU and a limit of detection of $4x10^{-7}$ RIU for sampling at telecom wavelengths. While such a fiber works quite well for bulk refractive index measurement, its utility for biosensing may be limited due to the expense and difficulty of functionalizing a 10 cm long, 4 micron fiber hollow core with probe molecules. Additionally, such a system does not lend itself to multi-analyte sensing.

2.2f Reflective Fiber Sensors

Fiber sensors leverage existing telecommunication fiber technology to form sensors based on changes in fiber reflectance modulated by changes in refractive index of the ambient medium. Various versions include Bragg gratings etched into the fiber cladding [16] and Fabry-Perot tipped fibers [17], each of which has a reported RIU resolution of $4x10^{-5}$ RIU. A unique aspect of fiber sensors is that due to low optical losses, very long fibers can be used to probe locations that would be hard to reach with other sensors, such as the bottom of a well or deep in the ocean. However, fiber sensors do not typically include integrated reference regions, so they are highly susceptible to temperature fluctuations. Additionally, external equipment is typically required on the non-sensing end of the fiber for optical readout.

2.2g Slot Waveguide Sensors

Slot waveguides employ a unique guiding structure, whereby a “slot” is cut into a traditional ridge waveguide, enabling increased interaction between the guided mode and the analyte medium, as shown in Fig. 2.7c, which is reproduced from ref. [19].

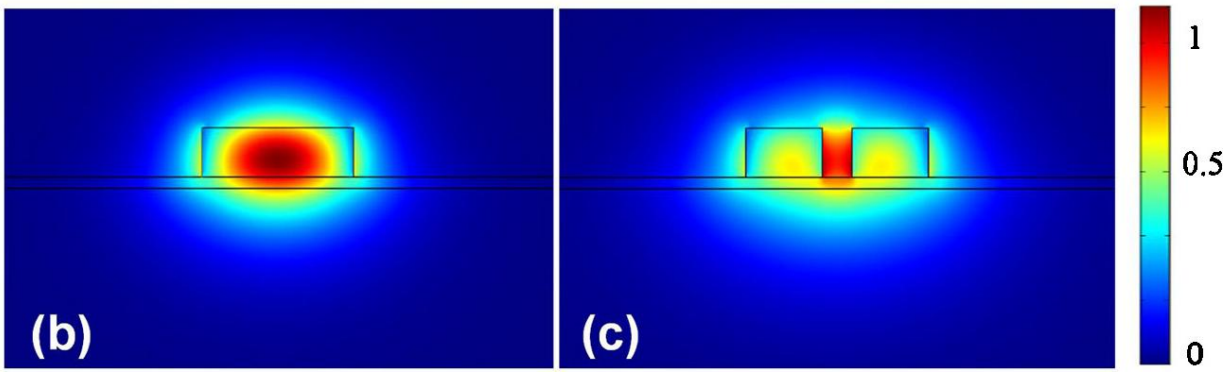

Figure 2.7: Comparison of Electromagnetic Field distribution for a b) ridge waveguide and a c) slot waveguide

Note that for a ridge waveguide, the greatest field density resides within the waveguide core. This portion of the field is not used for sensing. In contrast, for a slot waveguide, the greatest field density is present in an analyte medium.

Slot waveguides were first introduced in 2004 by Almeida *et al.* in a paper titled "Guiding and confining light in void nanostructure. [20]" On the surface, slot waveguides appear to have more promising performance characteristics than traditional ridge waveguide structures, as there is increased interaction with the probing medium. However, experimental data reveal that even the best slot waveguides exhibit bulk sensitivity, which is inferior to other sensing platforms. For instance, Barrios *et al.* reported a bulk sensitivity of 212/nm per RIU and a resolution of $2x10^{-4}$ RIU [21], which is significantly below the demonstrated refractive index resolution of the LEAC chip (4×10^{-6}). The bulk sensitivity is well below established values for SPR, which range from 970 to 13,800 nm/RIU [22]. In "Ultrasensitive Nanomechanical Photonic Sensor Based on Horizontal Slot-Waveguide Resonator," Barrios established a limit of detection of $5x10^{-3}$ RIU [23]. In 2012, Tu *et al.*, demonstrated an improved SiNx slot waveguide sensor with a refractive index of $1.29x10^{-5}$ [24]. Slot waveguides have been employed for various biosensing and environmental sensing applications. including sensing BSA with a sensitivity of 16 pg/mm^2 [25] and non-specifically sensing acetylene gas at in room air [26].

Despite the increased mode overlap with the sensing medium, slot waveguides exhibit relatively low sensitivities, especially compared to SPR and ring resonators. This implies that the change in effective index and hence, modal confinement is less affected by refractive index changes than other sensing platforms. This contrasts sharply with a LEAC device brought close to cutoff, where small changes in refractive index can shift the device from being cutoff, resulting in a large change in modal confinement from approximately zero to a finite value.

2.2h Plasmonic Nanohole Array Sensors

Plasmonic nanohole array sensors are a relatively new plasmon based sensing platform, whereby arrays of nanoholes are fabricated in a metal film (typically gold or silver) on a dielectric substrate. A light source is placed above the holes and the optical transmission is recorded with a camera located on the opposite side of the array. The transmission is sensitively modulated by refractive index changes in the region in close proximity (~100 nm) to the holes, and sensitivities in excess of 16,600%/RIU have been recorded [68]. While demonstrated nanohole arrays require significant external instrumentation including, microscope objectives and Peltier-cooled CCDs, they hold the promise of significant throughput, as multiple arrays of nanohole arrays can be imaged simulataneously. Furthermore, nanohole arrays do not require excitation of an optical waveguide, which simplifies optical coupling into the system. For systems requiring throughput of thousands of analytes, plasmonic nanohole arrays hold much promise.

2.3 Comparison to FET-based Sensors

Like optoelectronic sensors, FET sensors can also be used for real-time binding measurements. FET sensors also leverage CMOS fabrication technology and have the added advantage of being fully electrical devices, which do not require optical sources or detectors. Nearly all FET-based sensors utilize the effect of analyte binding in the gate region to induce a change in either the transistor's transconductance parameter or threshold voltage. FET biosensors have been demonstrated for a wide range of biological assays [29-31].

However, the all-electrical simplicity of FET bionsensors has a drawback. The devices are highly sensitive to changes in both ion concentration and pH in the analyte environment, since they function as exquisitely sensitive charge sensors. The sensors probing volume is limited by Debye screening [32], which serves to neutralize charge on the sensor surface through formation of a charge double layer. Human serum has an ionic concentration of 0.9%, comparable to intravenous saline, and thus contains roughly 9 grams of NaCl per liter of fluid. This is equivalent to 9/58= 0.155 M. The Debye length is given by the equation below, where κ^{-1} is the Debye length and *I* is the ionic strength. For human serum the Debye length is just 0.8 nm.

$$\kappa^{-1}(\mathrm{nm}) = \frac{0.304}{\sqrt{I(\mathrm{M})}}$$

Thus any charge located more than 0.8 nm away from the FET surface is effectively screened by the double layer. Most antibody linker chemistries are at least several nm in length, such that bound analyte would exist outside of the probing region at human serum concentrations. In contrast, most evanescent wave sensors, including the LEAC chip can probe ~80 nm at a 1/e falloff intensity. It must be noted that processing steps, such as DI water dilution can be used to decrease the ionic strength of the solution. For instance a 100:1 dilution would increase the Debye length to 8 nm. However, this comes at the expense of reducing the analyte concentration by a factor of 100. As such, most FET experiments are performed at fixed low ionic strength buffered solutions. Despite these apparent drawbacks, there is still an intense research and development effort underway to improve and commercialize FET sensors due to their superior sensitivity in low-ionic strength, buffered solutions [33].

A potential drawback of FET biosensors is the intrinsic linkage between the signal and the ambient pH. For instance, Kim *et al.* demonstrated a positive change in conductance for a n-type Si-FET for prostate specific antigen (PSA) in a slightly acidic medium (pH=6.0), whereas a decrease in conductance was observed for PSA binding in a slightly basic (pH=7.8) medium [33]. The data is displayed in Fig. 2.8. The

reason for the change in conductance is straightforward. PSA has an isoelectric point of pH=6.9, in a basic medium PSA loses a proton, and thus has a negative charge. In an n-type FET, the negative charge attracts holes, and therefore depletes the channel of carriers, leading to a decrease in conductance. Impressively, a limit of detection (LOD) of 1 fg/mL (30 aM) of PSA was observed. It is notable that the experiment was carried out under non-physiological conditions. Namely, the Debye length was artificially increased by suspending the PSA in a very low ionic concentration of just 6 uM, increasing the Debye length to 124 nm from the 0.8 nm value, which would be found in human plasma. This is equivalent to diluting a normal physiological serum sample by a factor of roughly 26,000. Thus an LOD repsentative of physiological condutions would be 5.2 pM, which is still a very good LOD.

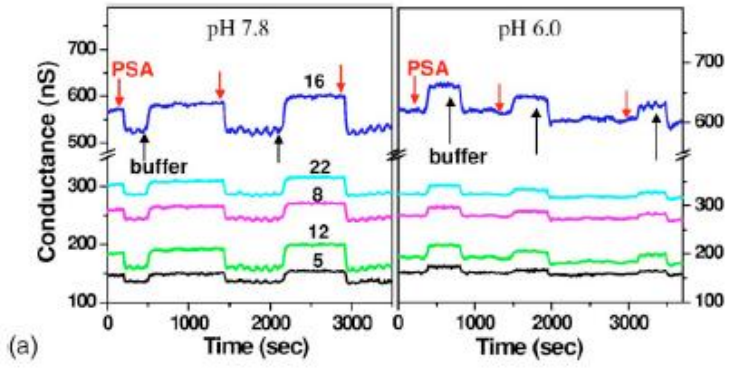

Figure 2.8: Effect of pH on Si-FET signal when detecting PSA

2.4 Label-Free Mechanical Sensors

Mechanical biosensors are the other major class of label free biosensors, and include microcantilever sensors [34-36] and quartz crystal monitor (QCM) sensors [37]. The sensors rely on the mechanical forced produced by mass binding to the sensor surface. In microcantilvers, analyte binding produces a change in deflection angle or resonance frequency, whereas for QCM, analyte binding produces a shift in the resonance frequency of oscillation. For example, Wu *et al.* optically measured the cantilever deflection to sense PSA at concentrations ranging from 0.2 ng/mL to 60 µg/mL. In contrast, Shekhawat *et*

al. built a microcantilever into the gate region of a MOSFET, enabling deflection angles of just 5 nm to be measured all electronically, permitting detection of streptavidin at a concentration of 100 fg/mL [36]. The experimental setup and conductance curves from ref. [36] are displayed in Fig. 2.9.

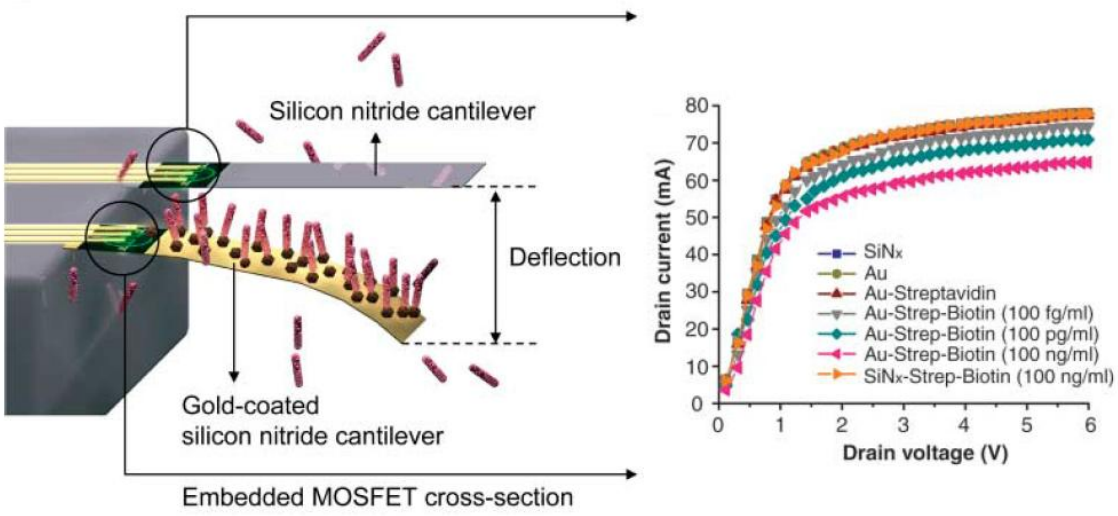

Figure 2.9: Microcantilever diagram and conductance curves for various concentrations of streptavidin.

QCM sensors rely on a quartz crystal, which oscillates at a base frequency of 10-20 MHz. The change in resonance frequency is proportionally to the change in mass on the crystal surface. QCM has been used for a variety of biosensing application, including detection of cholera toxin at 10^{-13} M and Herpes Simplex virus at single viron concentrations [37]. A drawback of QCM sensors is that they are highly temperature dependent and sensitivity is limited in aqueous sensing envrionments, as the density of proteins is often not that different from the water molecules being displaced. Typically, QCM experiments are performed after washing steps in dry air or a vacuum. Interestingly, Tombelli *et al.* have shown SPR to be more sensitive than QCM in detecting viral proteins [38].

2.5 Comparison to Lateral Flow Immunoassay Biosensors

A major advantage of the LEAC chip is its simplicity compared to other photonic sensing platforms. In this context, it is essential to mention the most affordable and simplest of portable biosensors. Lateral

flow immunoassays (LFIs) are robust and simple colorimetric diagnostic devices, which employ a paper-based (nitrocellulose) test strip housed in a plastic package. LFIs can be used to detect a variety of analytes, including toxic agents [39], drugs [40], biomarkers and infectious diseases [41-44] from raw fluid specimens, including water samples, saliva, urine, serum and whole blood. Commercialized versions of LFIs include urine-based pregnancy tests [45] and saliva-based HIV tests [46].

In contrast to other sensing platforms, lateral flow immunoassays (LFIs) do not require external readout equipment or an external power source [47]. Due to this inherent simplicity, they are typically inexpensive and ideal for point of care environments, particularly those where a simple binary (positive or negative) diagnostic reading is required.

The major drawbacks of LFIs are a lack of sensitivity compared to ELISA, the inability to provide analyte concentration information without external readout equipment [48], the inability to perform real-time binding measurements and the inability for the sensing layer to be re-used. For biomarkers, such as C-reactive protein (CRP) and heat shock protein 70 (HSP70) [49], it is the concentration that provides diagnostic value rather than the mere presence of the analyte. Thus, the LEAC chip may be advantageous in settings where expensive and bulky external readout equipment cannot be deployed.

The operating principle behind lateral flow immunoassays is straightforward and illustrated in Fig. 2.10, reproduced from ref. [40].

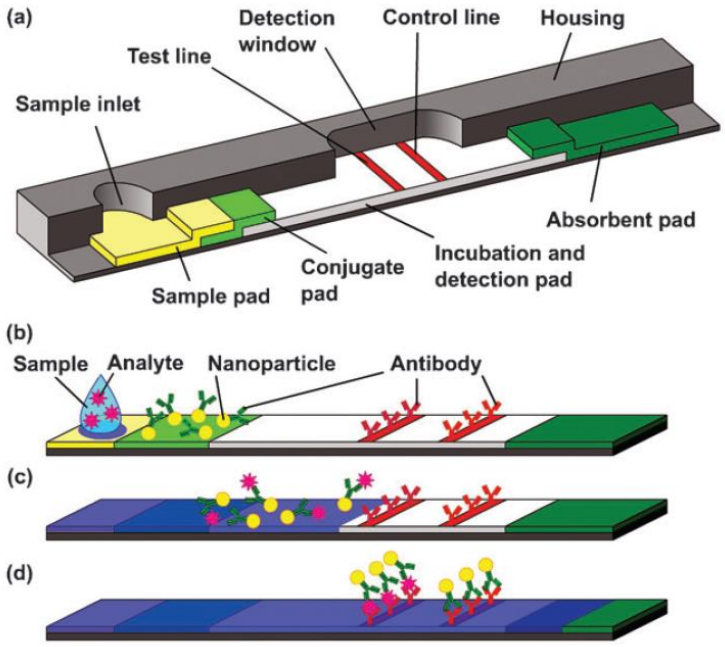

Figure 2.10: Lateral Flow Immunoassay

In a typical LFI, the fluid sample specimen (such as a drop of blood) is added to the sample well. Then a buffer solution is added to the well, which causes the sample to move along the paper test strip via capillary and wetting forces. As the fluid sample moves along, it picks up a labeling antibody (typically conjugated to colloidal gold). If the analyte being tested for is present, it will bind to the labeling antibody. As the analyte-labeling antibody complex moves down the paper strip, it first encounters a detection line, which is impregnated with a detection antibody directed against a different region of the analyte than the labeling antibody. Only if the analyte is present will the labeling antibody become immobilized on the detection line causing a change in color. If the analyte is not present, there is ideally no change in color as the labeling antibody will not bind to the detection line. A control line is located after the detection line. It is functionalized with a different probe molecule, which always binds to the labeling antibody, regardless of whether or not the analyte is present in the fluid sample. It exists to show that the test has been carried out properly by ensuring that the labeling antibody has had a chance to reach the control region.

The test is read visually, whereby a darkened detection line indicates presence of the analyte, so long as the control line has also been darkened. In the less common competitive assay format, the presence of the analyte competes with a label probe molecule for binding spots on the detection line. In this case, a blank or unchanged detection line indicates the presence of the analyte.

2.6 Aromatic Hydrocarbon Water Contaminant Sensors

To deploy the LEAC technology in a direction well-suited for refractive index-based sensing, the LEAC sensor has been functionalized for detection of the aromatic hydrocarbon contaminants benzene, toluene and xylene (BTX) in groundwater using a Teflon AF sensing film [51,52]. We have demonstrated that BTX contaminants preferentially diffuse into the film with partition coefficients exceeding two orders of magnitude. As BTX contaminants diffuse into the porous, low index (n=1.31) film, the film's refractive index increases leading to a measurable signal change. We have demonstrated detection of benzene, toluene and xylene at concentrations of of 359 ppb, 249 ppb and 103 ppb, respectively. The chip is readily capable of broad-based exclusionary sensing, but can also be used to identify single BTX analytes based on measurement of their unique diffusion coefficients into the film, provided that a single dominant contaminant is present.

As transporting water samples back to laboratory for analysis can be time-consuming and expensive, it is especially important for groundwater sensors to be portable, have low energy requirements and provide rapid sensing capabilities. In order to detect contamination events in real-time, it is equally important that the sensor has the potential to be embedded in the vicinity of potential contaminant sources for long-term monitoring and not require an operator for sample processing. This is an area, where the LEAC chip's small form factor, non-ionic sensitivity and potential for full integration may be very advantageous.

Current state-of-the art sensing technologies such as gas chromatography-mass spectrometry (GC-MS) [53-54] and gas chromatography-flame ionization detector (GC-FID) [55-57] can selectively detect BTX contaminants with exquisite sensitivity at ppt concentrations. In both GC-MS and GC-FID, the fluid is

typically pre-treated via techniques such as dynamic headspace trap sampling, in order to enrich the concentration of volatile contaminants in the sample medium. Then the volatiles are spatially separated using a chromatography column with flow driven by an inert carrier gas. For GC-MS, volatiles are identified by their charge to mass ratio in conjunction with time of flight diffusion data. In contrast, for GC-FIC, where all volatiles are combusted in a hydrogen flame producing ions measured as a current, chromatic separation is the chief means for analyte identification. As it is not economically feasible or environmentally friendly to run carrier gases, burn hydrogen and power a high-voltage mass-spec equipment around the clock, there is presently a need develop lower-cost portable sensing technologies.

In recent years, a number of groups have developed increasingly portable devices capable of detecting BTEX solutes in water. These devices include absorption spectroscopy based sensors in the UV [58], near-IR [59-61], mid-IR [62,63] and IR [64], quartz crystal microbalance sensors [65], enzymatic fluorescence based sensors [66], and surface wave acoustic sensors [67]. While these devices generally have simpler instrumentation requirements than either GC-MS or GC-FID, they still require significant external instrumentation, including optical spectrum analyzers, network analyzers, external broadband sources and external optics. The sensing performance and external equipment required for each sensor is summarized in Table 2.

Table 2.2: BTX Contaminant Sensors

Sensing Modality	Limit of Detection Range	External Components
LEAC Chip [52]	~100 ppb	PCB board and laser diode
GC-MS [53]	~0.1 ppt	mass spec, GC column, cryo trap, etc.
GC-FID [55]	~0.1 ppt	FID, GC columne, liquid phase microextraction
UV Abs. Spectroscopy [58]	300 ppt	bubble extractor, UV sources, UV spectrometer
NIR Abs Spectroscopy [59]	1 ppm	NIR source, NIR spectrometer
Mid-IR Spectroscopy [63]	~1 ppm	Mid-IR source, Mid-IR spectrometer
Quartz Cyrstal Monitor [65]	300 ppb to 5 ppm	Stanford Research Systems QCM, carbon nanotubes
Enzymatic Biosensor [66]	300 ppb for toluene only	LED, spectrometer, specialized enzyme
Surface Acoustic Wave [67]	~500 ppb	pizeo crystal, frequency generator, readout circuitry

2.7 Summary

Researchers have made impressive strides for developing label-free biosensor instrumentation and portable BTEX sensors. Each sensor presented is unique in terms of sensing mechanism, external instrumentation requirements, cost and form factor. The remainder of this dissertation describes both the research that has gone into optimizing the LEAC chip's sensing performance and experimental validation of its performance in practical sensing applications, including bulk refractive index sensing in fluids, groundwater contaminant sensing and biosensing.

Chapter 2 References

[1] Ward, C. L., M. H. Dempsey, C. J. A. Ring, R. E. Kempson, L. Zhang, D. Gor, B. W. Snowden, and Margaret Tisdale. "Design and performance testing of quantitative real time PCR assays for influenza A and B viral load measurement." *Journal of clinical virology* 29, no. 3 (2004): 179-188.

[2] M. Sumetsky, R.S. Windeler, Y. Dulashko, and X. Fan, "Optical liquid ring resonator," *Optics Express*, 2007, 15, 14376-14381

[3] K.D. Vos, I. Bartolozzi, E. Schacth, P. Bienstman, R. Baets, "Silicon-on-Insulator microring resonator for sensitive and label-free biosensing," *Optics Express*, 2007, 15 7610-7615

[4] M. Iqbal, M. A. Gleeson, B. Spaugh, F. Tybor, W. G. Gunn, M. Hochberg, T. Baehr-Jones, R. C. Bailey, and L. C. Gunn, *IEEE J. Sel. Top. Quant*., 2010, 16 (3), 654-661.

[5] D. Monzon-Hernandez and J. Villatoro, "High resolution refractive index sensing by means of a multiple-peak surface plasmon resonance optical fiber sensor," *Sens. Actuators B*, 2006, 115, 227-231.

[6] Radan Slavík, Jiří Homola, "Ultrahigh resolution long range surface plasmon-based sensor," *Sens. Actuators B*, 2007, 123, 10-12.

[7] Preechaburana, Pakorn, et al. "Surface Plasmon Resonance Chemical Sensing on Cell Phones." *Angewandte Chemie* 2012, 124,11753-11756.

[8] Z. Tian, S. Yam, J. Barnes, W. Bock, P. Greig, J. Fraser, H. Loock, and R. Oleschuk, "Refractive Index Sensing With Mach-Zehnder Interferometer Based on Concatenating Two Single-Mode Fiber Tapers," *IEEE Phontonics Technology Letters*, 2008, 20, 626-628.

[9] Z. Tian, S. Yam, H. Loock, "Refractive index sensor based on an abrupt taper Michelson interferometer in a single-mode fiber," *Optics Letters*, 2008, 33, 1105-1107.

[10] B. Luff, J. Wilkinson, J. Piehler, U. Hollenbach, J. Ingenhoff, and N. Fabricius, "Integrated Optical Mach-Zehnder Biosensor," *J. Lightwave Technol*., 1998, 16, 583-592.

[11] Crespi, A., Gu, Y., Ngamsom, B., Hoekstra, H. J., Dongre, C., Pollnau, M., ... & Osellame, R. (2010). Three-dimensional Mach-Zehnder interferometer in a microfluidic chip for spatially-resolved label-free detection. *Lab on a Chip*, 10(9), 1167-1173.

[12] Lillie, J. J., Thomas, M. A., Jokerst, N. M., Ralph, S. E., Dennis, K. A., & Henderson, C. L. (2006). Multimode interferometric sensors on silicon optimized for fully integrated complementary-metal-oxide-semiconductor chemical-biological sensor systems. *JOSA B*, 23(4), 642-651.

[13] Ymeti, A., Kanger, J. S., Greve, J., Lambeck, P. V., Wijn, R., & Heideman, R. G. (2003). Realization of a multichannel integrated Young interferometer chemical sensor. *Applied Optics*, 42(28), 5649-5660.

[14] Mandal, S., & Erickson, D. (2008). Nanoscale optofluidic sensor arrays. *Optics Express*, 16(3), 1623-1631.

[15] D. Wu, B. Kuhlmey and B. Eggleton, "Ultrasensitive photonic crystal fiber refractive index sensor," *Optics Letters*, 2009, 34, 322-324.

[16] A. Iadicicco, S. Campopiano, A. Cutolo, M. Giordano and A. Cusano, "Refractive Index Sensor Based on Microstructure Fiber Bragg Grating," *IEEE Photonics Tech. Letters*, 2005, 17, 1250-1252.

[17] Z. Ran, Y. Rao, W. Liu, X. Liao and K. Chiang, “Laser-micromachined Fabry-Perot optical fiber tip sensor for high-resolution temperature-indepenent measurement of refractive index,” *Optics Express,* 2007, 16, 2252-2263.

[18] Vollmer, Frank, and Stephen Arnold. "Whispering-gallery-mode biosensing: label-free detection down to single molecules." *Nature methods* 5, no. 7 (2008): 591-596.

[18b] Armani, Andrea M., Rajan P. Kulkarni, Scott E. Fraser, Richard C. Flagan, and Kerry J. Vahala. "Label-free, single-molecule detection with optical microcavities." *science* 317, no. 5839 (2007): 783-787.

[19] Liu, Qing, Xiaoguang Tu, Kyung Woo Kim, Jack Sheng Kee, Yong Shin, Kyungsup Han, Yong-Jin Yoon, Guo-Qiang Lo, and Mi Kyoung Park. "Highly sensitive Mach–Zehnder interferometer biosensor based on silicon nitride slot waveguide." *Sensors and Actuators B: Chemical* 188 (2013): 681-688.

[20] Almeida, Vilson R., Qianfan Xu, Carlos A. Barrios, and Michal Lipson. "Guiding and confining light in void nanostructure." *Optics letters* 29, no. 11 (2004): 1209-1211.

[21] Barrios, Carlos A., Kristinn B. Gylfason, Benito Sánchez, Amadeu Griol, Hans Sohlström, Miquel Holgado, and Raphael Casquel. "Slot-waveguide biochemical sensor." *Optics letters* 32, no. 21 (2007): 3080-3082.

[22] Homola, Jiří, Sinclair S. Yee, and Günter Gauglitz. "Surface plasmon resonance sensors: review." *Sensors and Actuators B: Chemical* 54, no. 1 (1999): 3-15.

[23] Barrios, Carlos Angulo. "Ultrasensitive nanomechanical photonic sensor based on horizontal slot-waveguide resonator." *Photonics Technology Letters, IEEE* 18, no. 22 (2006): 2419-2421.

[24] Tu, Xiaoguang, Junfeng Song, Tsung-Yang Liow, Mi Kyoung Park, Jessie Quah Yiying, Jack Sheng Kee, Mingbin Yu, and Guo-Qiang Lo. "Thermal independent silicon-nitride slot waveguide biosensor with high sensitivity." *Optics express* 20, no. 3 (2012): 2640-2648.

[25] Barrios, Carlos A., Maria Jose Banuls, Victoria Gonzalez-Pedro, Kristinn B. Gylfason, Benito Sanchez, Amadeu Griol, Angel Maquieira, Hans Sohlström, Miquel Holgado, and R. Casquel. "Label-free optical biosensing with slot-waveguides." *Optics letters* 33, no. 7 (2008): 708-710.

[26] Robinson, Jacob T., Long Chen, and Michal Lipson. "On-chip gas detection in silicon optical microcavities." *Optics Express* 16, no. 6 (2008): 4296-4301.

[27] Erickson, T.A.; Lear, K.L., "Optimization of the Local Evanescent Array-Coupled Optoelectronic Sensing Chip for Enhanced, Portable, Real-Time Sensing," *Sensors Journal, IEEE* , vol.13, no.5, pp.1905,1913, May 2013

[28] Homola, J., Yee, S. S., & Gauglitz, G. (1999). Surface plasmon resonance sensors: review. *Sensors and Actuators B: Chemical*, *54*(1), 3-15.

[29] Goda, Tatsuro, and Yuji Miyahara. "Label-free and Reagent-less Protein Biosensing using Aptamer-modified Extended-gate Field-effect Transistors."*Biosensors and Bioelectronics* (2013).

[30] Gao, Xuan PA, Gengfeng Zheng, and Charles M. Lieber. "Subthreshold regime has the optimal sensitivity for nanowire FET biosensors." *Nano letters* 10.2 (2009): 547-552.

[31] Allen, Brett Lee, Padmakar D. Kichambare, and Alexander Star. "Carbon Nanotube Field-Effect-Transistor-Based Biosensors." *Advanced Materials* 19.11 (2007): 1439-1451.

[32] Nair, Pradeep R., and Muhammad A. Alam. "Screening-limited response of nanobiosensors." *Nano letters* 8.5 (2008): 1281-1285.

[33] Kim, Ansoon, et al. "Ultrasensitive, label-free, and real-time immunodetection using silicon field-effect transistors." *Applied Physics Letters* 91.10 (2007): 103901-103901.

[34] Ziegler, Christiane. "Cantilever-based biosensors." *Analytical and bioanalytical chemistry* 379, no. 7-8 (2004): 946-959.

[35] Wu, Guanghua, Ram H. Datar, Karolyn M. Hansen, Thomas Thundat, Richard J. Cote, and Arun Majumdar. "Bioassay of prostate-specific antigen (PSA) using microcantilevers." *Nature biotechnology* 19, no. 9 (2001): 856-860.

[36] Shekhawat, Gajendra, Soo-Hyun Tark, and Vinayak P. Dravid. "MOSFET-embedded microcantilevers for measuring deflection in biomolecular sensors." *Science* 311, no. 5767 (2006): 1592-1595.

[37] Marx, Kenneth A. "Quartz crystal microbalance: a useful tool for studying thin polymer films and complex biomolecular systems at the solution-surface interface." *Biomacromolecules* 4, no. 5 (2003): 1099-1120.

[38] Tombelli, S., M. Minunni, E. Luzi, and M. Mascini. "Aptamer-based biosensors for the detection of HIV-1 Tat protein." *Bioelectrochemistry* 67, no. 2 (2005): 135-141.

[39] Hossain, SM Zakir, Roger E. Luckham, Meghan J. McFadden, and John D. Brennan. "Reagentless bidirectional lateral flow bioactive paper sensors for detection of pesticides in beverage and food samples." *Analytical chemistry* 81, no. 21 (2009): 9055-9064.

[40] Wennig, R., M. R. Moeller, J. M. Haguenoer, A. Marocchi, F. Zoppi, B. L. Smith, R. De la Torre et al. "Development and evaluation of immunochromatographic rapid tests for screening of cannabinoids, cocaine, and opiates in urine." *Journal of analytical toxicology* 22, no. 2 (1998): 148-155.

[41] Ahn, Jae Soon, Sunga Choi, Sang Ho Jang, Hyuk Jae Chang, Jae Hoon Kim, Ki Bong Nahm, Sang Wook Oh, and Eui Yul Choi. "Development of a point-of-care assay system for high-sensitivity C-reactive protein in whole blood." *Clinica chimica acta* 332, no. 1 (2003): 51-59.

[42] Mens, Petra F., Aart van Amerongen, Patrick Sawa, Piet A. Kager, and Henk DFH Schallig. "Molecular diagnosis of malaria in the field: development of a novel 1-step nucleic acid lateral flow immunoassay for the detection of all 4 human< i> Plasmodium</i> spp. and its evaluation in Mbita, Kenya." *Diagnostic microbiology and infectious disease* 61, no. 4 (2008): 421-427.

[43] Lindsley, Mark D., Nanthawan Mekha, Henry C. Baggett, Yupha Surinthong, Rinrapas Autthateinchai, Pongpun Sawatwong, Julie R. Harris et al. "Evaluation of a newly developed lateral flow immunoassay for the diagnosis of cryptococcosis." *Clinical infectious diseases* 53, no. 4 (2011): 321-325.

[44] Schramm, Willfried, Stephen E. Wade, Gustavo Barriga Angulo, Patricia Castillo Torres, and Anthony Burgess-Cassler. "A simple whole-blood test for detecting antibodies to human immunodeficiency virus." *Clinical and diagnostic laboratory immunology* 5, no. 2 (1998): 263-265.

[45] Butler, Stephen A., Sarah A. Khanlian, and Laurence A. Cole. "Detection of early pregnancy forms of human chorionic gonadotropin by home pregnancy test devices." *Clinical chemistry* 47, no. 12 (2001): 2131-2136.

[46] Gallo, Dana, J. Richard George, John H. Fitchen, Andrew S. Goldstein, and Michael S. Hindahl. "Evaluation of a system using oral mucosal transudate for HIV-1 antibody screening and confirmatory testing." *JAMA: the journal of the American Medical Association* 277, no. 3 (1997): 254-258.

[47] Andreotti, Peter E., George V. Ludwig, Anne Harwood Peruski, James J. Tuite, Stephen S. Morse, and L. F. Peruski. "Immunoassay of infectious agents." *BioTechniques* 35, no. 4 (2003): 850-861.

[48] Posthuma-Trumpie, Geertruida A., Jakob Korf, and Aart van Amerongen. "Lateral flow (immuno) assay: its strengths, weaknesses, opportunities and threats. A literature survey." *Analytical and bioanalytical chemistry* 393, no. 2 (2009): 569-582.

[49] Eapen, Danny J., Pankaj Manocha, Riyaz S. Patel, Muhammad Hammadah, Emir Veledar, Christina Wassel, Ravi A. Nanjundappa et al. "Aggregate risk score based on markers of inflammation, cell stress, and coagulation is an independent predictor of adverse cardiovascular outcomes." *Journal of the American College of Cardiology* (2013).

[50] Mark, Daniel, Stefan Haeberle, Günter Roth, Felix von Stetten, and Roland Zengerle. "Microfluidic lab-on-a-chip platforms: requirements, characteristics and applications." *Chemical Society Reviews* 39, no. 3 (2010): 1153-1182.

[51] Erickson, Tim A., Rajvir Nijjar, Matt J. Kipper, and Kevin L. Lear. "Characterization of plasma-enhanced teflon AF for sensing benzene, toluene, and xylenes in water with near-IR surface plasmon resonance." *Talanta* 119 (2014): 151-155.

[52] Lab on a Chip Publication (in press hopefully)

[53] H. Kim, S. Kim, and S. Lee, *Talanta*, 2012, **97**, 432-437.

[54] H. Faraji, M. Tajbakhsh, and M. Helalizadeh, *Analytical Methods*, 2012, **4**, 3372-3380.

[55] A. Sarafraz-Yazdi, Z. Es' haghi, and S. Sepehr, *Analytical Methods*, 2010, **2**, 746-752.

[56] A. Sarafraz-Yazdi, A. H. Amiri, and Z. Es'haghi, *Talanta*, 2009, **78**, 936-941.

[57] Y. Assadi, F. Ahmadi, and M. Hossieni, *Chromatographia*, 2010, **71** 1137-1141.

[58] S. Camou, A. Shimizu, T. Horiuchi, and T. Haga, *IEEE Sensors*, 2009, 2021-2024.

[59] K. Lima, I. Raimundo, and M. Pimentel, *Sensors and Actuators B: Chemical*, 2007, **125**, 229-233.

[60] J. Buerck, S. Roth, K. Kraemer, M. Scholz, and N. Klaas, *Journal of hazardous materials*, 2001, **83**,11-28.

[61] W. Lai, S. Chakravarty, X. Wang, C. Lin, and R. Chen, *Applied Physics Letters*, 2011, **98**, 023304.

[62] R. McCue, J. Walsh, F. Walsh, and F. Regan, *Sensors and Actuators B: Chemical*, 2006, **114**, 438-444.

[63] B. Pejcic, L. Boyd, M. Myers, A.Ross, Y.Raichlin, A. Katzir, R. Lu, and B. Mizaikoff. *Organic Geochemistry*, 2013, **55**, 63-71.

[64] A. Silva, M. Santana, M.Pimentel, I.Raimundo, and Y. Almeida, *Sensors and Actuators B: Chemical*, 2009, **139**, 222-230.

[65] B. Pejcic, M. Myers, N. Ranwala, L. Boyd, M. Baker, and A. Ross, *Talanta*, 2011, **85**, 1648-1657.

[66] Z. Zhong, M. Fritzsche, S. Pieper, T. Wood, K. Lear, D. Dandy, and K. Reardon, *Biosensors and Bioelectronics*, 2011, **26**, 2407-2412.

[67] F. Bender, F. Josse, R. Mohler, and A. Ricco, *14th International Meeting on Chemical Sensors*, 2012, 473-476.

[68] Lesuffleur, Antoine, et al. "Laser-illuminated nanohole arrays for multiplex plasmonic microarray sensing." *Optics express* 16.1 (2008): 219-224.

Chapter 3: Performance Enhancement and Extended Capabilities of the 2nd Generation LEAC Chip

3.0 Development of the 2nd Generation LEAC Chip

The 1st generation Avago-fabricated LEAC chip that was used for sensing dried proteins [1] had several limitations, including high scattering loss, noisy photodetectors and a corresponding low signal to noise ratio (SNR). Furthermore, the chip lacked real-time measurement capability and was not compatible with fluids. For practical environmental and biosensing applications, a high SNR and fluidic compatibility are essential features.

In order to address the Avago chip's limitations, the LEAC chip was substantially redesigned. Major changes included implementation of low scattering loss waveguides, implementation of on-chip photocurrent reference regions, development of high-SNR Schottky barrier photodetectors, a new chip layout to support fluidic compatibility, optimization of waveguide dimensions based on rigorous simulations, and building a real-time, multi-channel data acquisition system. As a direct result of these changes, the 2nd generation LEAC chip's LOD has been improved by over two orders of magnitude. Additionally, the chip can now be used for sensing multiple analytes in wet environments. To provide an overview of the chapter, a brief explanation of each design improvement is described below. Subsequent sections of this chapter provide more exhaustive details.

3.0a Scattering Reduction

Several changes were implemented to reduce scattering loss. First, a continuous photodetector array was implemented, which enabled a smooth mode transition between photodetectors. In contrast, the segmented photodetector array of the Avago chip caused significant scattering due to mode mismatch in

the oxide region between the PolySi (polysilicon) photodetectors. Second, the waveguide width was increased, in order to reduce sidewall scattering losses. Third, photolithography was improved by using a very thin resist and reflowing it to smooth out the sidewalls. Fourth, the lower cladding material was changed from PECVD oxide to thermal oxide. PECVD oxide has significant surface roughness and is highly porous [2], which results in both surface and bulk scattering defects. Lastly, for biosensing chips, the core was changed from PECVD nitride to ALD-deposited HfO_2, which enabled full passivation in even high conductive environments.

3.0b Noisy Photodetectors and Low Photo to Dark Current Ratio

The Avago chip metallurgy included PolySi/Ti/Al contacts, which resulted in significant noise, likely from traps within the PolySi. A maximum SNR of ~120 was reported in ref. [1]. Also, IV Curves showed a lack of Schottky barrier. In order to form high Schottky barrier (SB), low-noise contacts, several different MSM photodetector designs were implemented. First, single crystal, silicon-on-insulator (SOI) p-type 100-200 ohm-cm wafers were used with p-Si/Ti/Al contacts. Photodetectors with a SB height of 0.53 eV and SNR of over 1200 were realized. These photodetectors had acceptable SNR for chip's fabricated with lossy PECVD oxide. However, when a thermal oxide was grown on top of the same substrate and etched, the barrier height dropped to ~0.43 eV and dark currents increased from ~15 nA to over 400 nA, turning the low-noise photodetectors into noisy photoconductors. (Recall that thermal oxide is required to produce a chip with low scattering losses.) Much effort went into using methods to artificially raise the barrier height on p-type thermal oxide chip photodetectors, such as plasma etching, chemical treatments and depositing a thin layer of oxide. None of these methods worked for thermal oxide chips.

In a last ditch effort, a n-type 1-5 ohm standard single crystal silicon substrate was used with the contact metallurgy switched from p-Si/Ti/Al to either n-Si/Au/Cr/Al or n-Si/Pt/Cr/Al, in order to create a high Schottky barrier height on n-type Si. Fortunately, high Schottky barrier (~0.7 eV) photodetectors were

realized on thermally oxidized chips employing this metallization scheme. Dark currents of <1 nA were realized with an SNR of ~3000-8000. This was a major step forward, as chips could now be fabricated with low-noise photodetectors and low-loss waveguides.

3.0c Fluid Handling

The chip's layout was changed using a new mask set to accommodate a fluidic channel. A fluid channel compatible with the chip was designed in Solidworks and fabricated in the CSU machine shop. Fig. 3.1 shows the general layout used for the PECVD oxide chip, while Fig. 3.2 shows the channel design and a photograph of the channel mounted to a LEAC chip. Please note that the PECVD chip was not well-passivated when handling conductive fluids, so thermal oxide in conjunction with ALD-deposited halfnia and Teflon AF were used as a moisture barrier for the wet passivation.

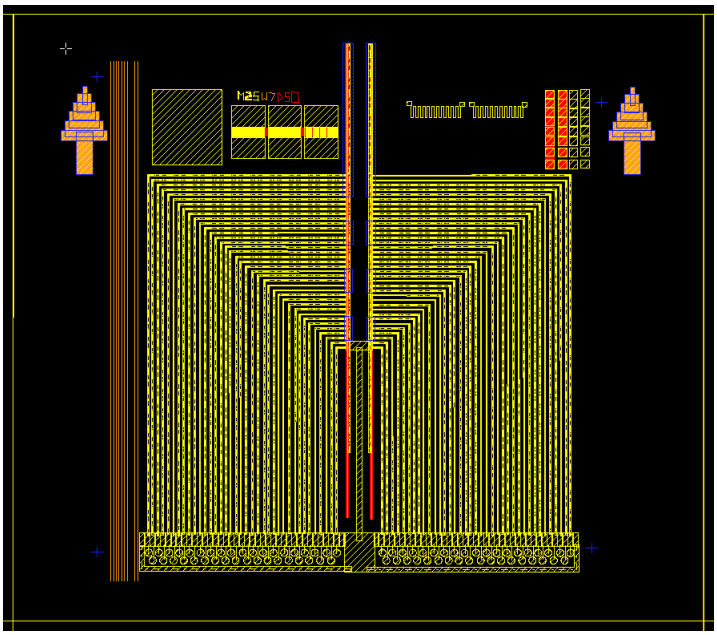

Figure 3.1: LASI Layout of 2nd Gen Chip. The chip is 1.2 cm x 1.4 cm. Two waveguides are seen in the center of the image, extending from the top and truncating several mm before the bottom. A photodetector is located beneath each waveguide. The photocurrent from each waveguide is measured by placing a probe card on the small rectangular probing pads near the bottom of the image in yellow. The small circles adjacent to the probe pads are available for wire bonding. As can be seen from the image, the majority of chip space is used for metal routing wires, which enable photocurrent measurement at specific locations along the waveguide. This mask set was exclusively used for oil RI sensing experiments.

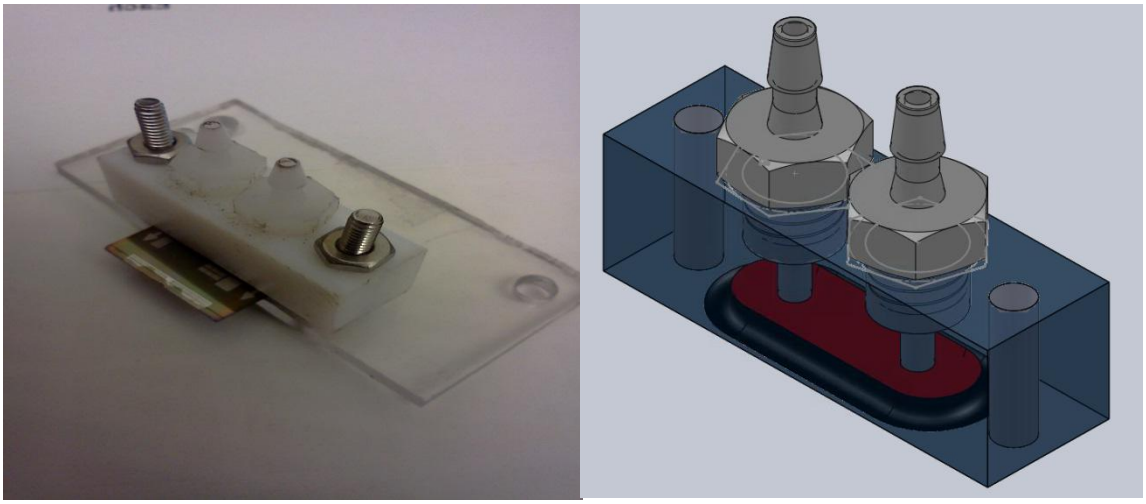

Fig 3.2: Fluid channel fabrication and design

3.0d Real-Time Measurement Capability

Real-time measurement capability is essential for both binding kinetics and diffusion measurements. To allow for portability, a custom, 8-channel, single-supply, transimpedance amplifier (TIA) circuit was simulated and implemented on a PCB board. The amplifier circuit is connected to the LEAC chip using a probe card, and an external ADC is connected to a computer running Labview for automated data acquisition. Up to 8 channels can be measured simultaneously, for real-time data acquisition. Fig. 3.3 is a picture of the 8-channel TIA PCB layout.

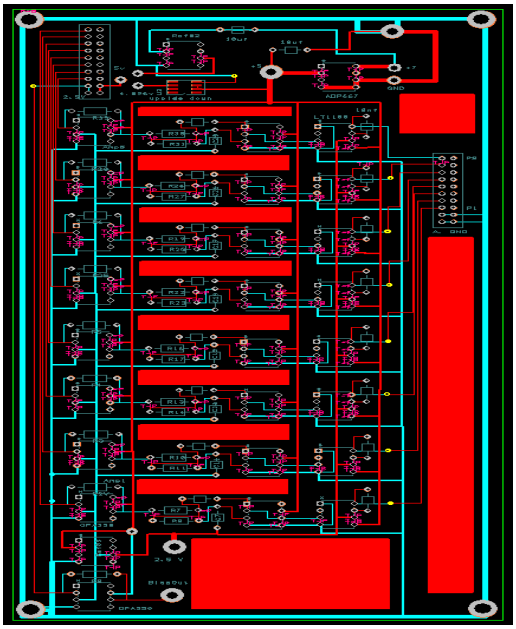

Fig 3.3: PCB Layout for n-type transimpedance amplifier for n-type thermal oxide chips

3.0e Fluidic Sensing Capability

The 1st generation LEAC chip was designed to work in air. Many measurements of interest take place in liquids. As such, the LEAC's waveguide dimensions were optimized for both oil sensing and aqueous biosensing using a number of rigorous simulation tools, including Optiwave FDTD software, FIMMPROP eigenmode expansion software and a full-vector finite difference modesolver. These tools enabled the effects of core thickness, core width, core index, lower cladding thickness, wavelength, scattering and upper cladding index to be numerically investigated. From simulation results, these variables were tuned to maximize signal modulation, while permitting sufficient mode propagation to generate a strong signal in all sensing regions.

3.1 Motivation for An Improved Development Process and Chip Design

During the first year of my graduate studies, very little progress was made in fabricating a functional LEAC chip. I initially started fabricating chips using a mask set designed by one of Dr. Lear's former graduate students and a PolySi starting wafer. Similar to the Avago chip, the PolySi/Ti/Al metal contacts

produced noisy photodetectors. For an entire semester, I failed to produce a chip with a waveguide that could either couple light or propagate sufficient light into the chip's sensing region. Some problems resulted from a total lack of knowledge in proper microfabrication procedures, especially photolithography. Fig. 3.4 shows one of the first waveguides I fabricated in the CSU cleanroom. As one may guess, it had exceptionally high scattering losses, resulting from significant sidewall roughness and photoresist scum remaining on the waveguide.

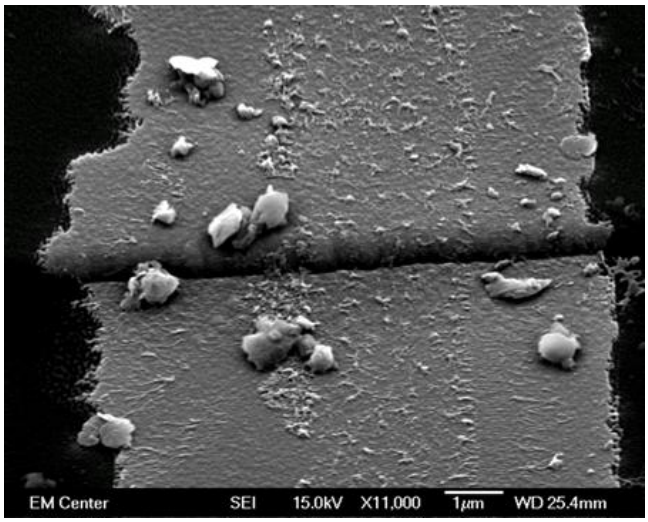

Figure 3.4: One of the first waveguides the author fabricated in the CSU cleanroom had exceptionally poor optical characteristics

Even when photolithography was improved (Fig. 3.5), significant scattering resulted from a 250 nm step that was built into the waveguide due to a design flaw in the mask set I inherited. Segmented detectors (discussed in Section 3.6) produced additional scattering losses.

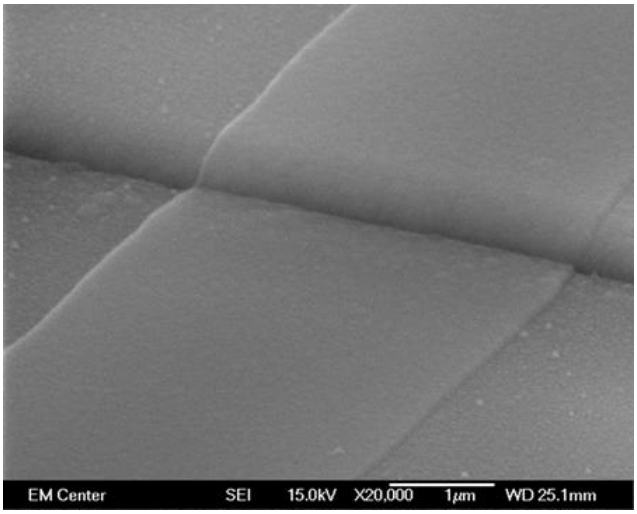

Figure 3.5: Step in waveguide resulted in significant scattering

There were also issues related to quality and dimensions of the dielectric films used to build the chip's waveguide. The standard recipes provided in the CSU PECVD log book resulted in extremely brittle films, which cracked during polishing, resulting in very poor waveguide facets that didn't couple light (Fig. 3.6). Additionally, a former student had constructed significant portions of the chip holder on the polisher out of double-sided sticky tape, which caused the chip to bounce around on the polishing wheel, increasing forces on the waveguide facet, which served to further aggravate the fracturing problem.

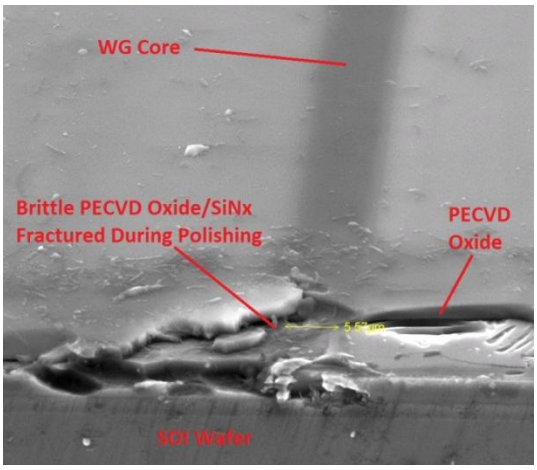

Figure 3.6: Initially, brittle PECVD films produced waveguide facets with nearly zero percent coupling efficiency

Furthermore, prior device models [3] produced by another graduate student indicated that a 500 nm thick lower cladding would provide an optimal signal. In reality, such a thin lower cladding results in attenuation losses exceeding 1000 dB/cm, causing nearly all of the light to leak out of the waveguide within several hundred microns. Without a robust device model, it was not possible to quantitatively understand how the waveguide's dimensions affected device performance. (In fact, the magnitude of photodetector coupling is exponentially sensitive to both lower cladding and core thickness.)

After some time, chips were finally fabricated with waveguides that could propagate light into the sensing region (Fig 3.7a). However, when SU8 polymer was patterned on the chip to form a microfluidic channel, light was observed to almost entirely scatter out of the waveguide, as shown in Fig 3.7b). It was later determined the light was cutoff due the large mode mismatch at the air/SU8 and SU8/water interfaces.

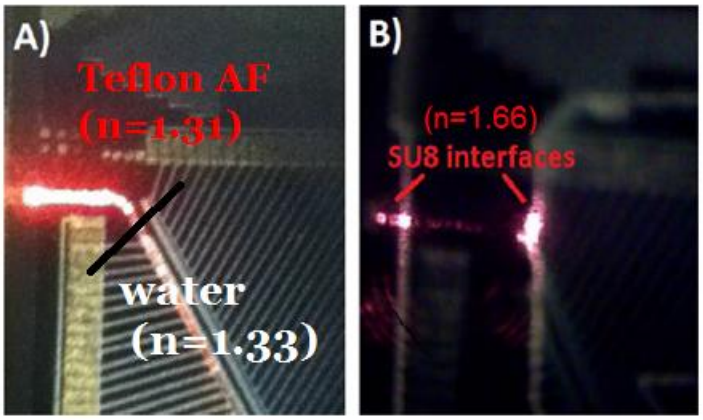

Figure 3.7: A) Guided mode propagation in air and B) mode cutoff due to scattering at SU8 interface

The long series of initial failures proved to be a valuable learning experience, providing the impetus to rigorously understand the physics underlying the LEAC chip and develop both the materials science knowledge and fabrication expertise necessary to develop an optimized 2nd generation LEAC chip, which has pushed the envelope of the sensing platform and improved the chip's LOD by a factor of roughly 100x.The development process was guided by both a rigorous analysis and significant experimental work with the goal of optimizing the chip's sensitivity, improving the LOD by increasing photodetector SNR,

and enabling real-time measurement in fluids. The development process was guided by a robust device model, which quantified how device sensitivity and LOD were functions of scattering, waveguide dimensions, and photodetector precision. The device model and corresponding physics are now presented, as they provide a context for significant changes to the waveguide structure and photodetector discussed later in the chapter.

3.2 Device Modeling

The fundamental analytical equation that motivates design the LEAC chip's waveguide structure is the well-known formula [4] for the evanescent decay length constant *d* of planar dielectric waveguide with effective index N_{eff} and cladding index $n_{cladding.}$

$$d = \frac{1}{\frac{2\pi}{\lambda}\sqrt{{N_{eff}}^2 - {n_{cladding}}^2}} \text{ (Eq. 3.1)}$$

Based on Eq. 3.1, an interesting phenomenon happens when the waveguide is designed to be close to cutoff. At cutoff, the denominator is zero, so the evanescent tail length is infinite and there is no guided mode. However, a small increase N_{eff} due to analyte binding or diffusion into the waveguide's upper cladding results in a finite value for *d* and the development of a guided mode. At first glance, for a waveguide fabricated right at cutoff, the photocurrent modulation $(\Delta I/I_o)$ for a very small index change appears to infinite, as the smallest change in N_{eff} causes coupling to go from infinity to a finite value. As first described by Yan *et al*. [5], for binding of a very thin adlayer, the light intensity modulation ratio (sensitivity) at a distance s_{lc} below the core for evanescent decay constants with the adlayer γ_{ad} and without the adlayer γ_o is given by,

$$\frac{\Delta I}{I_o} = -2(\gamma_{ad} - \gamma_o)s_{lc} \text{ (Eq. 3.2)}$$

Thus the normalized response is proportional to the separation distance *s* between the core and photodetector. In theory, one could achieve a nearly infinite sensitivity by placing the photodetector

hundreds of decay lengths below the core. Both theoretical analysis and numerical simulations indicate Eq. 3.2 to be correct. However, there is a fundamental tradeoff. For large values of s_{lc}, there is very little optical power coupled into the optical detector and the small signal becomes overwhelmed by a combination of background scattered light and photodetector noise. Furthermore, numerical simulations indicated that the presence of the Si photodetector itself, even when located several decay lengths below the waveguide core, fundamentally alters the shape and characteristics of the guided mode. A number of simulation tools were employed to model the LEAC chip's waveguide and fine tune device parameters subject to scattering and photodetector noise. The 2nd generation LEAC chip's waveguide structure was modeled using OptiWave FDTD software, FIMMPROP Eigenmode Expansion software, and a Matlab-compatible full-vector finite difference mode solver.

3.2.1 FDTD Modeling

FDTD (Finite Difference Time Domain) was initially used for device modeling as it is the most rigorous simulation technique available. OptiWave FDTD software was used to simulate the effect of protein adlayer thickness on photodetector coupling. Unfortunately, FDTD had several major drawbacks. Due to time and memory constraints, only a 2-d structure could be simulated, and it took over six hours to run a simulation for a 200 micron length waveguide on a quad-core machine. However, FDTD simulations did reveal reveal a particularly interesting feature of mode propagation in simulated LEAC devices, which included the Si photodetector.

A 2d LEAC waveguide structure was simulated with a water (n=1.33) upper cladding, 70 nm SiNx (n=1.8) core, and 1750 nm SiO_2 (n=1.46) lower cladding fabricated on top of a 5 micron thick (n=3.84 + 0.013i) Si wafer. The initial mode launched into the structure was calculated based on using on the dielectric layers of the structure (i.e. no Si). The evanescent field shift effect is seen in FDTD modeling, as evidenced by the decreased intensity falloff for thicker protein adlayers. As indicated in Fig 3.8, the

software was unable to launch a fully guided mode into the waveguide structure, as evidenced by the damped oscillations in the TE Mode intensity.

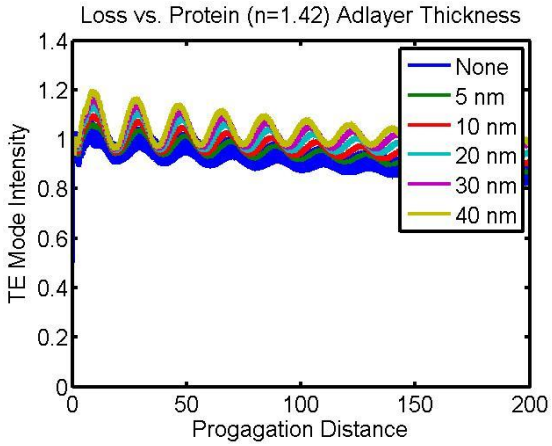

Figure 3.8: FDTD Modeling Results of a 2-d Structure

A cross section of the mode structure revealed something particularly interesting. The cross section was taken after a propagation length of 150 microns, indicated by the red line in Fig. 3.9a. A plot of the cross section is shown in Fig. 3.9b.

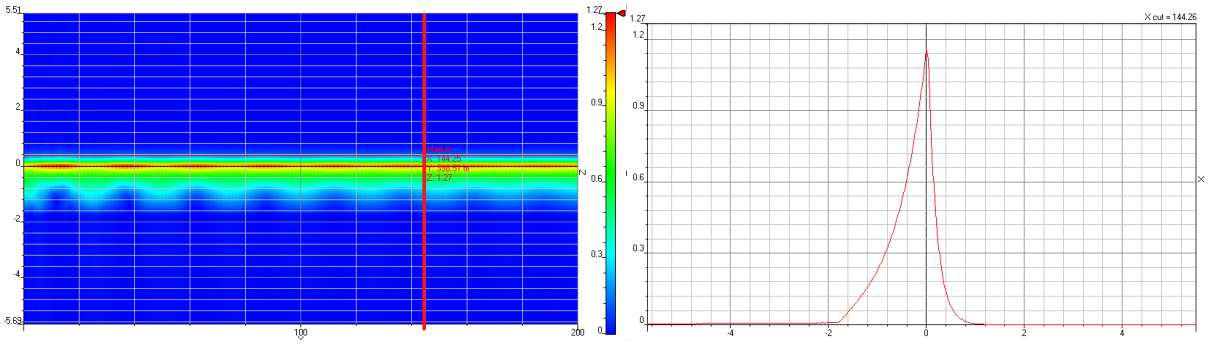

Fig. 3.9: A) Red line indicates where cross section is taken. B) Field plot of cross section which shows "mode pinching" caused by the presence of the Si photodetector

For a waveguide structure with no silicon, the evanescent decay into the lower cladding is typically smooth. In contrast, the presence of the Si photodetector causes the electric field strength to abruptly drop at the SiO_2/Si interface. The presence of the photodetector fundamentally alters the shape of the mode, causing it be "pinched off" at the interface. This effect was further confirmed by the other simulation tools. Given time constraints and the desire to simulate the full cross section of the waveguide structure, the application of FDTD modeling was limited to the effects described in this section in addition to visualizaing the importance of upper cladding mode matching (section 3.6c) and designing a grating coupler (Appendix E).

3.2.2 FIMMPROP

FIMMPROP is optical simulation software, which uses the eigenmode expansion method. It works by slicing the structure into multiple horizontal layers in the vertical direction, finding the modal solutions to each layer, and then stitching together a solution for the total structure based on E-field continuity. FIMMPROP can rapidly solve for solutions of 2D structures, but like FDTD, it is rather slow at simulating 3D structures. For this reason, it was only used predominantly for grating coupler design. However, like FDTD, several 2-d simulations were performed to model the effect of lower cladding thickness on photodetector coupling magnitude. Notably, 2D FIMMPROP results of planar waveguides (infinite width) were found to be in reasonable agreement with full-vector finite difference mode solver results as described in 3.2.3. (The mode solver was used as the primary simulation tool). The plot below shows both FIMMPROP and Modesolver results for photodetector coupling loss for a 4micron wide waveguide with a 70 nm thick SiNx core (n=1.8) for various oxide (n=1.46) lower cladding thicknesses. The upper cladding is water (n=1.33).

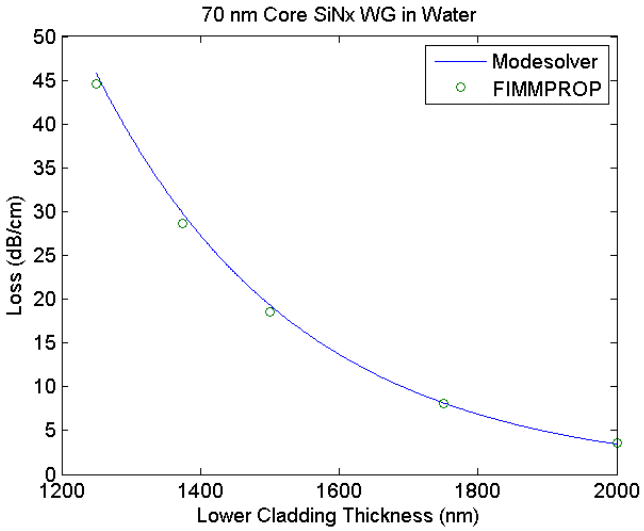

Figure 3.10: Agreement between FIMMPROP and Modesolver Results

FIMMPROP was also used to study the effect of lower cladding thickness and ambient sensing medium on device modulation for a 5 nm thick protein adlayer. For a 100 nm core waveguide with a 1500 nm lower cladding operating in air, the modulation response *M*, defined as $M=1-I_{final}/I_{initial}$ for a 5 nm thick protein film (n=1.42) is 4.8%/nm vs. 1.6%/nm for a 70 nm core waveguide in water. Thus, the LEAC chip is about 3 times more sensitive, while working in air than in water. The increased responsivity in air is likely due to the increased perturbation in air (Δn=0.42) vs. water (Δn=0.09) The stronger the perturbation, the greater the signal. This general statement can be proven somewhat rigorously using perturbation theory [4]. The change in the propagation constant $\delta\beta$ by a perturbation $\Delta\varepsilon$ for the single-mode field distribution $E(x,y)$ is given by

$$\delta\beta = \frac{\omega}{4}\iint E(x,y)^{*}\,\Delta\varepsilon(x,y)\,E(x,y)\,dxdy \quad \text{(Eq. 3.3)}$$

Eq. 3.3 serves as a guiding equation for designing evanescent field sensors. It shows the greatest change in propagation constant, and hence effective index can be achieved by both maximizing the field overlap with perturbation and increasing the index contrast of the perturbation. Short of changing the index of the ambient sensing medium from water to air, there is relatively little that can be done to increase $\Delta\varepsilon$, so

sensor design is limited to engineering a device structure, which maximizes field overlap and provides a precise measurement of the change in field distribution.

3.2.3 Full-Vector Finite Difference Modesolver

The full-vector finite difference modesolver [6] first described by Fallahkhair *et al.* was used as the primary simulation tool for device modeling as its provides rigorous modal solutions to Maxwell's equations, calculates solutions in several minutes (rather than hours) and importantly, enables simulation of the ridge waveguide's cross section, rather than assuming an infinite planar waveguide. This in turn, allows waveguide dimensions to be tailored, so that only a single mode is supported (Appendix H). An initial round of simulations for core widths of 2, 3, 4, 5, 6, 7 and 8 μm showed that a 4 μm was the largest width that could support a single mode for waveguides far enough from cutoff so as to allow a sufficient amount of optical power to reach the sensing region. The 4 μm core width w is preferred over smaller single mode widths to reduce sidewall scattering losses, which are proportional to $1/w^4$ [7]. As such, all simulations described in this section correspond to 4 μm core width. To further reduce sidewall scattering losses, the ridge structure need to be only partially etched. For all simulations, an etch depth equal to 50% of the core thickness was used, which was the same etch depth used for LEAC chips fabricated for experiments.

The modesolver proved to be an exceptionally accurate tool for modeling the LEAC chip and was used optimize waveguide dimensions for all upper cladding sensing environments. Confidence in the simulation tool was arrived at from several angles. First, the modesolver was found to be in nearly perfect agreement with analytic solutions for a planar waveguide when a 100 micron wide waveguide was used to approximate a planar waveguide. Second, the modesolver was found to be in reasonably good agreement with 1-d commercial software packages. Most importantly, experimental results were found to be in excellent agreement with modesolver predictions, as discussed in chapters 4, 5 and 6.

Modal solutions for LEAC chips designed for oil sensing, BTEX sensing, and biosensing are shown in Fig. 3.11. A description of each waveguide is provided in Table. 3.1. In Fig. 3.11, the lateral lines indicate the position of the upper cladding, lower cladding, and silicon, respectively. The thin core is not visible in the image, but is located just above the line separating the upper and lower cladding regions. The fraction of the field present in the upper cladding sensing region is found to be much higher for the oil sensing waveguide than the biosensing and BTX sensing waveguides, consistent with the evanescent field shift effect.

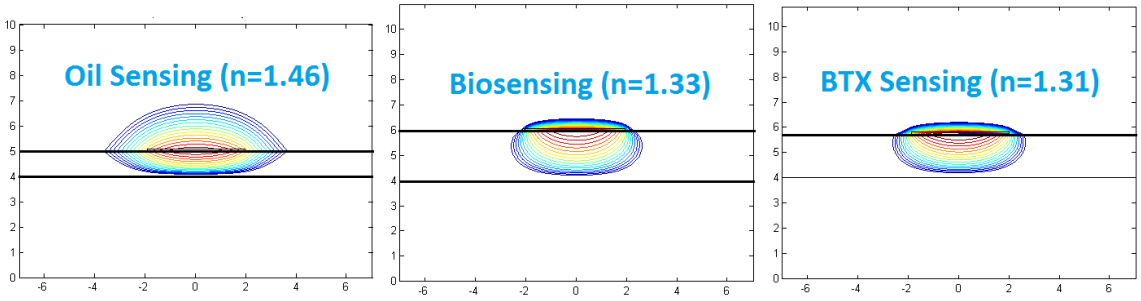

Figure 3.11: Modesolver simulation results for fundamental TE Mode of LEAC waveguides used for sensing in different upper cladding environments. The biosensing waveguide (middle) is designed to work with a water (n=1.33) upper cladding, whereas the BTX sensing waveguide is designed to work with a Teflon AF (n=1.31) upper cladding. The tick marks are given in units of microns. The very thin core is indicated by the slightly thicker line adjacent to the upper cladding.

Table 3.1: Waveguides Used for Experiments in Chapters 4, 5 and 6

Upper Cladding	**Oil (n=1.46)**	**Water (n=1.33)**	**Teflon (n=1.31)**
Waveguide Width (microns)	4	4	4
Lower Cladding Index	1.46	1.46	1.46
Lower Cladding Material	PECVD Oxide	Thermal Oxide	Thermal Oxide
Core Material	Si Nitride	Hafnia	Si Nitride
Core Thickness (nm)	30	37.5	70
Core Index	1.8	2.05	1.8
Oxide LC Thickness (nm)	1250	1900	1700
Contact Metallization	p-Si/Ti/Al	n-si/Au/Cr/Al/Cr/Al	n-si/Au/Cr/Al
Photodetector Coupling (dB/cm)	13	8	16
% Optical Power in Upper Cladding	48.6	15.2	9.8
Sensitivity (%/RIU)	8880	2590	1720
Effective Index (N_eff)	1.461	1.4663	1.464
Waveguide Used for:	Oil Sensing	Biosensing	BTX Sensing

The modesolver is used to solve for leaky modes of the LEAC waveguide structure and compute the magnitude of photodetector coupling in dB/cm. It works by using the finite-difference method to compute modal solutions to the Helmholtz equation:

$$\nabla^2 E(x,y) + [k_o^2 n^2(x,y) - \beta^2]E(x,y) = 0$$

Since the mode is leaky, the propagation constant has both real and imaginary components. The photodetector coupling coefficient α in units of dB/cm is then given by the formula

$$\alpha = \frac{\frac{4\pi}{\lambda} imag(N_{eff})}{100} * 4.34 \, .$$

The dimensions of the waveguide were optimized for sensing in oil (n=1.46-1.461), aqueous (n=1.33-1.331) and Teflon AF (n=1.31-1.311) upper cladding environments based on modesolver simulations. Generally speaking, device sensitivity is maximized by driving the waveguide closer to cutoff, and photodetector coupling magnitude decreases as both core thickness and lower cladding thickness increase.

3.3 Signal Modulation and Device Sensitivity

Signal modulation *M* is defined as the fractional change in photodetector coupling from its initial value P_o to its final value P_f, such that $M = (1-P_f/P_o)$. The sensor sensitivity, d*M*/d*n* is given units of %/refractive index unit (RIU) and parameterizes the fractional change in coupled light intensity for a given change in refractive index. Let α_o and α_f be the coefficients of evanescent power coupling before and after a Δn=0.001 RIU increase. Assuming a 300 μm (.03 cm) photodetector length *l*, the modulation at the first sensing detector for a scatter-free waveguide is given by

$$M = 1 - \frac{1-e^{-\alpha_f l}}{1-e^{-\alpha_o l}} \quad \text{(Eq. 3.4).}$$

Fig. 3.12 is a plot of scatter-free sensitivity and photodetector coupling vs. lower cladding thickness for a 37.5nm hafnia core biosensing waveguide. The simulated RIU change is Δn=0.001, from *n*=1.33 to *n*=1.331. As predicted by Eq. 3.2, signal modulation increases linearly with lower cladding thickness. However, notice that as sensitivity increases, the magnitude of photodetector coupling decays exponentially with lower cladding thickness. Consistent with Eq. 3.2, the sensitivity increases linearly with core-detector distance (lower cladding thickness).

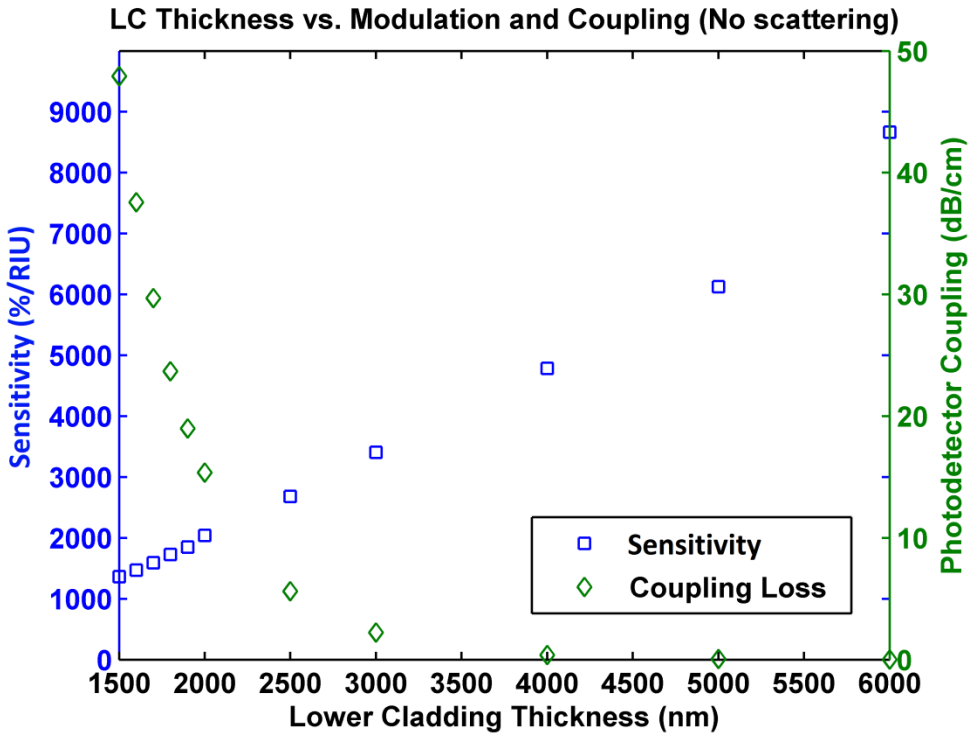

Figure 3.12: Plot of scatter-free modulation and photodetector coupling for H=37.5 nm hafnia core biosensing waveguide covered in Teflon Af

Thus in theory, signal modulation can be increased indefinitely by simply increasing the lower cladding thickness. Unfortunately, while modulation increases linearly with lower cladding thickness, photodetector coupling, and hence detected evanescent optical power, decrease exponentially. As a result, for large detector separations, the evanescent signal quickly becomes overwhelmed by light scattered due to imperfections in waveguide. The optimal lower cladding thickness thus depends on the magnitude of scattered light absorbed by the chip's photodetectors. The effect of scattering on device performance is discussed in the next section.

3.4 Effect of Scattering on Modulation and Device Sensitivity

The effect of absorbed scattering loss *s* must be taken into account when optimizing device performance, as scattering confounds measurement of the evanescently coupled signal. Assuming isotropic scattering,

approximately 45.7% of scattered light is incident on the underlying photodetector ($\tan^{-1}(12.5/1.7)$). Of this 45.7%, only about 60% is absorbed due to the angular averaged Fresnel reflectance. Thus, only about 27.4% of the total scattered light is actually absorbed by sensing region photodetectors. The modulation when scattering is taken into account M_s is then given by,

$$M_S = 1 - \frac{(1-e^{-\alpha_o l}) + (1-e^{-sl})}{(1-e^{-\alpha_f l}) + (1-e^{-sl})} \quad \text{(Eq. 3.5)}$$

Note that as *s* increases, modulation decreases. Scattering is detrimental to device sensitivity on two fronts. First, it reduces the amount of power in the guided mode, thereby leading to increased amplifier noise due to the higher required gain and increased proportional shot noise. Secondly, a high scattering background confounds measurement of the evanescently coupled signal, thereby reducing device sensitivity. Fig. 3.13 is a plot that shows sensitivity as a function of the magnitude of absorbed scattered light in dB/cm. The plot reveals that sensitivity is ultimately limited by scattering and that the optimal lower cladding thickness depends on the intrinsic scattering properties of the waveguide.

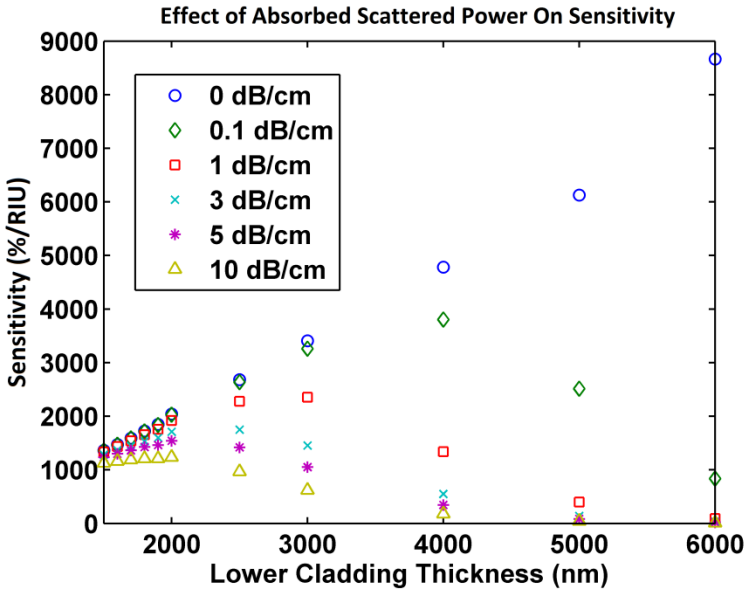

Figure 3.13: Effect of scattering on modulation for a 37.5 nm hafnia core waveguide operating in an aqueous solution

The dimensions of the waveguides used for experiments (Table 3.1) were selected by assuming 3 dB/cm of absorbed scattered optical power. As predicted by Eq. 3.3, the sensitivity of each waveguide varies by according to the % of optical power available to probe the upper cladding sensing region. The oil sensing waveguide has a simulated ideal sensitivity of 8800%/RIU with 48.6% of guided mode optical in the upper cladding, whereas the BTX sensing waveguide only has 9.8% of its guided mode in the upper cladding and sensitivity of only 1720%/RIU. From a waveguide design perspective, the best way increase sensitivity for bulk refractive index sensing is to increase the amount of optical in the upper cladding sensing region. This can only be accomplished by making the waveguide symmetric. For BTX sensing, this would entail using a lower cladding made from Teflon AF or some other low-index polymer.

3.5 Concluding Thoughts from Modesolver Simulations

Simulation results indicate that device sensitivity is highly dependent on the lower cladding (n=1.46) thickness t, waveguide core height H, core index and the magnitude of absorbed scattered power. Thus, in order to maximize sensitivity and target a specified photodetector coupling magnitude, the waveguide had to precisely tuned, while still achieving a single mode condition. Interestingly, the evanescent coupling for single mode waveguides was found to exhibit an inverse exponential dependence on both core and lower cladding thickness as indicated in Fig. 3.14 for a 4 micron wide hafnia (n=2.05) waveguide operating in water (n=1.33). This behavior is anticipated from Eq. 3.2.

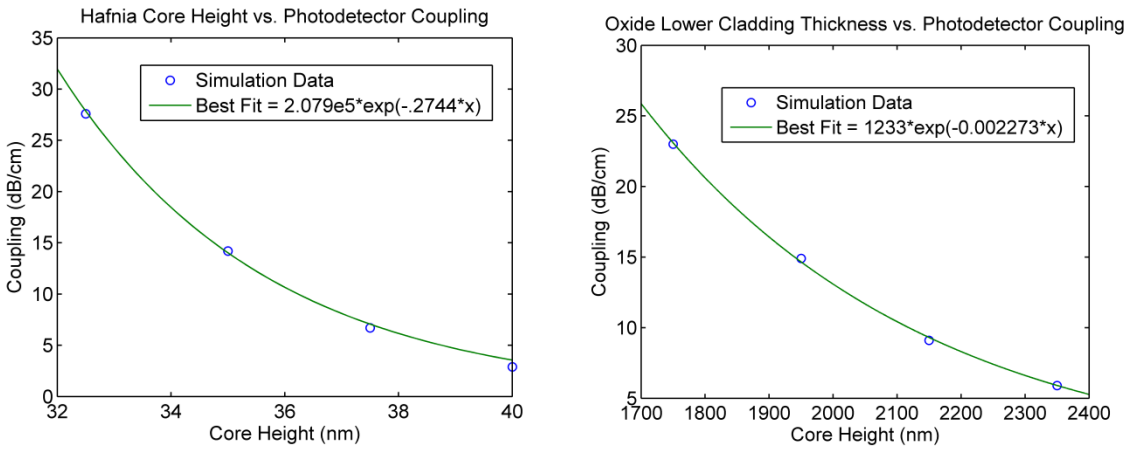

Figure 3.14 Exponential coupling dependence on core height and lower cladding thickness for hafnia core waveguides. A 35 nm core height was used for the lower cladding variable experiments, while a 1950 nm lower cladding was used for the core height variation experiment.

Interestingly, modesolver results indicate that optimal sensitivity is not necessarily achieved when the waveguide core height in designed to be at cutoff. The optimum core thickness depends on the lower cladding thickness. For increasing lower cladding values, the waveguide should be designed to be at cutoff. However, for thinner lower cladding values, the waveguide should be designed to be slightly above cutoff. The reason for this phenomenon can be understood from Eq. 3.3. For thinner lower cladding value, the Si has the effect of pulling the guided mode down into the Si. Near cutoff, the mode is pulled down so far that the guided mode's interaction with the upper cladding sensing region is less than that of a guided mode from a slightly thicker core. This key result is found for the SiNx (n=1.8) core used for BTX sensing experiments, where 2.2 dB/cm of absorbed scattered power is taken into account (Fig. 3.15).

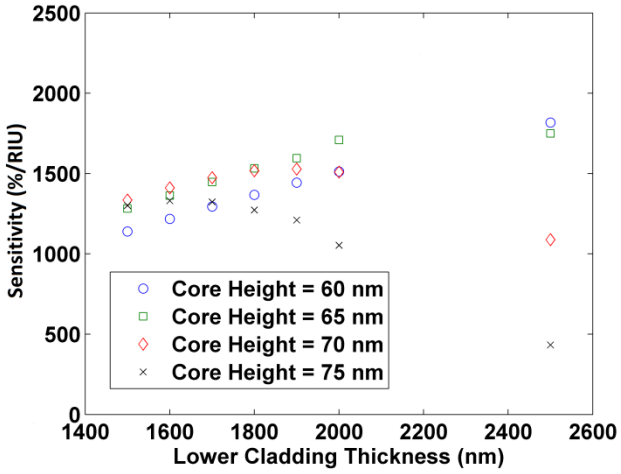

Figure 3.15: Effect of lower cladding thickness on optimal core height

The preceding analysis demonstrates that device sensitivity is highly dependent on waveguide dimensions, and is ultimately limited by scattering. From Eq. 2.1, the sensor's LOD depends on both sensitivity S and measurand noise δX. The next section deals with the engineering approaches taken to reduce scattering to improve the chip's LOD. Subsequent sections deal with photodector optimization, which was used to decrease δX.

3.6 Approaches Taken to Reduce Waveguide Scattering

Multiple approaches were taken to reduce waveguide scattering, including implementation of new continuous photodetector architecture, using more optically robust dielectric films for waveguide fabrication, increasing the waveguide's width, using improved photolithography practices to reduce core sidewall roughness, and lastly incorporating mode-matched reference regions along the waveguide. These approaches are now discussed in detail.

3.6a Implementation of Minimally Scattering Continuous Photodetector Array

The 1st generation LEAC chip featured separate individual photodetectors along the waveguide. This structure is depicted along with the waveguide from a top view perspective in Fig. 3.16. Each

photodetector was formed by a 250 nm thick "island" of polysilicon (pink) electrically isolated by silicon dioxide (white area). As each detector forms an isolated "pixel" underneath the waveguide, this particular design is an excellent approach for measuring evanescently coupled photocurrents at specific locations along the waveguide. However, it introduces a light propagation design flaw. As the guided mode transitions from regions with underlying PolySi to regions with underlying oxide, there is a large mode mismatch (due to the high index contrast), which introduces a significant amount of scattering. Experimental results described later in this section indicate a scattering penalty of at least 50 dB/cm.

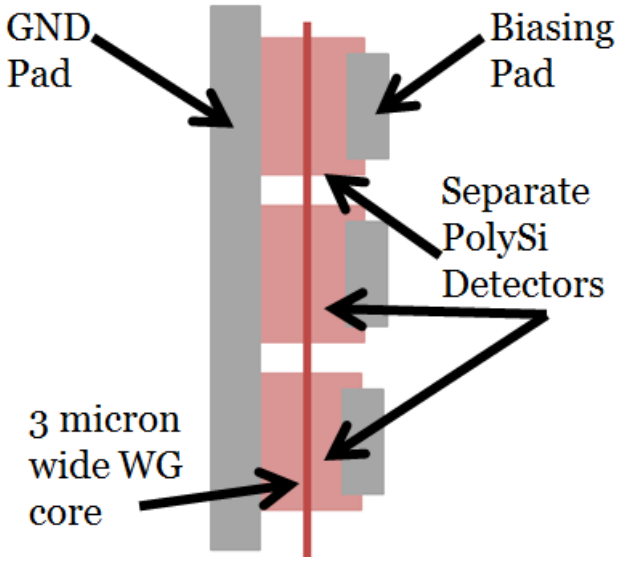

Figure 3.16: 1st Generation Photodetector Design with a Segmented Photodetector Array

In order to resolve the issue of excess scattering introduced by the individual detector approach, a unique continuous photodetector array with photocurrent localization capability was implemented on the 2nd generation LEAC chip. This configuration obviates the need for chemical-mechanical polishing and eliminates segmented detector-related mode mismatch. Fig. 3.17 is a diagram of the continuous photodetector array used for p-Si/Ti/Al photodetectors [8]. The design employs a biasing circuit, which sweeps away carriers generated in adjacent upstream and downstream regions away, enabling localized photocurrent measurement in each detector region.

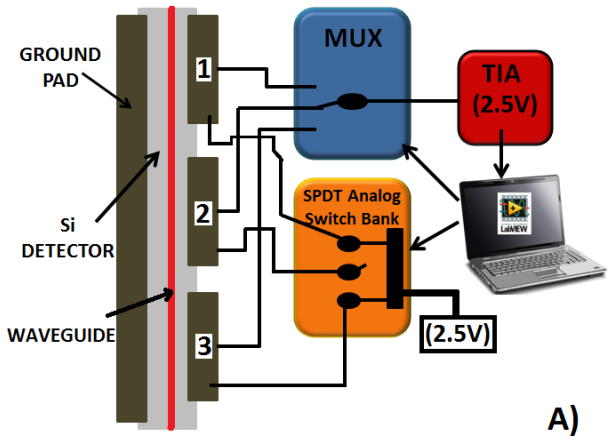

Figure 3.17: Diagram of continuous photodetector array

The continuous photodetector functions as follows. All detector pads are held at a constant bias voltage of 2.5V. Since the silicon is p-type, each individual detector metal-semiconductor contact is reverse biased, whereas the large shared GND contact is forward biased. The photocurrent localization circuit works by effectively sweeping away carriers generated by detectors #1 and #3, so that they are not collected by detector #2. Carriers generated in the vicinity of detector #2 are collected and converted to a voltage using a single-supply transimpedance amplifier (TIA). The voltage from the TIA is then fed into an ADC, linked to a computer running Labview for fully-automated photocurrent measurements.

A simple experiment was undertaken to evaluate the performance of the biasing circuit. A single-mode fiber was placed on top of individual detectors in the detector region. Fig. 3.18 demonstrates the photocurrent localization capabilities of the biasing circuit, when the fiber was placed directly on top of detector #10. In both cases, the direct illumination saturated #10. However, it is essential to note that the photocurrent is only well-localized when the biasing circuit is used, as significant photocurrents are measured on adjacent detectors when the biasing circuit is turned off. This problem would only be compounded when light is coupled into the waveguide and light is present in all detector regions, further validating the need to implement the photocurrent localization biasing circuit.

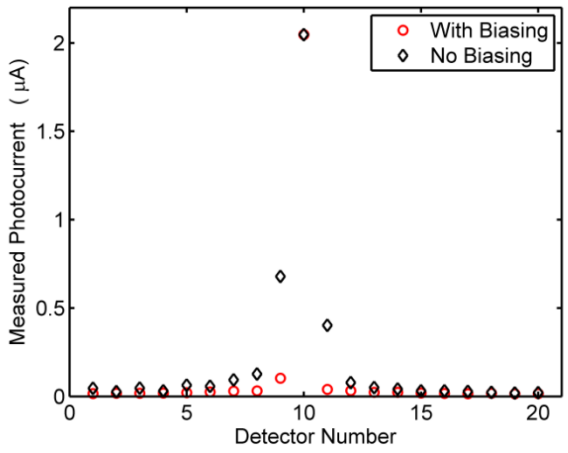

Figure 3.18: Demonstration of photocurrent localization on the continuous photodetector array

By implementing a continuous photodetector array and increasing the waveguide width from 3 microns to 4 microns, scattering loss was reduced to just 21 dB/cm from roughly 77 dB/cm on the 1st generation chip. Scattering loss was estimated from images of attenuated scattered light (Fig. 3.19), which were used to estimate total waveguide loss, which includes loss from scattering, photodetector coupling and absorption in SiO_2 and SiN_x. Assuming negligible absorption loss, *Total Loss= Scattering Loss + Photodetector Coupling Loss*. *Scattering Loss* is then calculated based on device modeling for *Photodetector Loss*. The figure below shows a false color image of waveguide scattering and the fitted exponential decay curve. Given a total loss of 44 dB/cm and model-estimated photodetector coupling of 23 dB/cm, scattering loss was calculated to be 21 dB/cm. (A monochrome camera with linear responsivity was used for measurements).

By incorporating a continuous photodetector and slightly increasing the waveguide with by 1 micron, scattering loss was reduced by approximately 56 dB/cm compared to the 1st generation chip. While this was a big improvement, 21 dB/cm of scattering still created significant problems in terms of reducing sensitivity and light propagation to multiple sensing regions along the waveguide. Assuming 20 dB/cm of evanescent coupled power, the useful propagation length, defined as the length to 95% power attenuation was only 3.25 mm. While still achieving the approximately same sensitivity, the usable waveguide length

could be increased to roughly 6 mm by reducing scattering losses to 8 dB/cm. Thus, other approaches were investigated to further reduce scattering.

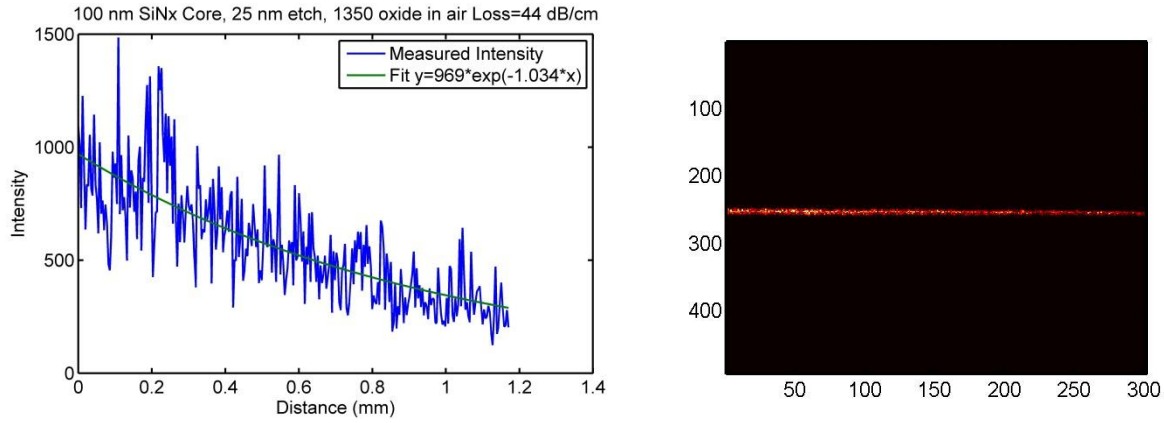

Figure 3.19: Waveguide Loss Analysis. Curve fit of guided mode decay and attenuated scattered light image from waveguide.

3.6b Analysis of Fabrication Tolerances and Material Properties on Scattering

As mentioned previously, waveguide scattering was initially reduced from ~90 dB/cm to 21 dB/cm by integrating a continuous photodetector and increasing the waveguide width. This processing step was motivated by literature reports, which indicated that waveguide sidewall roughness can be the dominant scattering loss mechanism. In general, losses in ridge waveguides are inversely proportional to the fourth power of the waveguide's width [7,9]. However, this model is based on the assumption that both the lower, core, and upper cladding materials are of high optical quality. Internal experimental results indicate that PECVD oxide and nitride are far inferior to thermally grown films or atomic layer deposited films. Increased losses result from both bulk scattering defects and surface roughness. During the initial phase of the project, we were unable to fabricate waveguides that allowed visible light to propagate more than 1 mm. As discussed in Appendix F, by tuning the PECVD deposition parameters, we able to improve the optical quality of oxide and nitride films to the point that light could be coupled for oil waveguides with a loss of ~10 dB/cm. The SEM images in Fig. 3.20 show the dramatic impact that PECVD deposition

parameters can have on waveguide surface roughness and film quality. The left image shows a “bumpy” waveguide exhibiting high surface roughness, whereas the right image shows a much smoother, higher quality waveguide.

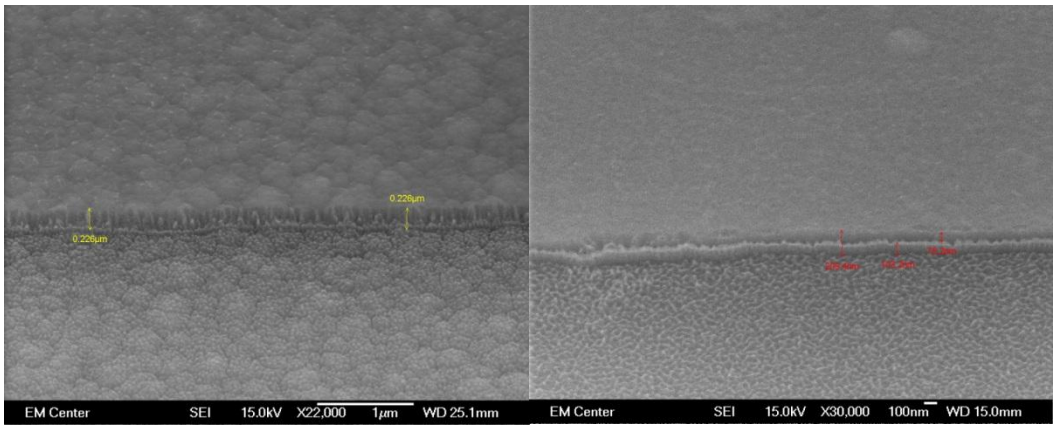

Figure 3.20: Effect of PECVD deposition parameters on waveguide surface roughness

Despite improvements in film quality, PECVD Surface roughness of ~2 nm rms was measured for both optimized PECVD oxide and nitride films using AFM (Fig. 3.21). From SEM images, sidewall roughness was estimated to be 50-100 nm.

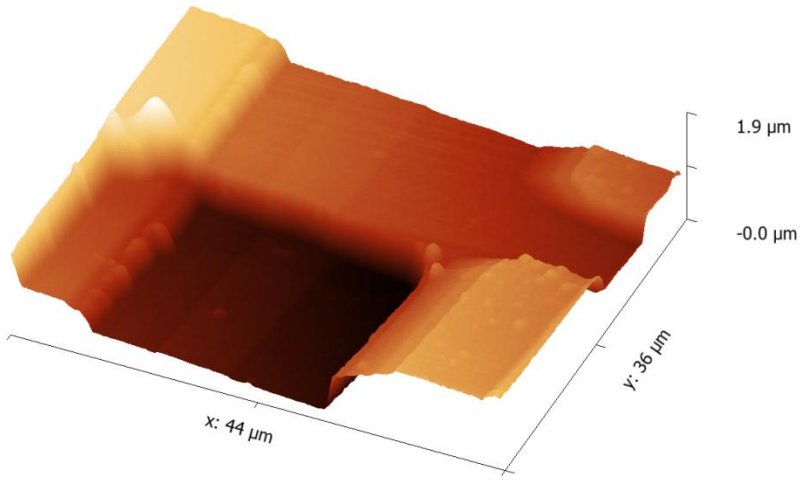

Figure 3.21: AFM images of LEAC structure used to measure surface roughness

The models of Payne and Lee [9,10] were used to study the effects of planar surface roughness and sidewall roughness on waveguide scattering, respectively The results for the 7 micron waveguide with oil (n=1.46) at 654 nm are shown in Fig. 3.22 for sidewall scattering loss (left) and planar scattering surface loss (right) as a function of σ (rms surface roughness) and L_c (autocorrelation coefficient). Per literature reports, rms surface roughness of thermally grown oxide is ~0.5 nm rms [11], which in part explains the reduced scattering seen in chips made with thermally grown oxide vs. PECVD oxide with ~2 nm rms surface roughness.

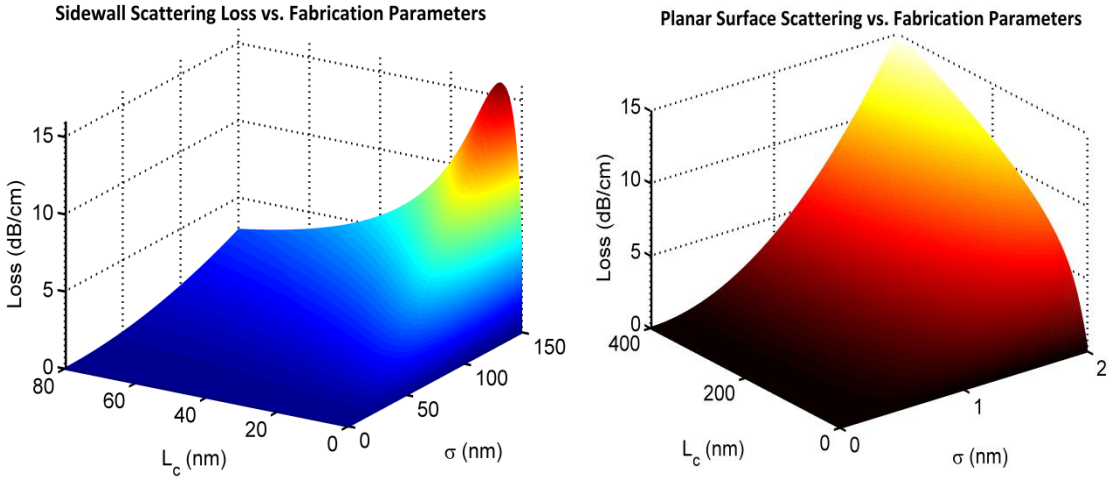

Figure 3.22: Model Estimates for sidewall and planar scattering loss as a function of surface roughness σ and autocorrelation coefficient L_c

From Fig 3.22 (left), it can be seen that sidewall scattering loss in less than 5 dB/cm provided that sidewall surface roughness is less than 100 nm. From Fig. 3.22 (right), it can be seen that planar scattering loss for PECVD oxide with σ= 2 nm is less than 15 dB/cm, whereas for thermal oxide, loss is always less than 2 dB/cm. These upper bound loss estimate of 20 dB/cm is consistent with the measured scattering loss of 10 dB/cm. Total loss depends on both material quality and fabrication tolerances.

A fundamental understanding of the physics of the scattering loss motivated several major design changes. The process flow was radically changed to accommodate the use of thermally grown oxide.

Additionally, for the final version of the 2nd generation chip, ALD-deposited hafnia/alumina nanolaminate films [12] were used for the waveguide core. By combining thermal oxide with ALD-deposited hafnia films surface roughness was dramatically reduced. In conjunction with employing a thinner photoresist and improved photolithography techniques, scattering loss was reduced to just 8 dB/cm for hafnia waveguides covered in Teflon AF. SEM images of a 2nd generation LEAC chip fabricated with a thermal oxide lower cladding and ALD-hafnia core are in Fig. 3.23.

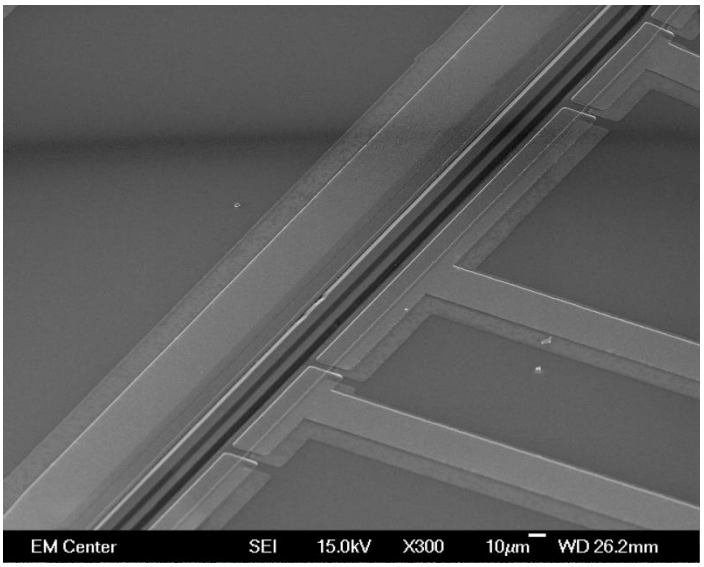

Figure 3.23: SEM images of 2nd generation LEAC chip fabricated with a thermal oxide lower cladding and hafnia core. Note the improvement compared to the images in Fig. 3.20.

3.6c Implementation of Mode-Matched On-chip Photocurrent Reference Regions

In addition to improved sensitivity, the 2nd generation chip features on-chip photocurrent reference regions. On the chip, each reference region is followed by a sensing region, permitting measurement of normalized photocurrents used to correct for fluctuations in coupled light intensity and temperature related drift. (The normalized photocurrent is computed by dividing the sensing region photocurrent by the reference region photocurrent) An example of a chip layout with reference region followed by a sensing region is provided in Fig. 3.24, where light is assumed to propagate from right to left. The

diagram shows eleven individual MSM photodetectors with a shared ground pad and the waveguide in the middle. As mentioned in the fabrication section, the on-chip reference region is integrated by covering specific detector regions with a fixed index upper cladding.

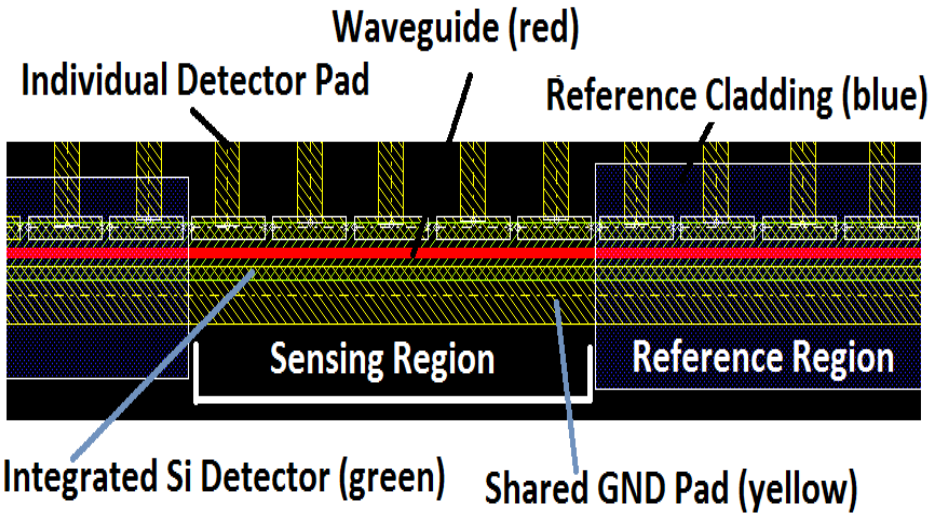

Figure 3.24: Layout showing the waveguide and integrated MSM photodetectors used to form reference and sensing regions on the LEAC chip

The refractive index of the upper cladding reference region cannot be chosen arbitrarily. An experiment revealed light to be almost entirely scattering out of the waveguide when SU8 (n=1.66) was employed as a reference region as shown previously in Fig. 3.7. Furthermore, FDTD simulations revealed the importance of mode-matching between reference and sensing regions. As shown in Fig. 3.25, the guided mode is greatly attenuated when transitioning from an oxide upper cladding region to a water upper cladding region.

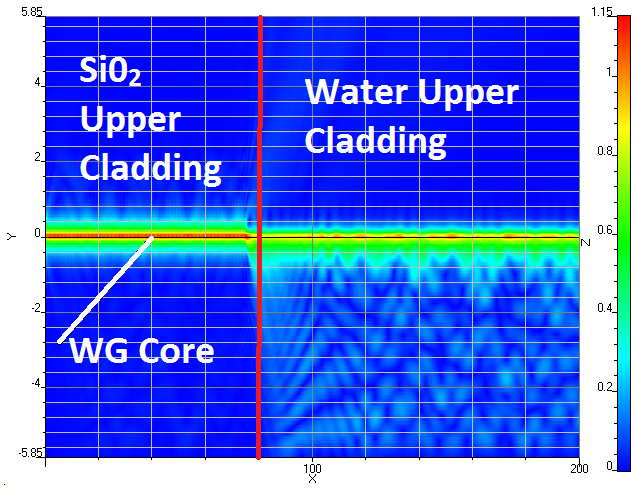

Figure 3.25: FDTD results indicate the importance of mode matching between reference and sensing regions

Modesolver simulations provide a means to compute the fraction of light scattered and transmitted at mode-mismatched interfaces. The power transmission *T* at each interface is computed by calculating the square of the mode overlap integral [4]

$$T = \left[\frac{\int |\boldsymbol{E}_1^* \boldsymbol{E}_2| \mathrm{dA}}{\sqrt{\int |\mathbf{E}_1|^2 \int |\mathbf{E}_2|^2 \mathrm{dA}}}\right]^2 \text{(Eq. 3.6)}$$

Fig. 3.26 shows the optical power transmission percentage as a function of detector region refractive index for a reference region of n=1.46. Power transmission is well over 95% if the index is matched within 0.02 RIU. However, notice that for a predominately aqueous detector region (n=1.33), the power transmission is only 60%. Thus, 40% of guided optical mode power is scattered out at the interface. Such a strong scattering signal can saturate detectors and reduce modulation.

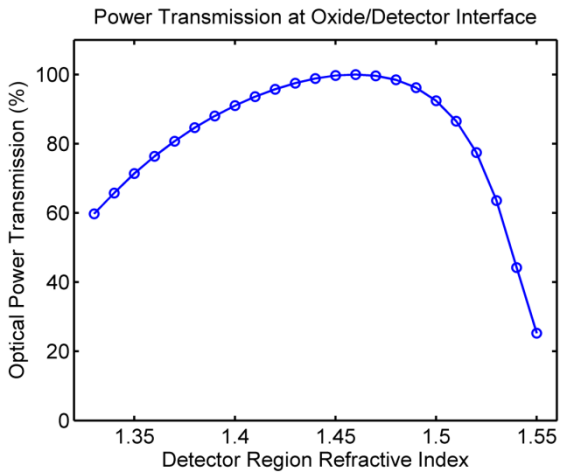

Figure 3.26: Effect of refractive index mismatch on transmission at the reference/sensing region interface for n=1.46 reference region.

On BTEX sensing chips, the entire waveguide is covered by Teflon AF, and is therefore inherently well matched. For oil sensing, $Si0_2$ is used for mode matching. For biosensing experiments, Teflon AF (n=1.31) is used for mode-matching to aqueous solutions. Based on modal calculations, the close mode-matching leads to 99.3% transmission. As such only 0.7% of guided mode power is scattered out. To reduce the impact of scattered light on the signal, a 100 micron sweep detector is integrated at the water/Teflon interface followed by a 300 micron sensing detector.

By employing multiple changes to reduce scattering and tuning waveguide dimensions, device sensitivity to bulk upper cladding refractive index changes can be maximized. For a given electromagnetic field distribution, bulk index sensitivity can be related to surface sensitivity for biosensing applications [13]. However, device sensitivity is only part of improving the chip's LOD. The next section discusses optimization of the chip's photodetectors, in order to reduce δX, in accordance with Eq 2.1.

3.7 Photodetector Optimization

In addition to implementing a continuous photodetector design with on-chip reference regions, several other key improvements were made to significantly increase the sensing performance of the 2nd

generation chip's MSM photodetectors. The Polysilicon/Ti (10 nm)/Al(390nm) MSM photodetectors on the 1st generation chip [5] had an SNR of just ~100. In addition to producing significant scattering, there were multiple issues that limited performance, as discussed below.

First, as the PolySi layer was 250 only nm thick, only a fraction of total evanescent field optical power was detected. A thicker absorbing layer would have permitted more light to be detected. Second, the thin 10 nm Ti adhesion layer may have proved insufficient to prevent aluminum from diffusing into direct contact with PolySi, leading to the formation of Ohmic contact with polysilicon upon annealing that produced relatively high dark currents. Third, compared to crystalline silicon, polysilicon has several inferior material properties. Due to its non-crystalline structure, traps are formed in the bulk semiconductor, which produce temporal fluctuations in the measured photocurrent creating a noisy photodetector. In addition, due to multiple grain boundaries, the carrier lifetime is much shorter, which reduces the collection efficiency of photo-generated carriers.

3.7a Photodetectors on p-type SOI wafers

To address these issues, a new photodetector design was implemented using a lightly doped (100-200 ohm-cm p-type, 10 μm silicon-on-insulator wafer with p-Si/Ti/Al contact metallurgy as shown in Fig. 3.27. To prevent aluminum diffusion and spiking into the silicon, a thick (250 nm) layer of Ti was employed.

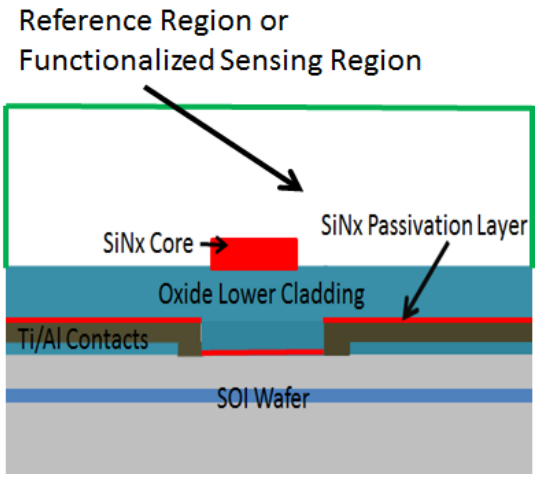

Figure 3.27: Device cross section showing the p-Si/Ti/Al MSM photodetector used for chips fabricated with PECVD oxide

This design was originally selected because Ti adheres particularly well to Si, and forms a Schottky barrier contacts with p-type Si, which limits dark currents. A barrier height was extracted from temperature variation measurements (Fig. 3.28) and found to be 0.531 eV, consistent with values reported in the literature [15]. The barrier height in eV is extracted from the slope divided by (q/k).

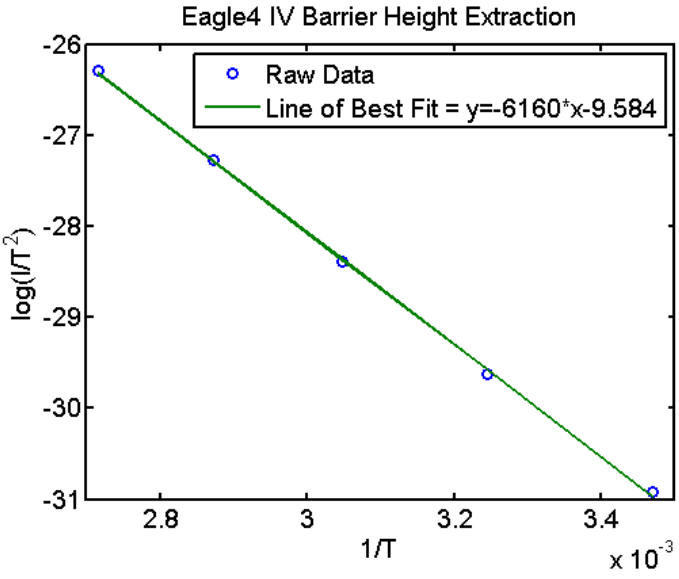

Figure 3.28: Temperature variation measurement for barrier height extraction

Using this photodetector design, dark currents of just 15-25 nA were realized with corresponding photocurrents of ~1 uA for light coupled from a 30 mW laser diode. As shown in Fig. 3.29, a SNR ratio of 1243 was measured compared to 130 for the 1st generation LEAC test chip, providing about an order of magnitude improvement in photodetector SNR.

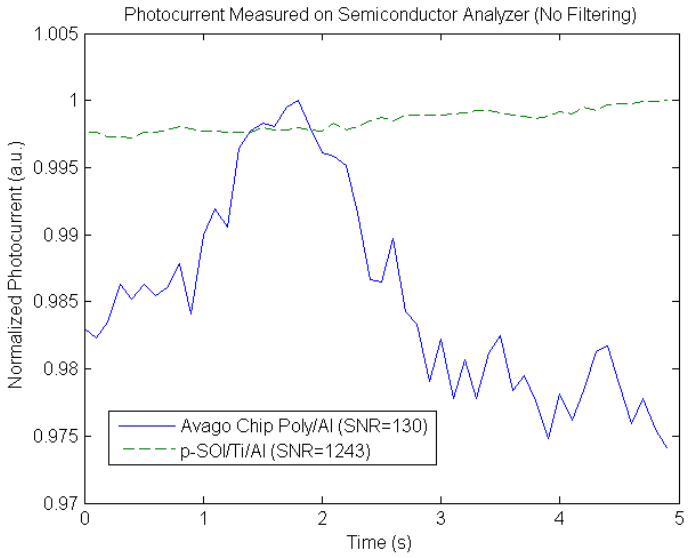

Figure 3.29: Comparison of p-SOI/Ti/Al photodetectors of 2nd generation LEAC chip to the Avago 1st generation PolySi photodetectors.

The p-SOI/Ti/Al photodetectors were also characterized by IV Curve measurements. Fig. 3.30 shows measured dark currents and photo currents under ~900W/m^2 illumination intensity. Notice the significantly greater collection efficiency for 2nd generation silicon photodetectors.

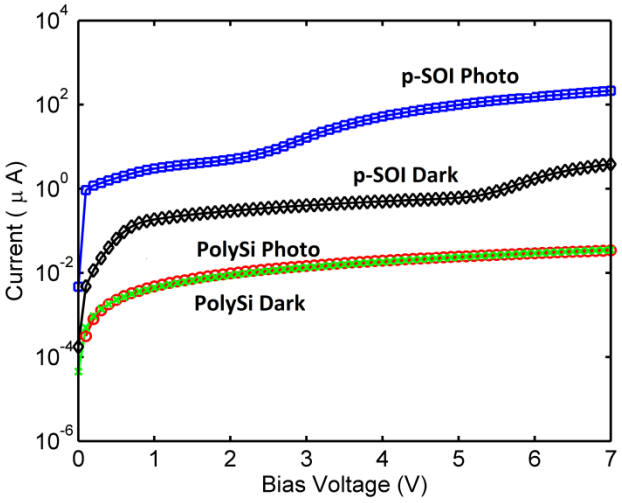

Figure 3.30: IV Curves for 1st generation (PolySi) and 2nd generation p-SOI/Ti photodetectors

3.7b Effect of Silicon Oxidation on P-type MSM Photodetectors

As described above, the p-SOI/Ti/Al photodetectors worked quite well when used in conjunction with a fabrication scheme employing PECVD oxide and contacts to polished Si. However, recall that compared to thermal oxide, PECVD oxide waveguides have a significant disadvantage in terms of scattering. Chips employing PECVD oxide were deemed unsuitable for both BTX and multi-analyte biosensing experiments because of scattering and passivation issues. When the same Ti/Al metallurgy was used on SOI wafers that had been thermally oxidized to form the waveguide lower cladding and the wet etched to reveal the silicon to form MSM contacts, the photodetector performance was dramatically degraded, and dark currents increased significantly as shown in Fig. 3.31.

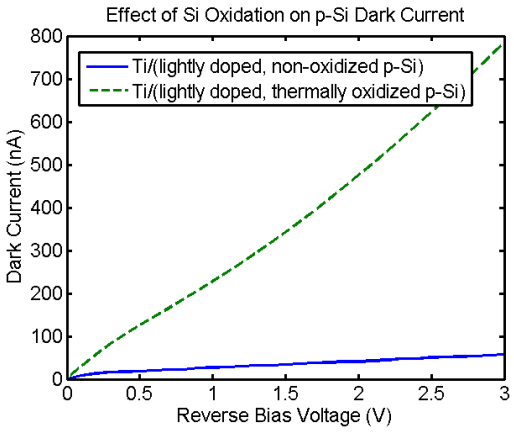

Figure 3.31: Effect of thermal oxidation on Ti/p-Si dark currents

Dark currents increased to hundreds of nA or more, implying a reduction in Schottky barrier height. Temperature variation measurements indicated a barrier height of ~0.4 eV. Additionally, p-type thermal oxide chips had very poor photodetector response uniformity, whereby chips were fabricated where one photodetector would have a dark current 2000 nA and an adjacent photodetector would have a dark current of only 400 nA.

The large change in photodetector behavior came somewhat of a surprise, but is consistent with multiple reports [16-18] in the literature, which state that metal-semiconductor Schottky barrier height is highly dependent on the surface treatment of the semiconductor preceding evaporation. Oxidation tends to increase the surface state density, leading to Fermi level pinning [19,20]. The deviation in photodetector dark currents results from the exponential dependence of dark current on barrier height. Typically, the dark current in MSM photodetectors is dominated by thermionic emission [21],

$$J = AT^2 e^{-(q\Phi_{BN}/kT)}\left[e^{(qV/kT)} - 1\right]$$

Where J is the current density (A/cm^2); A is the Richardson constant (=32 A cm^{-2} K^{-2} for p-Si); T is the temperature, q is the electron charge, Φ_{BN} is the Schottky barrier height; k is Boltzman's constant, and V is the applied bias voltage. Under reverse bias of more than a few kT, the dark current density simplifies to,

$$J = -AT^2 e^{-(\frac{q\phi_{BN}}{kT})} \qquad \text{(Eq. 3.7)}$$

There is an exponential dependence of dark current on the barrier height. Figure 3.32 shows the calculated dark current for a LEAC chip detector with a contact area of (100 µm x 10 µm) as a function of temperature. Here we assume that current flow is gated by the reverse biased detector pad as the large shared ground pad is forward biased. Note that a change in barrier height of only a few hundredths of an eV can result in a huge change in dark current. Furthermore, lower barrier height photodetectors are more susceptible to temperature related drift.

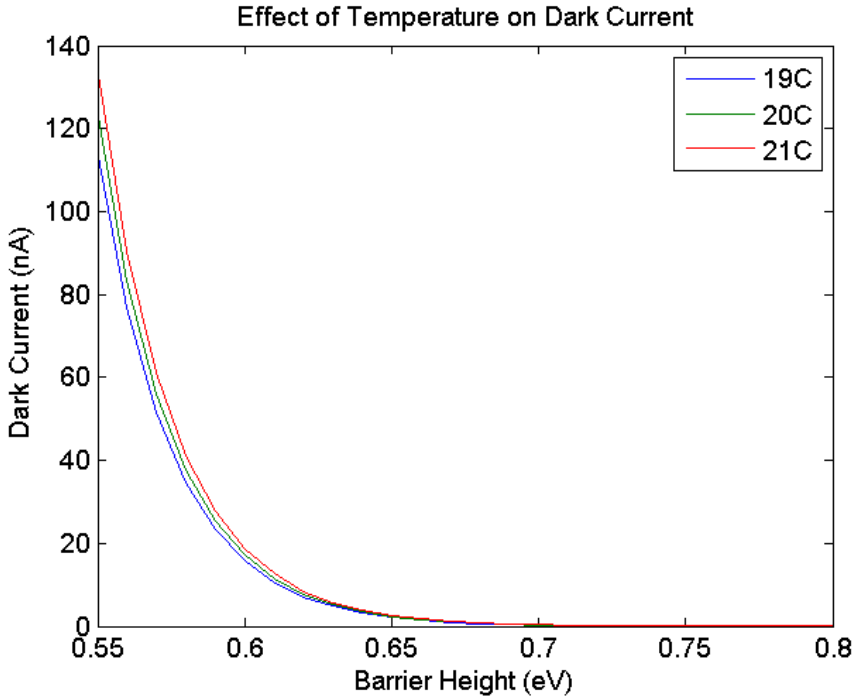

Figure 3.32: Effect of temperature and barrier height on dark current

From the plot it can be inferred that the PECVD oxide chips had a barrier height of ~0.53 eV, whereas the barrier height for the first fabrication run of thermal oxide chips was ~0.44 eV, despite having the same Ti/Al metallization scheme. It is common for there to be some degree of variation in barrier heights of nominally identical MSM photodetectors fabricated on the same chip [22]. A typical standard deviation is ±0.02 eV. Note that as the barrier height is lowered, this variation in barrier height corresponds to much

larger fluctuations in dark currents among detectors. Furthermore, lower barrier height photodetectors are much more susceptible to temperature-related drift and photoconductive gain [23]. Thus, performance tends to increase with barrier height for metal-Si-metal photodetectors. It is important to note that annealing temperature can also have a significant impact on barrier height. Generally speaking, the barrier height decreases as temperature increases, corresponding to the formation of metal silicides and metal/silicon diffusion at the metal-semiconductor interface.

Many attempts were made to raise the barrier height for p-Si/Ti contacts on silicon that had been thermally oxidized. The included hot water oxidation at 80°C to reduce the interface state density [20], wet etching in KOH and BOE, plasma etching in CF4, depositing 3 nm layers of thermal oxide or PECVD oxide onto the contacts before metal deposition, and trying different contact metals, such as Ni and Cr. None of these methods reliably produced photodetectors with a SNR exceeding 1,000.

3.7c Photodetectors on n-type Si Wafers using Au and Pt Contacts

Initially, p-type wafers had been selected as they permit fabrication of high Schottky barrier MSM photodetectors using relatively cheap metals, such as Ti and Al. In contrast, these metals form ohmic contacts on n-type Si. As nature would have it, relatively expensive noble metals, such as Au and Pt are required to form high Schottky barrier photodetectors on n-type Si. After failing to produce high performance photodetectors on thermally oxidized p-type wafers, chips were fabricated on thermally oxidized, prime, 1-5 ohm-cm, n-type wafers using Au as a contact metal. While gold adheres reasonably well to Si, it adheres very poorly to oxide. As such, a Cr (7 nm)/Au (13 nm) metal adhesion layer was first deposited over the oxide region of the chip, in order to permit n-Si/Au(45 nm)/Cr(20 nm)/Al(70 nm) contacts to formed during a second metal deposition, whereby Au was used as the contact metal, Cr a barrier layer, and Al as a metal for probe pads. Fig. 3.33 is a diagram of a chip fabricated with using thermal oxide and this metallization scheme before waveguide core patterning. The thermal oxide (Tox) is shown in blue with adhesion and contact metal layers.

Figure 3.33: n-type thermal oxide chip cross section

Fortunately, the application of n-Si/Au/Cr/Al contacts enabled high performance photodetectors to be fabricated on low-scattering loss thermal oxide chips. Dark currents of just ~1 nA were measured, corresponding to a barrier height of ~0.7 eV after a 300 °C anneal. The increased barrier height yields chips with improved temperature stability, improved resistance to photoconductive gain [23] and better detector uniformity. Using a new transimpedance amplifier design, which produced a 2V bias across the photodetector contacts, chips were consistently fabricated with photodetector signal to noise ratios exceeding 3,000. As shown in Fig. 3.34, n-Si/Au photodetectors with an SNR exceeding 8,000 have been fabricated on LEAC chips.

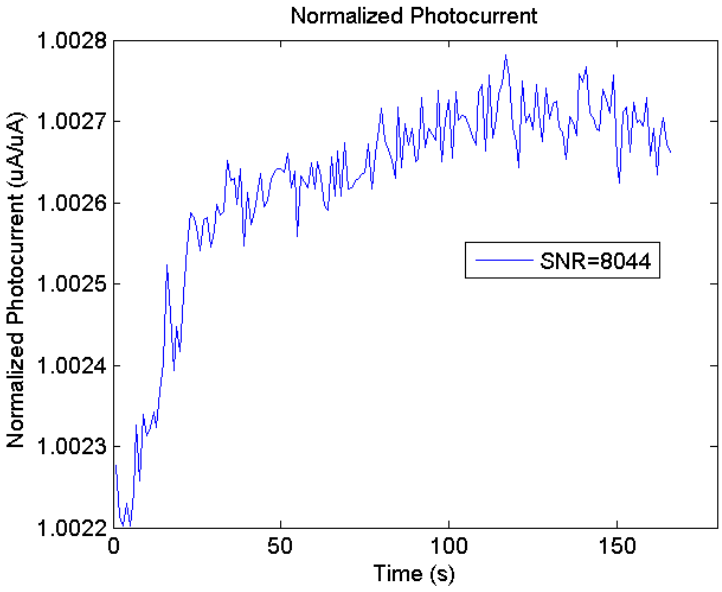

Figure 3.34: Normalized photocurrent on LEAC chip with high SNR n-Si/Au/Cr/Al MSM photodetectors

In addition to Au on 1-5 ohm-cm Si, several other contacts were experimentally investigated. These included Au contacts on undoped Si and Pt contacts on 1-5 ohm-cm Si. Photo and dark current IV curves are shown for n-type photodetectors along with the Avago chip from comparison in Fig. 3.35. The curves are taken from averaging measurements over eight photodetectors.

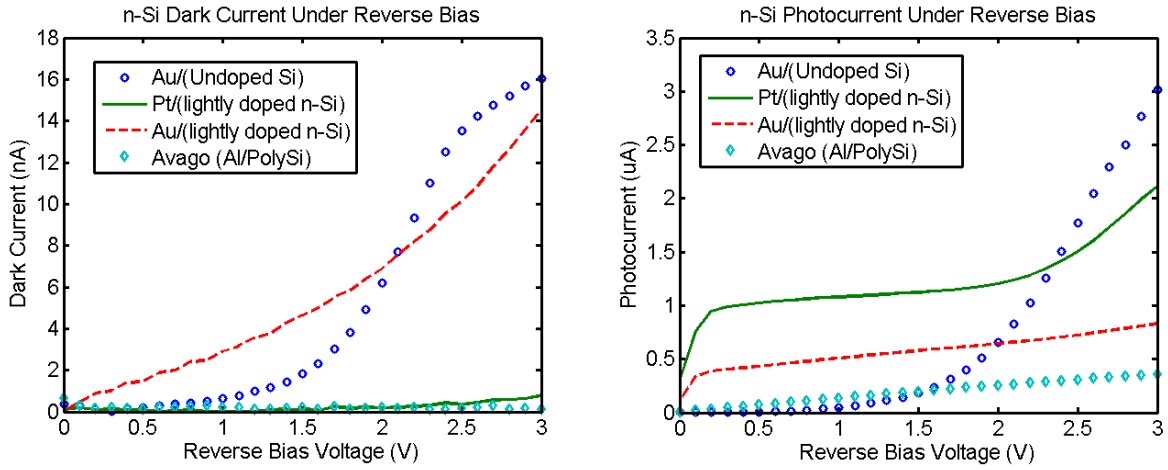

Figur 3.35: IV curves of MSM photodetectors fabricated on n-type Si

Out of all chips fabricated, n-Si/Pt chips were found to have the best performance characteristics. While both Au and Pt have a large flat band, indicating minimal photoconductive gain from 0 to 2V, the collection efficiency is significantly higher for Pt vs. Au, which likely results from recombination centers caused by Au diffusion. While there is variability from chip to chip, Pt chips consistently had lower measured dark current than Au chips and a signal to noise ratios typically exceeding 5000, corresponding to a higher Schottky barrier height (~0.75 eV). Despite the performance advantages of using n-Si/Pt detectors, Pt detectors were not used for sensing experiments because Pt chips could not be reliably fabricated due to Pt adhesion issues. Table 3.2 provides summarizes the photodetector development process.

Table 3.2: Summary of photodetector development. All barrier heights were extracted from Eq. 3.7 with the exception of PECVD Ti/p-Si, which was extracted from both I vs. 1/T slope measurements and Eq 3.7. The heights were found to be in good agreement 0.53 eV (slope measurement) vs. 0.5 eV (Eq. 3.7).

Starting substrate	250 nm PolySi	10 um SOI	10 um SOI	prime grade Si	prime grade Si
Doping	Unknown	p-type, 100-200 Ω-cm	p-type, 100-200 Ω-cm	n-type 1-5 Ω-cm	n-type 1-5 Ω-cm
Oxide Type	PECVD	PECVD	Thermal	Thermal	Thermal
Metallization	Ti/Al	Ti/Al	Ti/Al	Au/Cr/Al	Pt/Cr/Al
Barrier Height (eV)	not measured	0.53 +/- .02	0.44 +/- .03	0.71+/- .02	0.75 +/- .02
Dark Current Range	5 nA	15-25	400-2000	0.8-2	0.3-1.0
Typical SNR over 10 min.	120	1200	300	3200	5600

3.8 Concluding Remarks

The approaches described in this chapter have resulted in the development of a 2nd generation chip, which is significantly improved relative to the 1st generation chip. Based on the analysis presented, the chip's photodetector SNR has been improved by a factor of approximately 27. By reducing scattering from 85 dB/cm to 8 dB/cm, the chip's sensitivity has been significantly improved. Assuming a baseline sensitivity of 2000%/RIU and a coupling efficiency of 15 dB/cm, then from Eq. 3.5, sensitivity has been improved a factor of 4.3. Therefore, from Eq. 2.1, the chips LOD has been improved by a factor of 27*4.3=116, more than two orders of magnitude. In addition to an improved LOD, the 2nd generation chip features extending

capabilities for real-time sensing in wet environments. In subsequent experimental chapters, practical sensing applications for the 2nd generation LEAC chip are demonstrated.

Chapter 3 References

[1] Yan, Rongjin, N. Scott Lynn, Luke C. Kingry, Zhangjing Yi, Richard A. Slayden, David S. Dandy, and Kevin L. Lear. "Waveguide biosensor with integrated detector array for tuberculosis testing." *Applied Physics Letters* 98, no. 1 (2011): 013702.

[2] Zhang, Xin, K-S. Chen, R. Ghodssi, A. A. Ayon, and S. Mark Spearing. "Residual stress and fracture in thick tetraethylorthosilicate (TEOS) and silane-based PECVD oxide films." *Sensors and Actuators A: Physical* 91, no. 3 (2001): 373-380.

[3] Yi, Zhangjing, Rongjin Yan, Timothy A. Erickson, Rashid Safaisini, and Kevin L. Lear. "Optimization of waveguide structure for local evanescent field shift detection." In *SPIE OPTO*, pp. 79410L-79410L. International Society for Optics and Photonics, 2011.

[4] Yariv, A and Yeh, P. Photonics. Sixth Edition. Oxford University Press.

[5] Yan, Rongjin, Santano P. Mestas, Guangwei Yuan, Rashid Safaisini, and Kevin L. Lear. "Response of local evanescent array-coupled biosensors to organic nanofilms." *Selected Topics in Quantum Electronics, IEEE Journal of* 15, no. 5 (2009): 1469-1477.

[6] A. Fallahkhair, K. Li and T. Murphy, "Vector finite difference modesolver for anisotropic dielectric waveguides," *J. Lightwave Technol*., 2008, 26, 1423-1431.

[7] D. Bulla, B. Borges, M. Romero, N. Morimoto, L. Neto, and A. Cortes, "Design and fabrication of SiO2/Si3N4 CVD optical waveguides," *Proc. Microwave and Optoelectronics Conf*., SBMO/IEEE MTT-S, APS, LEOS (IMOC'99), 1999, 2, 454-457.

[8] T. Erickson and K. Lear, "Optimization of the Local Evanescent Array-Coupled Optoelectronic Sensing Chip for Enhanced, Portable, Real-Time Sensing," *Sensors Journal, IEEE* , vol.13, no.5, pp.1905,1913, May 2013

[9] F. Payne and J. Lacey, "A theoretical analysis of scattering loss from planar optical waveguides," *Optical and Quantum Electronics*, 1994, 26, 977-986.

[10] K. Lee, D. Lim, H. Luan, A. Agarwai, J. Foresi and L. Kimerling, "Effect of size and roughness on light transmission in a Si/SiO2 waveguide: Experiments and model," *Appl. Phys. Letters*, 2000, 77, 1617-1619.

[11] Tan, C. S., et al. "Low-temperature thermal oxide to plasma-enhanced chemical vapor deposition oxide wafer bonding for thin-film transfer application." *Applied physics letters* 82.16 (2003): 2649-2651.

[12] Gabriel, Nicholas T., and Joseph J. Talghader. "Thermal conductivity and refractive index of hafnia-alumina nanolaminates." *Journal of Applied Physics*110.4 (2011): 043526-043526.

[13] Berini, Pierre. "Long-range surface plasmon polaritons." *Advances in Optics and Photonics* 1, no. 3 (2009): 484-588.

[14] Pownall, Robert, et al. "Geometry dependence of CMOS-compatible, polysilicon, leaky-mode photodetectors." *Photonics Technology Letters, IEEE*19.7 (2007): 513-515.

[15] Aboelfotoh, M. O., and K. N. Tu. "Schottky-barrier heights of Ti and TiSi 2 on n-type and p-type Si (100)." *Physical Review B* 34, no. 4 (1986): 2311.

[16] Hanselaer, P. L., W. H. Laflére, R. L. Van Meirhaeghe, and Felix Cardon. "The influence of a HF and an annealing treatment on the barrier height of p-and n-type Si MIS structures." *Applied Physics A* 39, no. 2 (1986): 129-133.

[17] Aboelfotoh, M. O., and K. N. Tu. "Schottky-barrier heights of Ti and TiSi 2 on n-type and p-type Si (100)." *Physical Review B* 34, no. 4 (1986): 2311.

[18] Yu, A. Y. C., and E. H. Snow. "Surface Effects on Metal-Silicon Contacts."*Journal of Applied Physics* 39, no. 7 (2003): 3008-3016.

[19] Cowley, A. M., and S. M. Sze. "Surface States and Barrier Height of Metal-Semiconductor Systems." *Journal of Applied Physics* 36.10 (1965): 3212-3220.

[20] Angermann, H., et al. "Wet-chemical passivation of Si (111)-and Si (100)-substrates." *Materials Science and Engineering: B* 73.1 (2000): 178-183.

[21] Cetin, H., et al. "Ti/p-Si Schottky barrier diodes with interfacial layer prepared by thermal oxidation." *Physica B: Condensed Matter* 364.1 (2005): 133-141.

[22] Detavernier, Christophe, R. L. Van Meirhaeghe, R. Donaton, Karen Maex, and Felix Cardon. "Ballistic electron emission microscopy study of barrier height inhomogeneities introduced in Au/n-Si Schottky contacts by a HF pretreatment." *Journal of applied physics* 84, no. 6 (1998): 3226-3231.

[23] Soares, Schubert F. "Photoconductive gain in a Schottky barrier photodiode."*Japanese journal of applied physics* 31.part 1 (1992): 210-216.

Chapter 4: Experimental Demonstration of Real-Time Oil Refractive Index Sensing and Multi-Analyte Dry Sensing Capability

4.0 Chapter Overview

After a significant fabrication process development effort, experiments were conducted to investigate both the real-time refractive index sensing and multi-analyte sensing capabilities of the PECVD oxide LEAC chip fabricated on p-type silicon with a p-Si/Ti/Al metallization scheme [1]. The PECVD oxide chip proved adequate for oil sensing, as oils are non-conductive and therefore did not short out the chip's integrated photodetectors. In this chapter, the experimental setup is first described; then experimental results are presented. Subsequent analysis reveals excellent agreement between results and device modeling. It is worth mentioning that different fabrication schemes were employed for LEAC chips used in both BTEX sensing and biosensing in aqueous environments, as discussed in chapters 5 and 6.

4.1 Real-Time Refractive Index Sensing Proof of Concept Experiment

Real-time refractive index sensing was demonstrated using oils with different refractive indices. Chips were fabricated in accordance with the process flow described in Appendix A1, whereby the first five detectors were covered in PECVD oxide with all remaining detectors exposed to the sample fluid.

For all experiments, light is first end-fire fiber coupled into the waveguide with a fiber excited by a red laser diode centered about 660 nm as shown previously in Fig. 1.2. The localized photocurrent at each detector $I_{det,i}$ is measured at a sampling rate of 4kHz using the biasing circuit described in Chapter 2 and Appendix C. A probe card is used to probe the chip's metal output pads. The dark current at each detector

was subtracted from the measured current, in order to compute the photocurrent To normalize for fluctuations in coupled light intensity due to source instability and fiber movement, the photocurrent I_{ref} in the 3rd detector in the upstream reference region is measured immediately after each detector channel measurement, in order to calculated the normalized photocurrent of $I_{normalized,i}=I_{det,i}/I_{ref}$. A diagram of the experimental setup is shown in Fig. 4.1.

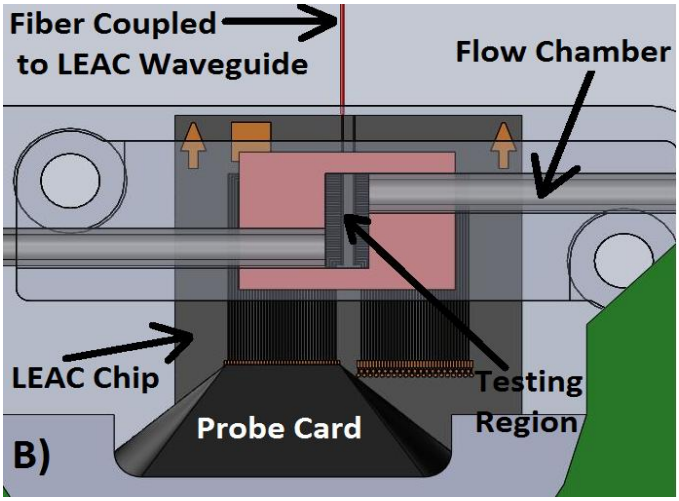

Figure 4.1: Oil sensing experiment

Sesame oil, peanut oil, and a 50:50 sesame oil/peanut oil blend were used as fluids for the experiments. Both oils have negligible absorption at 660 nm, as measured by absorption spectrometry. The refractive indices of sesame (n=1.4722), peanut (n=1.4680), and blend (n=1.4702) were measured using an Abbe refractometer. Both static and real-time measurements were performed.

4.2 Static Sensing

In the first experiment, each oil was injected into the fluidic channel; then flow was stopped and photocurrents were measured for 2 seconds on each channel. The purpose of this experiment was to determine the sensitivity of the device for a relatively long sampling time and observe photodetector coupling at different points along the waveguide. To improve signal to noise, photocurrent measurements were averaged over the 2 second acquisition time window. Results are shown in Fig 4.2.

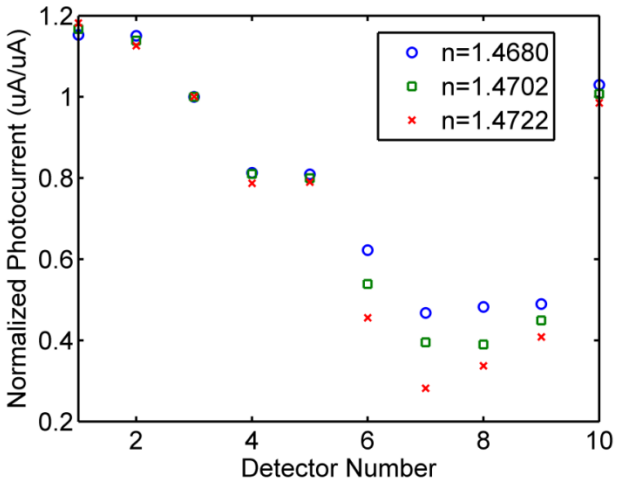

Figure 4.2: Static Refractive Index Sensing. In the reference region (detectors #1-5), the measured photocurrent is similar. In the sensing region (detectors #6-10), there is a dramatic difference in the measured photocurrent. The photocurrents are normalized by dividing the measured photocurrent on a given detector by the measured photocurrent on detector #3, the reference photodetector.

4.3 Analysis of Static Measurements

As expected, the measured photocurrents in the reference region (detectors #1-5) are nearly identical, owing to the fixed upper cladding index. In the sensing region (detectors #6-#10), measured photocurrent increases as refractive index decreases, due to three sensing mechanisms: field shifting, transmission, and index-dependent scattering. The normalized photocurrent decreases due to scattering and photodetector coupling losses as light propagates down the waveguide. Without a prior calibration on each sensing detector using fluids of known refractive index, exact refractive index determination using the current device would be difficult, as there is not a precise relationship between the shift in photocurrent and change in refractive index on all detectors.

We attribute this behavior to two likely causes: localized scattering defects and slight deviations in photodetector response. First, localized scattering defects, observed as ~1μm^2 bright scattering spots along the excited waveguide would elevate the measured photocurrent in the corresponding detector

region and reduce modulation. Second, the photodetectors exhibited slight deviations (+/-5%) in photodetector response under uniform lamp illumination. These deviations would influence the measured photocurrent without a priori calibration on each detector.

Despite this shortcoming, the chip is very sensitive to small changes in refractive index. For analysis, detector #7 is judiciously selected, as it provides the best sensitivity out of all detectors in the sensing region. It exhibits the greatest change in photocurrent (ΔI) for the fixed refractive index difference (ΔRIU) between sesame and peanut oil (0.0042). For 8000 photocurrent measurements over 2 seconds, the standard deviation of the normalized photocurrent was 0.006. This gives a photocurrent standard error ($SE_{photocurrent}$) of 0.006/sqrt(8000) = 6.7×10^{-5}. The 95% confidence intervals for the uncertainty in photocurrent (δI) is then given by $3.92 \times (SE_{photocurrent}) = 2.63 \times 10^{-4}$. $\Delta RIU/\Delta I$ = 0.0176 RIU/normalized photocurrent unit. Assuming a linear photocurrent response, the minimal resolvable change in refractive index is then $(\Delta RIU/\Delta I)(\delta I) = 4.6 \times 10^{-6}$ RIU for static measurements, according to this analysis method. If one applies Eq. 2.1, the limit of detection is 1×10^{-4} RIU.

When reporting a LOD, it is necessary to report the method used to calculate it. The large difference between the two reported LOD values is a statistical in nature. With a large number of repeated measurements (8000), the true mean value can be better statistically resolved, corresponding to a lower limit of detection. Eq. 2.1 does not have any weighting based on the number of sample measurements taken, it is purely based on the overall noise level in the system. For experimental purposes, one should be able to reliably differentiate two reference solutions with refractive index values separated by the statistically implied LOD. If one can differentiate the two solutions with a 95% confidence interval by applying a t-test, then a strong statistical argument can be made for the lower LOD. Due to difficulty in preparing reference solutions with such precision, this experimental work was not undertaken.

4.4 Real-Time Sensing

In the second proof of concept experiment, real-time measurements were performed by flowing oils into the fluidic chamber in the following order: sesame, blend, peanut, sesame. Photocurrent was measured on the second detector in the sensing region (#7) and normalized to the third detector in the reference region (#3). Oils were injected manually using a syringe in 20 second intervals and care was taken to strain relieve the tubes, in order to minimize coupling misalignment caused by fluid flow. Real-time refractive index sensing results are shown in Fig. 4.3.

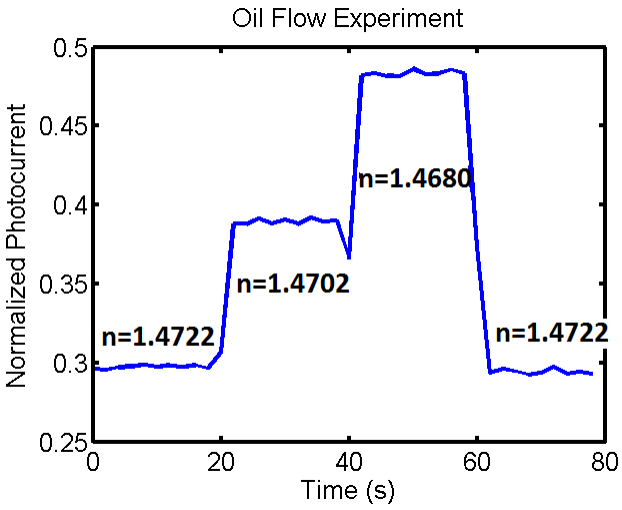

Figure 4.3: Real-Time Refractive Index Sensing. Three fluids of known refractive index were flowed through the chamber in 20 second intervals to validate the real-time sensing capabilities of the chip. As expected, the photocurrent is modulated by changes in the refractive index, and decreases as refractive index increases.

4.5 Analysis or Real-Time Results

In a manner nearly identical to static measurements, the photocurrent increases as fluids of decreasing refractive index flow through the channel. Notably, the photocurrent returns to its initial value when sesame oil (n = 1.4722) once again flows through the channel. The data are significantly more noisy than the static measurements. The increased noise is likely caused by deviations in fiber coupling efficiency

due to slight mechanical displacements caused by fluid flow in the channel. While the coupling is normalized by alternating sensing detector and reference detector photocurrent measurements, it was not normalized using simultaneous measurements due to limitations of our data acquisition system. (A new DAQ has since been built, which is capable of simultaneous measurements (within 250 μs). The average standard error for each flow period is $6x10^{-4}$ compared to $6.7x10^{-5}$ for the static measurement. Using a parallel analysis, the 95% confidence intervals for the uncertainty in photocurrent (δI) is then given by $3.92x(SE_{photocurrent})= 2.3 \times 10^{-4}$. $\Delta RIU/\Delta I = 0.0176$ RIU/normalized photocurrent unit. Assuming a linear photocurrent response, the minimal resolvable change in refractive index is then $(\Delta RIU/\Delta I)(\delta I) = 4.1x10^{-5}$ RIU for real-time measurements.

4.6 Comparison to Modeling Predictions

Analysis shows that the device modeling predications are in excellent agreement with experimental results when the total modulation is computed for the entire sensing region. In the analysis, the first and last detector in the sensing region are omitted, as there photocurrents are impacted by scattering at the reference/sensing region interface caused by a slight mode mismatch. Modesolver results predict $\Delta Loss$ = 17.49 dB/cm for n=1.4680 and 11.72 dB/cm for n=1.4722. This corresponds to a scatter-free modulation of 33%. This is reasonably close to the measured modulation of 30%.

Results are in even closer agreement when the effects are scattering are incorporated into the model (Eq. 3.5). Scattering loss was estimated by curve fitting the guided mode decay on another chip with the same waveguide core dimensions, but a 3 micron thick lower cladding, so that photodetector coupling loss would be negligible. The results are shown in Fig. 4.4. From the curve fit, scattering loss is calculated to be 10 ± 2 dB/cm.

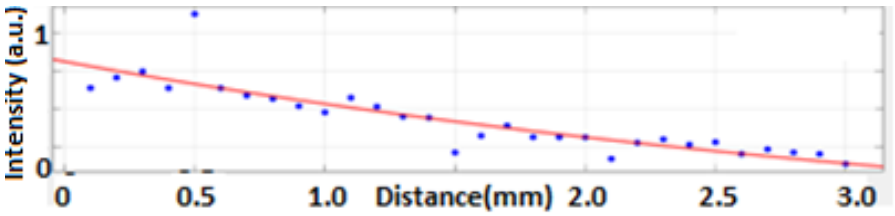

Figure 4.4: Curve fit to estimate scattering loss on a LEAC chip with a 3 micron thick lower cladding

When scattering is incorporated into the model, the predicted modulation is 28.3 ± 1%. This is very close to the measured modulation of 30%. It must be noted that due to processing limitations, scattering values were observed to vary by as much as 10 dB/cm between chips fabricated on the same wafer. The chips with lower scattering loss values were selected for experiments.

4.7 Initial Demonstration of Multi-Analyte Capability

An important feature of the 2nd generation LEAC chip is that the reduced scattering losses allow light to propagate farther down the waveguide, thereby enabling multiple reference and sensing regions along the waveguide to be accessed. To demonstrate the multi-analyte sensing capability of 2nd generation chips, a 40 nm thick layer of 1:4 diluted S1818:PGMEA photoresist was spun onto a chip with a 1500 nm lower cladding and a 100 nm core thickness (designed to work in air). A mask was made so that 5 groups of alternating 300 micron long reference and sensing regions were patterned on the chip. Each group consisted of three individual 100 micron long photodetectors. The reference regions consisted of an air upper cladding, whereas the sensing regions were covered in photoresist. The results are shown in Figure 3.5, which includes both the raw data and modulation data, wherein the reference regions have all been arbitrarily set to zero for easy readout (right).

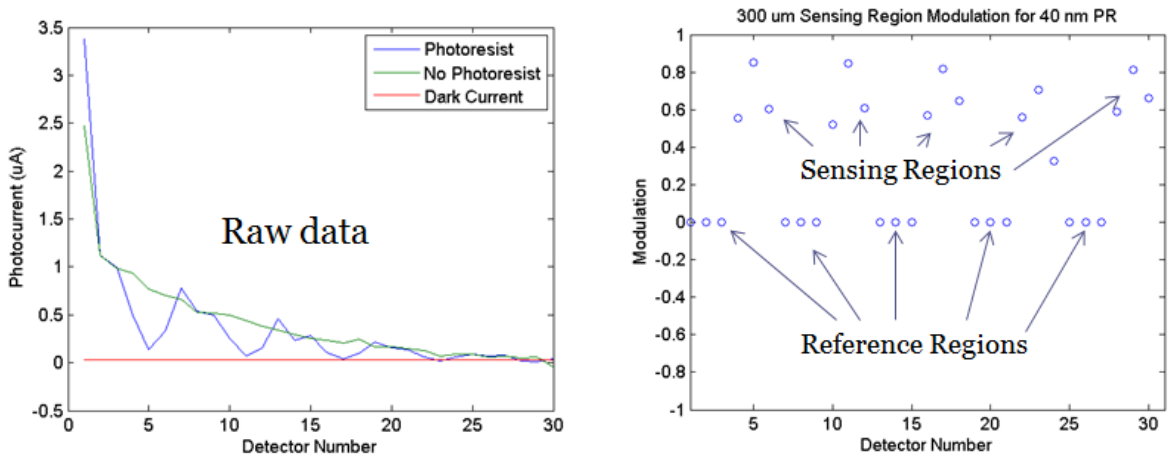

Figure 4.5: Multi-analyte sensing experiment. Raw data (left) and correction modulation (right)

Note the nearly identical modulation response in the first three sensing regions and the rightmost sensing region. The 4th sensing region from the right exhibits a slightly reduced modulation, despite having the same 40 nm thick upper cladding. The reduced modulation is likely caused by a scattering defect in this region of the waveguide, as seen from a localized bright spot in this location of chip when light is coupled into the waveguide. The lack of uniformity is typical of waveguides fabricated using PECVD oxide, due to the relatively poor film quality. It is anticipated that this issue could easily be overcome in a commercial fabrication facility, which employed both thermally grown oxide and nitride, as losses of less than 0.1 dB/cm have been reported for such waveguides [2].

4.8 Conclusion

Both real-time oil refractive index sensing and multi-analyte dry sensing have been experimentally demonstrated on LEAC chips employing a PECVD oxide lower cladding and PECVD nitride core with p-Si/Ti/Al photodetector metallurgy. Oil sensing results were found to be in excellent agreement with device models based on full-vector finite difference modesolver simulations [3].

Chapter 4 References

[1] Erickson, T.A.; Lear, K.L., "Optimization of the Local Evanescent Array-Coupled Optoelectronic Sensing Chip for Enhanced, Portable, Real-Time Sensing," *Sensors Journal, IEEE* , vol.13, no.5, pp.1905,1913, May 2013

[2] J. Bauters, M. Heck, D. John, D. Dai, M. Tien, J. Barton, A. Leinse, R. Heideman, D. Blumenthal, J. Bowers, "Ultra-low-loss high-aspect-ratio Si3N4 waveguides," *Optics Express*, 2011, 9, 3163-3174.

[3] A. Fallahkhair, K. Li and T. Murphy, "Vector finite difference modesolver for anisotropic dielectric waveguides," *J. Lightwave Technol*., 2008, 26, 1423-1431.

Chapter 5: Experimental Demonstration of the LEAC Chip for Real-Time Sensing of BTEX Contaminants in Groundwater with a Teflon AF Sensing Film

5.0 Chapter Overview

The LEAC chip can be functionalized for environmental sensing applications. In this chapter, the LEAC chip's capabilities for sensing BTEX (benzene, toluene, ethylbenzene, and xylene) contaminants in groundwater at sub-ppm concentrations with no sample preparation are presented. Superhydrophobic Teflon AF is used as a sensing film, which preferentially absorbs BTEX contaminants. The first part of this chapter presents the surface plasmon resonance (SPR) experiments and analysis used to characterize Teflon AF as a sensing film. The second part of this chapter discusses the sensing performance of actual LEAC chips functionalized with Teflon AF for BTEX sensing. This chip is demonstrated for broad-based exclusionary detection of hydrophobic contaminants and a limit of detection of 359 ppb, 249 ppb and 103 ppb is established for benzene, toluene, and xylenes, respectively. Effects from sample temperature fluctuations and potential interfering contaminants are evaluated. Single analyte selectivity is demonstrated by employing a diffusion theory model, which permits identification of the solute's diffusion coefficient, assuming the contaminated water sample contains a single dominant contaminant.

As described in Chapter 3, competing sensing technologies, such as GC-MC and GC-FID require complex instrumentation and typically cost thousands of dollars. Given the LEAC chip's relatively low instrumentation costs and small form factor, this particular environmental sensing application may be a potential commercialization avenue for the LEAC chip. The details of this chapter are largely based on two journal publications, "*Characterization of plasma-enhanced teflon AF for sensing benzene, toluene,*

and xylenes in water with near-IR surface plasmon resonance [1]," and "*An Integrated Optoelectronic Chip for Sensing Aromatic Hydrocarbon Contaminants in Groundwater* [2]."

5.1 Introduction and Motivation

Aromatic hydrocarbons such as benzene, toluene, ethylbenzene and xylenes (BTEX) are carcinogenic and hazardous to human health even at relatively low concentrations [3-5]. To ensure the safety of municipal water supplies, the EPA has mandated maximum allowable concentrations of 5 ppb, 1 ppm, 700 ppb and 10 ppm for BTEX, respectively. In recent years, industrial activities related to hydrocarbon production and transportation have resulted in BTEX contamination of water supplies. For instance, pipeline leaks have resulted in benzene contamination of groundwater in Parachute, Colorado [6] and well water in Jackson, Wisconsin [7]. Additionally, hydraulic fracturing activity has been indicated as the cause of BTEX and gasoline-range organic contamination of the Pavilion, Wyoming aquifer [8].

Due to the increased health risks and remediation costs associated with larger contamination events, there is a strong motivation to develop portable, low-cost technologies, which can automatically sense BTEX contaminants and localize contamination events in real-time. Current state-of-the art sensing technologies such as gas chromatography-mass spectrometry (GC-MS) [9-10] and gas chromatography-flame ionization detector (GC-FID) [11-13] can selectively detect BTEX contaminants with exquisite sensitivity at ppt concentrations. However, due to cost, size, and energy requirements, these systems are not typically deployed in the field as real-time monitoring systems. Current monitoring methods typically involve sample collection in the field and transport back to a lab where the assay can be performed, resulting in delayed results and increased analysis costs [14]. Thus, there is a need to develop robust, field-deployable sensing technologies. The LEAC chip may prove to be a useful technology to fill this market niche.

5.2 Characterization of Teflon AF as a Sensing Film for BTX Contaminants

Teflon AF is an amorphous fluoropolymer, which can readily be spin-coated onto sensors, forming a chemically stable, hydrophobic film [15]. Due to its low refractive index (n=1.31) [15], excellent stability in a variety of chemical environments [16], extreme hydrophobicity [17], and high fractional free volume [18], Teflon AF films are well-suited for refractive index-based detection of BTX contaminants. As BTX have a significantly higher index [19] (n~1.48 at 1040 nm), partitioning into Teflon AF leads to a measurable increase in the film's refractive index. Near-IR SPR experiments were used to characterize the performance of Teflon AF films for BTX sensing.

5.3 Teflon AF Film Preparation for SPR Experiments

For SPR experiments, a separate Teflon /gold/SF-10 glass SPR sensing substrate was used for each analyte. Sensing substrates were prepared by first thermally evaporating a 2.5 nm Cr adhesion layer onto cleaned SF-10 glass slides [20], followed by deposition of 47.5 nm of Au at a rate of 0.1 nm/s. After metal evaporation, a 2950 nm Teflon AF 1600 sensing layer was deposited on top of the Au layer by spin-coating and curing as described in ref. [1].

5.4 SPR Measurements

A Nicolet SPR 100 connected to a Nicolet 8700 FT-IR spectrometer was used to acquire SPR data in the Kretschmann configuration by using an SF-10 prism and index matching fluid. Sample solutions were introduced into the SPR flow cell using a peristaltic pump and fluid was drawn from the middle of the sample reservoir. SPR spectra were acquired at a rate of 8 Hz and 32 spectra were averaged over 4s to improve the signal-to-noise ratio. A center-of-gravity weighting function was used to estimate the absorption peak λ_o. All experiments were initialized with the SPR absorption peak at approximately 1040 nm. Oxygen plasma etched Teflon sensing substrates were used for all experiments, except for comparison experiments between etched and non-etched films, which were carried out for the BTX solutes at a concentration of 30 ppm.

5.4a Advantage of Using Oxygen Plasma Etched Films

Oxygen plasma etching renders the Teflon AF surface superhydrophobic [21]. In Fig. 5.1, the SPR peak shift vs. time is plotted for oxygen plasma etched and non-etched films exposed to a 30 ppm solution of benzene. As indicated by Fig. 5.1, plasma etching enhances analyte solute uptake, leading to an increased peak shift. In triplicate measurements, the increased surface hydrophobicity was found to increase the film's sensitivity to benzene, toluene, and xylenes at concentrations of 30 ppm by 50 ± 3%, 53 ± 2 %, and 58 ± 4%, respectively, during the five minute sample period. For all remaining experiments, only oxygen plasma enhanced films were used.

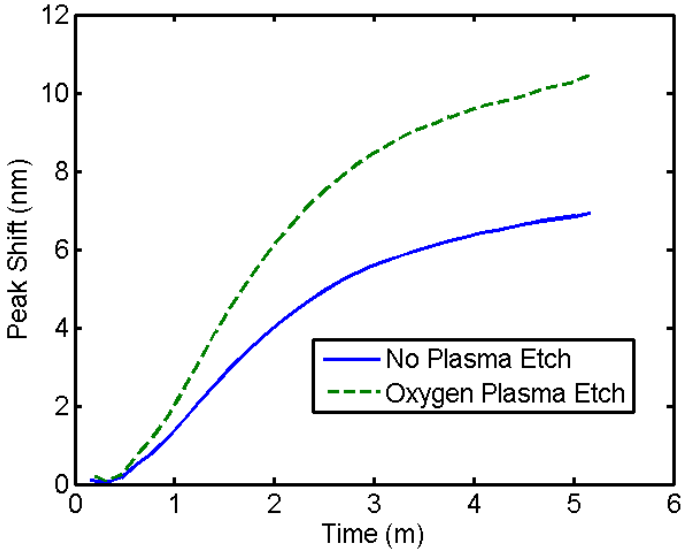

Figure 5.1: Effect of oxygen plasma etching on Teflon AF film sensitivity to benzene (30 ppm).

5.4b SPR Data for Calculating the LOD, Diffusion and Partition Coefficients

A characteristic SPR peak position vs. time trace is shown in Fig. 5.2 for benzene at concentrations of 1, 3, 10 and 30 ppm. DI Water is pumped through the flow cell after each benzene run in order to remove the diffused solute and bring the signal back to baseline. While regeneration time increases with solute concentration, no significant hysteresis is observed. Notably, the 1 ppm concentration can be readily distinguished from baseline, indicating a sub-ppm limit of detection for SPR.

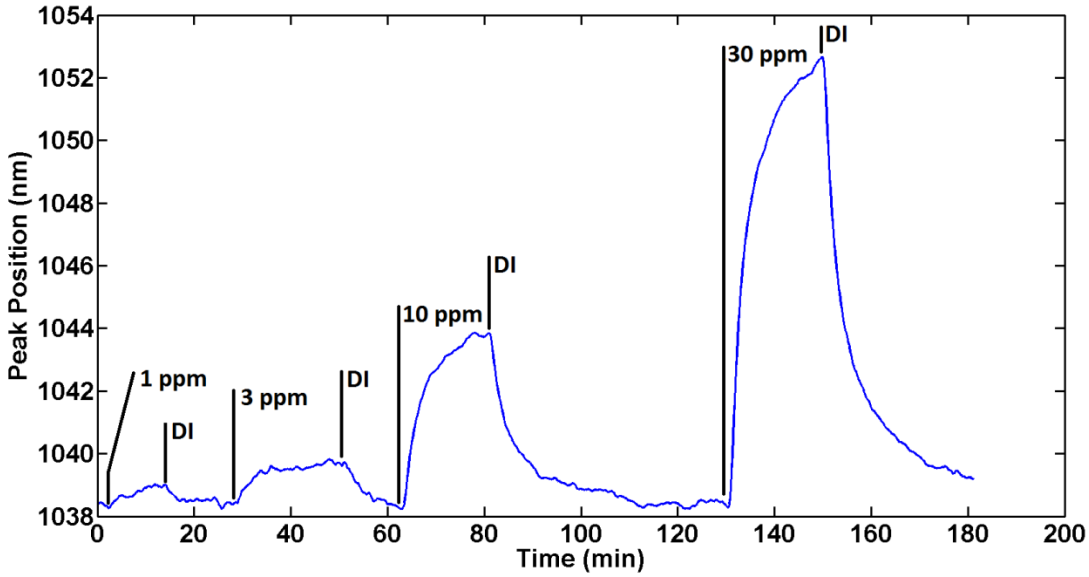

Figure 5.2: SPR time trace vs. peak position for benzene. The times at which deionized water (DI) and different concentrations of benzene (1, 3, 10, and 30 ppm) were introduced into the flow cell are annotated on the plot. The first 1 ppm concentration of benzene was added at 2 minutes to the flow cell which had previously been filled with DI water.

An identical set of experiments was repeated for xylene and toluene, as well as n-hexane at a single concentration (30 ppm). The bulk index change of the film Δn_{bulk} can readily be determined by multiplying the shift in peak position by the SPR's measured responsivity. The responsivity of the SPR system was measured to be 1.14×10^4 nm/RIU by linear regression fitting (r^2=0.998) of sucrose solutions [22] at concentrations of 0, 0.25, 0.5, and 1% on a Teflon-free gold substrate.

5.4c Analytical Extraction of Diffusion and Partition Coefficients

The partition K and diffusion D coefficients were extracted by fitting the observed index change Δn_{bulk} in the Teflon film to a one-dimensional diffusion model, which is justified by the planar film geometry. For a concentration C (#/cm^3), diffusion direction z, and time t, the diffusion equation is given by:

$$\frac{dC}{dt} = D\frac{d^2C}{dz^2} \quad \text{(Eq. 5.1)}$$

The initial concentration of solute in the film is taken to be zero. The boundary condition at the solution/film interface is set by assuming the contaminant concentration in the uppermost film layer (z=z_{film} =2950 nm) is immediately equilibrated [23], such that $C(z=z_{film},t) = KC_o$, where C_o is the concentration of the solute in solution. A no-flux boundary condition (dC/dz=0) was used for the Teflon/Au interface at z=0. For these boundary conditions, the solution of the diffusion equation is given by [24],

$$C(z,t) = KC_o - \frac{4KC_o}{\pi}\sum_{n=0}^{\infty}\frac{(-1)^n}{2n+1}exp\left\{\frac{-D(2n+1)^2\pi^2 t}{4{z_{film}}^2}\right\}\cos\left\{\frac{(2n+1)\pi z}{2z_{film}}\right\} \quad \text{(Eq. 5.2).}$$

As a given solute permeates into the film, its concentration and hence the localized change in refractive index $\Delta n(z)$ are governed by the diffusion equation. Thus, the evanescent tail of the supported surface plasmon probes a varying range of concentrations, and further analysis is required to relate the observed peak shift to z-dependent concentration profile of the film.

At 1040 nm, gold has a complex dielectric function [25] of -47.88+2.911i . Assuming a refractive index of n=1.31 for the Teflon film [15], the evanescent field decay length [26] is approximately 656 nm. As such, the field probes a relatively thick region of the film in the z-direction and perturbation theory [26] is used to relate the measured value Δn_{bulk} to the localized refractive index change in the film $\Delta n(z)$ caused by analyte diffusion. For an evanescent field $E(z)=E_o exp(-\gamma z)$, where γ=1/656 nm, the measured effective bulk index change Δn_{bulk} is related to position-dependent index change $\Delta n(z)$ by:

$$\Delta n_{bulk} \approx \frac{\int_0^{z_{film}} E(z)\Delta n(z)E(z)\,dz}{\int_0^{z_{film}} E(z)E(z)\,dz} = \frac{\int_0^{z_{film}} \Delta n(z)\exp(-2\gamma z)\,dz}{\int_0^{z_{film}} \exp(-2\gamma z)\,dz} \quad \text{(Eq. 5.3).}$$

As an approximation, the integral is only carried out to the edge of the film (z_film = 2950 nm), as 99.99% of the evanescent field intensity is located within the film.

In order to extract *K* and *D* from the diffusion model, Eq. 5.2 was calculated for a wide matrix of diffusion (*D*=2,000:20:30,000) and partition coefficients (*K*=0:1:1,500) to yield *C(z)* for each analyte in 4 second intervals over a range of 15 minutes. The localized refractive index change *Δn(z)* was computed using the Lorentz-Lorenz relation [15] with *C(z)* , polarizability α_c and solute-free Teflon film index *n*=1.31. For the change in local index *Δn(z)*, the relation can expressed as,

$$\frac{(n+\Delta n(z))^2-1}{(n+\Delta n(z))^2+2}-\frac{n^2-1}{n^2+2}=\frac{1}{3\epsilon_o}C(z)\alpha_c \quad \text{(Eq. 5.4)}$$

,

and numerically solved for *Δn(z)*. Polarizability of each analyte at 1040 nm was computed using Cauchy fits to the data in Ref. 13 and then applying the standard Lorentz-Lorenz relation [27]. After solving for *Δn(z)* for each analyte, Eq. 5.3 is then used to relate *Δn(z)* to the measured SPR bulk refractive index Δn_{bulk} as a function of time. Lastly, *K* and *D* are then extracted from the diffusion theory model, using a least-squares fitting algorithm, which minimizes the residual between the measured data (Δn_{bulk} vs. time) and the model over a 15 minute interval. In the context of curve fitting, *K* and *D* are independent parameters, as *D* only affects the shape of the fitted curve, and *K* only affects the magnitude of the total signal, serving as a multiplicative constant. The data and fitted curves for 30 ppm solutions of xylene, toluene, benzene, and n-hexane are displayed in Fig. 5.3. As seen in Fig. 5.3, there is excellent agreement between the experimental data and diffusion model-based fit. 1 ppm, 3 ppm, and 10 ppm concentration of the aromatic hydrocarbons were analyzed in the same manner.

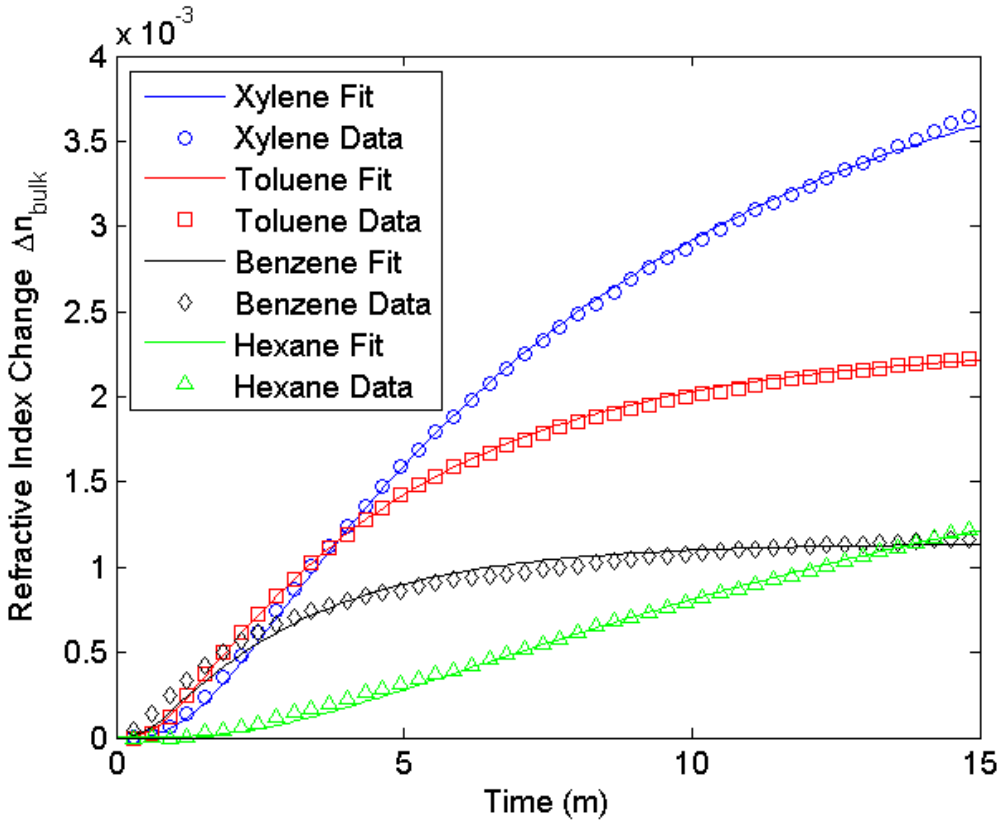

Figure 5.3: Measured bulk refractive index change and model based fit for 30 ppm concentrations of xylene, toluene, benzene, and hexane.

The extracted *K* and *D* for each concentration are provided in Table 5.1 along with maximum error bounds, indicated by brackets.

As a method to characterize measurement uncertainty, simulations were repeated for film thicknesses of 2,900 and 3,000 nm to account for variations in film thickness, yielding error bounds due to film thickness uncertainty $\delta d_{film.}$ Measurement uncertainty due to fitting error δfit was computed as follows. Using a mean film height of 2,950 nm, *K* and *D* were then independently varied until the residual was double the minimum residual value, yielding error bounds related to curve fitting. Maximum error bounds for both *K* and *D* were then computed by taking the sum of δfit and $\delta d_{film.}$

Table 5.1: Calculated diffusion (*D*) and partition coefficients (*K*) for aromatic hydrocarbons in Teflon AF 1600

Analyte	**Concentration (ppm)**	***D* (10^{-10} cm^2/s)**	***K* (C_{film} /$C_{solution}$)**
Benzene	30	2.06 [1.92 to 2.20]	258 [241 to 276]
	10	2.03 [1.86 to 2.31]	242 [230 to 254]
	3	2.01 [1.79 to 2.38]	235 [221 to 249]
	1	1.96 [1.61 to 2.50]	262 [233 to 291]
Toluene	30	1.37 [1.33 to 1.41]	451 [438 to 465]
	10	1.22 [1.14 to 1.31]	444 [423 to 464]
	3	1.12 [0.93 to 1.36]	432 [404 to 457]
	1	1.02 [0.84 to 1.43]	415 [380 to 460]
Xylenes	30	0.78 [0.76 to 0.80]	845 [824 to 862]
	10	0.75 [0.70 to 0.82]	832 [804 to 863]
	3	0.73 [0.66 to 0.82]	808 [736 to 868]
	1	0.71 [0.63 to 0.85]	788 [706 to 857]

5.5 Calculated Film Sensitivity and Limit of Detection Using SPR

At the concentrations tested, both the diffusion and partition coefficient are relatively constant for each analyte. The small range (<10% deviation) of partition coefficient values indicate a linear sensitivity (Δn/ppm), as previously demonstrated for BTX vapor sensing experiments [28]. The film's refractive index sensitivity to each BTX contaminant at full equilibrium was determined by linear fitting (r^2=0.97) to be to be $4.1x10^{-5}$/ppm, $7.1x10^{-5}$/ppm, and $1.4\ x10^{-4}$/ppm for benzene, toluene and xylenes, respectively.

The limit of detection (LOD) for each BTX analyte is calculated as follows. A 5-point moving average filter is first used to improve SNR. Δn_{bulk} was computed from the measured total peak shift $\Delta\lambda_o$ at 1 ppm, while the standard deviation $\delta\lambda_o$ was determined in DI water for 8 measurements (32s) in the period before analyte introduction. Three times the standard deviation, per the IUPAC definition [29], was found to be 0.103 nm, corresponding to a refractive index resolution of Δn=7.5x10^{-6}. Using this methodology, LODs for benzene, toluene, and the xylene mixture were found to be 183, 105, and 55 ppb respectively. These LOD values are significantly lower than the values found for vapor measurements in air [28] due in large part to increased film sensitivity resulting from higher partition coefficients for BTX diffusing from an aqueous environment rather than air. It is important to note that temperature stability or a method to account for temperature fluctuations is essential to achieving accurate and precise measurement values. Temperature variation measurements from DI water show a combined film/SPR system response ($\Delta n/\Delta T$) of 1.4x10^{-5}/°C. No measureable difference in SPR signal was observed between DI water and municipal tap water equilibrated to the same temperature.

5.6 Sample Matrix Interference Effects

In order to analyze the film's specificity and check for interference from other solutes, samples with a wide range of octanol-water partition coefficients [30] were also measured and analyzed. The film's sensitivity response (Δn/ppm) vs. octanol-water partition coefficient log(P_{ow}) is plotted in Fig. 5.4 for hexane (log(P_{ow})=4.0), xylene (log(P_{ow})=3.15), toluene (log(P_{ow})=2.73), benzene (log(P_{ow})=2.13), dichloromethane (log(P_{ow})=1.25), diethyl ether (log(P_{ow})=0.89), acetone (log(P_{ow})=-0.24), methanol (log(P_{ow})=-0.82), and ethylene glycol (log(P_{ow})=-1.36). As indicated by the logarithmic plot, there is a strong correlation between the Teflon-water partition coefficient and the octanol-water partition coefficients. A linear fitting of the data yields the equation: log(K)=0.659log(P_{ow}) + 0.738 (r^2=0.943). Thus, the film shows an increasing selectivity toward increasingly hydrophobic contaminants.

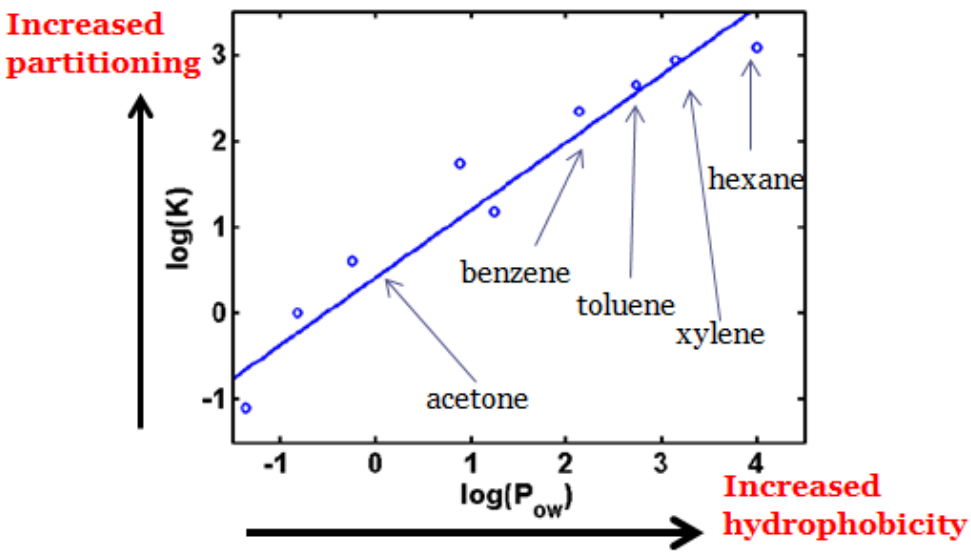

Figure 5.4: Measured Teflon-water partition coefficients (*K*) vs. octanol-water partition coefficients (P_{ow}). The film's sensitivity increases with analyte hydrophobicity as characterized by P_{ow}. There is an approximate linear dependence between the log of each partition coefficient, which provides a general method for predicting interference from other contaminants.

5.7 Concluding Thoughts for Teflon AF as a Sensing Film

While the proposed Teflon-film refractive index-based sensing mechanism does not exhibit the same level of specificity as either absorption or mass spectrometry based methods, it could readily be used for exclusionary testing of toluene or xylene, as the established limits of detection are well below the EPA maximum allowable levels [31] of 1 ppm for toluene and 10 ppm for xylene. While the measured LOD for benzene (183 ppb) is above the EPA maximum of 5 ppb, other SPR systems are capable of reducing the LOD to below 5 ppb. While the film's lack of specificity is a drawback, its high sensitivity to a broad range of hydrophobic contaminants may be advantageous for simultaneous screening of multiple potential hydrophobic contaminants, including polychlorinated biphenyl compounds [32]. A key advantage is that plasma-etched Teflon AF films may be used to functionalize any refractive index-based sensor for rapid exclusionary testing with no sample preparation.

5.8 BTEX Sensing with LEAC Chips

After extensively characterizing the BTX sensing properties of Teflon AF, LEAC chips were functionalized with Teflon AF, in accordance with the fabrication protocol in Appendix A2. Experiments were then run to evaluate the chip's BTX sensing performance. This LEAC BTEX sensing concept is visually summarized in Fig. 5.5. Light from a red (660 nm) laser diode is end-fire coupled into the chip's optical waveguide. An impermeable metal blocking layer (gray rectangle) prevents BTX contaminants from diffusing into the Teflon AF upper cladding in the chip's fixed index photocurrent reference region. In the downstream sensing region, BTX contaminants diffuse into the upper cladding. As a result, there is a decrease in photodetector coupling compared to the reference region, as indicated by the decreased optical intensity leaking into the underlying silicon. The decrease in coupling is measured as a decrease in photocurrent by the chip's integrated metal-silicon-metal (MSM) photodetector array. Each detector in the array has a length of 300 μm and a width of 25 μm. There are a total of eight photodetectors on the chip, one reference detector followed by seven sensing detectors. In Fig. 5.5, only the reference detector and the 1st and 2nd sensing detectors are depicted. Waveguide dimensions were optimized using the full-vector finite difference mode solver described in Chapter 3.

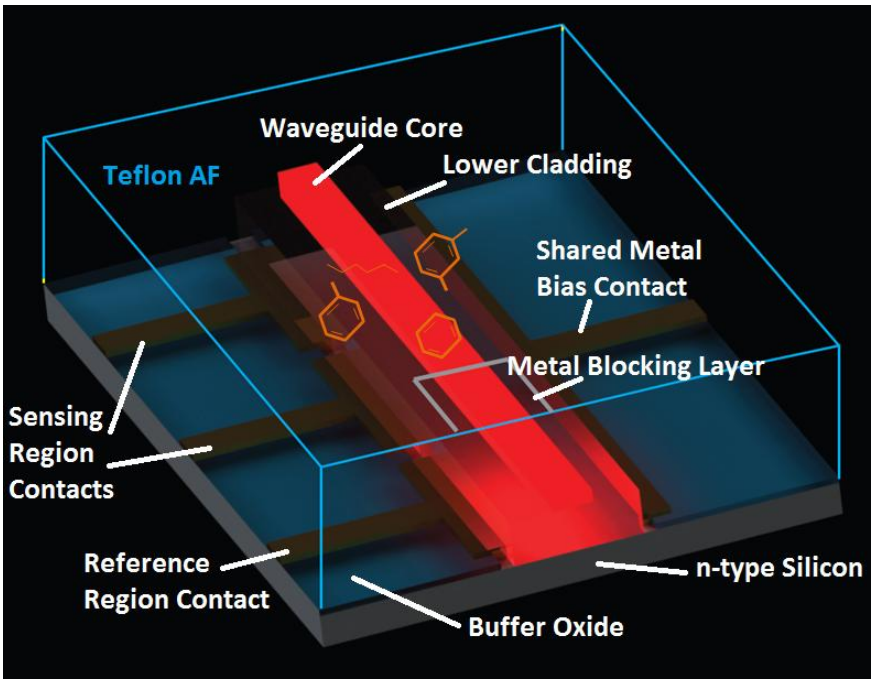

Figure 5.5: Diagram of Device Functionality

5.9 Brief Overview of LEAC BTX Sensor Fabrication

Chips are fabricated using standard photolithography, wet etching, dry etching, metal deposition, metal liftoff and thin film deposition techniques. The fabrication process flow is illustrated in Fig. 5.6. For brevity, photolithography and liftoff steps have been omitted from the diagram, but Futurrex NR9-1500P photoresist is used for wet etching; Futurrex NR71-3000P photoresist is used for metal liftoff, and Shipley S1808 photoresist is used for dry etching. While simulation results indicated that a 65 nm core and 2,000 nm lower cladding thickness would produce optimal sensitivity, a 70 nm core and 1,700 nm lower cladding thickness is ultimately employed, in order to render the device sensitivity less susceptible to small fluctuations ($\leq$ 2 nm) in core thickness. The fabrication process occurs as follows.

First, an RCA cleaned [33], n-type <100>, 1-5 ohm-cm prime grade wafer is thermally oxidized at 1150 °C to form a 1,700 nm SiO_2 layer using a dry-wet-dry oxidation scheme [34]. After photolithography, the

oxide is etched 1,600 nm with 6:1 buffered oxide etch (BOE), in order to from the waveguide's lower cladding.

In order to produce a high Schottky barrier, low dark current contacts for the integrated MSM photodetectors, Au is selected as the silicon contact metal [35]. However, Au adheres very poorly to oxide, so a thin layer of Cr/Au is deposited on top of the oxide to serve as a metal adhesion layer for the Au/n-Si contacts. After metal adhesion layer patterning, the remaining 100 nm of oxide is BOE etched to reveal the bare silicon. After photolithography, the Si native oxide layer is removed using a 3 second BOE dip followed by a deionized water rinse and N_2 drying. Then 35 nm of Au, 20 nm of Cr, and 75 nm of Al are deposited at 0.1 nm/s to form the integrated MSM photodetector array. Au, Cr, and Al serve as contact, barrier and probing metals, respectively [36]. After metal deposition, 70 nm SiN_x (n=1.80) is deposited using plasma-enhanced chemical vapor deposition (PECVD) [37]. The 4 μm waveguide core is formed after photolithography by dry etching the SiN_x 35 nm using a reactive ion etcher (RIE) flowing $CF_4/0_2$ (8%) at 50 sccm with a plasma power of 50W. After core formation, Teflon AF 1600 is spin coated onto the chip. As Teflon does not readily adhere to silicon nitride, a fluorosilane adhesion promoter is applied [1]. Then Teflon is spin coated onto the chip 4 times at 800 RPM. Between each spin coat, the film is cured in an oven at 300 °C for one hour with a 25 °C/min ramp time. After curing, the film is etched in an RIE for 5 seconds in oxygen plasma at a flow rate of 50 sccm and a power of 50W. The plasma etch is necessary to ensure that the layers of Teflon adhere to each other. This process yields a ~6 μm Teflon film as measured by white light spectrometry. After Teflon patterning, the film is once again plasma etched prior to the next photolithography step, in order to ensure photoresist adhesion to the Teflon. After photolithography, 200 nm of aluminum is deposited to form a BTEX impermeable blocking layer for the reference detector (Fig. 5.7). After this step, only the sensing region detectors are directly exposed to the analyte solution. This is done to prevent other regions of the chip from absorbing solutes from the sample volume. After the metal reference region patterning step, the remaining Teflon in the sensing region is oxygen plasma etched to a depth of 1200 nm. Teflon serves the dual purpose of sensing

film and insulating layer. Plasma etching has the added advantage of oxidizing the aluminum, forming a hydrophilic metal oxide capping layer [38]. In the next step (not shown in the Fig. 5.6) the remaining Teflon in the probe pad region of the chip is removed through oxygen plasma etching to permit electrical contact with the chip. In the final process step, the waveguide facet is polished, so that light can be end-fire coupled into the waveguide. Fig. 5.8 is an SEM image of the chip before Teflon coating and aluminum deposition.

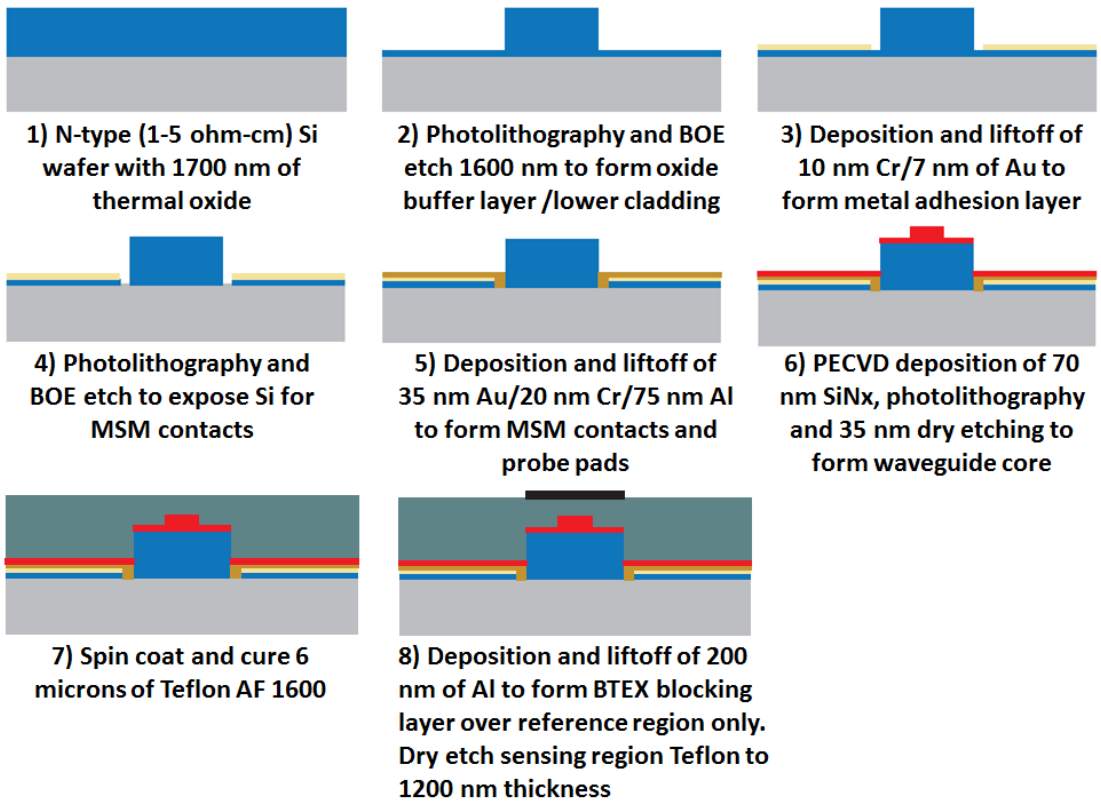

Figure 5.6: Fabrication Process Flow

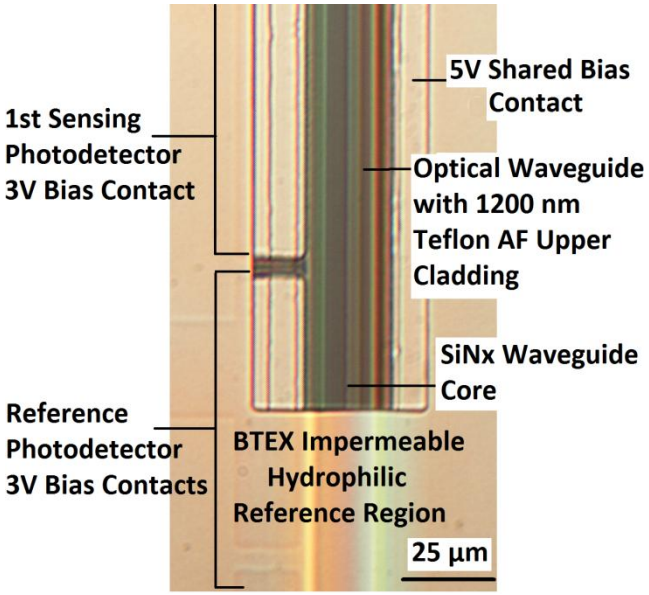

Figure 5.7: Optical microscope image of the chip's reference and sensing region with corresponding 300 µm reference and sensing photodetectors. The waveguide core and lower cladding are seen in the middle of the image. As BTX solutes can diffuse laterally, a 100 µm sweep detector is used to separate the reference detector from the 1st sensing detector.

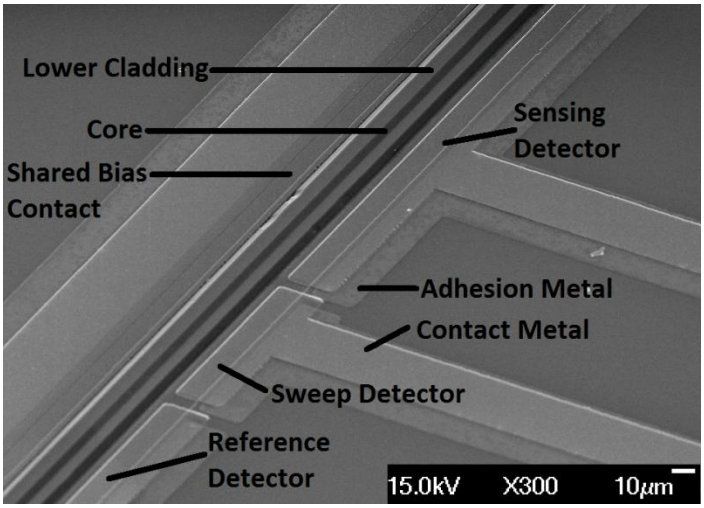

Figure 5.8: SEM image taken before Teflon AF and reference region patterning. The reference detector, sweep detector and first sensing detector are labeled in the image along with the shared bias contact. For n-type Si, the individual photodetectors are reverse biased at 2V, by applying a 5V bias to the shared contact and a 3V bias to the individual detectors. The apparent overlap of separate metal contacts is an artifact resulting from the 45 degree tilt at which the SEM image was acquired.

5.9 LEAC BTX Experimental Work

5.9a Experimental Setup

For all experiments, ~1 mW of optical power from a 660 nm laser diode was fiber-coupled into the waveguide using epoxy to secure the fiber to the facet. For fluid handling, a custom-machined flow cell with a volume of 200 μL was clamped onto the chip and sealed with a 1/16'' diameter O-ring. Sample solutions were manually injected into the fluidic chamber using a syringe. A probe card was used to contact the chip's readout pads for photocurrent measurement.

5.9b Data Acquisition System

Photocurrents on the chip's photodetectors were measured using a custom data acquisition system, which permitted simultaneous photocurrent measurement on all photodetectors at a sampling rate of 2 kHz. The

system consisted of a battery-powered, single-supply, 8-channel transimpedance amplifier (TIA) connected to an 8-channel ADC, which then interfaced with a computer running Labview for automated data acquisition. The TIA consisted of a gain stage, which ranged from 0.4 V/μA to 2 V/ μA depending on detector number (waveguide position). The gain stage was followed by a two-pole Butterworth 6 Hz low pass filter. To reduce drift and noise, "zero drift" op amps (LTC 1050, Linear Technology) were used for both amplifier stages. To collect generated carriers, a 2V bias is supplied across the contacts.

5.9c Signal Processing and Conversion to Normalized Photocurrent

Prior to each experiment, the dark current on each detector is recorded and averaged over a period of 8s to give $I_{dark,I}$ for each detector. The dark current on each detector is then subtracted from the measured current $I_{meas,i}$ when light is coupled into the waveguide, to give the photocurrent on the i_{th} detector $I_{det,i}$= $I_{meas,I}$ - $I_{dark,I}$. The dark current on each detector was approximately 400 pA, corresponding to a Schottky barrier height of 0.7eV [39-40].

To increase SNR, photocurrent measurements on all channels are averaged over 8s (16,000 samples total). After averaging, the raw photocurrent on the i_{th} sensing photodetector $I_{det,I}$ is normalized by dividing by the reference region photocurrent I_{ref} such that $I_{norm,i}$= $I_{det,I}$/ I_{ref}. The on-chip photocurrent reference region is used to correct for small changes in coupled light intensity and temperature-related drift, in order to resolve changes in photocurrent solely caused by solute diffusion into the chip's upper cladding sensing film. After reference photocurrent normalization, all photocurrents are divided by the maximum value on the 1st sensing detector ($I_{norm,1}$) so that all normalized photocurrent values are between 0 and 1.

5.9d BTEX Sensing Experiments

A series of experiments was conducted to characterize the sensing performance of six nominally identical chips (B1, B2, B3, X1, T1 and E1) fabricated on the same wafer. Experiments were designed, in order to

determine a limit of detection for BTX solutes, sensor reusability, sensor repeatability, and interference from other contaminants and temperature fluctuations.

5.9e Temporal Resolution of Solute Diffusion

For benzene, toluene and xylene sensing experiments, three separate chips (B1, T1, and X1) were used, respectively. To mimic true environmental sampling conditions, test solutions were prepared using water drawn from Horsetooth Reservoir (Fort Collins CO). (An initial experiment on chip X1 showed no measureable change in photocurrent when DI Water was injected into the flow cell followed by reservoir water, implying that any potential contamination in the reservoir was below the limit of detection of the system). Solutions of high-purity benzene, toluene, and a mixture of the three xylene isomers were prepared at concentrations of 1 ppm, 3 ppm, 10 ppm, and 30 ppm in reservoir water.

For each experiment, reservoir water is injected into the flow cell and data is recorded for two minutes in order to establish a baseline. Then the 1 ppm solution is injected and data is acquired for 15 minutes followed reservoir water injection and another 15 minute measurement period. This procedure is then repeated for the 3, 10 and 30 ppm concentrations. A time trace of the normalized photocurrent on sensing detector #1 is displayed for xylene in Fig. 5.9a. As expected, the photocurrent decreases as xylene diffuses into the film at increasing concentrations. As water flows into the channel, the xylene diffuses out of the film and the modulation returns to the baseline, indicating that the chip is likely reusable upon exposing the sensing region to clean water for a sufficient period of time.

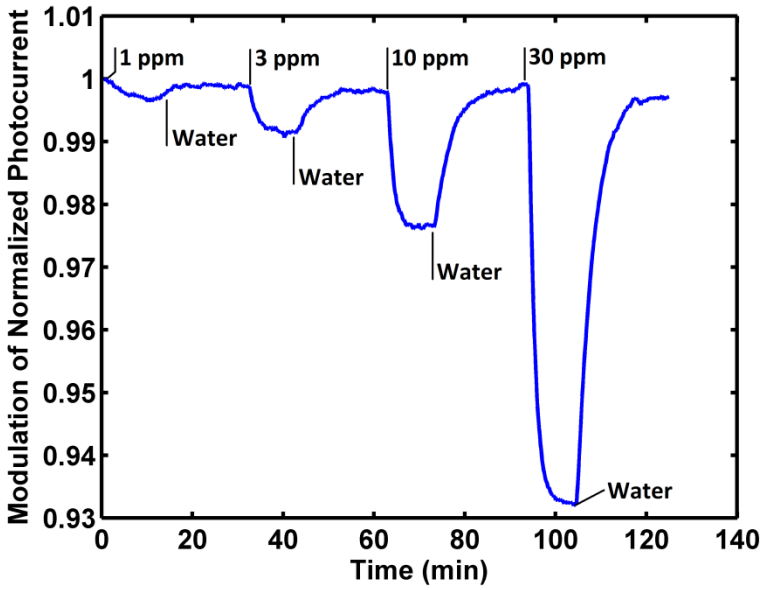

Figure 5.9a: Xylene Flow Experiment

An identical set of experiments was repeated for both benzene (Fig. 5.9b) and toluene (Fig. 5.9c). As indicated in the plots below, the data are far more noisy for both chip B1 (benzene) and chip T1 (toluene). Furthermore, there appears to be significant drift. These data indicate the large variability on chips made under current processing conditions. The sources of variability should be investigated in future work.

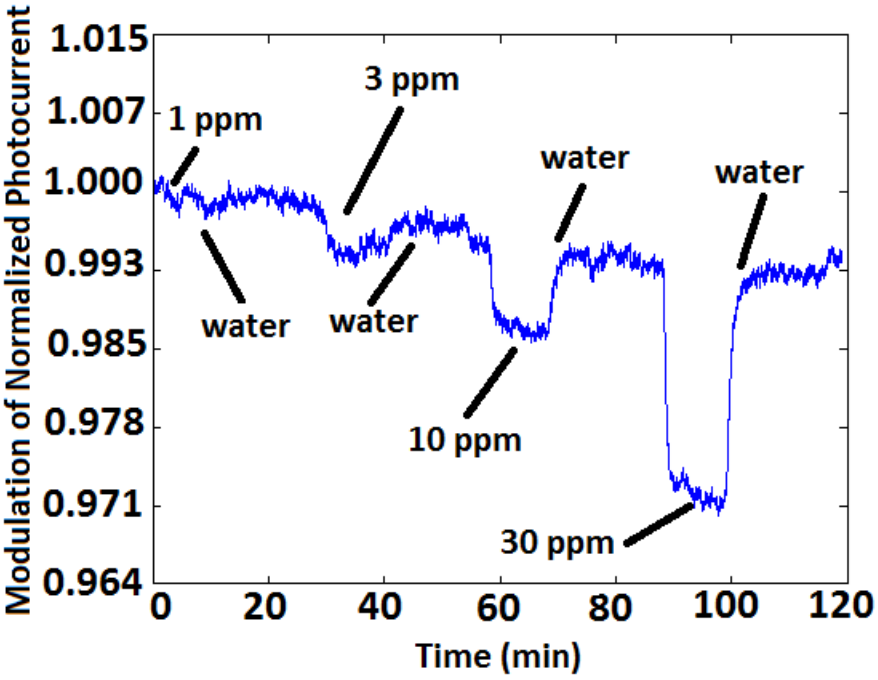

Figure 5.9b: Benzene Flow Experiment

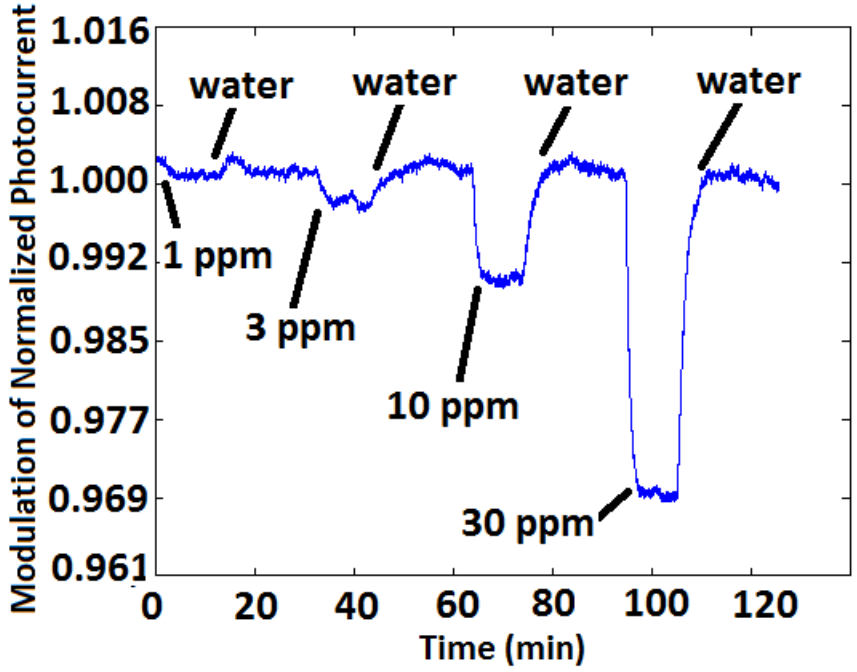

Figure 5.9c: Toluene Flow Experiment

5.9f Effect of Solute Diffusion on Mode Propagation

In order to investigate how solute diffusion affects light propagation and evanescent coupling along the length of the waveguide, a total of 7 sensing detectors were included on the chip. In Fig. 5.10, the measured raw photocurrent on each sensing detector is plotted for water and a water sample contaminated with 30 ppm of xylene, which was allowed to equilibrate for 15 minutes. The data from the chip's sensing detectors is shown and plotted vs. position along the waveguide from the first sensing detector. The raw photocurrent data is presented to demonstrate the effect of solute diffusion on evanescent coupling. (In order to resolve changes in evanescent photodetector coupling with higher precision, the reference photodetector must be used to compute the dimensionless normalized photocurrent.)

As a result of xylene diffusion into the sensing region, the calculated evanescent coupling strength decreases from α_{water}=6.89 cm^{-1} to α_{xylene}=6.49 cm^{-1}. The greatest change in modulation is found on the 1st sensing photodetector (M=8.4%), whereas the modulation on the 7th photodetector in only 1.4%. The decrease in modulation results from two competing effects. Due to the increased upper cladding index in the upstream sensing region, more optical power reaches the 7th photodetector. As a result, the decrease in localized photodetector coupling is counteracted by the increased optical power entering the 7th sensing region. Thus in practice, only the reference detector and the 1st sensing photodetector are required to detect contaminants.

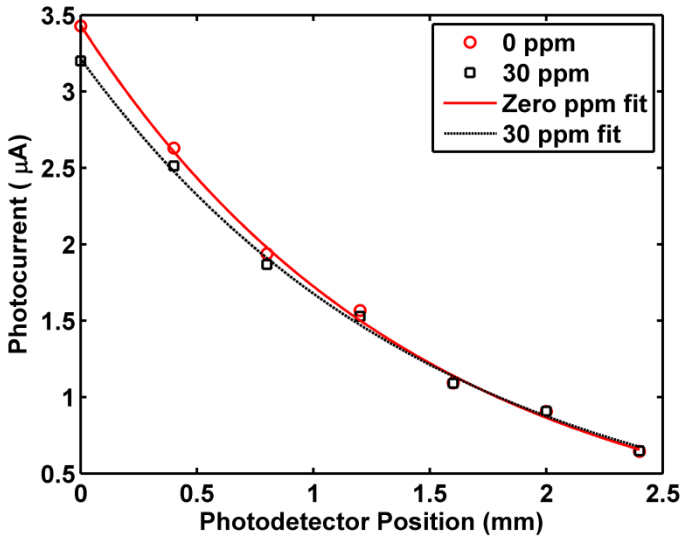

Figure 5.10: Effect of 30 ppm xylene on mode propagation.

5.9g Response Linearity

The responses of chips X1, T1, and B1 to 1, 3, 10 and 30 ppm concentrations of xylene, toluene, and benzene, respectively, are plotted in Fig. 5.11. Results are for a 15 minute equilibration time period at each concentration. A linear response is found for all BTX solutes, as indicated by R-square values exceeding 0.99 for all lines of best fit.

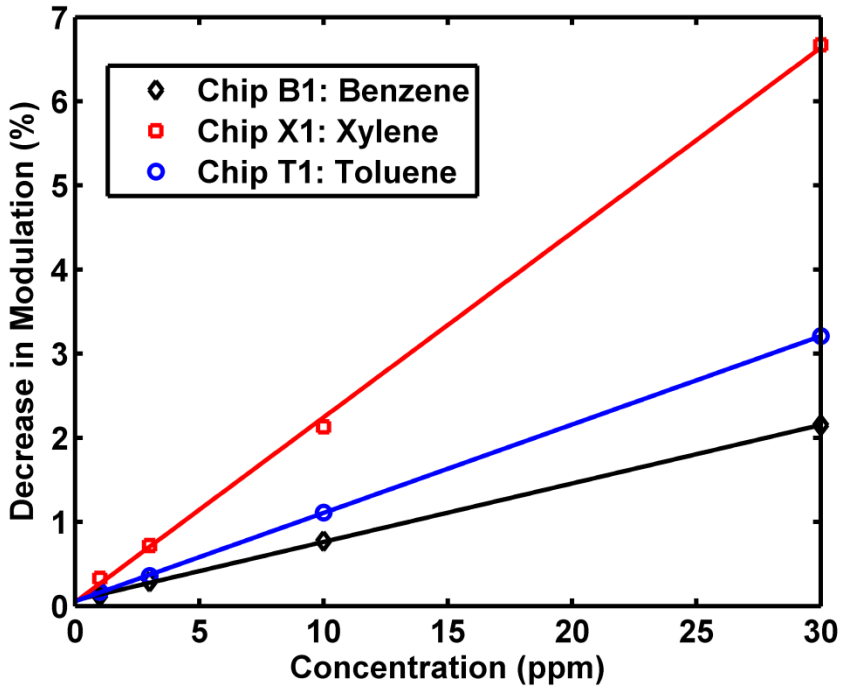

Figure 5.11: Modulation Response of Chips B1, X1 and T1 to benzene, xylene, and toluene, respectively at concentrations of 1, 3, 10 and 30 ppm

5.9h Device Repeatability

To evaluate measurement repeatability across multiple chips, the benzene flow experiment used for chip B1 was repeated on chips B2 and B3 at concentrations of 1, 3 10 and 30 ppm. The average standard deviation in sensitivity across the four concentrations tested is 18.3% for a 15 minute exposure period. The deviation in sensitivity between chips B1, B2 and B3 is likely caused by differences in scattering loss among the chips. Based on the scattering model presented in section 2.3, a waveguide with a scattering loss of 4 dB/cm would provide a sensitivity of 1,520%/RIU vs. 1,398%/RIU for a loss of 12 dB/cm, an 8% difference. While care was taken to prepare capped solutions identically followed by sonication before sample extraction with a syringe, it is possible that the deviation in response could have also resulted from concentration differences in the solution being sampled.

5.9i Effect of Temperature Fluctuations

For laboratory experiments, all sample solutions were allowed to equilibrate to room temperature in a controlled temperature environment. For field measurements, it would likely be more difficult to control the temperature of both the pure water reference solution used for establishing a baseline reading and the sample undergoing analysis. Additionally, if the chip were used for long-term monitoring, the ambient sample medium would likely undergo relatively large temperature fluctuations. In order to evaluate the effect of temperature on device performance, the following experiment was conducted on chip E1. First a room temperature water sample (22 °C) was injected in the flow cell. Then a sample of chilled ice water was injected into the sample flow cell, yielding a near-instantaneous temperature deviation of ~22°C. The maximum deviation in the normalized photocurrent was found to 0.44%, corresponding to temperature stability of 0.02%/°C. As can be inferred from the results presented in Section 5.10, a one degree °C temperature change would result in a 90 ppb, 200 ppb, and 350 ppb offset in measured results, which is comparable to the chip's LOD for a constant temperature measurment. Therefore, temperature must be controlled with sub-degree precision for the measurement to be reliable. Alternatively, a temperature sensor could be integrated on the chip and used to correct for temperature fluctuations via calibration.

5.9j Effect of Interference from Other Matrix Contaminants

A given water sample may contain a variety of ionic and nonpolar contaminants, in addition to BTX contaminants. Thus, it is important to investigate the effect of other potential sample matrix contaminants. Previously, solute uptake by Teflon films has been shown to exhibit a strong dependence [1] on the solute's octanol-water partition coefficient, P_{ow} [30]. Thus, 30 ppm of hexane ($\log(P_{ow})$=4.0) and 30 ppm of acetone ($\log(P_{ow})$=-0.24) were selected as test solutions to span a large range of octanol-water coefficients. To evaluate the effect of ionic contaminants, a 4% NaCl solution, used to mimic ocean water was used.

Chip E1, which had previously been use for temperature fluctuation measurements was used for the following experiment. First, a water baseline reading was taken. Then the 4% saline sample was injected into the flow cell and allowed to equilibrate for 10 minutes followed by a 15 minute water rinse. Then the acetone solution was injected, followed by a 15 minute water rinse. Lastly, the hexane solution was injected into the channel. The rinse step was included to avoid cross-contamination of the interfering solutes being analyzed and bring the film back to baseline. The data showed no measurable change for the 4% NaCl solution. The data for hexane and acetone solution are plotted in Fig. 5.12 where t=0 corresponds to the time when each solute is injected into the flow cell. The normalized photocurrent shift is 9.96 % for hexane, but only 0.16% for acetone, consistent with the partitioning behavior of these solutes into Teflon AF [1].

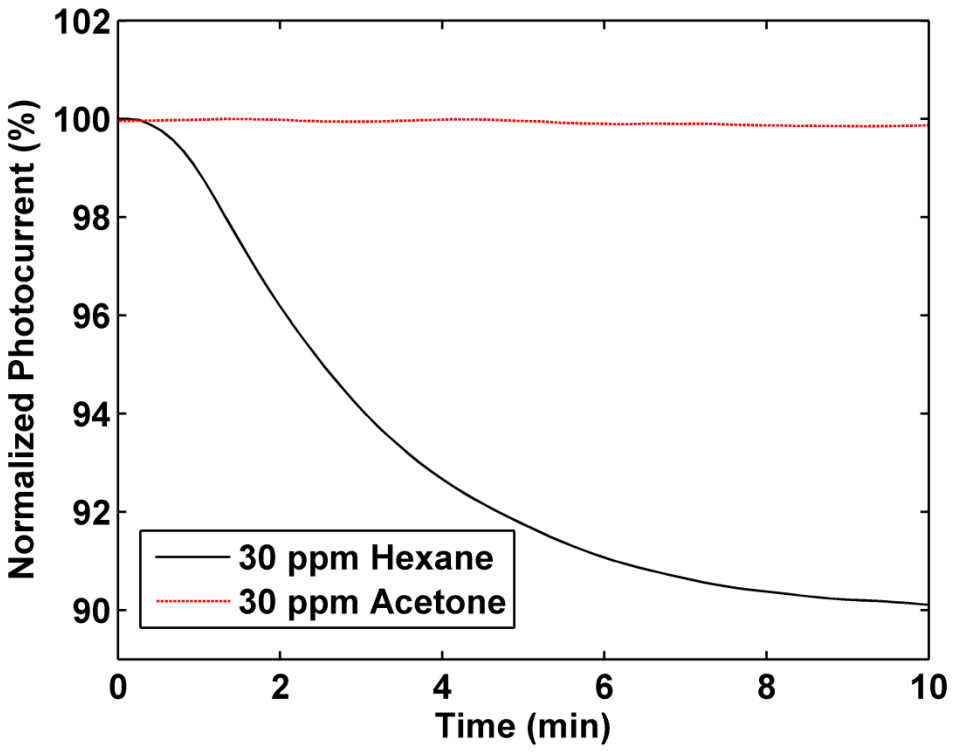

Figure 5.12: Modulation shift due to 30 ppm concentrations of acetone and hexane

5.10 Analysis and Discussion of Experiments

5.10a Experimental Device Sensitivity and Limit of Detection

The device sensitivity is 0.22%/ppm, 0.11%/ppm and 0.07%/ppm for xylene, toluene and benzene, respectively based on the lines of best fit in Fig. 5.11. In order to calculate the chip's limit of detection (LOD) for a five minute measurement time window, which is sufficient to allow nearly full equilibration for all BTX solutes, the data for the 1 ppm concentration tested (Fig. 5.13) were analyzed in the following manner. First, the change in normalized photocurrent ΔI_{norm} is calculated from t=0 to the average value for last five data points the sample window. Then the standard deviation σ in the normalized photocurrent is computed for last five data points in the sample window (t=4.46 to 5 minutes) Per IUPAC definition [29], the limit of detection is the given by LOD= $(3\sigma/\Delta I_{norm})$x(1 ppm) and is found to be 103 ppb, 249 ppb, and 359 ppb for benzene, toluene and xylene, respectively.

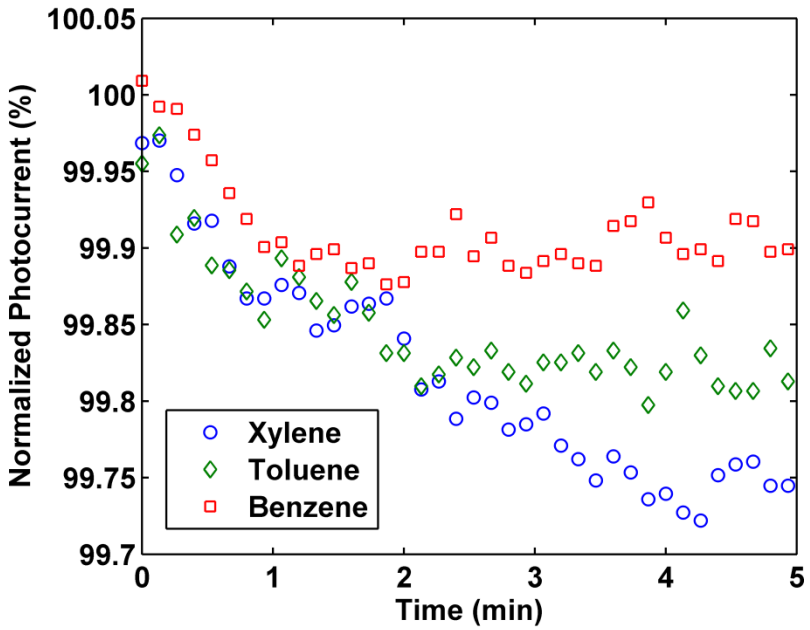

Figure 5.13: Modulation response to 1 ppm samples of benzene, toluene and xylene

5.10b Identifying Contaminants From Their Diffusion Coefficients

By employing a diffusion theory model, it is possible to identify individual BTX solutes based on extraction of their unique diffusion coefficients [1] provided that the solution contains only a single dominant contaminant. It must be stated upfront that using the diffusion coefficient as a single parameter has its limitations for molecular identification, as other potential contaminants could have similar diffusion coefficients.

The diffusion of BTX solutes in Teflon AF films has previously been shown to be obey the solution to the diffusion equation (Eq.1), where *K* is the solute's partition coefficient into the film; z_{film} is the film thickness, C_o is the solute's concentration in the contaminated water sample and *D* is the solute's diffusion coefficient [24].

$$C(z,t) = KC_o - \frac{4KC_o}{\pi}\sum_{n=0}^{\infty}\frac{(-1)^n}{2n+1}exp\left\{\frac{-D(2n+1)^2\pi^2 t}{4{z_{film}}^2}\right\}\cos\left\{\frac{(2n+1)\pi z}{2z_{film}}\right\} \quad \text{(Eq. 5.5).}$$

While curve fitting can be used to rigorously extract a solute's diffusion coefficient from the measured data [1], analysis shows that while the magnitude of the response (signal modulation) depends on both C_o *and K*, the shape of the diffusion curve and hence, the time to reach equilibrium is only dependent on *D*. From the time trace data shown for 30 ppm concentrations of benzene, toluene and xylene in Fig. 5.14, it is evident that the rate at which each contaminant reaches equilibrium in the film is unique. Reading from the plot, the time to reach equilibrium (slope≈0) is approximately 128 s, 184 s and 344 s for benzene, toluene and xylene respectively.

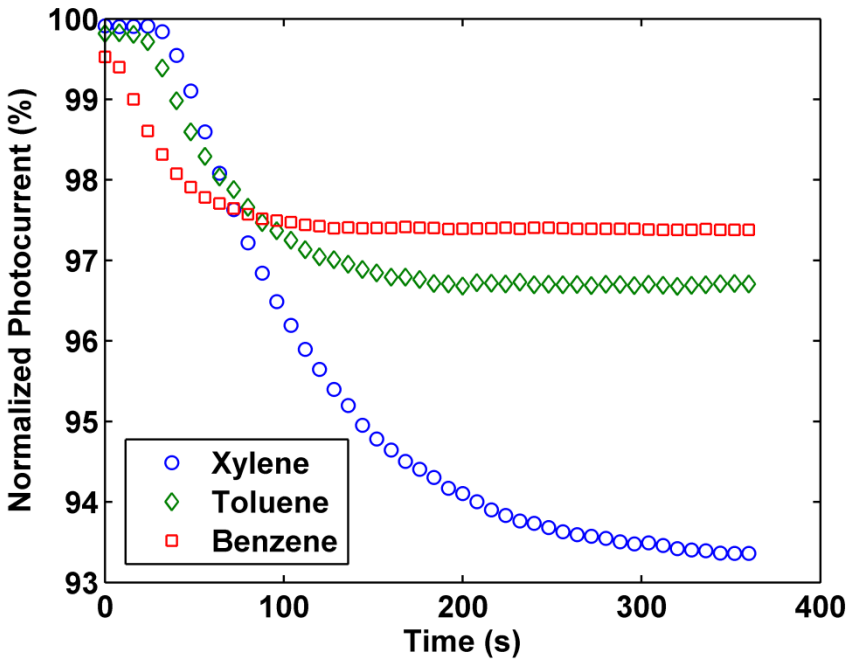

Figure 5.14: 30 ppm diffusion curves for xylene, toluene and benzene

From Eq. 5.5, the time for a solute with diffusion coefficient *D* to reach equilibrium for a 1200 nm thick film is plotted in Fig. 5.15. For the measured equilibrium times, the diffusion coefficients are estimated to be 2.22×10^{-10} cm^2/s, 1.54×10^{-10} cm^2/s, and 0.81×10^{-10} cm^2/s for benzene, toluene and xylene, respectively. These values are comparable (to within 10%) of previously published values [1]. For field measurements, this technique would permit a simple lookup-table approach for discriminating contaminants based on the measured diffusion coefficient.

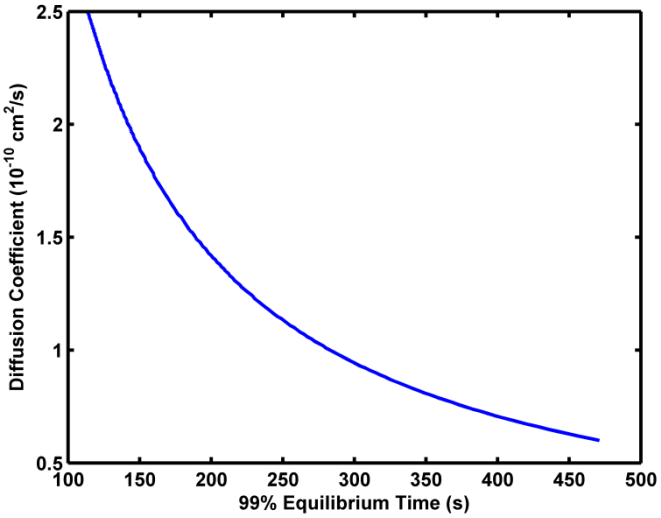

Figure 5.15: Diffusion coefficient vs. equilibrium time for a 1200 nm thick sensing film

5.10c Comparison to Other Sensing Platforms and Ways to Improve LOD

The chip's demonstrated limit of detection is below the EPA's maximum allowable concentration limit for toluene (1 ppm) and xylenes (10 ppm), but above the maximum allowable level for benzene (5 ppb) [31]. Systems which can resolve benzene at concentrations of 5 ppb or lower typically require external equipment for pre-concentrating the sample solution [9-11]. While external pre-concentration equipment could be used to further improve the LEAC chip's limit of detection, a key advantage of the chip is that it requires no sample pre-treatment and has very minimal external instrumentation requirements. By employing a grating coupler with a flip-chip laser [41], the chip would require no external optical hardware. Only electronic readout circuitry, which could potentially be integrated onto the chip, would be required, paving the way for a true lab-on-a-chip groundwater contaminant sensor.

The chip's demonstrated limit of detection is very comparable to surface acoustic wave [42] (LOD = 500 ppb for benzene), enzymatic [43] (LOD=276 ppb for toluene) and absorption spectroscopy systems [44,45] (LOD = 100-1200 ppb for xylene) presented in recent literature, which do require external optical hardware. While the LEAC chip does not provide the same level of multi-analyte identification as either

GC-MS, GC-FID or absorption spectroscopy, we have demonstrated that measurement of the solute's diffusion coefficient can be used to aid identification of contaminants in water samples containing a single dominant contaminant.

Ultimately, the chip's limit of detection depends on its sensitivity (%/RIU) and the SNR of the chip's integrated photodetectors. Assuming a partition coefficient of 800 for xylene (n=1.46) [1], the chip's measured sensitivity at 1 ppm is 1,804%/RIU which is comparable to the model simulated value of 1,500%/RIU. Simulation results indicate that a symmetric waveguide structure (lower cladding with index n=1.31) with scattering loss of 0.01 dB/cm [46] would provide a sensitivity of 6000 %/RIU. By modulating the laser and employing a lock-in amplifier [47], photodetector SNR could be further improved. These two potential improvements would likely yield a device with a significantly improved limit of detection.

5.11 Concluding Remarks on LEAC BTEX Sensing

The LEAC chip is capable of rapid (<3 min) detection of BTX contaminants. The chip is readily capable of broad-based exclusionary testing of hydrophobic contaminants, while measurement of the solute's diffusion coefficient can be used to assist in contaminant identification. A limit of detection of 359 ppb, 249 ppb, and 103 ppb has been demonstrated for benzene, toluene and xylene, respectively. Effects from other potential interfering contaminants have been characterized and the on-chip reference region has been shown to render the chip relatively immune to temperature fluctuations. The sensing platform has strong potential as a field-deployable measurement system or for consumers who may benefit from utilizing a relatively low-cost system to monitor the quality of water from household wells and faucets.

Chapter 5 References

[1] Erickson, Tim A., Rajvir Nijjar, Matt J. Kipper, and Kevin L. Lear. "Characterization of plasma-enhanced teflon AF for sensing benzene, toluene, and xylenes in water with near-IR surface plasmon resonance." *Talanta* 119 (2014): 151-155.

[2] Tim Erickson and Kevin Lear. Lab on a Chip.

[3] M. Smith, *Ann. Rev. of Public Health*, 2010, **31**, 133-148.

[4] V. Benignus, K. Muller, J. Graham, and C. Barton, *Environmental research*, 1984, **33**, 39-46.

[5] F.Gamberale, G. Annwall and M. Hultengren, *Scandinavian J. Work, Environment & Health*, 1978, 204-211.

[6] *Benzene from gas plant leak polluting water near Parachute Creek*, Denver Post, March 28, 2013.

[7] *Town of Jackson residents ponder aftermath of gasoline spill*, Milwaukee Journal-Sentinel, September 23, 2012.

[8] D. DiGiuli, *Investigation of Ground Water Contamination near Pavillion, Wyoming* (Environmental Protection Agency, Washington DC, 2011)

[9] H. Kim, S. Kim, and S. Lee, *Talanta*, 2012, **97**, 432-437.

[10] H. Faraji, M. Tajbakhsh, and M. Helalizadeh, *Analytical Methods*, 2012, **4**, 3372-3380.

[11] A. Sarafraz-Yazdi, Z. Es' haghi, and S. Sepehr, *Analytical Methods*, 2010, **2**, 746-752.

[12] A. Sarafraz-Yazdi, A. H. Amiri, and Z. Es'haghi, *Talanta*, 2009, **78**, 936-941.

[13] Y. Assadi, F. Ahmadi, and M. Hossieni, *Chromatographia*, 2010, **71** 1137-1141.

[14] "*A Review of Emerging Sensor Technologies for Facilitating Long-Term Ground Water Monitoring of Volatile Organic Compounds*," United States Envrionmental Protection Agency, August, 2003 (EPA 542-R-03-007).

[15] H. Zhang and S.Weber, Fluorous Chemistry (2012) 307-337.

[16] A. Polyakov, L. Starannikova, and Y. Yampolskii, J. Membrane Science 216(1) (2003) 241-256.

[17] F. Rupp, D. Axmann, C. Ziegler, and J. Geis-Gerstorfer, J. Biomedical Mat. Res. 62(4) (2002) 567-578.

[18] I. Pinnau, and L. Toy, J. Membrane Science, 109(1) (1996) 125-133.

[19] J. Rubio, J.Arsuaga, M. Taravillo, V. Baonza, and M. Cáceres, Experimental Thermal and Fluid Science 28(8) (2004) 887-891.

[20] B. Nelson, A. Frutos, J. Brockman, and R. Corn, Anal. Chem. 71(18) (1999) 3928-3934.

[21] J. Shiu, W. Whang, and P.Chen. J. Adhesion Sci. and Tech. 22(15) (2008) 1883-1891.

[22] W. Yunusand and A. Rahman, App. Optics 27(16) (1988) 3341-3343.

[23] J. Rim, P. Pinsky, and W. van Osdol, Ann. of Biomedical Engineering 33(10) (2005) 1422-1438.

[24] J. Crank, The Mathematics of Diffusion, Eq. 2.67, Oxford University Press, 1975.

[25] R. Olmon, B. Slovick, T. Johnson, D.Shelton, S. Oh, G. Boreman and M. Raschke, Phys. Rev. B 86(23), 235147 (2012).

[26] O. Wolfbeis and J. Homola, Surface Plasmon Resonance Based Sensors, Springer-Verlag, Berlin-Heidelberg-New York, 2006.

[27] M. Born and E. Wolf, Principles of Optics, Pergamon, London, 1980.

[28] R. Podgorsek and H. Franke, Applied Optics 41(4) (2002) 601-608.

[29] G. Long and J. Winefordner, Anal. Chem. 55(7) (1983) 712A-724A.

[30] J. Sangster, J. Phys. Chem. Ref. Data, 18(3) 1989 1111-1227.

[31] *2012 Edition of Drinking Water Standards* (Office of Water, Environmental Protection Agency, Washington DC).

[32] W. Shiu and D. Mackay, J. Phys. Chem. Ref. Data 10(4) (1986) 1175-1199.

[33] W. Kern, *Journal of the Electrochemical Society*, 1990, **137**, 1887-1892.

[34] R. Razouk and B. Deal., *Journal of the Electrochemical Society*, 1979, **126**, 1573-1581.

[35] M. Turner and E. Rhoderick, *Solid-State Electronics*, 1968, **11**, 291-300.

[36] B. Yan, T. Lin, D. Mao, and C. Yang, *Thin Solid Films*, 1989, **173**, 39-51.

[37] A. Gorin, A. Jaouad, E. Grondin, V. Aimez, and P. Charette, *Opt. Express*, 2008, **16**, 13509-13516.

[38] A. Bulusu, H. Kim, D.Samet, and S. Graham, *Journal of Physics D: Applied Physics*, 2013, **46**, 084014.

[39] M. Sağlam, F.Cimilli, and A. Türüt, *Physica B: Condensed Matter*, 2004, **384**, 397-403.

[40] C. Detavernier, R. Van Meirhaeghe, R. Donaton, K. Maex, F. Cardon, *Journal of Applied Physics*, 1998, **84**, 3226-3231.

[41] C. Liu, Y. Lin, M. Houng, and Y. Wang, *IEEE Trans. Compon. Packag. Technol.*, 2003, **26**, 635–641.

[42] F. Bender, F. Josse, R. Mohler, and A. Ricco, *14th International Meeting on Chemical Sensors*, 2012, 473-476.

[43] Z. Zhong, M. Fritzsche, S. Pieper, T. Wood, K. Lear, D. Dandy, and K. Reardon, *Biosensors and Bioelectronics*, 2011, **26**, 2407-2412.

[44] K. Lima, I. Raimundo, and M. Pimentel, *Sensors and Actuators B: Chemical*, 2007, **125**, 229-233.

[45] W. Lai, S. Chakravarty, X. Wang, C. Lin, and R. Chen, *Applied Physics Letters*, 2011, **98**, 023304.

[46] J. Bauters, M. Heck, D. John, D. Dai, M. Tien, J. Barton, A. Leinse, R. Heideman, D. Blumenthal, and J. Bowers, *Opt. Express*, 2011, **19**, 3163-3174.

[47] R. Yan, N. Lynn, L. Kingry, Z. Yi, R. Slayden, D. Dandy and K. Lear, *Applied Physics Letters*, 2011, **98**, 013702-013702.

Chapter 6: Passivation and Functionalization of the LEAC Biosensor for Detection of Cardiac Biomarkers

6.1 Biosensing Introduction

The LEAC chip is responsive to changes in upper cladding index in the region probed by guided mode's evanescent tail. As described in Chapter 3, the 1/e intensity falloff of the upper cladding evanescent field is roughly 90 nm. Thus, the guided mode is particularly sensitive to refractive index perturbations occurring in close proximity to the core. By immobilizing bio-recognition molecules, such as antibodies onto the waveguide core, the LEAC chip can be functionalized for biosensing. As shown in Fig. 6.1, the binding of a protein antigen to its correspond antibody, displaces water molecules. As protein (n~1.48) has a significantly higher refractive index than water (n~1.33), antigen binding results in a higher average refractive index in the probed region above the waveguide core, leading to less photodetector coupling and a reduction in measured photocurrent per the evanescent field shift mechanism. (The fabrication process flow for biosensing LEAC chips is provided in Appendix A3.)

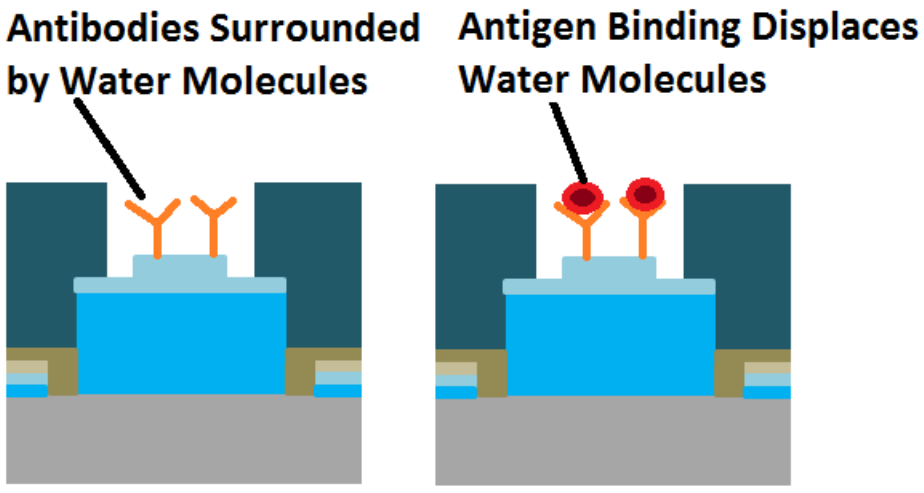

Figure 6.1: Antigen binding to immobilized antibody recognition molecules displaces water molecules resulting in a net sensing region refractive index increase

A commercial software package (FIMMPROP) was used to simulate the effect of protein adlayers on photodetector coupling. For a 1500 nm structure, simulation results indicate a modulation ($\Delta I/I$) sensitivity of 1.6%/nm of n=1.48 protein adlayers. The effect of a 20 nm adlayer on the electric field profile for a longitudinal waveguide cross section is shown in Fig. 6.2. There are two things worth noting in the figure. First, as light propagates from left to right, the field intensity decays as a result of photodetector coupling. Second, the 20 nm protein layer causes a very strong upward field shift, resulting in less photodetector coupling in the protein patterned region.

Interestingly, simulation results indicated that a 4.8%/nm modulation sensitivity could be achieved for a waveguide with an air upper cladding rather than water. The increased modulation sensitivity results from the fact that displacing air with protein provides a much stronger waveguide perturbation (Δn=0.48) than displacing water with protein (Δn=0.09). This result is consistent with Eq. 3.3. The remainder of this chapter describes the changes made to the LEAC structure to render it capable of sensing cardiac biomarkers in wet and conductive environments. A limited number of experimental results indicating the potential of the LEAC chip for multianalyte biosensing are presented.

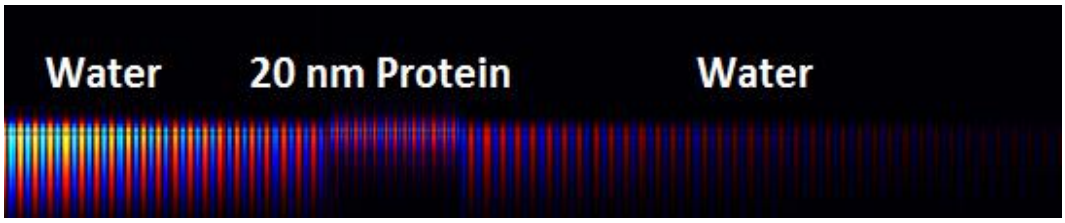

Figure 6.2: FIMMPROP simulation of the effect of a 20 nm layer on mode propagation. The image depicts the electric field intensity as the mode is guided from left to right. As the mode travels, the field strength attenuates due to substrate coupling. In the protein region, the field is shifted up and away from the underlying photodetector due to the local evanescent field shift effect.

6.2 Cardiac Biomarkers: CRP and TroponinI

There is a strong motivation to develop portable biosensing technologies that can rapidly deliver valuable diagnostic information with minimal sample preparation. Work was carried out to evaluate the LEAC chip's potential for sensing two important cardiac biomarkers, C-reactive protein (CRP) and TroponinI. CRP is a protein biomarker for systemic inflammation [2], which is normally present at concentrations of less than 10 mg/L in human serum. Studies have been conducted which indicate that patients with elevated CRP concentrations are at increased risk for cardiac infarction [3]. In contrast to CRP, TroponinI is a highly specific biomarker for diagnosing the occurrence of cardiac infarction, as it is released into the bloodstream by damaged cardiac myocytes shortly after a heart attack [4,5]. Troponin I is typically present at a concentration of less than 0.04 ng/mL in healthy patients, but becomes elevated within 3 hours of a heart attack, typically peaking in concentration within 32 hours and subsequently declining as the released protein in processed by the liver. To evaluate the feasibility or the LEAC chip for practical, multi-analyte biosensing applications, CRP and TroponinI were selected for detection.

6.3 Passivation by Atomic Layer Deposited Films for Biosensing Applications In Conductive Aqueous Environments

A specialized atomic layer-deposited (ALD) hafnia nanolaminate film, which formed the waveguide core, was required to successfully passivate LEAC chips for bionsensing experiments. Initially, we had planned to use LEAC chips fabricated with a SiNx core for biosensing experiments. Such chips had worked well for BTEX sensing in water as the entire sensing region was covered in several microns of hydrophobic Teflon AF, which formed a highly moisture-resistant passivation layer. However, for biosensing applications in ionic solutions, such as human serum or phosphate buffered saline (PBS), the waveguide core is directly exposed to the sensing medium as a Teflon film would prevent biomarker proteins from reaching the core sensing region. An initial set of experiments revealed a large increase in dark current

when SiNx core LEAC chips were exposed to PBS. As shown in Fig. 6.3, when PBS was dropped onto the SiNx chip's sensing regions, the dark current slowly increased to nearly 100 nA.

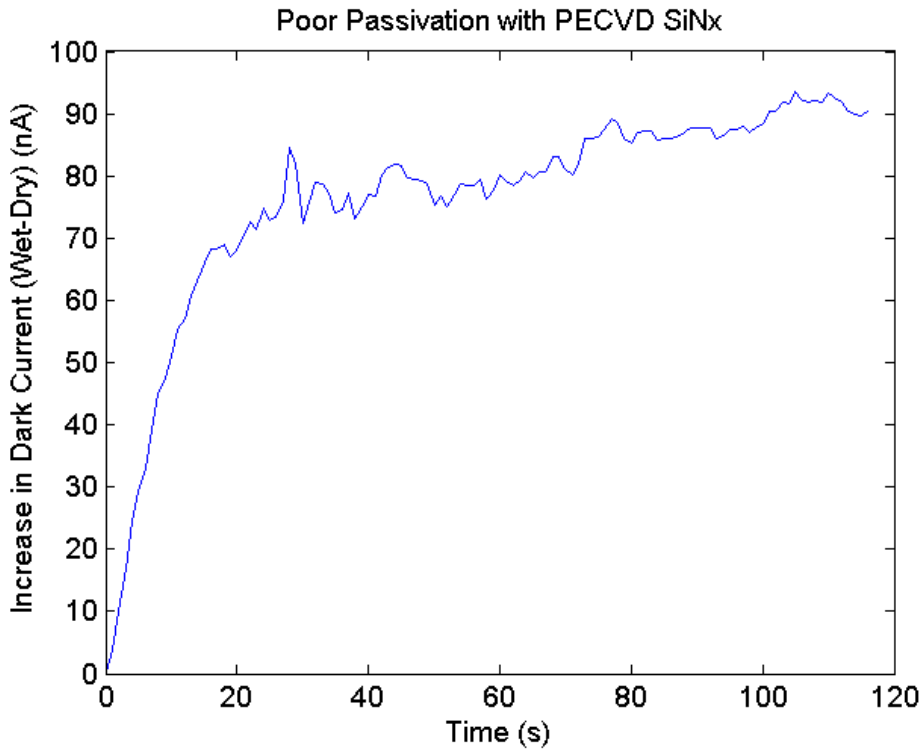

Figure 6.3: Poor passivation observed for PECVD SiNx

Given that photocurrent signals are roughly 1 μA, the magnitude of signal fluctuation caused by conductive solution "shorting" would severely compromise the chip's signal to noise ratio and the ability to resolve the small changes in current caused by protein binding. The lack of passivation with PECVD SiNx is notable given that it is used extensively in the semiconductor industry as a passivation layer. While SiNx works reasonably well for passivation in dry environments, its failure at passivation in wet environments has been observed by our group and noted by multiple groups throughout the literature [6], even for SiNx layers exceeding 500 nm.

To address the problem of excessive wet leakage currents, a hafnia nanolaminate film was deposited using plasma-enhanced atomic layer deposition (ALD) to form the waveguide core (n=2.05) instead of

PECVD nitride. The film consisted of a repeating stack of (5 alumina/100 hafnia) monolayers up to a thickness of 38-45 nm, terminating on a hafnia layer. Alumina alone could not be used as it slowly dissolves in water, necessitating the use of hafnia as a capping layer. We anticipated that the ALD hafnia nanolaminate film would provide superior wet passivation compared to PECVD SiNx based on prior work by Schindler *et al.* who demonstrated a 50 nm ALD alumina/halfnia/alumina/halfnia film stack deposited at 250C for passivating a FET-biosensor at voltages of up to 5V [7].

Indeed, the ALD hafnia nanolaminate film was found to have excellent wet passivation properties, as shown in Fig 6.4. After exposing the chip to PBS, wet leakage currents never exceeded more than 2 nA on any detector, and current fluctuations within the first 10 minutes were in the sub-nA range. After validating the ALD hafnia nanolaminate film as an excellent passivation barrier, its optical properties were characterized to ensure that it could be used to form the core of low scattering loss waveguides.

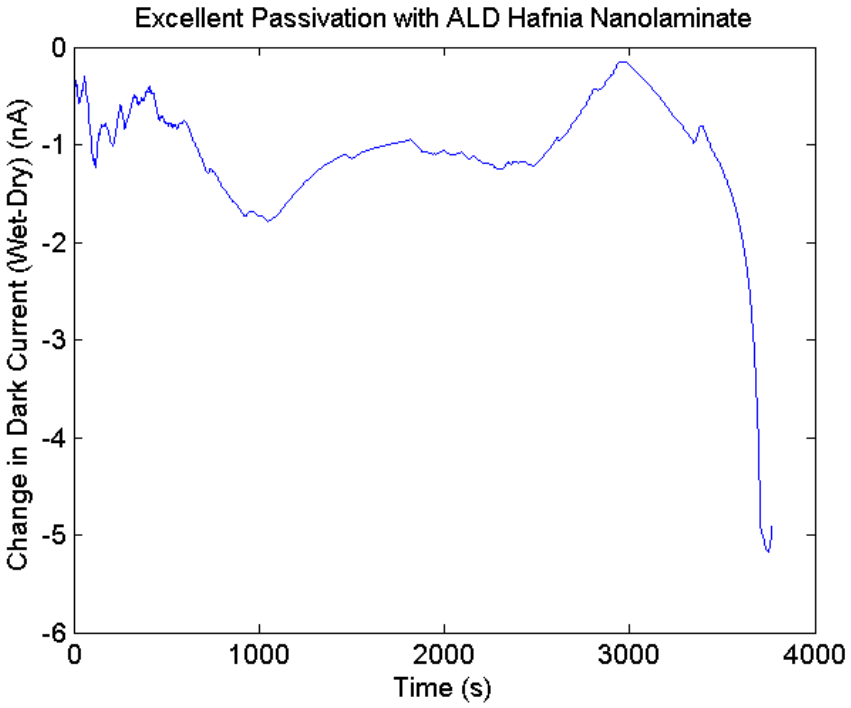

Figure 6.4: Excellent passivation observed for PECVD SiNx

6.4 Characterization of Hafnia Nanolaminate Core Optical Waveguides for Biosensing

Process requirements are stringent for forming high quality optical waveguides using ALD-deposited halfnia films [8]. Specifically, Gabriet *et al.* found large (6.2 nm) rms surface roughness for ALD-deposited halfnia films. However, halfnia films with a very thin alternating layer of alumina were found to have dramatically better optical quality. For instance, a 100 nm thick film deposited using 10 layers of the following pattern (5 alumina layers/100 halfnia layers) at 250C exhibited a rms surface roughness of just 0.75 nm. To identify optimal film parameters, scattering characterization measurements were carried out on both hafnia (H) and hafnia/alumina (HA) core waveguides. The waveguides had core height of 45 nm, etch depth of 17 nm, and core width of 4 μm. Teflon AF (n=1.31) served as the upper cladding, while 3 μm of oxide was used for the lower cladding—thick enough to ensure negligible (<0.1 dB/cm) of photodetector coupling.

Scattering loss on H/HA waveguides was measured as follows. Calibrated images of attenuated scattering were captured (Fig.6.5) as shown below, and then analyzed for scattering loss using an exponential curve fit. Results are shown for both HA and H core waveguide in Figures 6.6a and 6.6b, respectively.

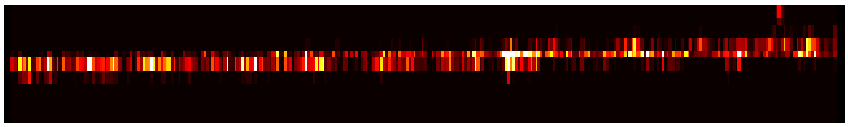

Figure 6.5: Camera image of guided mode with Matlab hot colormap

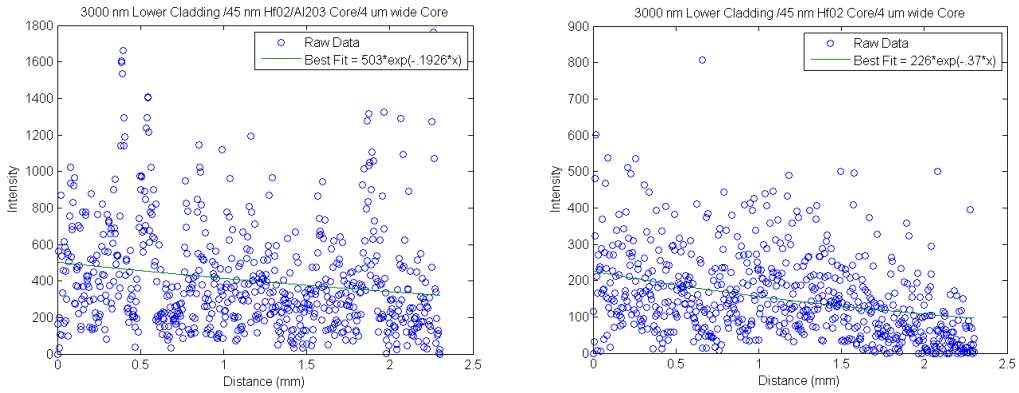

Figure 6.6: a) Exponential fit of loss from HA (left) and **b)** loss from H (right). Loss from HA<H. Three replicates on both HA and H were measured, with HA (8±2 dB/cm) found to have lower scattering loss than H (16±7). This is consistent with results from ref. 8. Given their superior optical properties, hafnia alumina (HA) nanolaminate films were deposited to the form the waveguide core on actual LEAC biosensing chips.

6.5 Functionalization of Hafnia Films for Biosensing

After test waveguide validation experiments, antibody immobilization was successfully demonstrated on hafnia films. This step is essential to functionalize the waveguide core's surface for biosensing applications, as the waveguide itself does not have intrinsic molecular recognition capabilities. The antibody immobilization process is pictorially summarized in Fig. 6.7 and a detailed protocol is provided in Appendix A3.

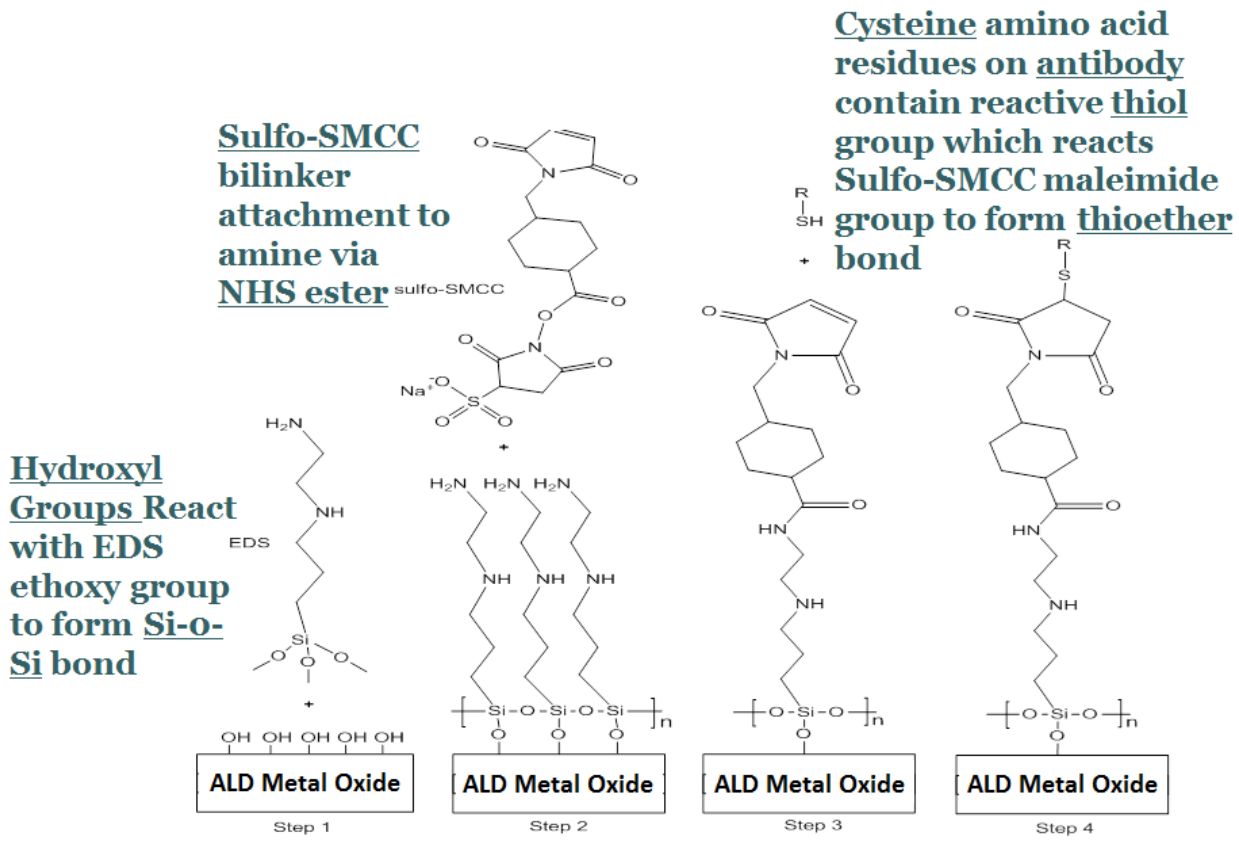

Figure 6.7: Antibody Functionalization Protocol for Hafnia Films

A brief summary of the functionalization scheme [9] is as follows. First, the surface is hydroxyl group (-OH) terminated by placing the chip in a piranha bath at room temperature for 15 minutes. The chemically robust hafnia film was not found to measurably etch in the acidic solution during this time frame, as confirmed by ellipsometry measurement. After this step, EDS silane is reacted with the –OH group, forming an amine terminated group. The heterofunctional crosslinker Sulfo-SMCC is then conjugated to the amine group via its NHS-Ester, leaving a maleimide group on Sulfo-SMCC available for antibody conjugation. The maleimide group then reacts with thiol groups on cysteins amino acid bonds, forming a thioether bond which links Sulfo-SMCC to the antibody.

FITC-labeled CRP was used to validate this protocol on hafnia. After Sulfo-SMCC conjugation three spots of anti-CRP (100 µg/mL) were printed on the hafnia substrate and allowed to incubate in a covered

petri dish. After 40 minutes of incubation in a humidified petri dish, anti-CRP was rinsed off with a 0.05% Tween 20 solution and DI Water. The substrate was then N2 dried. Then FITC-labeled CRP was incubated on the antibody spotted region for 20 minutes and then rinsed off with Tween 20, followed by a DI water rinse and N2 dry. The spotted region was then imaged with a fluorescence microscope. The results are shown in Fig. 6.8, which indicates CRP binding to the hafnia substrate. The realization of functioning hafnia test waveguides, a validated antibody immobilization scheme and the excellent passivation properties of hafnia set allowed us to proceed with biosensing experiments on actual LEAC chips. However, one more obvious hurdle first needed to be overcome.

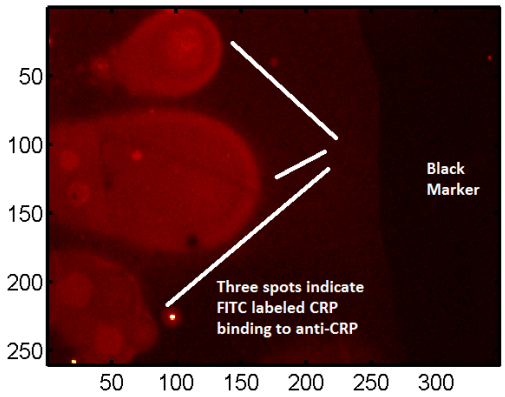

Figure 6.8: Fluorescently labeled CRP binding to anti-CRP immobilized on hafnia

6.6 Prevention of Full Teflon AF Adhesion in the Chip's Sensing Region

It was found that films could not be functionalized by simply plasma etching the Teflon AF covering the reference region, as some residual hydrophobic residue remained, even at etch periods exceeding 20 minutes. Given the Teflon AF etch rate of 700 nm/min, this etch period should have been sufficient to fully remove the ~4.5 micron of Teflon covering the waveguide core. It was later determined that the adhesion promoter had irreversibly and covalently bound to hafnia surface, leaving an approximate monolayer that inhibited antibody immobilization. To prevent this situation, NR71 photoresist was used as a blocking layer to prevent adhesion promoter from reaching the chip's sensing regions. After spin coating and curing the adhesion promoter at 115C, the liftoff resist was readily removed, yielding an

adhesion promoter-free region on the chip surface. Without the presence of adhesion promoter, Teflon AF could be readily etched from the sensing region surface, yielding a hafnia layer which could readily be functionalized with antibody probe molecules. An image of the "clean" sensing region is shown in Fig. 6.9.

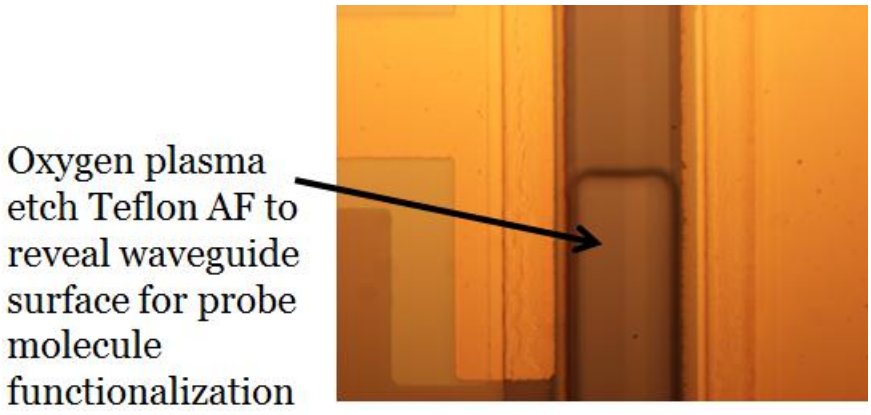

Figure 6.9: Image of clean, Teflon-free sensing region

6.7 Experimental Results on Hafnia LEAC Chips for Aqueous Biosensing

After successfully validating the hafnia nanolaminate film for passivating LEAC chips, forming low loss waveguides and demonstrating that such films could be functionalized with antibodies, experiments were set to be conducted on actual LEAC chips with hafnia nanolaminate core waveguides. To be clear, the waveguides had been validated on planar chips with a 3 micron lower thermal oxide lower cladding. We fully expected the waveguides to function on LEAC chips, despite the different surface topography. (Recall that the waveguide core lies on top of a ~1.5 micron thermal oxide strip which is 20 microns wide and about 1 cm in length, in the direction of light propagation. Surprisingly, the waveguides on numerous chips did not function as expected, and guided light rapidly attenuated within 1 mm from the coupling facet. Guided decay was characterized using monochrome camera images of the scattered light, identical to the method used to characterize hafnia test waveguides. As shown in Fig. 6.10, the guided mode was found to attenuate at a rate of at least 62 dB/cm.

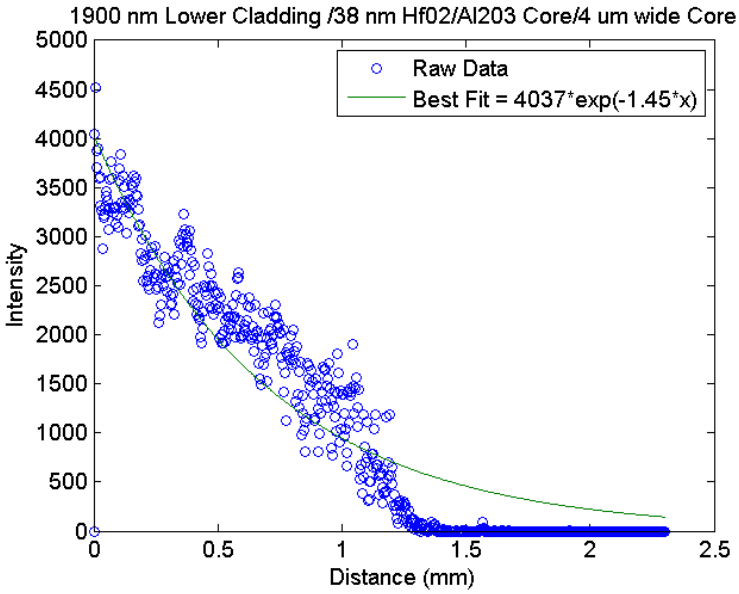

Figure 6.10: High scattering losses (~47 dB/cm) were observed for hafnia core waveguides on LEAC chips

For a model-based photodetector coupling of 15 dB/cm, the implied scattering loss is approximately 47 dB/cm or almost 600% higher than hafnia test waveguides. As the sensing region is located ~3 mm from the coupling facet, on many chips, there was no light left in the waveguide to provide a signal in the sensing region. This behavior was surprising as SiNx core LEAC chips had been reliably fabricated using the same process flow, which permitted enough optical power to reach the sensing region to generate photocurrent signals in excess of 1 μA.

A series of SEM images were taken to troubleshoot the root cause of failure for hafnia waveguides. It was found that high scattering loss waveguides exhibited excessive surface roughness in close proximity the polishing facet, as shown in Fig. 6.11.

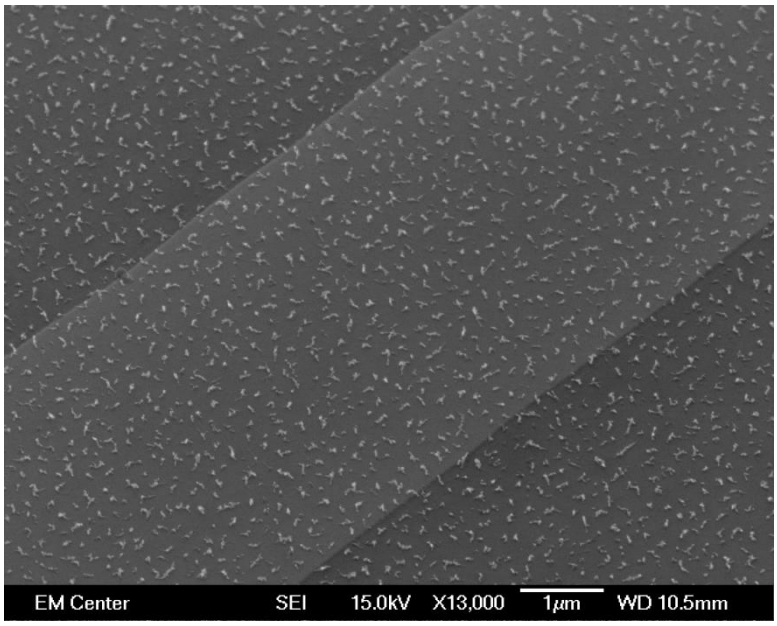

Figure 6.11: Excessive surface roughness on hafnia waveguides located close to the waveguide facet

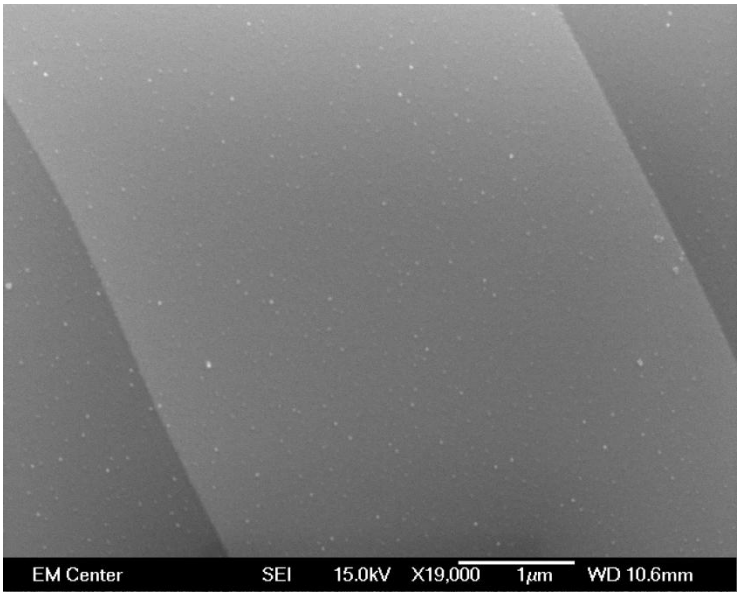

Figure 6.12: Much less surface roughness located farther away from the facet

However, only minimal surface roughness was found on portions of the waveguide located much farther (~3 mm) from the chip's facet in the chip's sensing region, as shown in Fig. 6.12. Given these observations made across multiple waveguides, it was determined that the polishing process produced a

mechanical failure in the hafnia film, resulting in cracking or film delamination under stress. This hypothesis is further confirmed by the fact that smooth waveguides were always observed on unpolished chips. It is thus recommended that a grating coupler be implemented on future chips or that the film be modified to be more resistant to stress-related fatigue.

Due to the film failure, that evidently resulted from polishing-related trauma, very low yields were observed on hafnia core chips. Of the eight chips polished, only one chip was observed to have functioning waveguide, which permitted any visible light to reach the sensing region. As each chip has 4 waveguides, this gives a total process yield of 1/32 = 3.1%.

A simple real-time refractive index experiment was conducted on this chip (Bio #3). To evaluate the ability of the chip to measure real-time refractive index changes in a highly conductive fluid (without shorting out), solutions of DI water (n=1.33250) and 3x concentrated PBS (n=1.33330) were alternately injected into a flow cell covering the chip every 30 seconds. The results are shown in Fig. 6.13 and are quite noisy, as the fiber was not glued to waveguide facet for this experiment out of caution to avoid potentially damaging the waveguide facet on the one functioning waveguide we were able to fabricate. The results show proof-of-concept as the normalized photocurrent drops by ~5% each time the higher index PBS is injected into the flow cell. If the chip were sensitive to solution conductivity rather than refractive index, the photocurrent would have increased. Thus, the hafnia thin film was validated in this instance to prevent leakage currents, even when the chip was covered with a highly conductive solution.

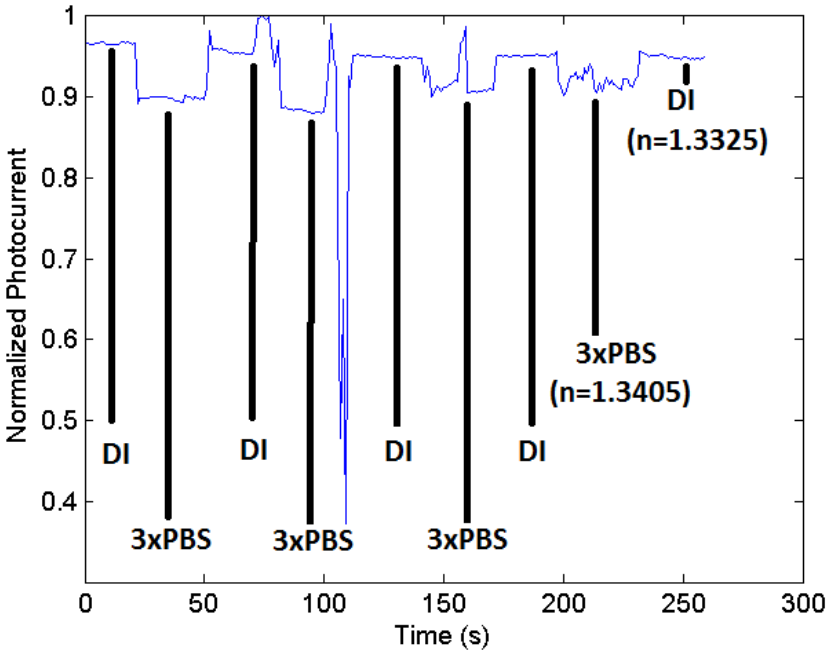

Figure 6.13: Real-time refractive index sensing with DI water and 3x PBS

After acquiring this noisy data, we attempted to glue the fiber to the chip's facet, in order to get high SNR data, as the chip is sensitive to fluctuations in coupled light intensity. However, the facet was damaged during the fiber gluing procedure preventing light from be coupled into the waveguide. The chip was then re-polished, but the waveguide was likely damaged during the second polish, as the guided mode rapidly attenuated and there was discernible optical signal from the chip's sensing region.

Clearly, these experimental results were quite disappointing, as every effort had been made to validate the biosensing design prior to integrating the waveguide on actual LEAC chips, including making test waveguides and validating the hafnia film for wet passivation and antibody passivation. It is somewhat surprising that the polishing process seems to damage hafnia waveguides only on actual LEAC chips, rather than on the fully planar test waveguides. While the root cause of failure is excessive surface roughness induced by polishing, it is still unclear what physical mechanism is responsible for the surface roughness on LEAC chips vs. test waveguides. One may hypothesize that either the metallization or steeper surface topography contributes to film stresses or adhesion failure, but clearly more failure

analysis experiments are warranted. We had hypothesized that the deposition of hafnia on top of the gold contact traces had contributed to film failure due to poor adhesion. However, after changing the fabrication process flow to deposit metal only after hafnia had been deposited directly on top of oxide did not seem to greatly affect the process yield. Given these results, the exact physical mechanism behind the cause of failure is currently unresolved. It would be worthwhile to implement chips with a grating coupler, which would likely improve coupling efficiency and eliminate film problems induced by polishing. It would be also worthwhile to fabricate a new batch of test waveguides, in order to verify that the film's optical and mechanical parameters had not changed from the first deposition run. However, given that the hafnia films were deposited by an expert with years of fabrications experience at the Center for Integrated Nanotechnology, it is unlikely that film quality changed dramatically between the initial run used for test waveguides and the final deposition run performed several weeks later on actual LEAC chips.

6.8 Experimental Results on SiN_x LEAC Chips for Dry Biosensing of TroponinI

Due to the low process yield described above for hafnia core wavguides, a simple experiment was undertaken on a SiNx core LEAC chip to validate the chip for sensing TroponinI in a dry biosensing environment, which is inherently not capable of wet biosensing because it shorts out. For this experiment, a LEAC chip was fabricated with a SiNx waveguide with a 90 nm core height, 4 micron core width, and a lower cladding thickness of 1.9 microns. Air served as the upper cladding. Using the antibody immobilization process described in Appendix A3, the chip was functionalized for sensing TroponinI, by incubating 50 μg/mL of anti-TroponinI in PBS (Santa Cruz Biosciences, sc-8118) over detectors #2-4 for 20 minutes. Before drying, the anti-TroponinI droplet was immediately rinsed off using PBS, a 0.5% solution of Tween 20 in DI Water, and lastly DI water before gently blow-drying the chip in nitrogen. Immediately after drying the chip, the chip was incubated in a 3 mL solution of TroponinI (sc-8118p) in PBS at a concentration of 1 μg/mL for 20 minutes. After incubating, the chip was once again rinsed off using PBS, 0.5% Tween 20 surfactant, and DI water before drying. Photocurrents on the chip were

measured before antibody patterning, after antibody patterning, and after exposure to the TroponinI antigen. The normalized photocurrent data is shown in Fig. 6.14. As expected, the photocurrent decreases as a result of anti-TroponinI patterning and further decreases as a result of TroponinI binding on sensing detectors (#2-4). The modulation ($1\text{-}I_{final}/I_{initial}$) data is given in Fig. 6.15.

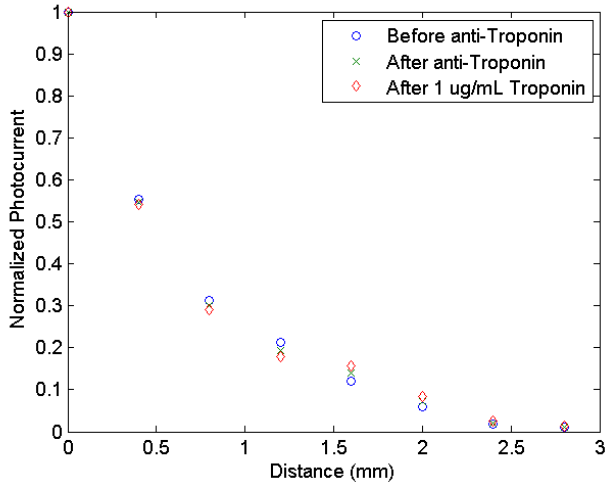

Figure 6.14: Photocurrent data for TroponinI binding experiment

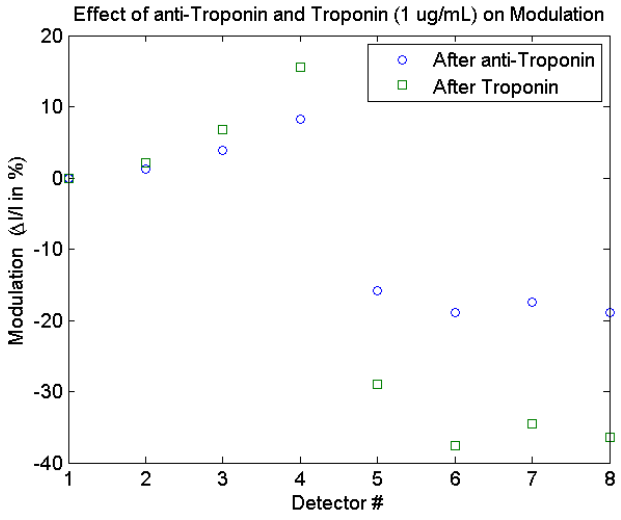

Figure 6.15: Modulation data for photocurrent measurements

The data show a significant increase in photocurrent reduction in the sensing region, as a result of antibody patterning and binding. The signal is strongest on the 4th detector, where a 6.7% signal change is seen after TroponinI binding. Interestingly, the modulation becomes negative in detector regions #5-8. Due to analyte binding in upstream regions, there is more light available to reach downstream regions as a result of antibody immobilization and analyte capture. Given a modulation noise of 0.1%, the one standard deviation limit of detection of the fourth (and best) detector is given by (0.1%/6.7%)*(1μg/mL) = 16.7 ng/mL. By way of comparision, modern lateral flow immunoassays can detect TroponinI in whole blood at concentrations of just 0.009 ng/mL [10]. Given these results, it is evident that lateral flow immunoassays, at present, have a clear advantage over the LEAC biosensor for medical diagnostics. However, lateral flow immunoassays cannot perform real-time binding measurements to extract kinetics. Provided that LEAC chips can be fabricated with functional waveguides and integrated light sources, they have tremendous potential in providing a low-cost platform for performing real-time binding experiments, similar to SPR. As described in Appendix J, the effect of surface roughness, due to uneven antibody binding should have a minimal effect on device performance for antibody-antigen layers with heights of less than 20 nm, covering a broad range of antigen-antibody complexes. However, due to the failure of hafnia core waveguides on actual LEAC chips, these theoretical predications have not yet been verified.

Chapter 6 References

[1] Vörös, Janos. "The density and refractive index of adsorbing protein layers."*Biophysical journal* 87, no. 1 (2004): 553-561.

[2] Black, Steven, Irving Kushner, and David Samols. "C-reactive protein." *Journal of Biological Chemistry* 279, no. 47 (2004): 48487-48490.

[3] Ridker, Paul M. "Clinical application of C-reactive protein for cardiovascular disease detection and prevention." *Circulation* 107, no. 3 (2003): 363-369.

[4] Antman, Elliott M., Milenko J. Tanasijevic, Bruce Thompson, Mark Schactman, Carolyn H. McCabe, Christopher P. Cannon, George A. Fischer et al. "Cardiac-specific troponin I levels to predict the risk of mortality in patients with acute coronary syndromes." *New England Journal of Medicine* 335, no. 18 (1996): 1342-1349.

[5] Melanson, Stacy EF, Milenko J. Tanasijevic, and Petr Jarolim. "Cardiac Troponin Assays A View From the Clinical Chemistry Laboratory." *Circulation*116, no. 18 (2007): e501-e504.

[6] Heer, F.; Franks, W.; Blau, A.; Taschini, S.; Hierlemann, A.; Baltes,H. CMOS microelectrode array for the monitoring of electrogeniccells. *Biosens. Bioelectron.* 2004, *20*, 358.

[7] Edlou, Samad M., Ali Smajkiewicz, and Ghanim A. Al-Jumaily. "Optical properties and environmental stability of oxide coatings deposited by reactive sputtering." *Applied optics* 32.28 (1993): 5601-5605.

[8] Lee, Michael, et al. "A novel biosensor based on hafnium oxide: Application for early stage detection of human interleukin-10." *Sensors and Actuators B: Chemical* 175 (2012): 201-207.

[9] Wu, Peng, Paul Hogrebe, and David W. Grainger. "DNA and protein microarray printing on silicon nitride waveguide surfaces." *Biosensors and Bioelectronics*21, no. 7 (2006): 1252-1263.

[10] Zhu, Jimin, Nengli Zou, Hongju Mao, Ping Wang, Danian Zhu, Huoyan Ji, Hui Cong et al. "Evaluation of a modified lateral flow immunoassay for detection of high-sensitivity cardiac troponin I andmyoglobin." *Biosensors and Bioelectronics*42 (2013): 522-525.

Chapter 7: Future Work

7.0 Chapter Overview

The LEAC chip has shown tremendous promise as a cost-effective sensing platform for groundwater contaminant sensing applications. Future work on the LEAC sensing platform should be geared toward achieving three important goals: true lab-on-a-chip miniaturization, identifying and making the chip work for additional applications for which it is well suited, and lastly, further improving the chip's sensing performance in terms of both sensitivity and LOD. Each of these suggested areas of future work are discussed in more detail below.

7.1 Stepping Stones to Achieving a True Lab-on-a-Chip

With additional engineering work, the LEAC sensing platform can be converted to a highly integrated lab on a chip. Presently only the waveguide sensing element and photodetectors are integrated on the chip. The light source, amplification circuitry, ADC and readout hardware are all off chip, making the LEAC chip more of a "chip-in-a-lab" than a true "lab-on-a-chip". With sufficient engineering work and investment, the LEAC chip can become highly integrated.

7.1a Light Source Integration

Rather than polishing the chip and using an external fiber-coupled laser to excite the waveguide, an efficient grating coupler with an adiabatic taper can be designed to obviate the need for polishing and improve coupling efficiency. Potential grating 1-d coupler designs are discussed in Appendix E. Further simulations and experimental work should be done to refine the design, so that a high efficiency grating

coupler can be fabricated. The designer must pay attention to interference effects related to upper and lower cladding thickness, which can have a very strong influence on coupling efficiency.

Unlike resonant sensing platforms which have very strict requirements on source linewidth and stability, the source requirements for the LEAC chip are somewhat relaxed. Experiments show that a low-cost ($2) laser diode works sufficiently well. To take advantage of the LEAC chip's small footprint and low cost compared to other sensing platforms, the light source should ideally be integrated onto the chip using a flip chip method [1]. End users are always looking for convenience and reliability in a product. While gluing a fiber to the end of the chip works sufficiently well for prototyping, full integration of the light source on chip would make the chip more robust and remove the need for external optical components, including the fiber and fiber coupling apparatus.

7.1b Photocurrent Readout Circuitry Integration

From a research perspective, there is much to be gained by integrating all circuitry which currently resides on a PCB board onto the chip. As a first step, the chip hardware engineer should integrate the transimpedance amplifier and corresponding low pass filters onto the chip. Along with light source integration, this would ensure that the chip could be plugged into a simple readout board with a microcontroller and low-energy Bluetooth to stream data to a computer, cell phone or other display device. Further improvements could off course be made by integrating ADCs and wireless communication links onto the chip. The designer, however, should be aware that heating could severely limit the chip's monitoring capabilities, as it has been shown that the chip's temperature-related modulation sensitivity is 0.02%/°C. Thus temperature fluctuations could contribute to significant noise. Therefore, the chip should be designed to have low power consumption and metal should be potentially added in places to serve as contacts for heat sinking. There are many challenges to full electronic integration that the designer must be aware of. Also, it is likely that dozens of mask layers would be required to fabricate such a chip, which would raise the production cost substantially.

7.1c Packaging

While efforts are underway to improve packaging, so that the chip be used without the probe card, there is much work that needs to be done in this area. In its present form, the area required for one sensing waveguide on the chip is compatible with the footprint of a DIP-14 package. By designing the contact pads in the appropriate configuration, the chip could potentially be integrated into a DIP-14 package, and the top of the package could be readily designed to contain fluidic housing for BTEX sensing. For biosensing, the package design might include a top layer that can snap into place after Ab printing in order to form a miniature, watertight fluidic channel. There are many potential creative avenues for improving the chip's packaging. Integration into a DIP package would ensure that chips could simply be readily snapped into place on a board containing a readout-display and other necessary circuitry.

7.2 Additional Applications

While the chip has been demonstrated for aromatic hydrocarbon sensing in groundwater, there may be other sensing areas which could prove to be fertile ground for the chip's development. Biosensing experiments should be conducted on the chip once issues regarding the hafnio nanolaminate film are resolved. The chip has yet to be demonstrated for either bio-threat sensing or for sensing explosives. It may be possible to functionalize the chip for these and other interesting applications.

7.3 Sensing Performance Improvements

Based on rigorous simulations and confirmation from experimental results, there are several things designers can do to improve the chip's (%/RIU) sensitivity. First and foremost, if sufficient scattering reduction can be achieved through improved fabrication tolerance and film quality, the lower cladding thickness can be increased to linearly increase sensitivity. However, as discussed in chapter 3, coupled power falls off exponentially, so designer must be aware of tradeoffs in terms of the shot-noise limit. Simulations and oil experiments also revealed a very promising avenue for sensitivity improvement. By implementing a symmetric waveguide structure, more evanescent power is available to probe the upper

cladding sensing region. As a result, sensitivity increases by roughly 500%. Interestingly, if the waveguide structure can be designed to be nearly perfectly symmetric, a very small core thickness of a few nm can be employed. Using this design, nearly 100% of the power is located outside of the waveguide core. The smallest perturbation, due to BTEX diffusion would cause the guided mode to become leaky, causing light to rapidly leak into the upper cladding leading to a sharp decrease in photocurrent for a very small upper cladding index increase. This design change would be both compelling an interesting. For a perfectly symmetric (n=1.31) BTEX waveguide with a 5 nm (n=1.8) core, the simulated sensitivity is 9600%. However, this would require making the waveguide's lower cladding out of Teflon AF or some other low index (n~1.3) material, such as Cytop with minimal (<10 dB/cm) of scattering loss.

7.4 Photodetector Improvements

Referring to chapter 2, the chip's limit of detection can be improved by reducing photocurrent noise in addition to improving device sensitivity. There are at least two methods for reducing photocurrent noise. Based on experimental results presented in the Appendix G, Pt should be used as a contact metal instead of Au, as it improves photodetector SNR in short-run experiments and the contacts are less susceptible to long-term drift. At the moment, this drift is thought to be caused by gold's tendency to diffuse into silicon and readily alloy with silicon. In contrast, Pt diffusion into silicon is minimal and only forms silicides at relatively high temperatures (~600°C). Furthermore, the high Pt barrier height renders the photodetectors less susceptible to photoconductive gain and temperature-induced fluctuations in dark current. Pt was not used for experimental LEAC chips due to difficulties with adhesion of Pt to Si.

In addition to improving the contact metallurgy, the excitation laser can be modulated and a lock-in amplifier can be used to further improve SNR. Presently, the system measures photocurrents with a 6 Hz two-pole Butterworth low pass filter (Appendix C). While the filter is very robust at removing high frequency noise, the system is susceptible to drift and other issues related to 1/f noise. By employing a

lock-in amplifier, both drift and noise bandwidth can be greatly reduced. Experimental results have shown that the chip's photodetectors can be modulated at several kHz, which is sufficient for a lock-in amplifier to work. Portable lockin-amplifiers, as reported in the literature [2] are readily capable of 1.5 Hz bandwidth precision. This would improve SNR by a factor of roughly four for white noise. In conjunction with employing a symmetric waveguide structure (nearly identical upper and lower cladding indices), the LEAC BTEX sensor's LOD could likely be improved by a factor of 20. This would bring the chip's LOD into the mid 10^{-7} RIU range and make the device competitive with SPR for bulk refractive sensing. This would be a major engineering accomplishment for a sensor integrated into a coin-sized package.

With the 2nd generation cheap, we have demonstrated fluidic compatibility, real-time sensing, a two order of magnitude improvement in limit of detection, and a practical real-world sensing application. However, there is still a significant amount of engineering work required to realize its full potential. This chapter has provided several potential avenues for future improvements to this uniquely portable sensing platform.

Chapter 7 References

[1] Fang, Alexander W., Hyundai Park, Oded Cohen, Richard Jones, Mario J. Paniccia, and John E. Bowers. "Electrically pumped hybrid AlGaInAs-silicon evanescent laser." *Optics express* 14, no. 20 (2006): 9203-9210.

[2] Novak, Lukas, Pavel Neuzil, Juergen Pipper, Yi Zhang, and Shinhan Lee. "An integrated fluorescence detection system for lab-on-a-chip applications." *Lab on a Chip* 7, no. 1 (2007): 27-29.

Appendix A1: LEAC Chip Fabrication Process Flow for PECVD Oxide Chips Used in Real-Time Oil Sensing Measurements

Successful LEAC chip fabrication requires careful attention to detail and a thorough understanding of each individual step in the entire process. Each step must be inspected with a microcope before moving onto the next step whenever possible. Note down all relevant parameters in the LEAC Process Control Sheet found at the end of this document. This is very helpful in pinpointing fabrication errors. Never start a first fabrication without reading through this entire document first and understanding every step in detail.

Often times, the photoresist does not spin on consistently or develop as intended. However, I have determined parameters after hundreds of rounds of trial and error that have a reasonably high success rate. Fortunately, all photolithography steps are reversible with a simple RR2/acetone/methanol/DI water cleaning. It is absolutely critical to use HMDS adhesion promoter before spinning on positive photoresist, and it is essential to inspect the chip after each photolithography stage. With the naked eye, it is possible to see if the photoresist has spun on evenly. For S1818, one should observe interference fringes, while for 2070 one should observe a uniform coating with a slightly rough texture, but no obvious bubbles or streaks. These defects are indications of poor spin on.

Additionally, deposition rates can often vary from day to day. This is true for etching rates as well. Therefore, it is absolutely necessary to use a dummy wafer at each step, so that oxide and nitride deposition and etching steps can be monitored. Always use fresh photoresist. Photoresist seems to lose performance in less than a day when in a pipette due to VOC evaporation resulting in viscosity changes.

The approximate time budget for fabrication is shown, excluding polishing time.

Process	**Time (hours)**
RCA clean	1
Buried Detector Oxide Deposition	0.5
4 Photolithography Steps	2
Metal Deposition+Liftoff	3
30 nm Nitride/ 1000 nm Oxide Lower Cladding Deposition	4
Nitride Core Deposition and Etching	1
Oxide Upper Cladding Deposition+Liftoff	5
Total=	**16.5**

PLEASE NOTE: Step 7, the via etch step has proven to be problematic. Occasionally the pads become over-etched, or some pads do not open up, or the HF etchant eats through the metal pads entirely in sections, potentially leaving metal in contact with the device layer, which would short out the chip. Tiny holes in the photoresist can lead to etching of the waveguide. While it is still included in the protocol for completeness and is needed to expose the testing structures on top of the chip, it is strongly recommended that a basic masking step be used to enable probing of the metal pads. This can be done by cutting a clean 2 mm x 12 mm piece of silicon wafer and covering the metal pads during PECVD oxide and nitride deposition steps for the lower cladding, waveguide core, and upper cladding. Double check to make sure all pads are covered with the tiny Si wafer mask.

Mask: Use the "Senior Design" Mask for all photolithography steps.

After experiments, clean the chip appropriately. Please see LEAC Chip Cleaning Protocol.

Step 1: Wafer Preparation

The wafer must be clean and free of any microscopic contaminants. Acetone sonication for degreasing followed by an RCA clean for contaminant removal are essential steps. Without them, pits and blisters tend to form on PECVD oxide. These pits and blisters, will cause shorting to the wafer substrate. Figure 1, at 5x magnification, shows a 200 nm layer of oxide deposited on a chip which was RCA cleaned (left) and a chip which was not RCA cleaned (right). Notice the defects on the chip that was not RCA cleaned.

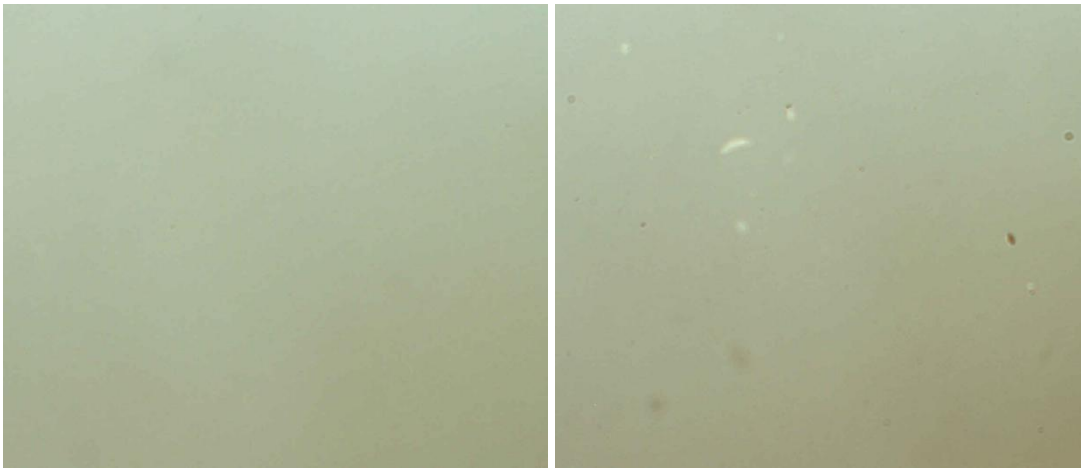

Figure A1: Effect of RCA cleaning on subsequent oxide deposition

1a) A quick note on wafer dicing. To prevent the wafer from being scratched, always spin and bake a thin layer of photoresist onto the device layer of the wafer before applying wafer dicing tape sheet to both sides of the wafer.

1b) After dicing wafer, place the wafer in a **clean** glass beaker filled 1 cm deep with acetone. Sonicate for 5 minutes. Remove wafer. Rinse with acetone, methanol, and water. Blow dry with nitrogen.

2) Perform RCA clean. There are three steps in RCA process, plus an extra DI water rinse. The RCA procedure is described in detail at: http://inside.mines.edu/fs_home/cwolden/chen435/clean.htm.

The procedure is outlined briefly below,

After a quick DI water rinse, the first step step is performed with a 50:50:250 mL solution of NH_4OH (ammonium hydroxide) + H_2O_2 (hydrogen peroxide) + H_2O (water) at 80 °C typically for 10 minutes. This treatment results in the formation of a thin silicon dioxide layer (about 10 Angstroms) on the silicon surface, along with a certain degree of metallic contamination (notably Iron) that is removed in subsequent steps. This is followed by transferring the wafers into a DI water bath.

The second step is a short, 15 second dip in a 1:50 solution of HF + H_2O at 25 °C, in order to remove the thin oxide layer and some fraction of ionic contaminants.

The third and last step is performed with a 50:50:300 mL solution of HCl + H_2O_2 + H_2O at 80 °C. This treatment effectively removes the remaining traces of metallic (ionic) contaminants. Following, the last step, the wafer is placed in a DI water bath from two minutes and then rinsed in DI water for 30 seconds, followed an N2 blow dry. Use teflon tweezers if possible.

Step 2: Buried Detector With High-Temperature, High Quality Oxide

1) Deposit 280 nm of high temp oxide (HTO) on wafer. Deposition rate is about 10.3 nm/minute, so run deposition for about **27 minutes**. Measure with ellipsometry and filmetrics to be sure. Prior to deposition, make sure chamber is clean. If there is flaking from the showerhead, wet a lint-free cloth with water and gently scrub. Then run CF4/02 plasma clean for 10 minutes. See Plasma Clean protocol for details.

a) **PECVD settings**

i) Temperature **350C**. Pressure start at 200 mT. Slowly raise to **500 mT** after all gases on. Pressure above 540 mT causes system to abort deposition for unknown reasons.

ii) Set power to 25W

iii) Uses gases 1,2,3 and set flow rates. N20 (70 sccm), He (600 sccm), SiH4 (70 sccm).

2) Remove wafer from PECVD, and place on paper cloth. Let it cool to room temperature. Pipette HMDS on the wafer. Spin at 3000 RPM for 15 second then stop. Pipette 2070 onto the wafer, being careful to form no bubbles. Set total spin time to 50 seconds. Spin on PR at 500-700 RPM for about 7 seconds, then ramp up to 5000 RPM. Inspect to make sure photoresist has spun on evenly. If not, remove photoresist with acetone, methanol, DI water, and repeat.

3) Pre-exposure bake for 2 minutes at 100C.

4) Photolithography: Use the 50 micron detector mask, and align wafer. Establish firm contact with mask and expose for 30 seconds on the left mask aligner.

5) Postbake at 110C for 100s. Then let wafer cool or blow with nitrogen

6) Develop in MIF300 developer for about 40s. Inspect photolithograpy with microscope. Make sure that the photoresist mirrors the mask structure. If it doesn't, repeat photolithography. If it passes inspection, go on to step 7.

7) Using Teflon tweezers, carefully place the chip in BOE (HF buffered oxide etch). The etch rate is 3.3 nm/second. To ensure complete etching, bath chip in BOE for two minutes. Then using Teflon tweezers remove from BOE and rinse under DI water for 20 seconds. Then place chip in clean DI water batch for one minute. Then remove chip and rinse in DI water again. The rinsing process ensures that all BOE has been removed from the surface of the chip and photoresist. In the last step, use acetone, methanol, and water to remove the photoresist. Fig. 2 shows a well-fabricated buried detector. Notice the clean lines and

etching only in the detector region. The hazy spots are an artifact of dust, which has collected in the microscope over many years.

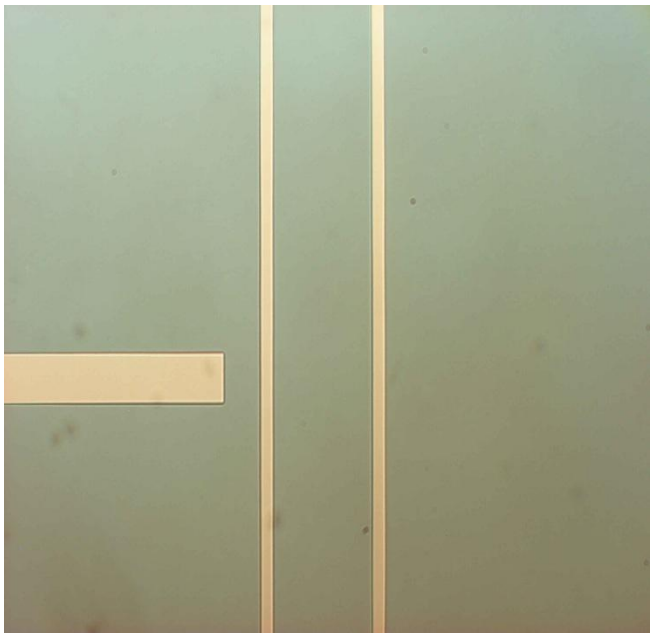

Figure A2: Buried Detector

Step 3: Metal Pad Fabrication

1) Pipette 2070 onto the wafer, being careful to form no bubbles. Set total spin time to 50 seconds. Spin on PR at 500-700 RPM for about 7 seconds, then ramp up to 5000 RPM. Inspect to make sure photoresist has spun on evenly. If not, remove photoresist with acetone, methanol, DI water, and repeat.

2) Pre-exposure bake for 2 minutes at 100C.

3) Carefully align metal mask. Use 20 micron or 25 micron pad separation mask. 15 micron makes waveguide alignment exceedingly difficult. Make sure alignment is good so that detector pads and ground pad over lap exposed silicon uniformly. Expose for 30 seconds on left aligner. Starting power should read about 274 Watts.

4) Postbake at 110C for 100s. Then let wafer cool or blow with nitrogen.

5) Develop in MIF300 developer for about 40s. Inspect photolithograpy with microscope. Make sure to not underdevelop (poor metal adhesion) or overdevelop (narrowed metal pad separation). Figure 3 is an example of excellent metal photolithography. Notice the overlap with the detector and clean pink regions, where there is no photoresist. This is where metal will be deposited.

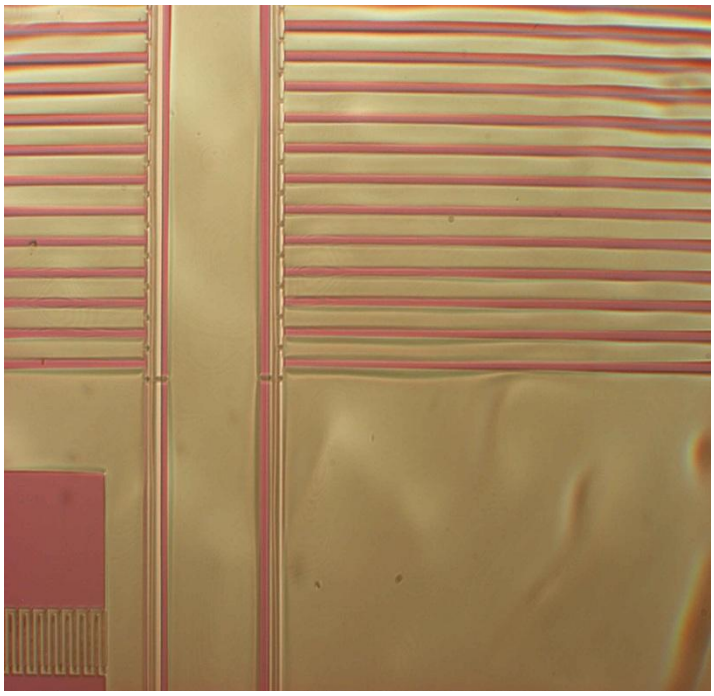

Figure A3: Metal photolithography

6) To thoroughly clean the contact region, do the following. Rinse with MIF300 directly from bottle for 3 seconds. Make sure the MIF300 flows from top to bottom of chip. Rinse with DI Water for 30 seconds. Then Dip in 1:1 clean HCl:DI water for 3 seconds. Then dip in clean 10% diluted BOE for 3 seconds. Then Dip in 1:1 HCl:DI Water once again for 2 seconds. Then thoroughly rinse for 30 seconds in DI water. The place chip in clean DI water bath for 30 seconds. Then rinse again with DI water. Then N2 blow dry wafer. The DI wash steps are needed to remove any residual acid from regions where Ti/Al is to be deposited.

7) Deposit 200 nm Ti, then 200 nm Al, preferably using electron beam evaporation, as this is known to form a cleaner contact than thermal evaporation. Always let the chip cool for 30 minutes under vacuum after evaporation or the aluminum will thermally oxidize.

8) Perform lifoff. Place chip in acetone in a **covered** petri dish for 30 minutes. Then sonicate in acetone for two minutes. Then rinse with acetone, methanol, and DI water. Never let acetone or methanol dry on this chip, as their evaporation leaves small contaminants due to the presence of impurities. Lastly, inspect to make sure all metal is lifted off and no residue is present on chip. Figure 4 shows what the chip should look like after metallization and liftoff.

Figure A4: Top and bottom of chip after Ti/Al Deposition. In the right image, the pad farthest to the left has a slight defect.

Step 4: Oxide Lower Cladding Deposition

1) Deposit 1500 nm of oxide using following PECVD settings. **The deposition process usually takes about 220 minutes.** Use a dummy wafer and monitor after 100 minutes to determine rate and adjust remaining deposition time accordingly.

a) **PECVD settings**

i) Temperature **250C**. Pressure start at 200 mT. Slowly raise to **500 mT** after all gases on. Pressure above 540 mT causes system to shutdown for unknown reason. Power set to 25W.

ii) Uses gases 1,2,3. N20 (70 sccm), He (600 sccm), SiH4 (70 sccm).

Step 5: Nitride Deposition for WG Core

1) Deposit *x* nm of nitride using the following settings. Rate is about 10 nm/min and index is 1.8-1.81. Deposition rate tends to vary from day to day. Always start with clean chamber. Run a 20 minute CF4/02 plasma clean after wiping chamber with a damp cloth. After determining rate and verifying index of refraction with ellipsometry, deposit nitride on actual sample and dummy sample. Use dummy sample to note index or refraction and thickness with ellipsometry. Is it within spec? If not, the LEAC chip may be ruined if you over-deposited. Etching to thin the SiNx layer will create roughness rendering the waveguide useless.

a) PECVD Settings

i) 47 Silane, 23 He, 7.6 sccm NH3.

ii) 50W. 250C. 3.5 mT. Time in minutes is desired sample height in nm/10.

2) Let chip cool to room temperature. Then rinse with DI water. Then N2 blow dry and dehydrate wafer on hot plate for 1 minute at 120C.

Step 6: Waveguide Fabrication

This is the most technical step of the entire process and is very difficult to execute consistently. Any sidewall roughness in the photoresist gets transferred to the nitirde layer during etching, which will dramatically increase the scattering loss of the waveguide rendering the chip poor or unusable. Prior to etching, INSPECT PHOTORESIST. USE FRESH PHOTORESIST.

1a) Spin on on HDMS adhesion promoter for 10s at 3000 RPM. Then apply S1818 and spin on at 7000 RPM for 30 seconds. Photoresist should have interference fringes and no bubbles.

1b) Pre-expsosure bake for 2 minutes at 100C.

1c) Place the chip in a clean beaker filled with DI water for 1 minute. This is needed to rehydrate the photoresist, as water is needed to catalyze UV-induced reaction in the photoresist. The local environment typically has typically very low relative humidity, and the manufacturer recommends a minimum humidity of 60%.

1d) Remove wafer from DI water and thoroughly N2 blow dry.

3) Carefully align WG mask. Waveguide width should be 7 microns although this dimension is pending future investigation, as the SiNx height must be precisely controlled to ensure single mode propagation. Make sure there is very firm contact between mask and wafer. Any gap will increase PR roughness.

4) Expose for 25s. Lamp should read 274 W prior to exposure.

5a) Develop carefully in AZ400k developer for 10s-25s in 5 second increments. Move the wafer up and down and left and right in a clockwise motion. Make sure not to overdevelop as this can will damage the photoresist. Once there is only scum on the wafer, dump out the old developer, rinse the dish and use new developer. Develop for a few seconds more, and inspect to make sure there is no visible scum. The idea is to remove all the exposed resist without damaging the resist that will form the waveguide.

5b) Prior to etching, a 5 minute reflow at 120C is recommended to reduce roughness. Start the hotplate at 100C and ramp up to 120C over a minute.

5c) After reflow, 02 plasma clean the wafer at 40W/40sccm to remove any residual scum that can't be seen under the microscope. Figure 5 is an example of acceptable waveguide photolithography at 100x magnification.

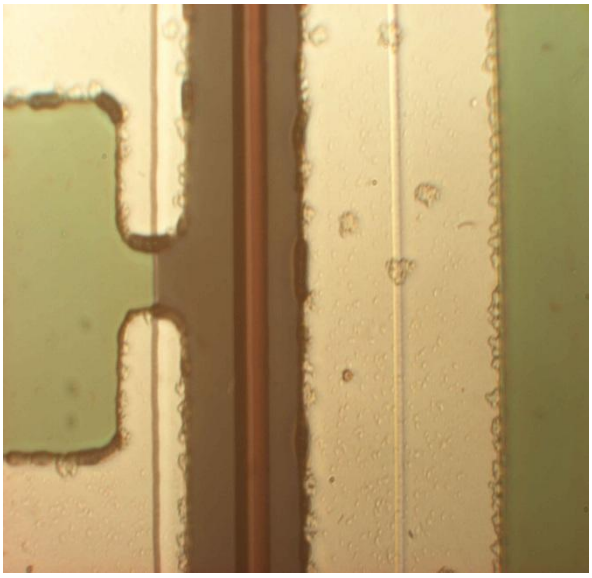

Figure A5: Waveguide photoresist before etching at 100x.

6) Using the dummy wafer from the Step 5, determine the nitride etch rate at 40 sccm CF4, 40W on low pressure setting using ellipsometry and 20 second etch steps. A typical rate is 33 nm/minute. Using the determined rate, fully etch or partially etch waveguide to desired depth. The current etch time is 70 s for a 50 nm SiNx core height. After this step, clean the chip with acetone, methano, and DI water to remove photoresist. N2 blow dry. Inspect under microscope and note any irregularities in the waveguide. The waveguide should look smooth or it will be excessively lossy. This step can make or break a LEAC chip. Figure 6 is an example of a high quality waveguide (left) at 100x magnification and defective waveguide (right).

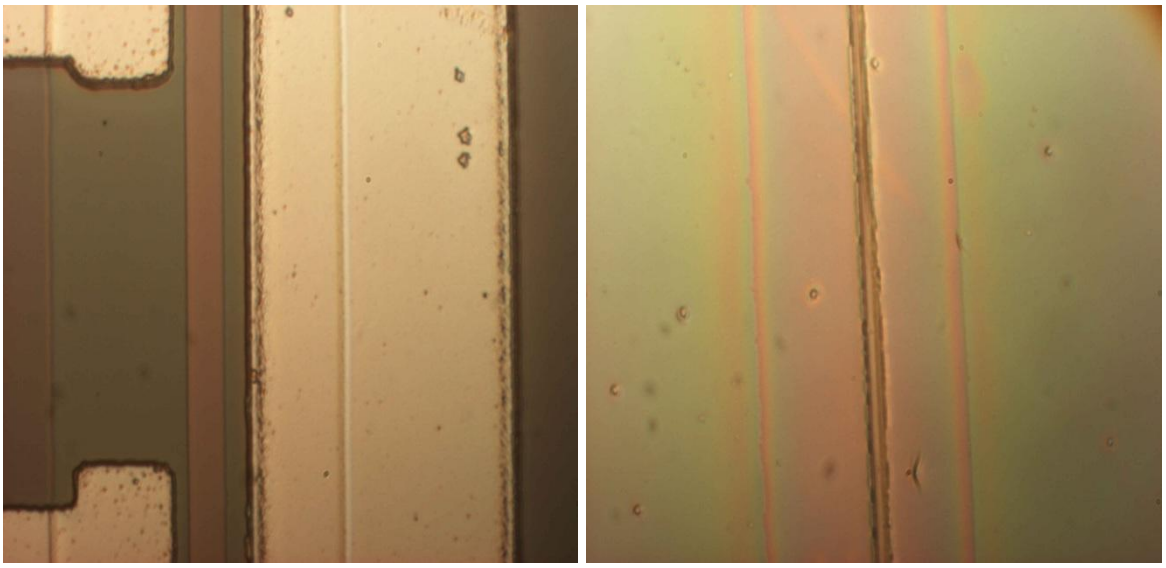

Figure A6: High quality 7 um waveguide at 100x (right). Low quality 3 um waveguide at 20x (right).

Step 7: Via Eteching

Note: Tiny holes in 2070 mask can cause HF to leak through destroying the waveguide. Never let HF reach the portion of the chip with the waveguide. Only dip the back metal pad region of the chip in HF for etching unless you want to probe the test structures on the top of the chip. Rinse down so that no HF touches the chip. No edge bead removal is necessary. Alignment can be done without it and edge bead removal can damage portions of the waveguide.

1) Pipette 2070 onto the wafer, being careful to form no bubbles. Set total spin time to 50 seconds. Spin on PR at 500-700 RPM for about 7 seconds, then ramp up to 5000 RPM. Inspect to make sure photoresist has spun on evenly. If not, remove photoresist with acetone, methanol, DI water, and repeat.

2) Pre-exposure bake for 2 minutes at 100C. Carefully remove edge bead with laser.

3) Align via mask. Make sure that all opening are inside metal pads or your can short the metal to the silicon by oxide undercutting. Expose for 30 seconds on left aligner.

4) Postbake at 110C for 100s. Then let wafer cool or blow with nitrogen.

5) Develop for about 60 second in MIF300. Rinse and N2 dry. Inspect to make sure vias have opened.

6) Poor Silox Vapox III into a clean plastic petri dish to a depth that will just reach the pads when the chip is vertically held in the etchant. (Also reuse the etchant. It is expensive and can be used for up to 20 chips. To get etchant in petri dish, do not poor from main bottle. Use the plastic covered bottle in the fume hood.) Etch the oxide covering the pads in 60 second increments by dipping the metal pad region of the chip into Silox Vapox III. Make sure the waveguide portion of the chip is not exposed to the etchant or you can damage the waveguide. Inspect at each step and do not stop until oxide is removed from pads. If uncertain, take chip out of the cleanroom and probe in C9. Do not overetch the metal as this will ruin the chip.

7) After etching is complete (as tested by probing). Rinse the chip and DI water for 60 seconds. Then use acetone to remove the 2070. Then rinse with methanol and water. N2 Blow Dry. The chip can be 02 plasma cleaned if it does not look perfectly clean.

Step 8: Oxide Reference Region Upper Cladding

1) 1) Pipette 2070 onto the wafer, being careful to form no bubbles. Set total spin time to 50 seconds. Spin on PR at 500-700 RPM for about 7 seconds, then ramp up to 5000 RPM. Inspect to make sure photoresist has spun on evenly. If not, remove photoresist with acetone, methanol, DI water, and repeat.

2) Pre-exposure bake for 2 minutes at 100C.

3) Align oxide upper cladding mask. Expose for 30 seconds on left aligner.

4) Postbake at 110C for 100s. Then let wafer cool or blow with N2.

5) Develop for about 60 second in MIF300. Rinse with DI water and N2 dry. Inspect to make sure development is complete.

6) Deposit at least 1200 nm of low temp oxide on the chip. Use the following PECVD settings. Be sure that the base plate temperature is not above 108C, ever, or the photoresist can permanently bake onto the chip. The deposition rate is approximately **5 nm/min**. Therefore, **the deposition time should be 240 minutes.**

a) **PECVD settings**

i) Temperature **105C**. Pressure start at 200 mT. Slowly raise to **500 mT** after all gases on. Pressure above 540 mT causes system to shutdown for unknown reason. Power set to 25W.

ii) Uses gases 1,2,3. N20 (70 sccm), He (600 sccm), SiH4 (70 sccm).

7) After oxide deposition is finished, sonicate chip in acetone for 10 minutes. Carefully remove remaining PR with a clean acetone soaked swab, only if necessary. Rubbing with a swab should be used as a last resort as it can damage the waveguide. Clean chip with acetone, methanol and water. Inspect for cleanliness. Chip should have no residue, and should appear shiny. Lastly, 02 plasma clean with 40 sccm 02 at 40W for 60s.

If all has gone well, you are now ready to polish. Figure 7 shows what the chip should look like after a successful liftoff (left) and failed liftoff (right).

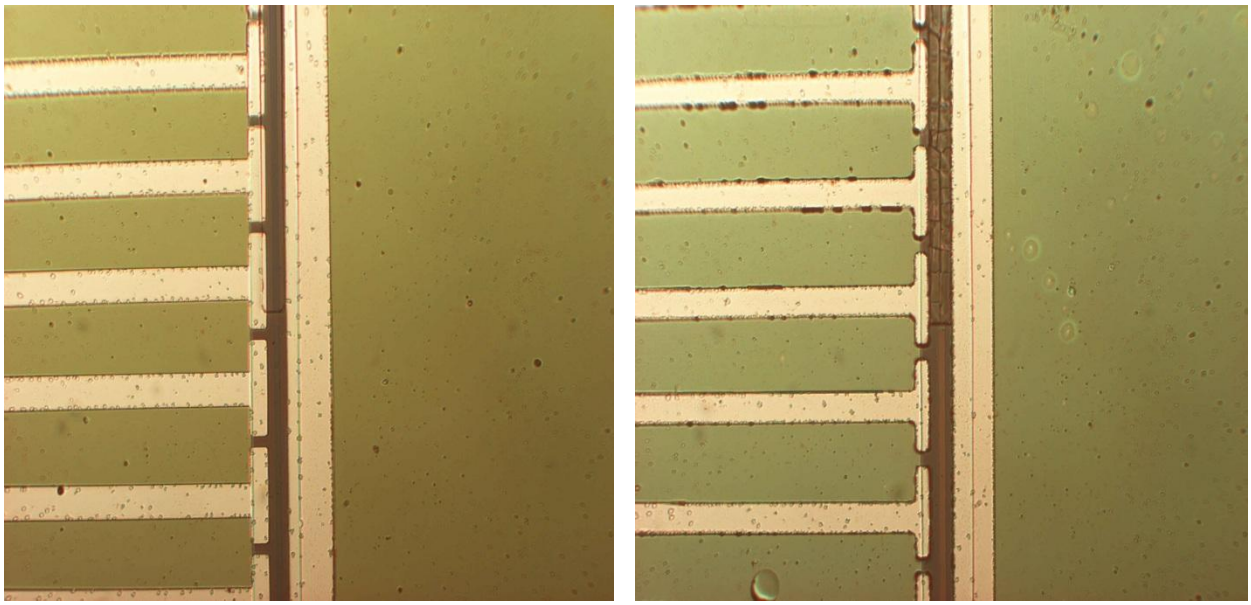

Figure A7: Good (left) and bad (right) upper cladding liftoff

Step 9: Polishing

Note: Polishing requires time, skill, patience, and good listening skills.

1) Cut a glass slide, so that it is slightly wider than the chip and fits into chip polishing holder.

2a) Place glass slide on the hot plate set at temperature setting 10. Apply tiny pieces of crystal bond and let them melt. Then with a metal tool, spread the crystal bond onto the slide. Wait up to 10 minutes for all bubbles to go way. Bubbles in the photoresist (even micron sized ones), can leave portions of the waveguide exposed to damage. After all visible bubbles are gone, place LEAC chip on top of crystal bond. Let the chip and crystal bond melt together for about 2 minutes. Then wearing gloves, align the chip. Lastly, place a flat microscope slide on top of the chip and apply force to uniformly sandwich the chip into the crystal bonds layer. The crystal bond layer should be as thin as possible. This increases its structural integraity, thereby preventing chips where it covers the waveguide. After this step, the crystal bond layer should be so thin that the chip can clearly be seen through the glass slide, as shown in Figure 8.

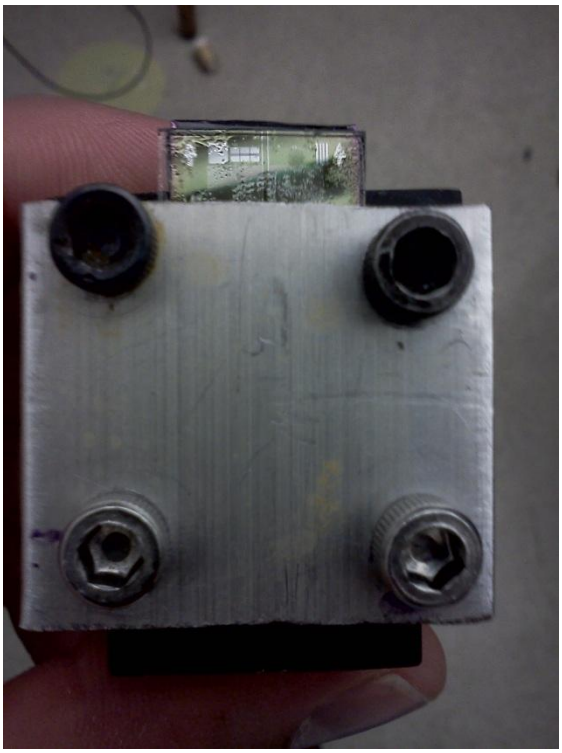

Figure A8: Properly mounted LEAC chip

2b) Since the glass slide is much longer than the chip, it is important to crystal bond a small (5mm x 5mm) piece of wafer (preferably, same thickness as the chip) on the back end of the glass slide that goes into the polishing holder. Follow the same bonding procedure as in 2a) and press down evenly to make sure the small wafer piece is glued perfectly flat to the glass slide surface. This small piece is necessary to prevent accidental cracking of the LEAC chip, and it also helps ensure that the waveguide facet is perpendicular to the waveguide z-direction.

3) Carefully mount the chip and glass slide package into the chip polishing holder as shown in Figure 8. Align arrow to make sure the chip facet polishes normal to the waveguide. Sometimes alignment can be tricky as it has to be eyeballed. Do not over-clamp the chip or you risk breaking the chip. When using the allen wrench, do not use the tee end to tighten the bolts, as this will result in excessive torque. It is best to use one's fingers to twist tighten the bolts by turning the main shaft of the allen wrench. Be very cautious,

as the chip can be ruined in a split second if too much pressure is applied. In an iterative process, tighten the four bolts, and see if you can get the chip to wiggle in the mount. If it is secure, you are done tightening. Do NOT over tighten, and do NOT under tighten.

4) Never let more than 1 mm of the chip overhand the glass slide. This will cause the chip to break free from the crystal bond, or worse, crack the chip.

5) Depending on your patience and the amount of chip that needs to be removed to reach the waveguide region, it may be necessary to carefully sand the glass and chip by hand.

6) Once the desired length has been reached, attach the chip polishing holder to the polisher. Polish using the 30 micron paper first. At first, there is little planarity so only light pressure and a slow spin power (.1A) can be used. As the chip becomes planar, minimal spring tension needs to be used and the spin power can be increased to .3A.

7) Once the chip has been completely polished to the correct length with the 30 micron paper, the edge of the chip should have a uniform appearance.

8) Now switch to the 12 micron paper. Minimal spring tension is necessary here. Just polish until there are no scratches and the chip is smooth. As seen under a macroscope, the chip should have a mirror-like appearance. Make sure the polishing paper is smooth before putting the chip down by petting it with your finger. If there are high pitched squeaking noises, you have to go back to the next coarser paper or adjust the angle of the polishing holder using the right upper screw on the mirror mount. To ensure you are making full contact with the 12 micron paper, use the permanent marker and polish for three seconds. If the marker is still on the facet in any place, you likely need to go to back to the 30 micron paper, as portions of the facet are not making full contact with the paper.

9) Polish on the 3 micron, 1 micron, 0.3 micron, and 0.1 papers. Use the marker test until you get to the 0.3 paper to check for planarity.

10) Importantly listen the chip is making and adjust the pressure and spin speed accordingly. Irregular squeaks or shuddering of the chip are bad signs. Make sure that the chip polish sounds smooth. The hallmark of a successful polish is often a smooth sounding polish when the chip has reached the 0.1 micron paper. This means that the chip is planar to within 100 nm. Such a waveguide facet easily couples light.

11) After polishing carefully demount the chip. Let it cool then clean with acetone, methanol and water. Make sure all crystal bond has been removed. Inspect the chip under the optical microscope. The polishing end should look smooth. Figure 9 shown an example of a successful polish (left) and poor polish (right). Light could not be coupled into the chip on the right because the waveguide facet has been chipped and damaged. Notice the rough polishing edge.

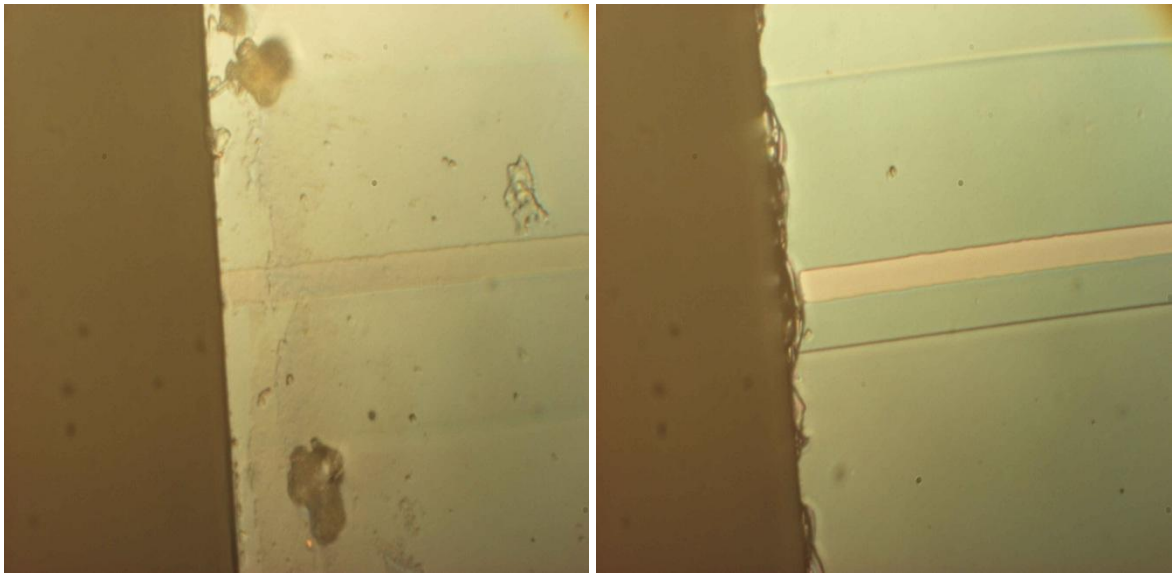

Figure A9: Smooth (left) and rough (right) polishing edge. Light does not couple into the waveguide on the right.

12) Try to couple light into the chip with laser fiber. If light does not couple, you may need to re-polish. If light couples, the chip is ready for testing!

Appendix A2: LEAC Chip Fabrication Process Flow for Thermal Oxide Chips Used for BTEX Sensing

Waveguide loss measurements indicated that thermal oxide could be used to fabricate waveguides with approximately an order of magnitude reduction in scattering loss compared to waveguides fabricated with PECVD oxide. A thermal oxide waveguide (1400 nm lower cladding/100 nm core) operating in air exhibited a loss of less than 4 dB/cm.

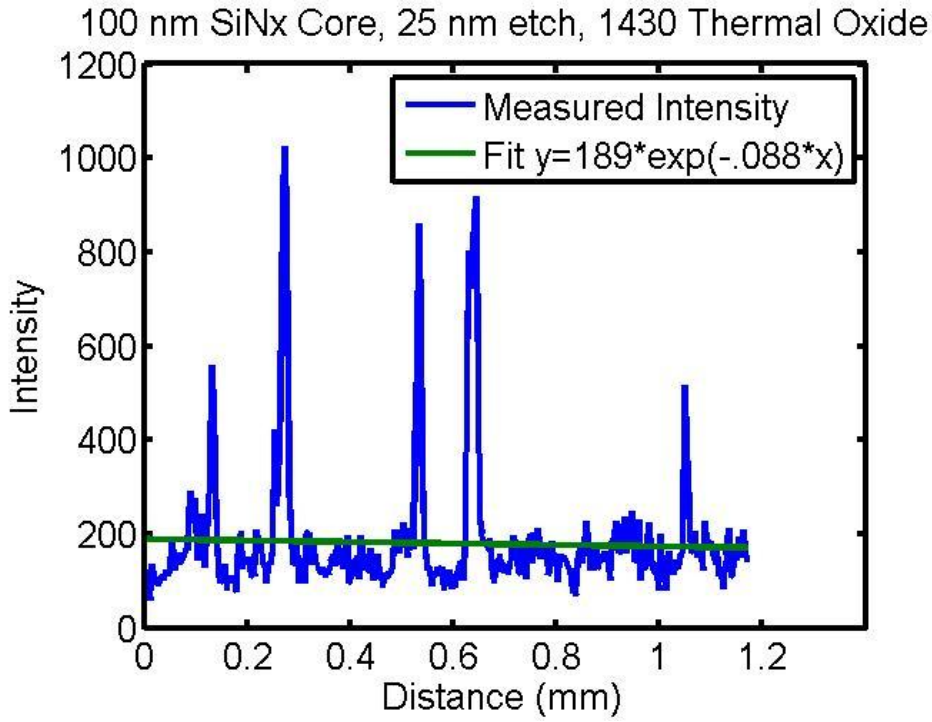

Figure A10: 4 dB/cm scattering loss from thermal oxide waveguide

Unfortunately, the thermal budget for growing thermal oxide exceeds 1000 °C, and thus the fabricated scheme must be dramatically modified from the PECVD approach to allow the waveguide lower cladding to be fabricated before metal contacts are deposited. Furthermore, the process of thermal oxidation changes the chemical interface of Silicon and additional steps are required to enable fabrication of low-dark current, low noise metal contacts. Furthermore, a new series of higher quality photoresists is required to withstand the relatively long buffered HF etching times. Taken together, the fabrication process for minimally scattering thermal oxide chips is very different than that for PECVD oxide chips. The process flow is described here. Please not that thermal oxide chips are made at the Colorado Nanofabrication Lab in Boulder using photoresists and other equipment, which are not present in the CSU cleanroom.

A2.1 Process Flow for High Performance LEAC BTEX Chips

These steps must be followed precisely, as experimental results emphatically demonstrate that the photodetector quality (SNR, dark current) is highly dependent on both the chemical environment photodetector silicon is exposed to prior to metal deposition AND the metallization stack and deposition rate. The waveguide index and thickness must be very close to spec. NOTE: Photolithography times are typical, but can very substantially based on lamp intensity, photoresist age and batch. Never let any dust get on the wafer or it will ruin the waveguide. Numbered masks are at the end of this document.

Starting Wafer) Use a prime-grade n-type 1-5 ohm Si wafer with a handle thickness of at least 500 microns. (Thinner wafers are prone to breaking) SOI does not necessarily have to be used, but may provide improved SNR. Do not use undoped wafers as the Schottky Barrier Height is lowered, leading to higher dark currents. To remove grease and dust, first clean the wafer using acetone, methanol and water. Then RCA Clean the wafer using the three step RCA process. Be sure to rinse thoroughly with DI water at the end of the process. Wafers should appear perfectly shiny and mirror-like. Microscope inspection should show a clean wafer with no debris or pores, in short a perfectly clean wafer.

1) **Thermal Oxidation**. Perform dry-wet-dry oxidation to ~1700 nm. The process involves loading the wafer into the furnace with oxygen flowing. Then ramping the temperature from 750 up to 1200C and then turning on the hydrogen. Let wafer oxidize for six hours in this environment. The turn off the hydrogen, and perform dry oxidation while the furnace cools from 1200C to 750C over the course of about 1 hour. Slowly remove wafers to avoid thermal shock and let cool to room temperature. Follow this procedure exactly, as the processing affects the interface state density and therefore the photodetectors.

2). **Lower Cladding and Oxide Insulating Layer Formation**. Etch with BOE to form lower cladding. For photolithography, use mask #1 and NR9 photoresist. Spin on at 4000 RPM. Bake at 150C for one minute. Expose for 20 seconds. Bake again at 100C for one minute. Develop with RD6 using spin and spray technique for ~10 seconds. Inspect photolithography under microscope. If good, then flood expose for an additional 20 seconds. Then hard bake at 150C for 60s. Next BOE etch until insulating oxide layer thickness is 120 nm. The BOE etch rate is ~80 nm/min. Monitor process will filmmetrics by stopping etch with 300 nm left and adjusting time accordingly. After BOE etch, bath sample in DI water bath for 30s. Then rinse in DI Water for 30 seconds. Then place in RR2 resist remover. Heat RR2 to 80C with wafer in it. This requires hot plate to be set at about 150C. After 5 minutes, rinse in acetone, methanol, and water. Inspect under a microscope to make sure all resist has been removed. If there is no visible resist, then descum in 02 plasma for 30 seconds at 50W.

3) **Deposit Chrome Gold Metal Adhesion Layer.** Using mask #2, perform photolightography with NR71. Bake at 150C for one minute and expose for 30s. Then bake at 100C for 90s. Then develop for about about ~7 seconds with RD6. Inspect under microscope. If sample passes inspection, then using CNL's thermal evaporator deposit 9 nm of Cr and 16 nm of Au. Make sure pressure is below 5e-6 Torr. Perform metal liftoff with RR2 with hot plate set to 150C. Then rinse with acetone, methanol and water. Make sure sample surface is clean and there is no remaining resist residue.

4) **Etch away photodetector oxide to reveal Si**. Using mask #3, perform photolighography using NR9. Bake at 150C for one minute and expose for 10 seconds then bake again at 100C for one minute. Then develop for about ~10s and hard bake for one minute at 150C. Inspect photolithography very carefully. Make sure the photoresist resembles the mask and that there is no bleed out. If photolithography passes inspection, then place sample in BOE for two minutes to etch away remaining oxide. Bathe in DI water for 30 seconds then rinse in DI water for 30 seconds. Then remove resist using acetone, methanol, and water. Inspect to make sure there has been no significant under etching of the oxide insulating layer, as this can cause a "short". If there is still resist left, RR2 resist remover may have to be used as before. Once the entire surface is clean, proceed to next step.

5) **Deposit Metal Semiconductor Contact Layer.** Using mask #4, perform NR71 photolighography as above. Inspect and be certain that all photoresist has been eliminated from photodetector area where the Si is exposed. Then dip in BOE for ~3 seconds to remove native oxide layer. Then rinse chip thoroughly with DI water for 30 seconds. Then dry chip with N2 under chip is completely dry. Next, immediately (within three minutes) load the chips into the thermal evaporator and pull a vacuum. Deposit metal in thermal evaporator after pressure is equal to or less than 2e-6 Torr. Make sure that deposition rate never exceeds 1 A/s or the metal can heat up and destroy the contact quality. Even if the relatively thick resist layer does not heat up above 150C due to its relative bulk, the temperature at the metal/semiconductor surface can deviate from this due to rapid conductive heat transfer as the vaporized metal (which vaporizes at well over 1000F lands on the semiconductor surface. With this in mind, deposit 45 nm of Au as the contact metal, 20 nm of Cr as the barrier metal and 75 nm of Au as the probing contact metal. After metal deposition, perform liftoff in hot (almost boiling) RR2. I typically set the hot plate to 250C for this step. Inspect liftoff. If there is no visible photoresist in the waveguide region of the chip, then perform an 02 plasma descum at for 30 seconds. To prevent the metal from peeling off in the next step, anneal the chip using the following procedure. Set hot plate to 100C then ramp up temperature to 200C. The ramp time should be several minutes. After the hot plate reaches 200C, then remove chip from hot plate. Blow dry with N2 to remove any potential dust.

6) **Deposit silicon nitride waveguide core/insulating layer.** Make sure chamber is clean. I typically wipe down the chamber with isopropanol and then perform an oxygen/CF4 plasma clean of the chamber for 10 minutes before depositing nitride. Once the chamber has been cleaned, load a Si dummy wafer (not your sample). Deposit "lsn nitride" for 15 minutes. The recipe should be for 200 He/200 silane/2 NH3 at 250C. After deposition on dummy wafer, measure index and thickness with ellipsometer. The index should be 1.81 and the deposition rate 5-6 nm/min. Adjust the silane and ammonia flow rates to bring the deposited film to within these specs. If the flow rate is too high, then the silane flow should be reduced by an amount proportional to the desired deposition rate decrease. If the index is too high, either increase the ammonia flow rate (range is 2-4 sccm always) or decrease the silane flow rate. Getting the PECVD "dialed in" can take some practice and often takes several hours, but it must be done as the wrong film index will ruin your sample.

After PECVD has been "dialed in" then load sample and a fresh Si dummy sample. Deposit for the appropriate length of time to give 80% of desired thickness. Then remove sample and perform ellipsometry. Based on this value, one can tune the remaining deposition time to give the desired

thickness. For BTEX chips, 69-71 nm is the preferred thickness range. The working range is 68-73 nm. Outside this range, the waveguide will either be too lossy or not deliver sufficient coupled signal.

7) Waveguide Etch Step. Etch nitride to form waveguide core. Using mask #5 and S1818 photoresist, perform photolighography. Spin coat at 6000 RPM then bake for 3 minutes at 100C. Expose for 4s using CSU left mask aligner. Then develop using 4:1 DI Water:AZ400K solution for about ~30 seconds. Immediately rinse and inspect waveguide after development. The chip should have a very thin film of photoresist left on it. At this point, reflow the photoresist on a hot plate at 115C for three minutes. Then 02 plasma clean in RIE for 60 seconds at 50sccm/50W. Inspect the photolighography under a microscope. At 20x, waveguide resist should appear almost perfect; only at 100x can sidewall roughness be seen. If PR passes inspection, the load sample in RIE along with 70nm SiNx dummy wafer (the one from the deposition). Etch away 35 nm of nitride using CF4 at 40 sccm/50W. I typically etch for 20s, then determine the etch rate (which varies depending on sample surface area) then etch for the remaining time based on the rate and thickness removed from the dummy wafer. Rinse chip with acetone, methanol and water. Then inspect under microcope.

8) S1808 removal step. S1818 tends to stick to the waveguide core in certain places. It must be removed or it will "contaminate" the upper cladding sensing region. In order to remove the resist, place the wafer in a fresh RR2 resist remover bath. The place on a hot plate set to 150C for ten minutes. Remove from hot plate, then place in acetone bath for one minute, then rinse with acetone, methanol and water. Next, oxygen plasma clean the chip in the RIE at 50W/50sccm for one minute. Inspect under microscope at 100x to make sure there is no resist residue. If chip passes inspection, rinse with DI water and blow dry with N2 to remove any dust that may have landed on the chip.

9) Teflon Adhesion Promoter Application

Adhesion Promoter Preparation

Teflon adhesion promoter has a short shelf life of several days, so it is best to mix up a fresh batch every single time or Teflon AF will not adhere to the substrate. The adhesion promoter is a fluorosilane in a solution of 100% ethanol. The adhesion promoter solution is prepared using the following procedure.

In a clean glass beaker,

Add **3 mL 100% ethanol** using a pipette

Lastly, add **70 uL of 1H,1H,2H,2H-Perfluorodecyltriethoxysilane, 97% (Alfa Aesar #L16585).**

Using the photoresist, mix the solution by drawing up into pipette and shooting solution back out.

Adhesion Promoter Spin-on and Bake

Spin the adhesion promoter onto the sample at 800 RPM for 30 seconds.

Place the sample on a hot plate set to 110C for 10 minutes. Remove the sample and let it cool for 1 minute.

Adhesion Promoter Spin-on and Cure

Place the sample onto the spinner. Apply Teflon AF and make sure there are no bubbles. Bubbles will cause the film to spin on non-uniformly. Be careful not to waste Teflon, as it costs $10/mL. Start the spinner at 100 RPM and ramp up to 500 RPM. Let spin at 500 RMP for 60 seconds. To create a uniform film, the Teflon film must be heated slowly to avoid rapid evaporation.

Teflon AF Deposition

Place the sample in an oven at room temperature. Ramp up to 250C and remove as soon as temperature reaches 250C or within 30 minutes. After letting sample cool to room temperature, oxygen plasma etch at 50W/50 sccm for 10 seconds. This must be done to get the next Teflon layer bind to prior layer. Repeat this entire procedure through 4 (four) coating cycles. Filmetrics inspection of the field should yield a layer thickness of 5500 +/-300 nm.

10) Blocking Layer Deposition. Once again oxygen plasma clean the chip for 5 seconds, so that photoresist will adhere. Spin on NR71 resist at 4000 RPM then bake at 150C for one minutes. Using mask #6, expose for 40 seconds, then bake again at 100C for 90 seconds. Develop mask in RD6 for ~7 seconds. Inspect chip to make sure all photoresist has been developed under microscope. If there is photoresist remaining, then develop further. After you see no photoresist be sure the further develop for 2 seconds. Inspect chip to make sure that photoresist remains over the pads and sensing region. Then oxygen plasma etch at 50W/50 sccm for 25 seconds to ensure proper binding of metal layer. Transfer chip to thermal evaporator. Pump thermal evaporator down to 4e-6 Torr or lower. Then deposit 100 nm of aluminum. After deposition, let chip cool for 20 minutes in evaporator under vacuum. Then remove chip from vacuum and perform liftoff in RR2 bath with hot plate set to 150C. Monitor chip and remove from bath as soon as liftoff has occurred. Immediately place chip in acetone bath and then rinse with acetone, methanol and water. Inspect chip under microscope to make sure liftoff has been success.

11) Via pad opening. Oxygen plasma etch chip at 50W/50 sccm for 5 seconds. Then spin on S1818 and bake at 100C for 2 minutes. Then remove chip and expose for 5 seconds using mask #7. Then develop to expose chips pads region. Oxygen plasma etch at 100W/50 sscm etch for 7 minutes. Rinse chip with acetone, methanol and water. Then repeat S1818 procedure. Then oxygen plasma etch at 100W/50sccm again for 6 minutes to remove all of Teflon. Then CF4 plasma etch at 50W/40 sccm for one minute to remove any remaining SiNx. Then rinse chip with acetone, methanol and water. Using the semiconductor analyzer, probe chip and make sure that pads have opened. If they have not opened, chances are that Teflon is still on the chip. In that case repeat the oxygen plasma etch, CF4 etch sequence, except reduce oxygen plasma time to 2 minutes and CF4 time to 30 seconds. (You have to apply S1818 again off course or the Teflon will be etched away from the sensing region).

12) Polish Chip. See Appendix A1, step 9 on chip polishing procedure.

13) Sensing Region Teflon Plasma Etching/Teflon Thickness Adjustment. Apply S1818 again using the same procedure, except this time use a fine swab to remove resist over sensing region. Oxygen plasma etch at 50W/50 sccm for two minutes. The plasma etch rate under this setting is 700 nm/minute, so this step removes about 1,400 nm of Teflon. Keep in mind that 5,500 nm is initially deposited on the chip. After four coatings, the polymer planarizes. Since the lower cladding thickness is 1,700 nm, there is initially 3,800 nm of Teflon AF on top of the waveguide core. The 35 seconds of etching prior to metal deposition reduces this value to about 3,400 nm. The final etch reduces this value to the target of 2,000

nm. The thickness may be further reduced to 1,000 nm, in order to reduce analyte transfer time to the core vicinity, but this is seen as a risky step. It would produce a factor of four reduction in response time, but if the value is reduced much beyond that, significant core power could protrude above the Teflon upper cladding, which is undesirable for a variety of reasons, such as shorting or the evanescent tail probing the solution rather than the functionalized sensing region.

14) Inspection

The LEAC chip should be inspected for defects, including metal peeling off the MSM contacts, and pits grooves or any form of contamination on the waveguide, including tiny pieces of metal. It is absolutely essential that no metal "flakes" remain on the waveguide or it will create a significant scattering center.

An image showing a LEAC BTEX chip of high fabrication quality is provided below.

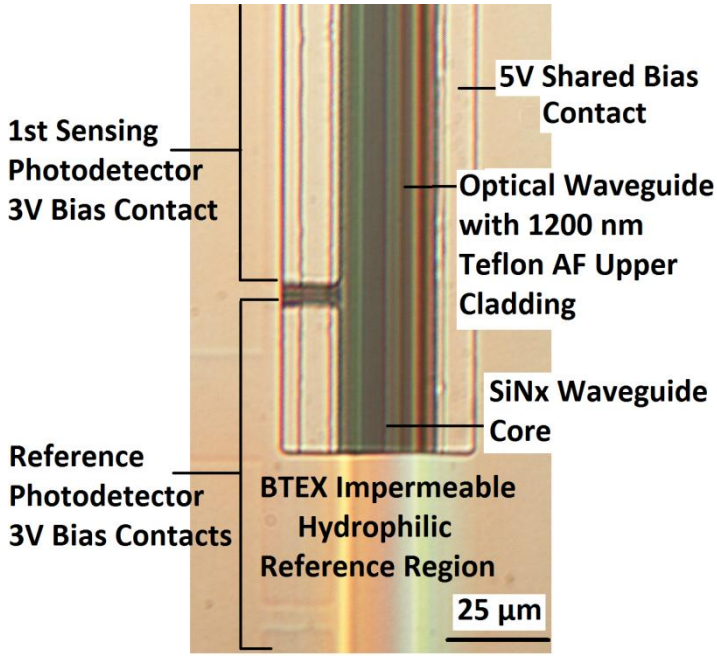

Figure A11: Microscope image of LEAC BTEX chip's reference and sensing regions

A2.2 Mask Set and Numbering

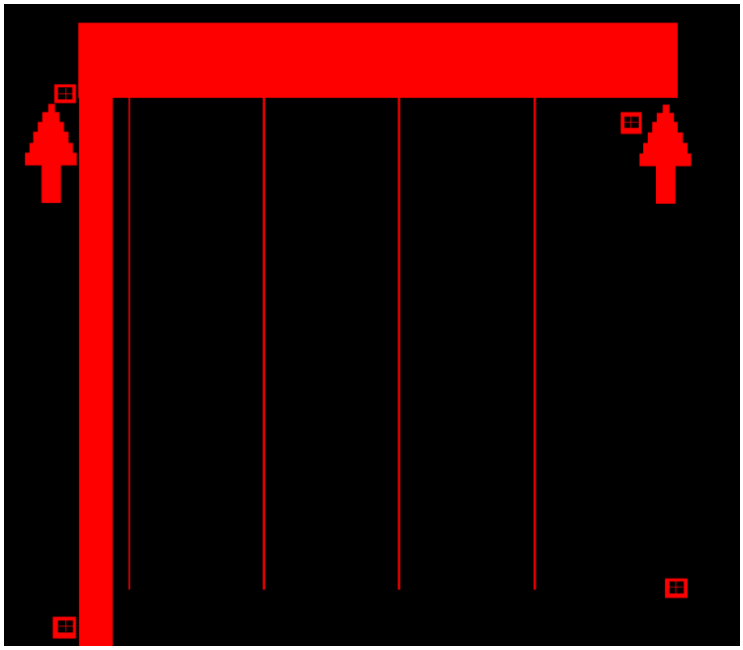

Mask #1: Oxide Etch

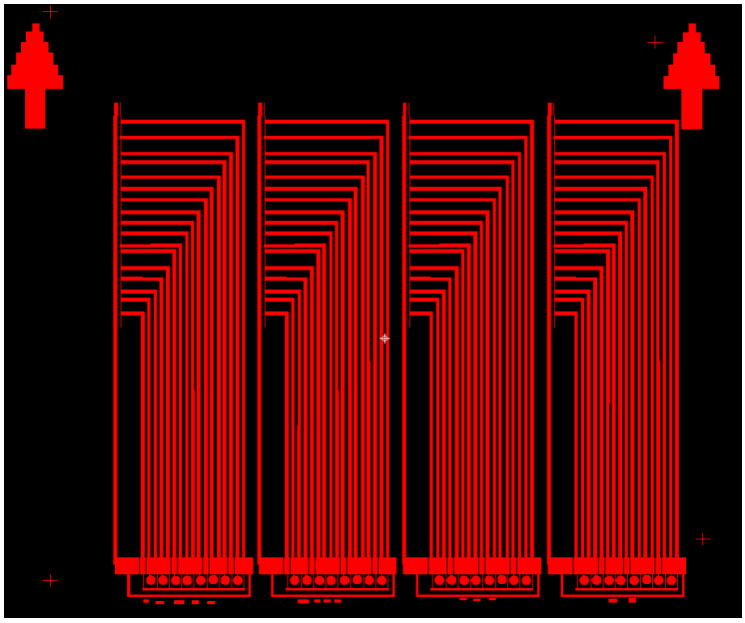

Mask #2: Metal Adhesion Mask for Cr/Au

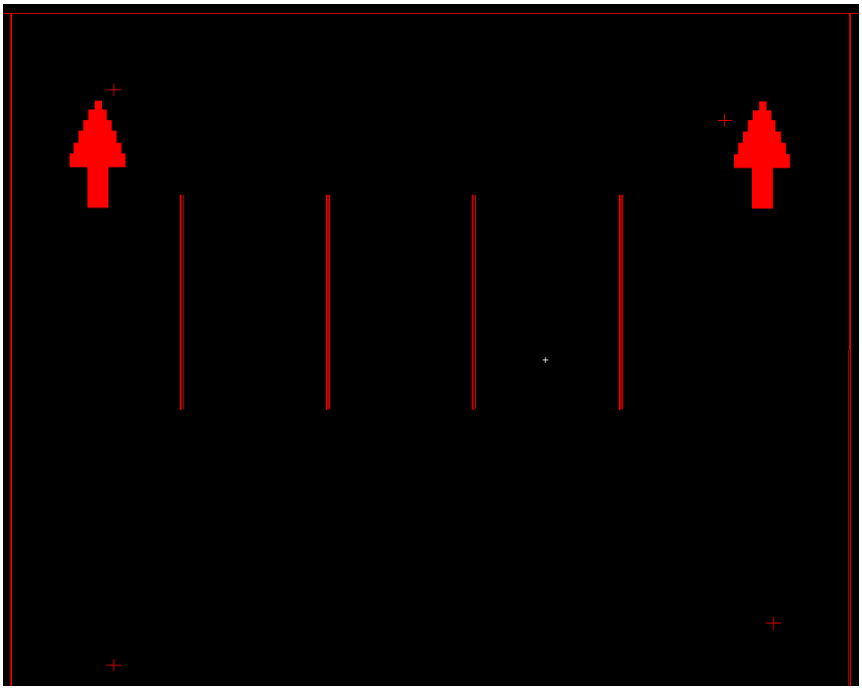

Mask #3: Detector Window Etch

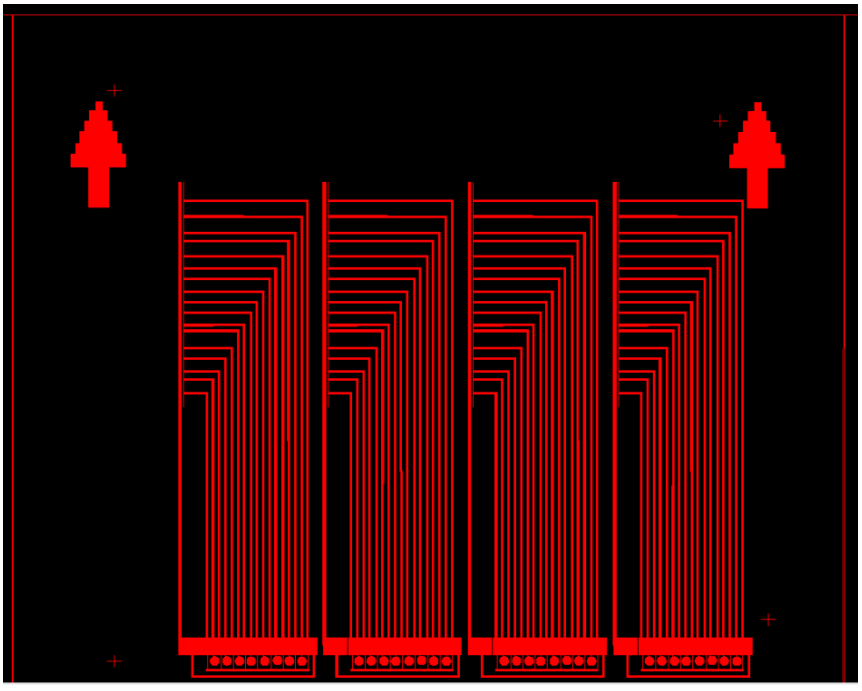

Mask #4: Contact Metal Mask (thinner metal lines than Metal Adhesion mask)

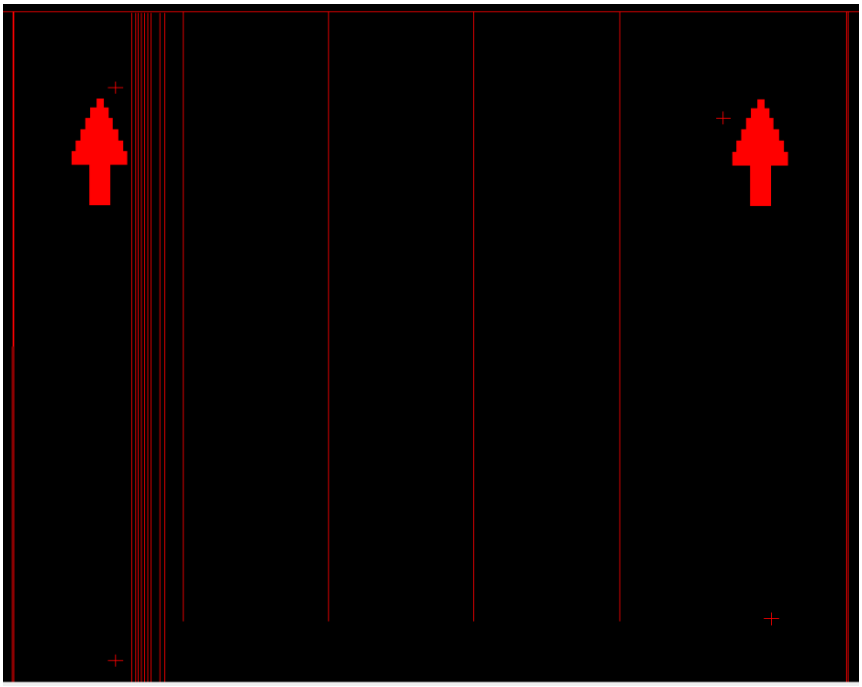

Mask #5: Waveguide Etch Mask

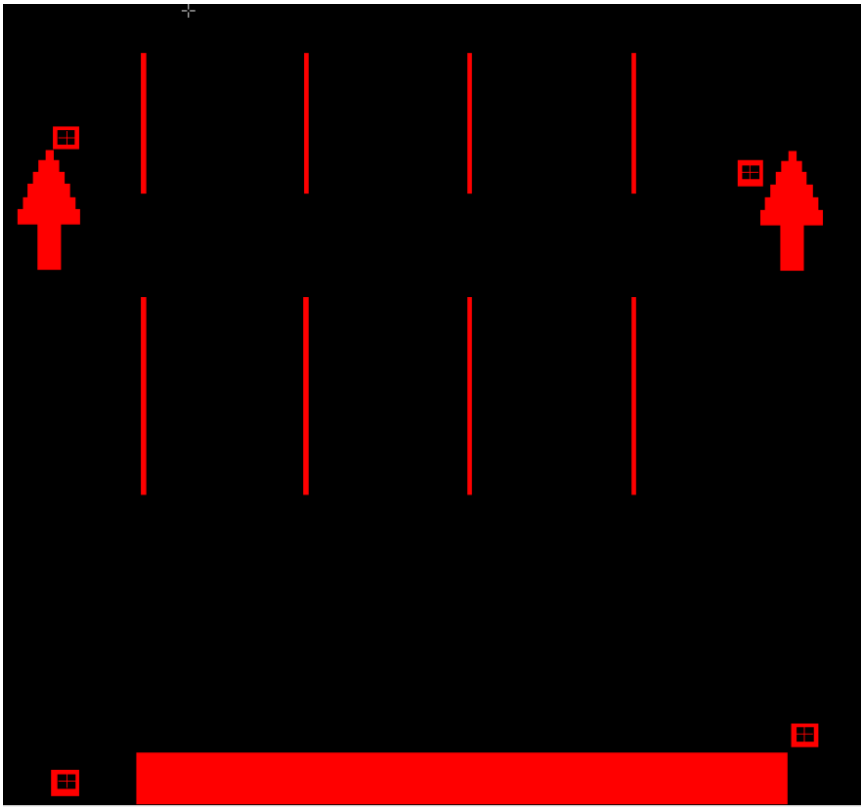

Mask #6: BTEX Blocking Layer Metal

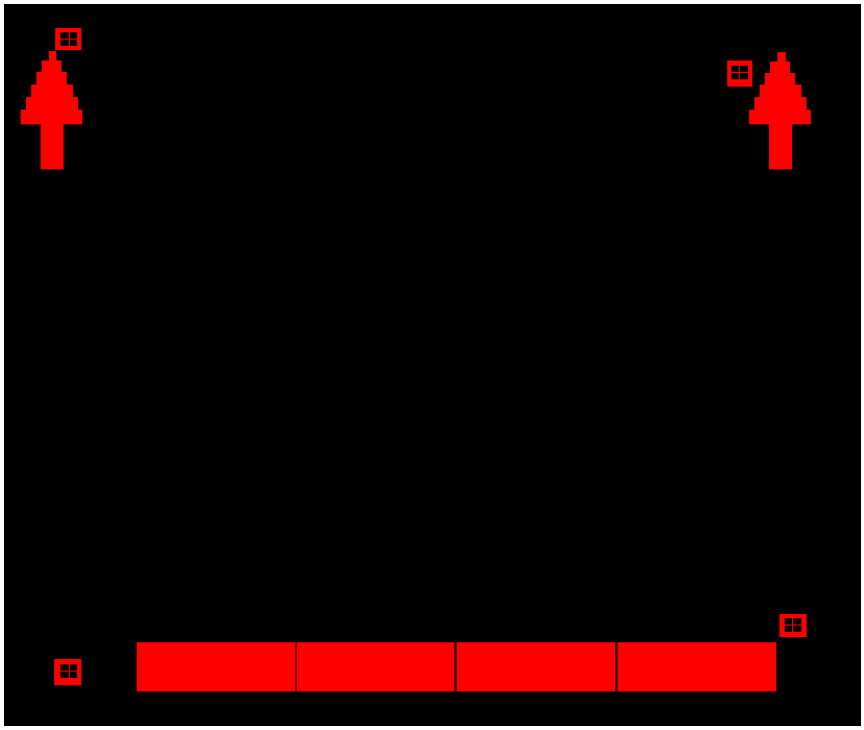

Mask #7: Pad Via Mask

Appendix A3: LEAC Chip Fabrication Process Flow for Thermal Oxide Chips Used for Biosensing

The fabrication process flow for biosensing chips is identical to A2, with several modifications. A new mask set is not required.

The core material is changed from PECVD nitride to ALD-deposited hafnia nanolaminate film (n=2.05) with a core thickness of 45 nm. The ALD hafnia nanolaminate is deposited immediately after lower cladding formation (before metallization), as the ALD film exhibits poor adhesion to gold. The ALD hafnia core was deposited by John Nogan at CINT according to the following protocol.

A3.1 Hafnia Process Detailed

Atomic layer deposition of the Al_2O_3 and HfO_2 was performed using a Picosun Sunale R150 hot-wall reactor operating at 250°C using Trimethylaluminum (TMA), Tetrakis(dimethylamido)hafnium(IV) (TDMAH) and deionized H_2O precursors. Both TMA and H_2O develop sufficient vapor pressure at room temperature for delivery into the medium pressure (3-4 hPa) reaction space. However, the low vapor pressure TDMAH requires the source temperature to be elevated to 75°C and for the Picosolid^{TM} boosting function to be enabled. To facilitate the necessary surface reactions to form Al_2O_3, TMA is pulsed for 100 ms into a 150 sccm N_2 carrier gas flow stream followed by a 6.0 s N_2 purge. Once the TMA reaction completes, H_2O is pulsed for 100 ms into a separate 200 sccm N_2 carrier gas flow followed by a 40.0 s N_2 purge. To form HfO_2, TDMAH is pulsed for 1.9 s into a 100 sccm N_2 carrier gas flow stream followed by a 15.0 s N_2 purge. Once the TDMAH reaction completes, H_2O is pulsed for 100 ms into a separate 200 sccm N_2 carrier gas flow followed by a 40.0 s N_2 purge. The 45 nm laminate consists of Al_2O_3 (A) and HfO_2 (H) deposited in the following sequence $A_{L1}/H_{L2}/A_{L3}/H_{L4}/A_{L5}/H_{L6}/A_{L7}/H_{L8}$ where A_{L1} – 0.5nm nucleation delay + 0.5 nm ALD growth (12 cycles), $A_{L3,L5,L7}$ – 0.5 nm (6 cycles), $H_{L2,L4,L6}$ – 10 nm (102 cycles) and H_{L8} – 13 nm (133 cycles).

A3.2 Hafnia Process Simplified

Atomic layer deposition of the Al_2O_3 and HfO_2 was performed using a Picosun Sunale R150 hot-wall reactor operating at 250°C using Trimethylaluminum (TMA), Tetrakis(dimethylamido)hafnium(IV) (TDMAH) and deionized H_2O precursors. At room temperature both TMA and H_2O develop sufficient vapor pressure for delivery into the medium pressure (3-4 hPa) reaction space. However, the low vapor pressure TDMAH requires the source temperature to be elevated to 75°C. To form Al_2O_3, TMA is momentarily pulsed into a N_2 carrier gas flow stream, and then the byproducts of this first reaction are purged from the reaction space with N_2. Once the first reaction is complete, H_2O is pulsed into a segregate N_2 carrier gas flow stream and the byproducts of this second reaction are purged completing growth of a monolayer of Al_2O_3. To grow a monolayer of HfO_2, a similar reaction sequence is followed using TDMAH and H_2O. Each of these self-limiting reaction cycles repeat in a specific order to achieve the desired thin film composition and rms roughness. The 45 nm laminate consists of Al_2O_3 (A) and HfO_2 (H) deposited in the following sequence $A_{L1}/H_{L2}/A_{L3}/H_{L4}/A_{L5}/H_{L6}/A_{L7}/H_{L8}$ where A_{L1} – 0.5nm

nucleation delay + 0.5 nm ALD growth (12 cycles), $A_{L3,L5,L7}$ – 0.5 nm (6 cycles), $H_{L2,L4,L6}$ – 10 nm (102 cycles) and H_{L8} – 13 nm (133 cycles).

After ALD hafnia nanolaminate deposition, the core is etched 15 nm to from a ridge using BCl_3 plasma etching at 150W (etch rate= 7nm/min). In order to reveal the Si to form the MSM contacts, NR71 is spun onto the chip. After a photolithography step, the remaining 30 nm of hafnia is dry etched (6 minutes in BCl_3 plasma at 150W). Then NR9 is used to protect the waveguide during the BOE wet etch of the remaining oxide to reveal the Si for metal contacts.

Second, as the piranha etch used to the clean the sensing region readily oxidizes aluminum, the metallization is changed from Au/Cr/Al to Au(40 nm)/Cr(20nm) /Au(50 nm). The Cr once again serves as an essential barrier layer to prevent Si diffusion in Au and subsequent surface oxidation, which makes it impossible to probe the chip for photocurrents.

Third, the sensing region of the chip is treated to ensure full Teflon AF removal. This is accomplished by first depositing NR71 photoresist over the sensing region prior to applying the adhesion promoter. After applying the adhesion promoter, the masking photoresist is removed using acetone, methanol and water sonication. After masking photoresist removal, the Teflon AF polymer is applied to the surface. Then a second photolithography process is performed followed by oxygen plasma etching to remove the Teflon AF from the sensing region. The chip is then cleaned with acetone, methanol and water. It is oxygen plasma etched for 15s at 50 sccm/50W. It is then placed in a piranha solution for 15 minutes, followed by a DI water rinse before antibody patterning. The same mask, shown below, is used for adhesion promoter blocking (with NR71 negative resist) and Teflon etching with positive resist (S1818). The etch rate for Teflon AF is the microRIE is 700 nm/min at 50 sccm/50W.

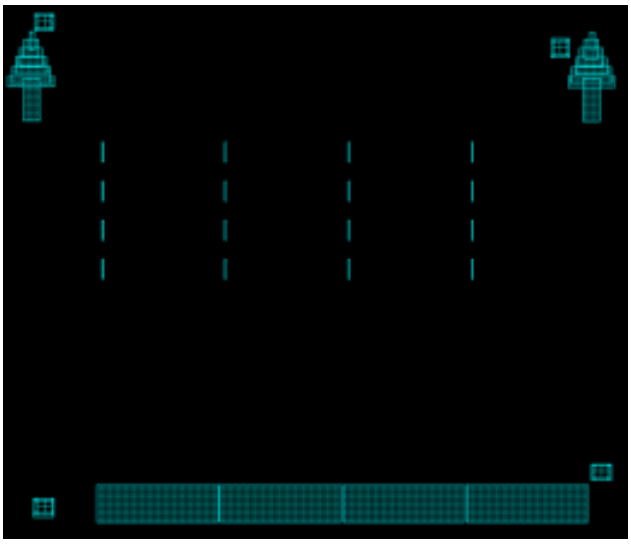

Figure A12: Teflon AF Etch Mask

The final mask set used for biosensing is shown below.

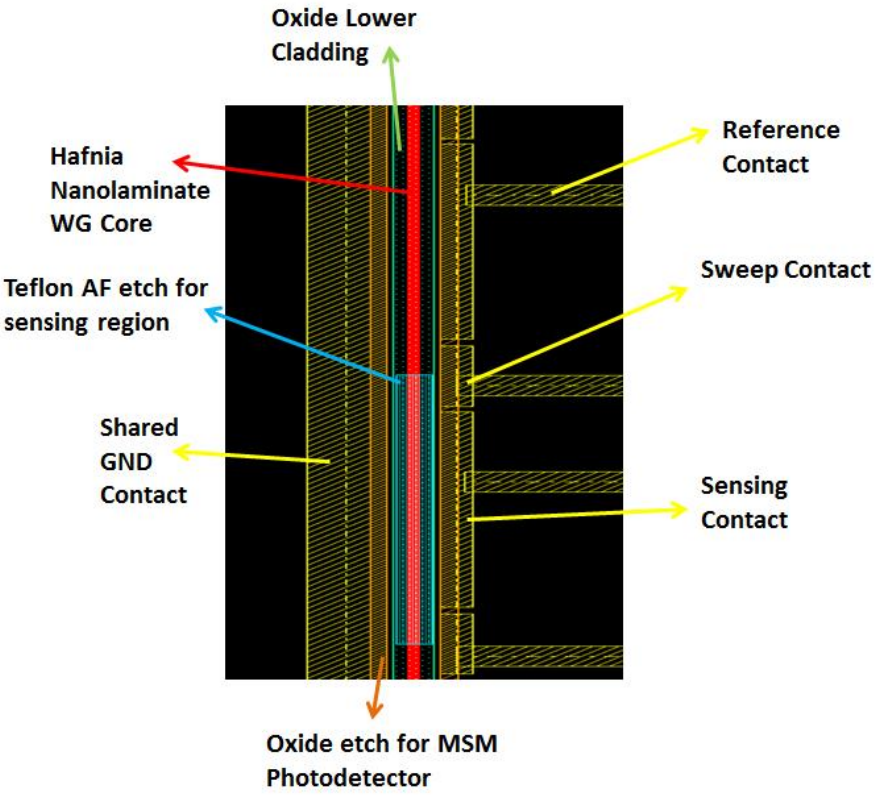

Figure A13: Final biosensing mask set

Cross sections of the device are shown below for both the reference regions (Teflon AF upper cladding) and sensing region (upper cladding exposed to sensing medium).

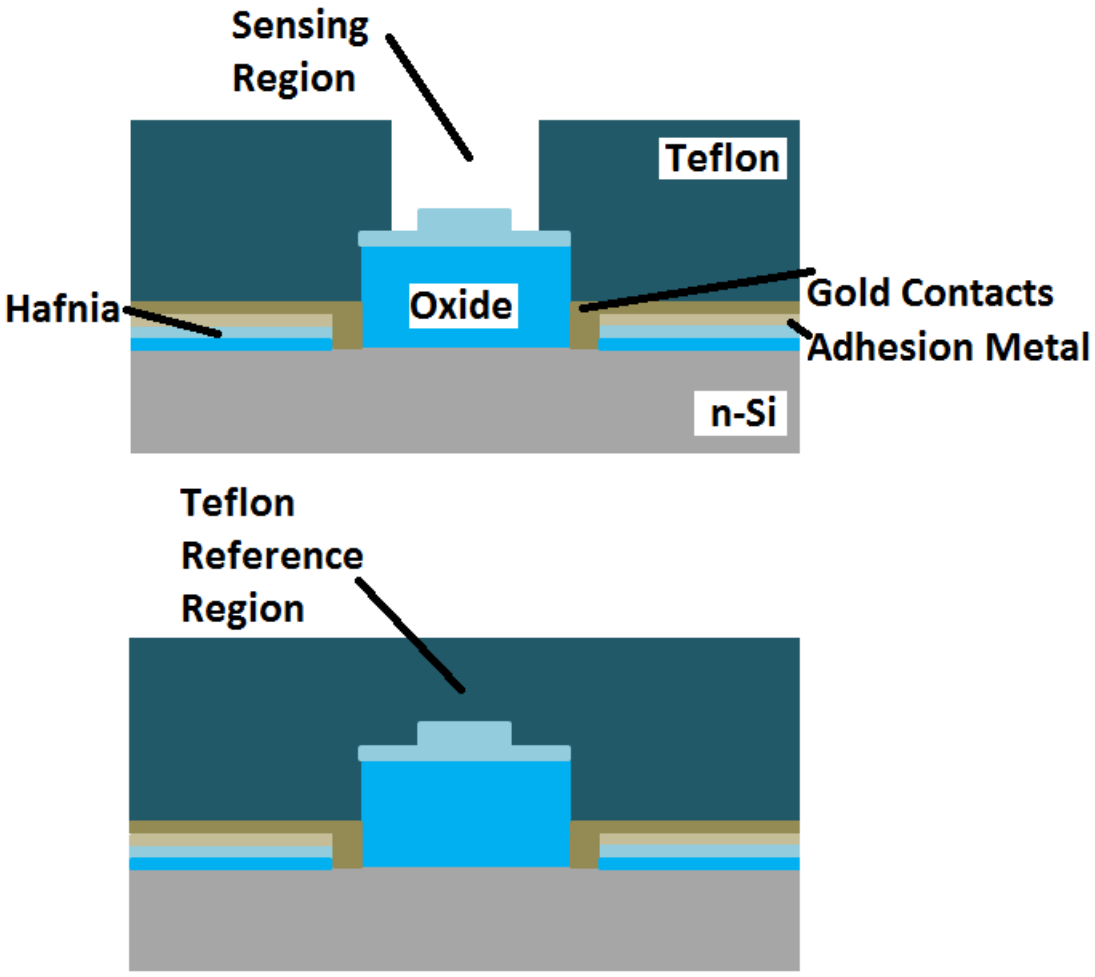

Figure A14: Biosensing cross sectional diagram

A3.3 Biosensing Functionalization

A3.3a Cleaning

Clean with acetone, methanol and water. Then piranha clean (2:1 sulfuric acid to hydrogen peroxide) for 15 minutes. Rinse chips with DI water and N2 dry.

A3.3b Silanization

Place chip in mixture of: 1 mL EDS, 1.5 mL DI, 18.5 mL methanol, 800 uL of glacial acetic acid for 20 minutes.

Rinse in methanol, DI, N2 dry.

Bake at 115C for 30 minutes.

A 3.3c NHS-Ester/Maleimide Linker Attachment

Remove Sulfo-SMCC from freezer and let warm up to room temp for at least an hour. Weight out 2 mg of Sulfo-SMCC in scintillation vial.

Prepare 50 mM HEPES buffer with pH=7.25 using 0.5 M NaOH to increase pH to 7.25.

Place 18 mL of HEPES solution in clean petri dish. Add 1 mL of HEPES buffer to 2 mg of Sulfo-SMCC in scintillation vial. Shake vigorously to dissolve the SMCC. Pour solution in petri dish. Then rinse out vial with another 1 mL of HEPES solution to make sure all SMCC is dissolved. Pour into Petri Dish.

Incubate chips in SMCC solution for3 hours at room temperature. Then rinse with DI water and blow dry. The chips are now ready for Ab attachment. The pH must always be kept at 7.2-7.4, as the NHS linker can hydrolyze at higher pH values, preventing amide bond formation. At a pH of 8, the half-life of NHS is approximately ten minutes, where it is over 8 hours at pH=7.3 at room temperature.

A3.3d Anti-CRP Ab Attachment

Prepare anti-X solution at a concentration of 50 ug/mL in HEPES. Print antibodies (suspended in HEPES solution) using specialized printing apparatus designed by Sean. The probe station camera is used to visually select the location of the printed spot. Place chips in petri dish lined with a wet cleanroom paper towel. Cover petri dish. Incubate for 20 minutes. Rinse chips with PBS/DI water then N2 dry.

A3.3e BSA blocking

Incubate chips in 5% BSA in HEPES solution for twenty minutes. Rinse with PBS (150 mM) 0.5% Tween 20 solution, then PBS then DI water. Then clean chip with N2. Tween 20 is a mild surfactant, which gently removes unbound protein without degrading the covalently attached protein.

A3.3f Run Experiments with Antigenic Determinant.

Appendix B: Integrated Testing Structures on LEAC Chips

The following key is used for each layer.

Yellow=Metal

Purple=Exposed Silicon

Red=Nitride for Waveguide

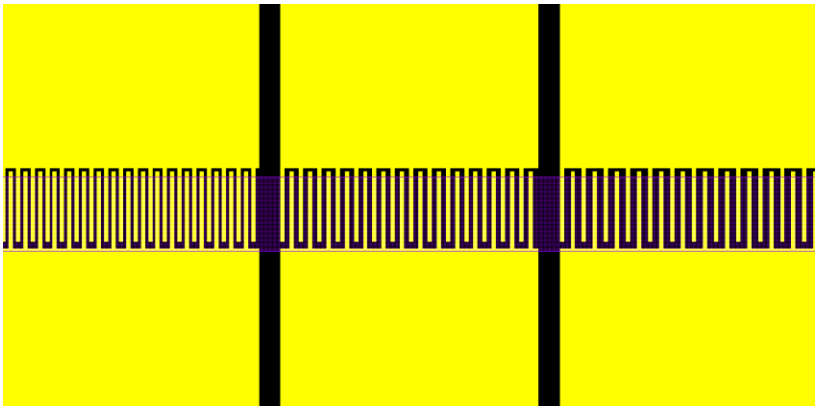

Figure B1: Interdigitated Photodetectors

Purpose: These are used to readily measure the effect of metal finger separation on both dark current and photocurrent. They can also be used to measure the frequency response of the detector for comparison to the frequency response of the LEAC's photodetector. They provide a good baseline comparison, as there are multiple reports of interdigitated photodetectors in the literature.

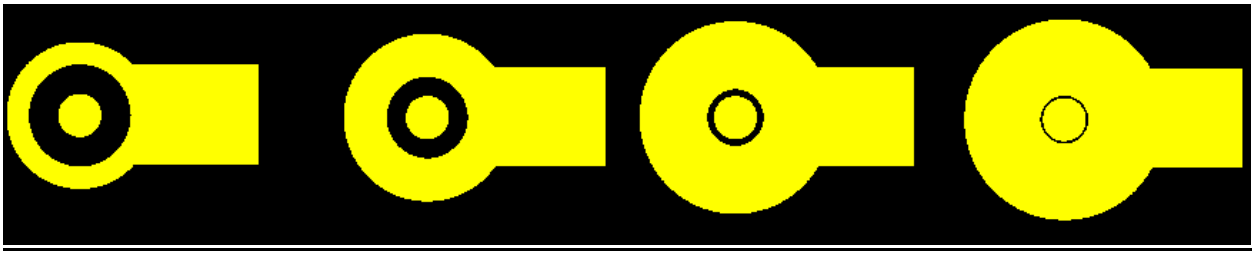

Figure B2: Sheet Resistance Circular Contacts

Purpose:

These enable one to measure the sheet resistance of the underlying substrate, which for the LEAC chip is Si. As the resistivity of the wafer can dramatically affect the dark current, these are important to have in order to verity that the sheet resistance meets the manufacturers spec. Additionally, they can be used to determine is a contaminating, conducting film is present on the surface of the wafer. A thin ionic film, left from etching could possible decrease the measured resistance.

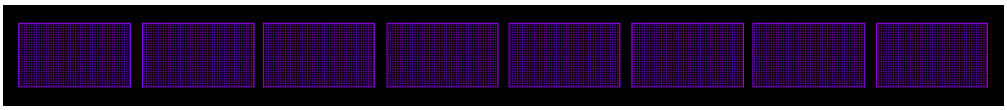

Figure B3: Etch Undercut Indicators

Purpose: These are used to give an indication of overetching undercut in the Si detector strip.

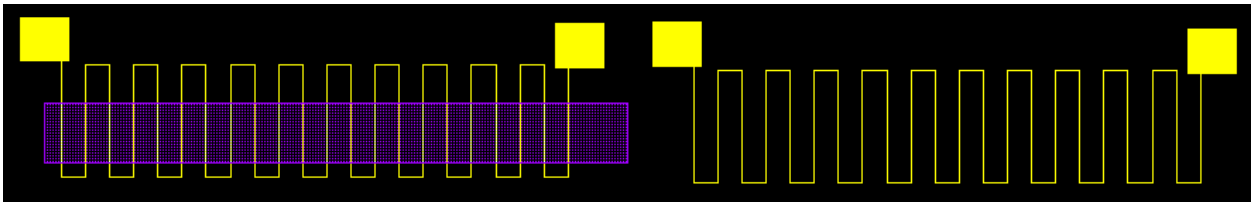

Figure B4: Metal Topography Integrity

Purpose: These are used to determine if the metal can transverse change in substrate height due to oxide etching, which is seen in the chip's integrated detector region. If the metal can transverse the 280 nm drop without breaking, a zero resistance should be measured on both the left and right structures when probes are placed on the squares.

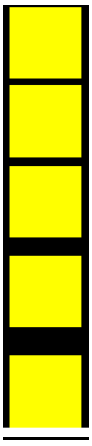

Figure B5: Oxide Breakdown Voltage Squares

Purpose: As the metal squares are all insulated by the intervening oxide, this enable one to check that the oxide is relatively-pinhole free, as zero current is expected when a voltage difference of 5V is applied to adjacent squares. As the voltage is increased, the oxide may begin to conduct to due breakdown. The enable one to measure the breakdown voltage as a function of separation distance.

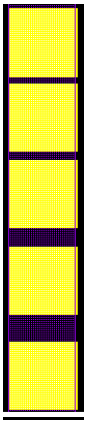

Figure B6: Photocurrent/Dark Current vs. Pad Separation Squares

Purpose: As these squares are not insulated by intervening oxide, one can probe them to determine the effect of separation distance on both dark current and photocurrent. This is similar to the interdigitated detector, except this structure bears more resemblance to the LEAC photodetector structure.

Appendix C: Transimpedance Amplifier Design

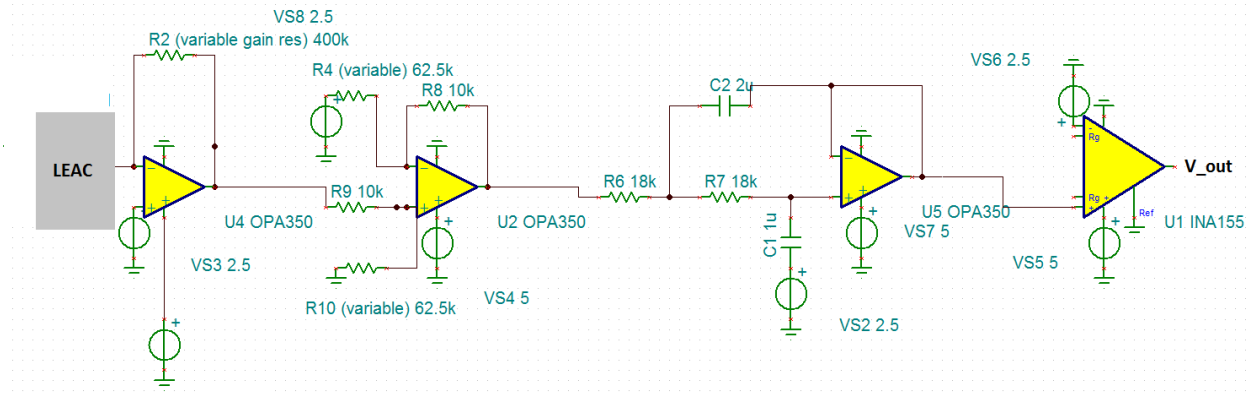

Figure C1: Transimpedance Amplifer Circuit Topology

As shown in Fig. 1, a portable, rail to rail single-supply, transimpedance amplifier was designed for converting to measured photocurrents into a voltage, which could be read into Labview using the ADC side of the Hytek USB.

Stage One

The first stage of the amplifier applies a 2.5V bias across the photodetector and converts the photocurrent into a voltage with a gain adjusted by the resistance of resistor R2. For a 400kΩ resistor, the gain of the first stage is 0.4V/μA. In general the gain is (R2/1MΩ)V/μA.

Stage Two

The second stage of the circuit is a voltage level shifter. The idea behind this stage was to subtract the observed dark current to increase the usable dynamic range of the ADC. After improving the photodetector, dark currents of just 20-30 nA were recorded, so it was not necessary to use the level shifter, and it was simply bypassed with a simple pin swap on the PCB. This stage is often referred to as a "boiler plate gain circuit" and a quick example highlighting its functionality is shown below.

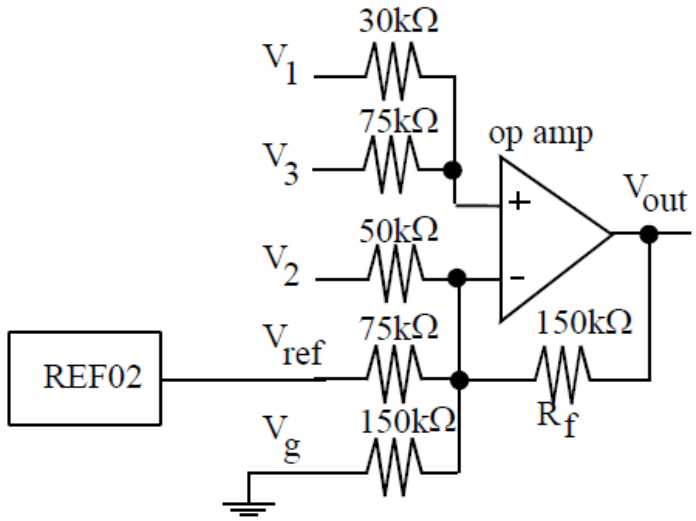

The gain of each voltage input is the feedback resistor R_f divided by the input resistance, so V_1 for instance, has a gain of five. Positive gains are connected to the positive terminal, while negative gains are connected to the negative terminal. The sum of all gains must equal unity, and the negative terminal on the op amp is connected go ground through a 150kΩ resistor to achieve this.

Figure C2: Boilerplate transimpedance amplifier design

Stage Three

The third stage of the TIA is a two-pole, Butterworth 6.2 Hz Low Pass Filter. In general for an n-pole Butterworth filter the Gain equation is:

$$\frac{V_{out}}{V_{in}} = \frac{1}{\sqrt{1 + {f/f_c}^{2n}}}$$

The low cutoff frequency of the filter reduces noise, but increases the necessary acquisition time for each channel due to the long step response. For the design, the convenience factor, x=1.8, and R_6=R_7=10kΩ*x=18kΩ. For C_1=0.5C_2, the cutoff frequency f_c is given by:

$$f_c = \frac{141.4\ \mu F}{2\pi x C_2}$$

Stage Four

The fourth stage of the employs an instrumentation amplifier as a second gain stage. The gain can be adjusted to either 10 or 50 by opening or shorting out the R_g feedback pins. A gain of 10 was selected to give a final circuit gain of (R2/100kΩ)V/μA.

General Design Considerations

In order to design a low-noise, portable amplifier, which could run from a battery and measure very changes in current (~10 nA), effort was invested in selecting op amps with low input bias current, low voltage offsets, low noise (per Hz) and low voltage drift. Additionally, all op amps and instrumentation amps function rail to rail within 10 mV. This is essential to take advantage of the full dynamic range of the circuit, thereby increase the range of measureable refractive index changes.

Appendix D: Amplifier Noise Characterization

Accurate photocurrent measurement is paramount to achieving high sensitivity on the LEAC biosensing platform. To characterize the transimpedance amplifier noise, two 500kΩ resistors were individually connected to channels #1 and #2 to, in order to draw a current of roughly 4 uA for the 2.0 V bias used for n-type MSM photodetectors. The data were normalized by dividing the current in channel #2 (sensing region) by the reference region channel #1. The normalized current is shown below. Note the tight standard deviation and no visually discernible drift during the five minute measurement time window. For 4s time averaging, a SNR of over 12,000 is observed.

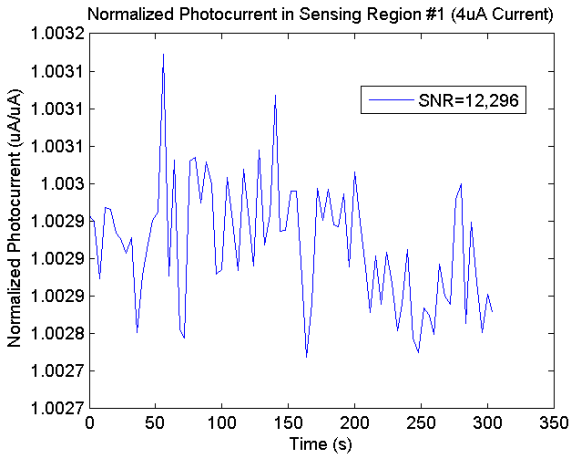

Figure D1: Amplifier data used for SNR calculation

The SNR ratio depends on the sample time. As indicated in the plot below, a sampling period of 16s, yields an SNR of ~18,000, whereas a 1s sampling period gives a reduced SNR of ~8,000.

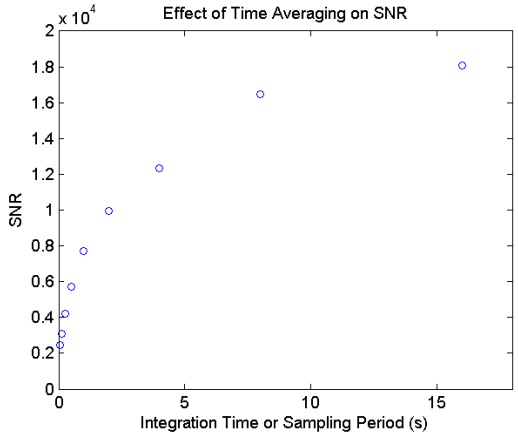

Figure D2: Effect of time averaging on SNR

Appendix E: Design of a Vertical In-plane Grating Coupler for the LEAC Biosensor

E.0 Grating Coupler Design Considerations

In general, there are three distinct methods for coupling light into waveguides: end-fire coupling, diffraction grating coupling, and prism coupling. In end-fire coupling, the waveguide facet is polished in a time-consuming manner by using lapping films of decreasing grit size, starting at 30 microns and working down to just 0.1 microns. End-fire coupling was used to couple light into LEAC chips as it was an established technique used by former graduate students. While end-fire coupling is a proven technique, requiring minimal engineering expertise, it has multiple major drawbacks.

First, the waveguide facet is often chipped and damaged during this mechanical process, which renders the chip unusable. The severity of chipping depends on the mechanical quality of the waveguide's core and cladding materials. Thermal Oxide ALD hafnia chips exhibit minimal chipping due the high film quality of these films. However, for PECVD oxide and Accuglass lower cladding waveguides, chipping occurs frequently during polishing.

The second major drawback is manufacturing limitations introduced by polishing. The processs to polish a waveguide facet is time-consuming and not amenable to mass production.

Third, light not coupled into the waveguide and launched parallel to the surface of the chip can scatter and hit downstream detectors, complicating measurement of evanescently coupled light.

Lastly, end-fire coupling dramatically inhibits the LEAC chip's potential as a coin-sized, robust, operator-friendly, highly-portable sensing platform. While fibers can be glued to the waveguide facet, a specialized mounting stage is still required.

The application of a vertical grating coupler would resolve all of the above issues, enabling high manufacturing throughput, wafer level testing, and waveguide excitation by flip-chip lasers. Additionally, a well designed grating couple potentially increase the coupling efficiency. Given that devices have moved to 20 nm lithography and below, as of 2014, an optical grating coupler can now be readily fabricated within manufacturing tolerances. While a number of different grating designs have been discussed in the literature, including blazed gratings and variable depth grating, only the square wave grating shown below can be readily fabricated. As such, this general grating design was chosen for the LEAC biosensor. The general fabrication scheme is to define the pattern using e-beam lithography, followed by a dry etching step. As a secondary constraint to facilitate optical coupling from non-fiber sources and enable wafer-level testing, a vertical in plane grating coupler was design as shown below. The grating is designed to couple light at an angle, relative to the wafer normal, at approximately zero degrees. As such, a flip-chip laser could mounted on top of the grating, removing the need for mechanical fiber alignment in an advanced production process.

As grating couplers alone are often the subject of entire dissertations, only the most salient aspects of grating coupler design are discussed. While, Rigorous Coupled Wave Analysis has been used in the past to design grating couplers, computational speed has now increased to the point that multi-core desktops are capable of performing full FDTD simulations on a 2-d grating structure (height = 10 micron and length = 200 micron) in less than 15 minutes. By applying the Grating Equation and then tweaking individual parameters, a high efficiency grating can be designed in a reasonable amount of time, provided that one has a general idea of how each design parameter affects the coupler's operation. The commercial OptiFDTD software package by OptiWave was used for all simulations discussed herein.

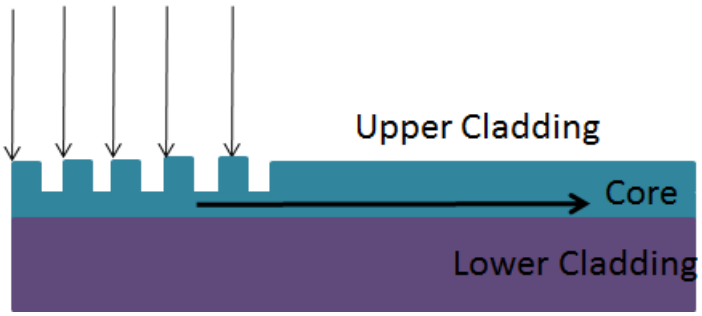

Figure E1: Grating coupler

Within the context of the design, there are six different variables, which must be tuned to optimize coupling efficiency. These are the grating period, grating etch depth, grating duty cycle, grating length, and the thickness of the upper and lower cladding. Several groups have shown that coupling efficiency is periodic with both and upper cladding and lower cladding thickness. While the upper cladding thickness can be readily varied without influencing device operation, the lower cladding directly influence substrate coupling, and thus a tradeoff must be considered in terms of maximizing coupler and overall device sensitivity. Several groups have shown that a grating duty cycle of 50% provides optimal coupling strength (coupling per unit length). For instance, Maire *et al.* showed that a 50% duty cycle was optimal for an oxide cladding/nitride core waveguide. Their results (left) and the corresponding waveguide structure (right) are shown below.

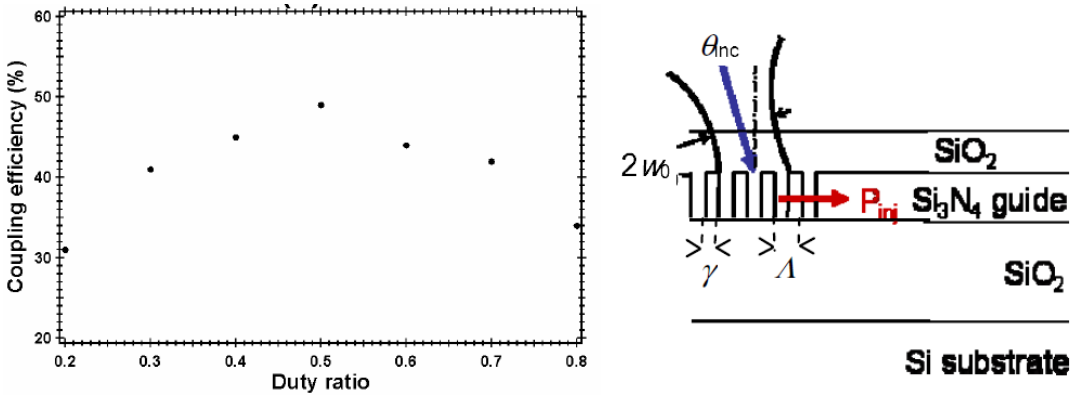

Figure E2: Effect of duty ratio on coupling efficiency

As such, a 50% duty cycle was assumed for the design, and no further effort was placed on optimizing grating duty cycle. The five remaining variables to optimize (period, etch depth, length, lower cladding thickness, upper cladding thickness) are discussed in detail below.

A resonant coupling between the guided TE Mode of a waveguide and the diffraction order of the grating is obtained when the Grating Equation is satisfied. The Grating Equation is given as:

$$k_o n_{inc} \sin(\theta_{inc}) + p\frac{2\pi}{T} = n_{eff} k_o$$

where n_{inc} is the effective index of the waveguide; θ_{inc} is the incident angle relative to the surface normal, n_{eff} is the effective index of the waveguide; T is the grating period, k_o is the wavevector in vacuum, and p is the grating order given by an integer. Note that if the effective index of the waveguide is known, the Grating Equation equation gives an exact prescription for what the grating period must be for a given incident angle. However, it is essential to note that the presence of the grating itself changes the effective index of the waveguide in the region of the grating and this must be taken into account. The degree by which the grating influences the effective index of the waveguide large depends on the grating height.

As coupling is desired at an incident angle of $\theta_{inc} = 0°$, the grating equation then becomes

$$\frac{2\pi}{T} = n_{eff} k_o,$$

which provides a good first guess for the grating period must be in order to achieve vertical coupling and is given by,

$$T = \frac{\lambda}{n_{eff}}.$$

The table below shows first estimates for the grating period for the following LEAC waveguide structures assuming a wavelength of λ=654 nm. An aqueous (n=1.33) upper cladding is assumed. It must be noted that the effective indices are computed for a planar waveguide, which has an effective index very similar to the 7 micron wide waveguides used on chip. The effective index is within 0.001 of the planar waveguide as validated by the UMD full-vector finite difference mode solver used to find the effective index of ridge waveguides. This is also supported by effective index method computations.

Table E1: Optimal grating design parameters

Waveguide (Lower Cladding/Core)	Effective Index (n_{eff})	Estimated Grating Period (nm)
Accuglass/Oxide/Teflon	1.3827	473
Oxide/Nitride/Oxide	1.4632	447

As stated previously, the presence of the grating does have a slight effect on the real effective index. By starting with the estimated grating period and modifying in small (1-2 nm increments) one can quite easily determine the optimal grating period using FDTD simulations. From reciprocity, a grating can either be used to couple light into a waveguide or to couple light out of it. To gauge the appropriate grating period, one simply launches a guided mode into the waveguide from the left side (similar to end-

fire coupling) and monitors the outcoupling angle. As a zero degree angle is desired, the grating period is modified until an outcoupling angle of zero degrees is achieved, as shown below. From the Grating Equation, note that if the outcoupling angle is negative, then the period must reduced, whereas a positive outcoupling angle implies that the grating period must be increased. In this step of the design, the grating etch depth and length must be selected. As we prefer to couple most of the light of the waveguide, a grating length of 75 microns is typical sufficient. For etch depth, it is good start by etching completely through the core. The results are shown below for an oxide/nitride waveguide with a 444 nm period.

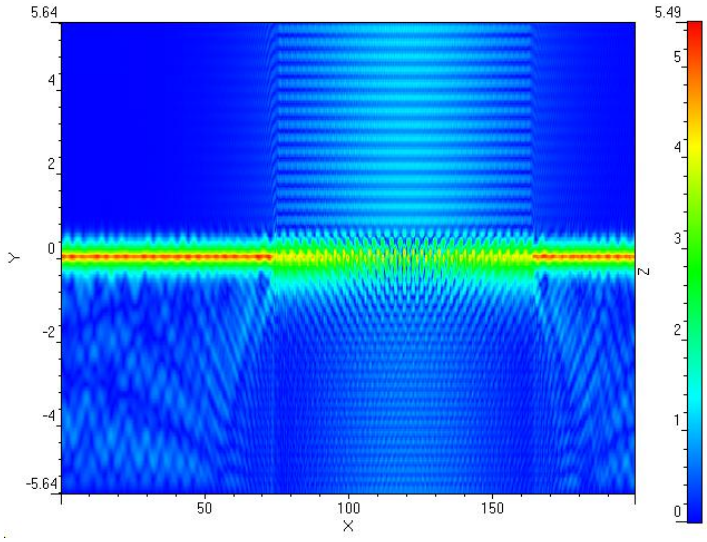

Figure E3: FDTD simulation if grating

A guided mode is launched into the single mode waveguide from the left side of the figure. It encounters the grating coupler and is scattered out.

E1. Implementing a Distributed Bragg Reflector (DBR)

Notice than in reverse, incoupled light would travel in two directions. To avoid this problem a DBR grating reflector is used, so that coupled light travels in the direction of the chip photodetectors. The DBR always has a period half that of the grating coupler, so in this case the DBR period is 222 nm. Notice the strong increase in directional coupling efficiency shown in the figure below.

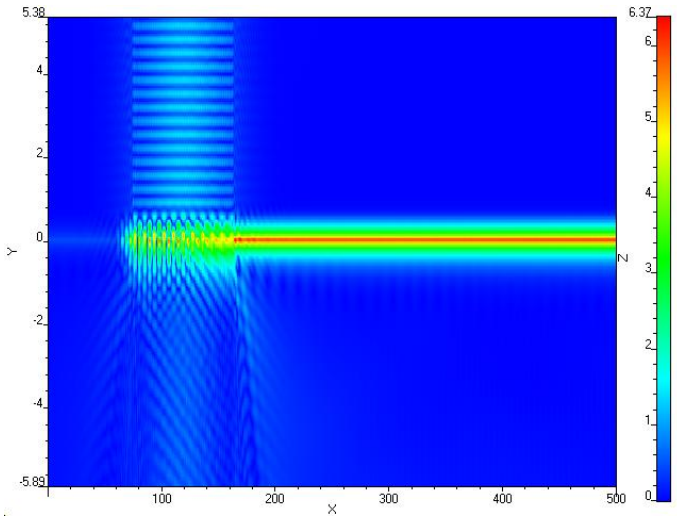

Figure E4: Grating enhanced with integrated DBR

With the correct period identified for the grating coupler, the grating coupler length and etch depth must be simultaneously optimized. As stated previously, changing the etch depth would affect the waveguide's effective index, and thus the period required for vertical coupling. As such, at this stage is best to leave the etch depth at the initial simulated value of one core thickness, and then determine the grating period length required to achieve sufficient coupling.

E2. Limitations on Grating Coupler Strength

If the coupling period is longer than desired, the grating strength (coupling per unit length) cannot be increased further by any simple method. Other methods to increase the grating strength include increasing the core/upper cladding index contrast. However, this method will not work for the LEAC chip due to the need to mode mismatch at the reference/sensing region interface. For instance, if one decides to have an air upper cladding in the grating region to increase the index contrast between the upper cladding and the core, several issues arise. First, a guided mode will likely not be supported in this region and second, if a guided mode is supported, transmission from an upper cladding to the aqueous sensing region would be minimal due to the index mismatch. For the LEAC biosensor, one is thus constrained to increasing the etch depth to achieve maximum grating strength. Etching more than the core thickness was not attempted. Grating strength is important as longer grating requires a large beam diameter. As the waveguide is rectangular in shape, much of the beam is wasted if the grating length becomes significantly larger than the waveguide's width. However, adiabatic tapers, mentioned briefly at the end of this Appendix, can be used to address this problem.

E3. Concurrent Optimization of Grating Coupler Length and Etch Depth

In general, light cannot be totally coupled into or out of a waveguide in a controlled manner over several wavelengths. It takes many microns for a grating coupler to operate effective, the idea is to outcouple light with a uniform phase front (phase perpendicular to the direction of propagation), so that light from a gaussian laser beam can be coupled into the waveguide via reciprocity.

As discussed by Bates *et al.* a beam coupled out by a grating coupler should match the profile of the input beam when used for coupling light into the waveguide. To wit: "A grating coupler with a constant groove depth produces a constant leakage rate. A beam coupled out by such a grating coupler has a characteristic exponential decay profile. If the grating coupler could be modified to shape the beam profile, then the input coupling efficiency could be improved, and the outcoupled beam profile could be optimized for specific applications." Using the input/output beam matching principle, Bates *et al.* developed a variable depth grating coupler using sophisticated fabrication techniques, which was engineered to both couple in and couple out a Gaussian beam. Their work demonstrates the important of matching the grating to the profile of the input beam.

As the experimental ion milling technique used by Bates is not amenable to mass production and not available for LEAC chip fabrication, the square wave grating is justified. The reported maximum efficiency of a square wave grating to be 81%, which does not appear to be a major limitation. Using FDTD, the grating coupler strength was computed for both oxide/nitride and Accuglass/oxide LEAC waveguide structures. This grating strength parameter is often referred to in the literure as α "alpha", and has unite of per unit length.

The figure below was used to calculate α for fully-etched oxide/nitride waveguide for grating length of 22, 44, and 88 microns.

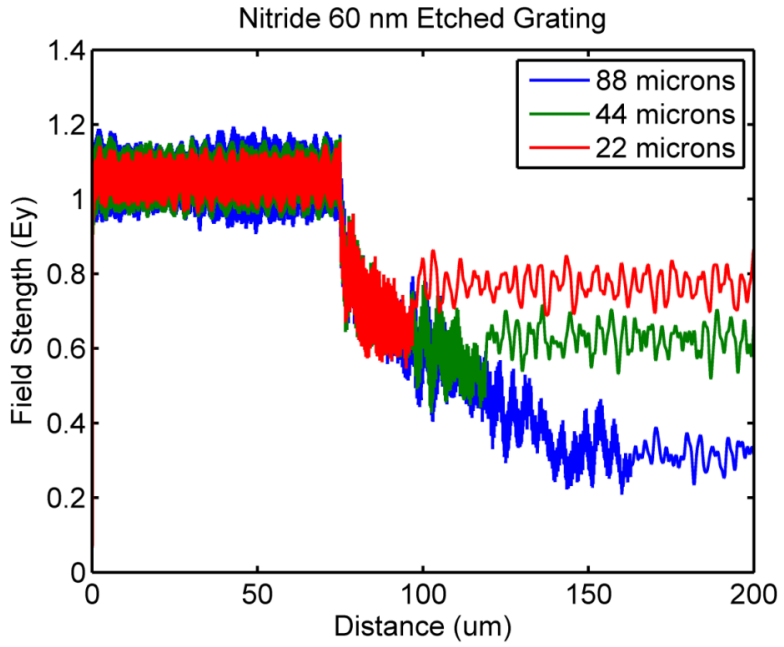

Figure E5: Effect of grating length on coupling

The grating begins at x=75 microns. Notice that 88 microns is sufficient to couple most of the light out of the grating. Given that intensity is the field strength squared, the 44 micron grating is sufficient to couple out about 75% of the light. The grating strength parameter alpha can be computed be fitting the field decay line as shown below.

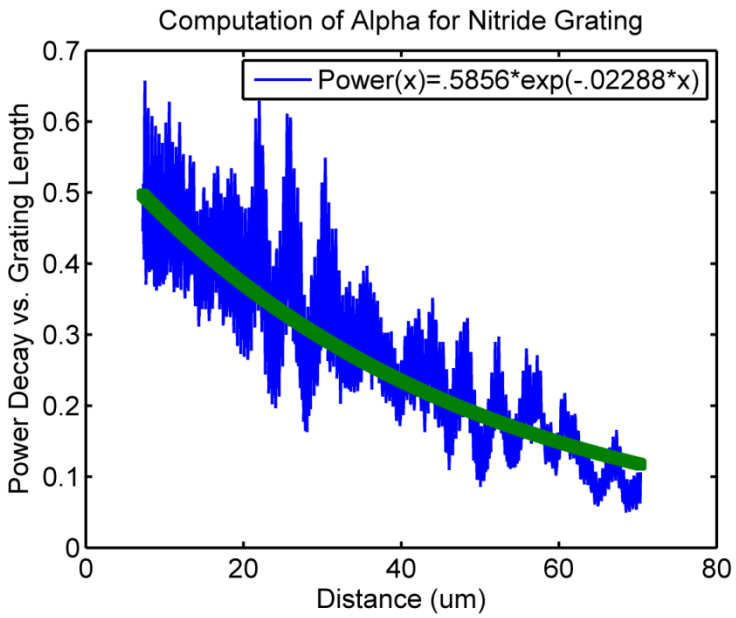

Figure E6: Computation of grating alpha parameter

As expected, the grating strength is much less for the Accuglass/oxide/Teflon waveguide than the oxide/nitride/oxide waveguide as there is less index contrast. With the grating strength parameter alpha known, the optimal beam waist can be computed. Letting the coupling length $L_c = 1/\alpha$. The optimal beam waist is given by,

$$w_o = 1.37 L_c \cos(\theta_{inc}) = 1.37 L_c.$$

Thus a higher grating strength parameter corresponds to a shorter coupling length, and in turn, a smaller beam waste. A smaller beam waist is desirable if one plans on coupling light from a single mode fiber, which for a 654 nm wavelength, has a beam diameter of roughly 4 microns.

While FDTD can be used to compute the effect of etch depth on the grating strength parameter alpha, it is worthwhile to note, that for design purposes, an analytical approximation exists. Assuming that the guided mode in the upper cladding has an evanescent decay constant γ, then the penetration depth δ into the upper cladding is $\delta=1/\gamma$. Provided that the etch depth $d_e < \delta$, then α varies as d_e^2. For LEAC waveguides, which are designed to be near cutoff, the penetration depth (1/e falloff) is typically 400-800 nm, which is far greater than the core thickness (60-220 nm). As such, the grating strength parameter is always in the parabolic region of the curve shown below, and will thus always be proportion to the etch depth squared.

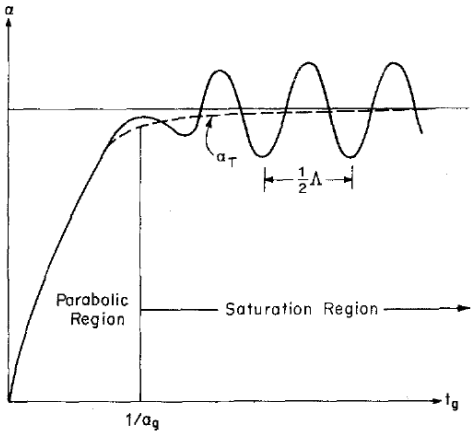

Fig. 8. Typical variation of the leakage α versus the height t_g in a rectangular dielectric grating

Fig E7: Effect of cladding thickness on coupling efficiency

E4: Effect of Upper and Lower Cladding Thickness

As demonstrated by Emmons *et al.*, both upper and lower cladding thickness can have a dramatic impact on coupling efficiency due to multiple reflections producing interference effects. From FIMMPROP simulations, like the one shown below,

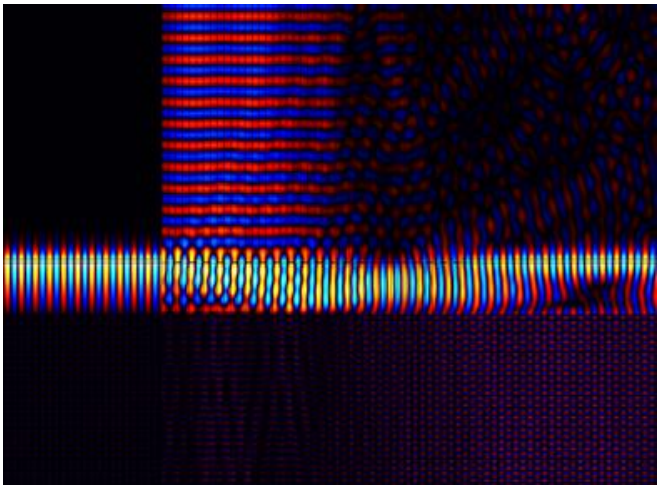

Figure E8: Coupling efficiency with appropriate lower cladding thickness

the LEAC chip should design to have a lower cladding thickness of 1200 +(n*654/2) nm for constructive interference. Lower cladding thickness values of of 1200 +(n*(654/4)+327) nm would lead to distructive interference, and thereby minimize coupling efficiency. The structure above was simulate for a 70 nm thick SiNx waveguide with a 440 nm grating period 50% duty cycle, and fully etched grating. The grating is covered with Teflon AF (n=1.31). This is the grating design for both Teflon AF and aqueous sensing LEAC chips.

Appendix F: PECVD Deposition of Higher Quality $Si0_2$ and SiN_x for the LEAC Biosensor

F.0 Introduction

Plasma enhanced chemical vapor deposition (PECVD) is a well-established semiconductor processing technique, which can be used to deposit dielectric thin films at low temperatures [1]. In PECVD, a plasma is formed when precursor gases flowing through a low-pressure chamber are excited by an RF source. The deposition substrate is placed at the bottom of the chamber on a baseplate heated to a temperature of 100-350°C. The plasma species react on the heated substrate to form a conformal dielectric thin film.

While the plasma gases are more inclined to react on the heated substrate and baseplate, thin film deposition occurs on nearly all surfaces of the chamber. A white powdery substance, most likely silicon dioxide or nitride, tends to collect on unheated surfaces of the chamber. As such, it is necessary to clean the chamber in between deposition runs, as the gas showerhead can become clogged and the powder can fall onto the substrate, thereby producing a non-uniform deposition. A typical cleaning procure involves wiping the chamber with methanol and a cloth wipe, followed by a CF4 plasma clean for 30 minutes, as outlined in the LEAC Fabrication Protocol.

F.1 Application to LEAC Biosensor

Two common thin films deposited using PECVD are silicon dioxide ($Si0_2$) and silicon nitride (SiN_x), which are critical elements in the LEAC biosensor structure. $Si0_2$ forms the waveguide lower cladding and upper cladding reference regions, whereas SiN_x forms the waveguide core and is used at the bottom of the lower cladding to form an insulating moisture barrier. PECVD enables the low-temperature deposition of these films over the LEAC's Ti/Si metal-semiconductor-metal contacts, which degrade rapidly at temperatures above 250 °C.

The quality of these two films can have a dramatic impact on LEAC performance. Excessive surface roughness, stress cracks and voids can lead to undesirable scattering losses in the waveguide, while excessive absorption can lead to rapid attenuation of signal light in the guided mode. Both scattering and absorption compromise the signal to noise ratio. In addition, the refractive index and thickness of each film must be precisely controlled in order for the waveguide to work as engineered. Lastly, as the sensing regions of the LEAC must be bio-fluid compatible, the combined thin film structure should perfectly insulate the MSM contacts from any conductive fluid, which could short out the sensor. Such a wet dark current would confound measurement of the photocurrent generated by evanescently coupled light. Given the preceding considerations, ideal films should have a uniform refractive index, low absorption, a well-controlled deposition rate, atomic-level surface roughness, good mechanical stability and excellent insulating properties under wet conditions.

F.2 Deposition Variables and Film Characterization

For both SiN_x and $Si0_2$, the refractive index, deposition rate, and film quality all depend critically on the inert dilution gas and precursor gas flow rates as well as the chamber deposition parameters. These are substrate temperature, chamber pressure, RF power, and RF frequency. While the CSU Cleanroom PECVD has a fixed frequency of 13.56 MHz, which is considered high-frequency (HF), other PECVD units also have a low frequency (LF) setting, which has a range of 10-500 kHz. As such, only the gas flow rates, temperature, pressure, and RF power could be varied using the CSU PECVD. Significant effort was

invested in optimizing all deposition variables, in order to produce high quality silicon nitride and silicon oxide films with nearly ideal properties. In the remainder of this appendix, the optimization of silicon nitride and silicon oxide for the LEAC biosensor are discussed in detail. Films deposited at CSU were characterized by Atomic Force Microscopy (AFM), SEM imaging, ellipsometry, reflectometry, and BOE etch rate for $Si0_2$ and CF_4 plasma etch rate for SiN_x.

No direct measurements of the absorption coefficients of SiN_x or $Si0_2$ thin films were made, as this requires a Photothermal Deflection Spectroscopy (PDS) system, which was not readily available. A literature review indicated that $Si0_2$ has a negligible absorption coefficient at longer visible wavelengths (654 nm) [2,3]. However, the absorption coefficient of SiN_x thin films can vary dramatically depending on deposition parameters [4,5]. As SiN_x forms the waveguide core, it is critical to deposit a film with a low absorption coefficient, in order to maximize light propagation down the waveguide.

F.3 PECVD Silicon Dioxide Deposition

High-quality $Si0_2$ films are deposited using the method developed by Batey *et al.*, which employs helium as a carrier gas [6]. This method is capable of producing stoichiometric oxide films, which have a refractive index and BOE etch rate nearly identical to thermally grown oxides. While Batey *et al.* initially determined that high-quality films could only be produced using low deposition rates (<8 nm/min), a subsequent process was developed to enable the deposition of high quality oxide at rates up to 113 nm/min [7]. The high deposition rate process uses higher gas flow rates, higher RF power and increased chamber pressure.

Three kinds of PECVD oxide are employed in LEAC fabrication. The first, referred to herein as high-temperature oxide (HTO) is deposited at 350°C and is used to form the buried detector metal insulation barrier. The second, referred to as mid-temperature oxide (MTO), is deposited at 250 °C and is used to fabricate the waveguide lower cladding. The third, referred to as low-temperature oxide (LTO), is deposited at 105°C and is used to form the upper cladding reference regions of the waveguide. The standard precursor gases for $Si0_2$ deposition available in the CSU cleanroom are nitrous oxide (N_20) and 2% silane (SiH_4) diluted in nitrogen (N_2). Helium is used as the carrier gas. It should be noted that oxygen and tetra-ethyl-ortho-silicate (TEOS) can also be used to deposit oxide [8]

The above oxides (HTO, MTO, LTO) are deposited using the following deposition parameters:

Gas Flow Rates: N_20 = 70 sccm, SiH_4 = 70 sccm, He = 600 sccm

Pressure = 520 mTorr

RF Power = 25 W

The deposition rate, refractive index and BOE etch rate are shown in Table 1. The deposition temperature has a strong effect on the film mechanical quality, as indicated by the BOE etch rate. High etch rates are strongly correlated with film porosity, as increased surface area, leads to higher etching rates.

Table F1: Effect of Temperature on Refractive Index and Etch Rate

Oxide Film Type	Rate (nm/min)	Refractive Index	BOE Etch Rate (nm/s)
Thermal Oxide	Varies w/ thickness	1.465	1.2
HTO	10.3	1.469	2.3
MTO	7.9	1.462	10
LTO	6.3	1.455	39

In the interest of maximizing the deposition rate and minimizing helium consumption, a quick study was undertaken to investigate the effect of He on the deposition rate and film quality. It was initially thought that by decreasing the carrier gas concentration, the deposition rate could be increased. As shown in Table 2 for LTO, the opposite is true. Higher He flows increases the deposition rate and film quality.

Table F2: Effect of He Flow on Deposition Rate and Film Quality

He Flow Rate (sccm)	Rate (nm/min)	BOE Etch Rate (nm/s)
50	1.3	165
150	2.1	135
300	4.6	68
600	6.3	39
900	6.4	34

While the CSU PECVD requires several hours to achieve cladding thicknesses in the 1-2 micron reqire, it worthwhile to note that a commercial production process could employ the high deposition rates discussed in [7]. For reference, the deposition rate as a function of N_20 flow rate is shown in Figure 1. The deposition parameters are 5 Torr, 350 °C, 2 W/cm^2. N_20: (1.4% SiH_4 in He) = 4:3. As shown in Figure 2, film quality increases with chamber pressure, particularly at lower temperatures [9]. Unfortunately, the maximum chamber pressure allowed by the CSU PECVD is 540 mTorr.

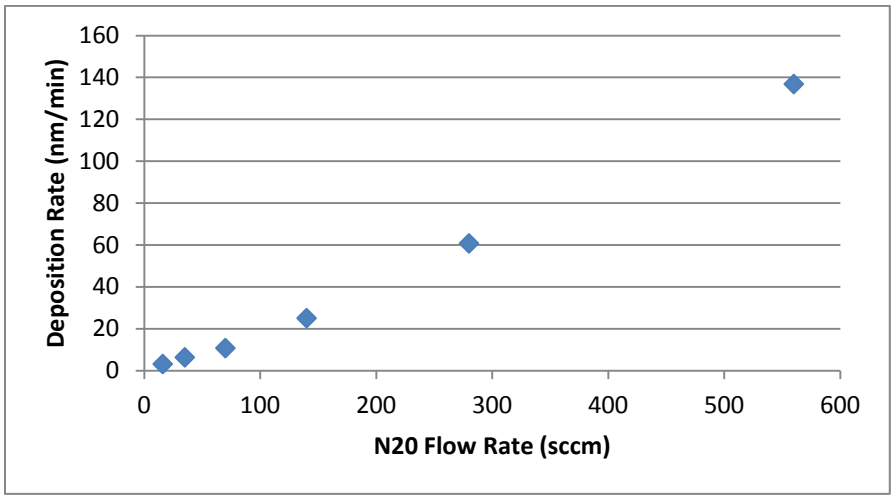

Figure F1: Deposition Rate vs. Precursor Gas Flow Rate

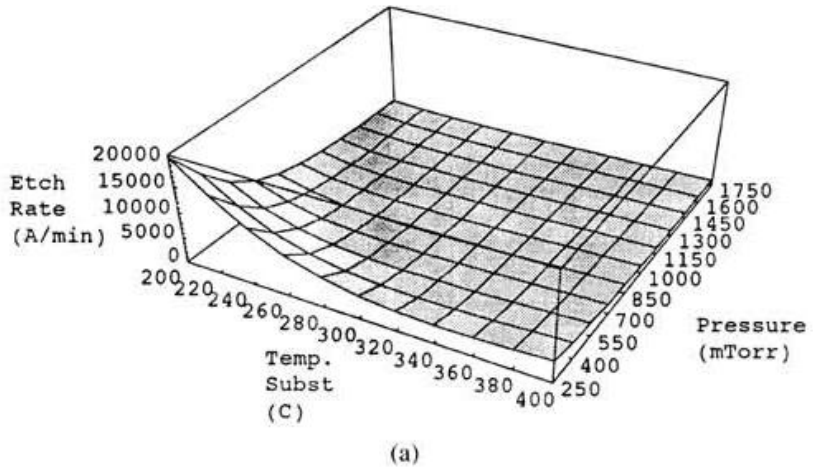

(a)

Figure F2: Effect of Temperature and Pressure on Film Quality (Etch Rate)

F.4 PECVD Silicon Nitride Deposition

SiN_x can have a refractive index of 1.8-2.2 in the visible range, depending on the deposition parameters. In order for the waveguide to function as designed, precise control of both the refractive index and deposition rate are critical. At higher refractive indices, light cannot be coupled to create a guided mode in the waveguide. As reported by Stutius *et al*. [10] , "Films fabricated by PECVD had refractive indices above n=2.1 and probably contained excess Si, which absorbs light at 632.8 nm." In order to maximize light propagation in the waveguide, film absorption must be minimized. Within the constraint of low absorption, a low-stress film is needed to prevent micro-cracking in the waveguide core.

The paper by Gorin *et al*. titled, "Fabrication of SiN_x waveguides for visible-light using PECVD: a study of the effects on plasma frequency on optical properties," discusses the deposition conditions required to produce high-quality nitride films with minimal absorption [5]. In this work, the propagation losses in planar waveguides were studied under a variety of deposition conditions. The authors demonstrate that low absorption in higher refractive index films can only be achieved by using Low-frequency PECVD. However, as indicated in Fig. 3, High-frequency PECVD systems, such as the one used in the CSU Cleanroom, can be used to deposit quality nitride films with minimal absorption losses if the NH_3/SiH_4 flow ratio is above 2.5. As shown in Fig. 4, such a flow ratio corresponds to films with refractive indices less than 1.88.

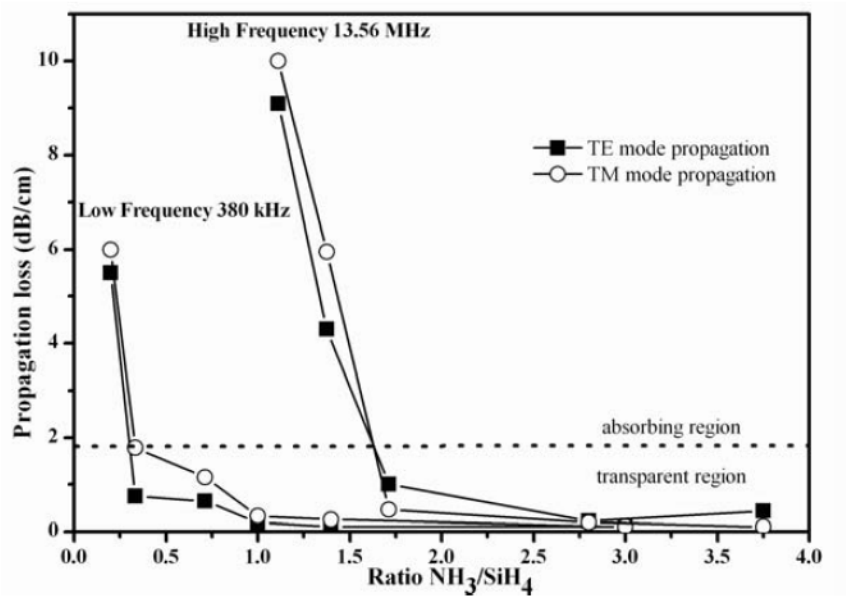

Figure F3: Effect of Ammonia to Silane Flow Ratio on Propagation Loss

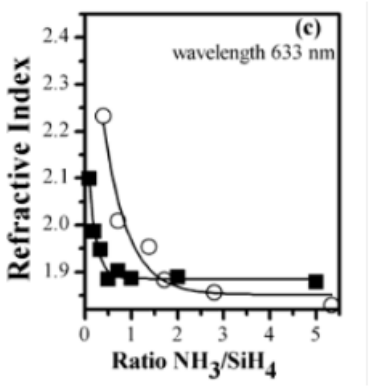

Figure F4: Effect of Ammonia to Silane Flow Ratio on Refractive Index

In addition to low absorption, film stress in nitride should be minimized, in order to ensure sufficient mechanical quality, which prevents microcracks. In "Characterization and Optimization of Low Stress PECVD Silicon Nitride for Producation of GaAS Manufacturing," Mackenzie *et al.*, demonstrate how helium dilution can be used to control film stress for different RF powers at 250°C [11]. As shown in Fig. 5, a film stress of approximately zero can be deposited when the N_2 to He percentage is 20%.

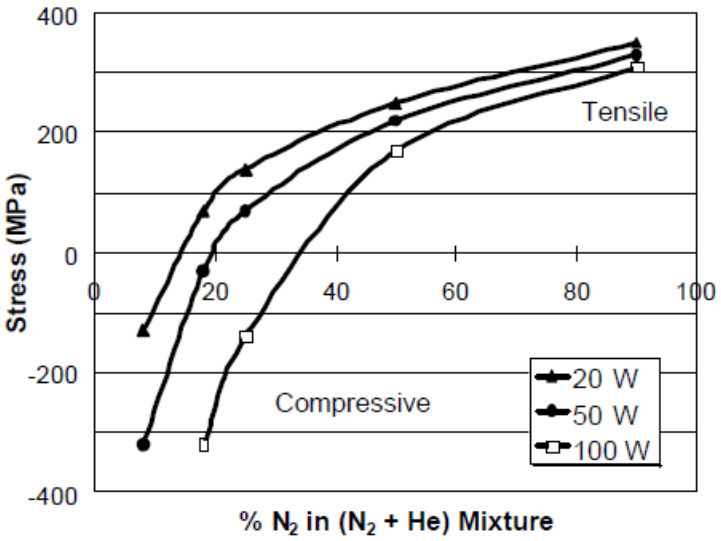

Figure F5: Effect of helium dilution on nitride stress

F.5 Optimization of CSU PECVD Nitride

The precursor gases available for nitride deposition in the CSU PECVD are 98:2 N_2 diluted SiH_4, NH_3, and He. By fine-tuning the ammonia to silane flow ratio and incorporating helium as a stress-modifying dilution gas, it is possible to deposit high-quality, low-absorption, low stress nitride films, using the CSU PECVD. These films have been successfully deposited, in order to form the core of single-horizontal mode, 7 micron wide, 45 nm tall, ridge waveguides with propagation losses of 6.8 dB/cm. Due to substrate coupling into the lower cladding, propagation losses due to absorption and scattering are likely significantly less than 6.8 dB/cm. Silicon nitride is deposited in the CSU Cleanroom with the following deposition parameters.

Gas Flow Rates: NH_3 = 7.7 sccm, SiH_4 = 47 sccm, He = 20 sccm

Pressure = 350 mTorr

RF Power = 50 W.

The film has a **refractive index of 1.804**, a **deposition rate of 10.1 nm/min**, and a **CF_4 plasma etch rate of 33 nm/min** at a power of 40W and a flow rate of 40 sccm. In order to consistently achieve the above film properties, the PECVD chamber must be thoroughly cleaned prior to deposition. This typically requires the chamber to be plasma-cleaned with CF_4 for 30 minutes after being wiped with methanol and DI water.

As a comprehensive reference, the book Film Deposition by Plasma Techniques [1], outlines how various deposition parameters affect the BOE etch rate, refractive index an deposition rate of nitride thin films. For a fixed SiH_4 to NH_3 flow ratio, refractive index decreases with increasing RF power, whereas the deposition rate increases and the BOE etch rates remains relatively flat. As the SiH_4 flow rate is increased, the deposition rate and refractive index increase, and the BOE etch rate decreases.

Appendix G: Platinum MSM Photodetectors

Summary Statement: n-Si MSM photodetectors employing Pt contacts offer improved performance over Au contacts, in terms of SNR, drift, and quantum efficiency.

G.0 Experiment

A PDB-C112 photodiode from Photonic Detectors Inc was used to determine the illumination intensity of the microscope's field of view. A photocurrent of 1.66 mA was measured and the photocurrent did not drift by more than 3% over several hours of measurement. Assuming a responsivity of 0.43 A/W, the optical power is 3.86 mW. Given the measured beam diameter of 2.6 mm, the optical intensity is then 0.73 mW/mm^2 or 727 W/m^2. Each of the LEAC's photodetectors has an area of (300 um x 32 um) and therefore 6.97 uW is incident on the photodetector surface. **Thus, a LEAC photodetector at 100% quantum efficiency would yield a photocurrent of 3.0 uA.**

For experiments, samples were placed under microscope illumination and the photocurrent and normalized photocurrent (sensing detector #1/reference detector #1) was measured for time periods ranging from several minutes up to an hour. The results strongly indicate that both photodetector quantum efficiency and performance (SNR and drift) are highly dependent on both contact metallurgy and annealing temperature.

Multiple experiments were carried out using different metallurgies and surface treatments on both n-type and p-type wafers, including p-type SOI wafers. To spare you further reading, I will state upfront that the best LEAC photodetectors realized were achieved using an n-type 1-5 ohm-cm prime grade wafer and platinum contacts annealed at 370C for one hour on a hot plate after silicon nitride deposition. In this writeup, I focus on the specific performance characteristics of Pt/n-si and Au/n-Si MSM photodetectors operating at bandwidth restricted by a two-pole Butterworth 6 Hz low pass filter. At such a frequency range, the photodetectors are subject to a large 1/f noise component. Modulation of optical excitation source at several kHz in conjunction with a lock-in amplifier would further improve the photodetector performance characteristics.

G.1 Affect of Annealing Temperature on Total Photocurrent and SNR

Photocurrents on the first two LEAC detectors were measured using an amplifier with a gain of 0.402 uA/V using the microscope illumination source described above. Data acquisition was interleaved at 2000 Hz, allowing near simultaneous photocurrent measurements (within 500 us). The data clearly indicate that SNR, photocurrent and quantum efficiency of the photodetectors are highly dependent on annealing temperature. Additionally, photodetector SNR, as measured by taking the mean/standard deviation of the normalized photocurrent, is highly dependent on annealing temperature. SNR is reported for a ten minute measurement period. For longer periods, SNR degrades due to drift. The data are summarized below in Table A for Pt contacts and Table B for Au contacts.

Table G1: Platinum Contacts

Annealing Temp (°C)	Mean Photocurrent (uA)	Quantum Efficiency (%)	SNR
No Anneal (~24)	0.29	9.6	161
250	0.91	30	145
330	2.09	70	1327
370	2.66	89	5871
450	1.41	47	27

Table G2: Gold Contacts

Annealing Temp (°C)	Mean Photocurrent (uA)	Quantum Efficiency (%)	SNR
No Anneal (~24)	0.08	2.7	1140
250	1.08	36	2869
330	1.24	41	360
370	1.68	56	67
450	7.9	Photoconductor (263%)	48

The data clearly show that SNR and quantum efficiency improve up to 370C, after which the contacts degrade rapidly. At 450C, the quantum efficiency is reduced by nearly a factor of two vs. the 370C anneal and the SNR deteriorates by several orders of magnitude.

Interestingly, for both the non-annealed chip and the 250C annealed chip, the SNR is low because there is an initial period of approximately several minutes whereby current flow changes the photodetectors properties. After the contacts are "worked in", this phenomenon subsides and SNR improves greatly. This can be seen in the plots below both samples. Such behavior was not readily observed for contacts annealed at higher temperatures.

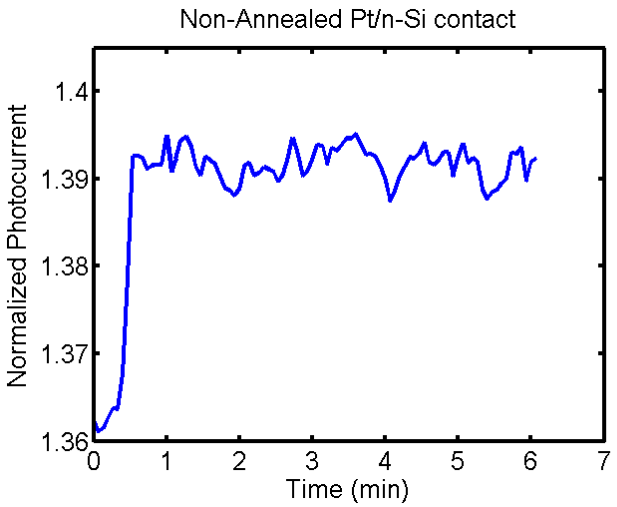

Figure G1: Change in photocurrent for non-annealed sample

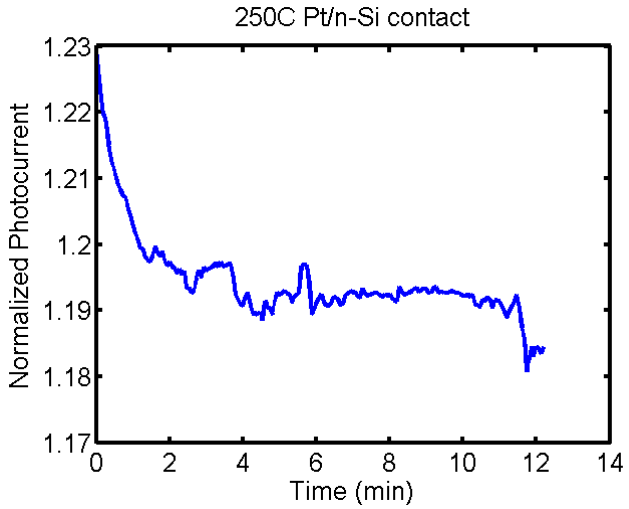

Figure G2: Change in photocurrent for 250C annealed sample

G2. Long Term Drift of Platinum MSM Photodetectors

Over long periods of time, the photodetectors were found to drift. Part of the drift may be attributed to fluctuations in lamp intensity and amplifier drift. For reference, we take the Pt photodetectors annealed at 370C, which had the best performance of all contacts tested. The photocurrent was measured overnight and yielded the following plots for raw photocurrent and modulation.

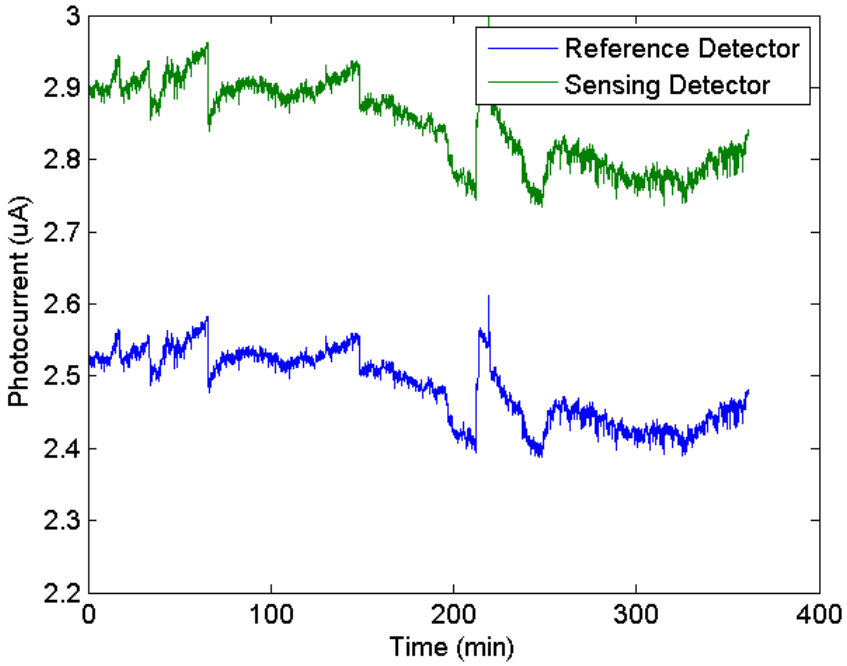

Figure G3: Raw Photocurrent Data from LEAC Pt MSM Photodetector Annealed at 370C

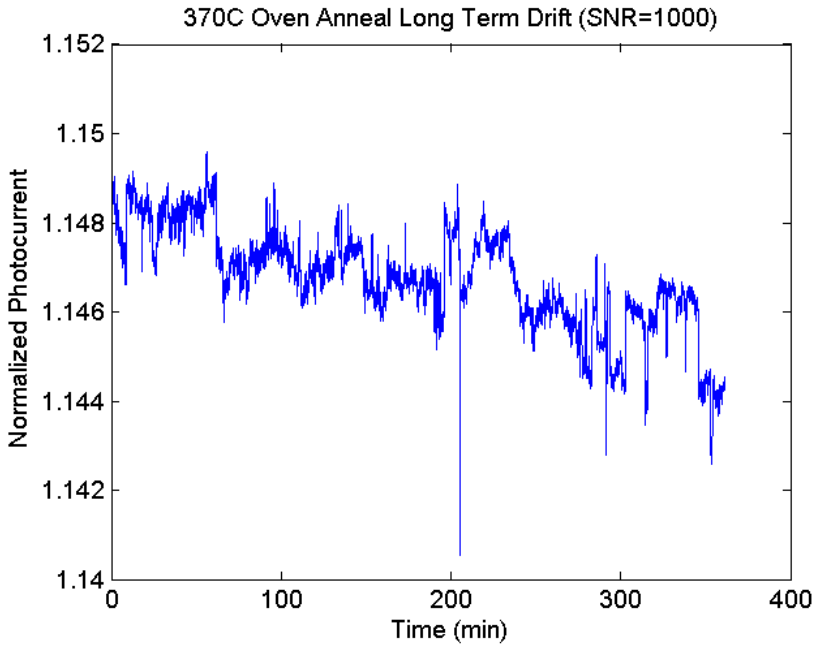

Figure G4: Drift in Normalized Photocurrent of Pt Photodetector

However, it must be noted that over shorter periods, such as ten minutes, which is a sufficient amount of time to perform a BTEX measurement, the SNR was found to be higher than 5000 when a 9-point moving average filter was employed for signal processing, as seen in the plot below.

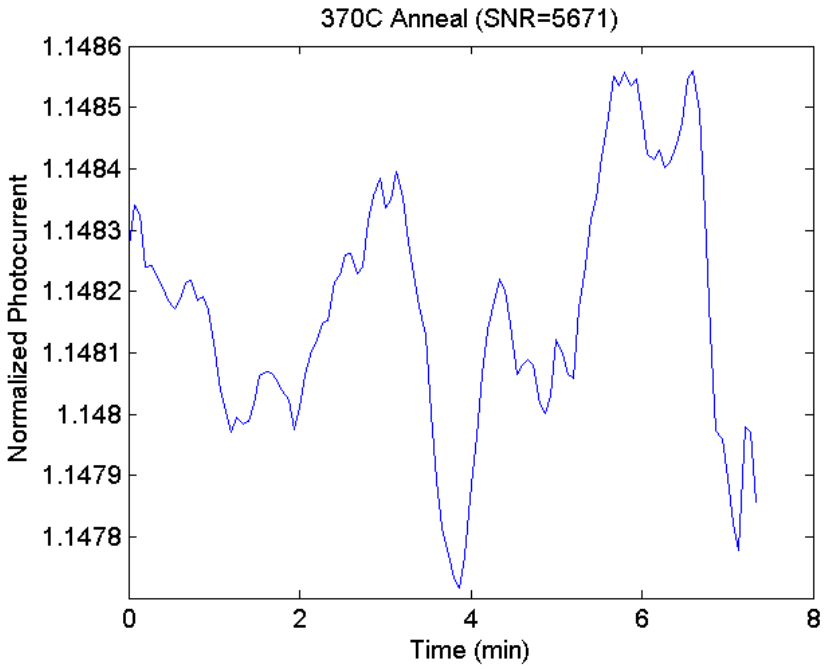

Figure G5: Minimal drift during 10 minute measurement time window for Pt MSM photodetectors

Appendix H: Single Mode Condition

LEAC chip waveguides are designed to be single mode, in order to avoid several problems with multi-mode waveguides. If a waveguide supports multiple modes, then coupled power can be transferred betweeen the various guided modes. As these modes have different effective indices, they also have different photodetector coupling magnitudes. This can lead to fluctuations in photodetector coupling, which are completely unrelated to any change in the waveguide's upper cladding sensing region. Generally speaking, a single mode condition can be achieved by either reducing waveguide core height or core width. Interestingly, modesolver simulation results indicate that single mode waveguides can still support leaky modes, which are nearly guided. These modes have sufficiently low loss, that power in these modes remains more than 2 mm down the waveguide, and they can thus effect the signal in the sensing region. The table below shows the dependence of waveguide width on photodetector coupling losses and the effective index of both the fundamental mode and the lowest-order non-guided leaky mode. The results are for the 65 nm core height/2000 nm lower cladding waveguide simulated for BTEX Sensing. Note that effective indices below 1.46 correspond to a non-guided mode, but that these modes can have relatively low losses. Only waveguides with widths of 4μm and below have 2nd order modes, which are sufficiently filtered out by the 2 mm waveguide runway. They are attenuated by more than 99.99%. However, for a 5 μm wide waveguide, the non-guided mode is only attenuated by 86% at 2mm and 95% at 3 mm. It is thus necessary to reduce the waveguide width to 4 μm, to avoid multi-mode interference interference and loss fluctuation issues. The same holds for aqueous sensing (Table 2).

Table H1: Single Mode Condition for BTEX Sensing with 65 nm core/2000 nm LC Waveguide/30 nm etch depth.

WG Width (μm)	**Effective Index of Fundamental Mode**	**Coupling Loss (dB/cm)**	**Effective Index of 2nd Mode**	**Coupling Loss**	**% Power in 2nd Mode at 2mm**
7	1.4627	13.7	1.4583	19.5	41
6	1.4626	13.9	1.4569	25.3	31
5	1.4623	14.3	1.4551	43	14
4	1.4618	15.2	1.4537	220	0.004
3	1.4611	17.1	1.4535	332	$2x10^{-5}$

Table H2: Single Mode Condition for Aqueous Sensing (*n*=1.333) with 65 nm core/2000 nm LC waveguide/30 nm etch depth

WG Width (μm)	**Effective Index of Fundamental Mode**	**Coupling Loss (dB/cm)**	**Effective Index of 2nd Mode**	**Coupling Loss**	**% Power in 2nd Mode at 2mm**
7	1.4617	17.2	1.4574	24.9	32
6	1.4617	17.5	1.4560	32.7	22
5	1.4613	18.0	1.4544	30.3	6
4	1.4609	19.1	1.4534	225	0.003
3	1.4601	21.5	1.4533	342	1.4×10^{-5}

Appendix I: Publications and Conferences

Paper: **Tim A. Erickson** and Kevin L. Lear, "Optimization of the Local Evanescent Array-Coupled Optoelectronic Sensing Chip for Enhanced, Portable, Real-Time Sensing," *IEEE Sensors*, (2013) **13** 1905-1913.

Paper: **Tim A. Erickson**, Rajvir Nijjar, Matt Kipper and Kevin L. Lear, "Characterization of Plasma-enhanced Teflon AF for Sensing Benzene, Toluene, and Xylenes in Water with Near-IR Surface Plasmon Resonance." *Talanta*, (2014) **119** 151-155.

Paper: **Tim A. Erickson** and Kevin L. Lear, "An Integrated Optoelectronic Chip For Sensing Aromatic Hydrocarbon Contaminants in Grounwater," Sensors and Actuators B, Accepted May 2014.

Paper: Yan, Rongjin, N. Scott Lynn, Luke C. Kingry, Zhangjing Yi, **Tim Erickson**, Richard A. Slayden, David S. Dandy, and Kevin L. Lear. "Detection of virus-like nanoparticles via scattering using a chip-scale optical biosensor." Applied Physics Letters 101, no. 16 (2012).

Conference: **Tim A. Erickson** and Kevin Lear, BMES 2012, "A Highly-Portable CMOS-based Optoelectronic Biochip for Real-Time Refractive Index-Based Sensing and Portable Diagnostics," October 2012.

Conference: **Tim A. Erickson** and Kevin Lear. Colorado Photonics Industry Association Annual Meeting 2013, "A Low-cost Optoelectronic Chip for Rapid Exclusionary Sensing of Hydraulic Fracturing Contaminants with No Sample Preparation," October, 2013.

Conference Proceeding: Yi, Zhangjing, Rongjin Yan, **Tim Erickson**, Rashid Safaisini, and Kevin L. Lear. "Optimization of waveguide structure for local evanescent field shift detection," SPIE OPTO, pp. 79410L-79410L. International Society for Optics and Photonics, 2011.

Appendix J: Antibody Scattering Analysis

J.0 Introduction

As previously discussed in Chapter 3, scattering reduces device sensitivity because it reduces modulation. Ideally, all photocurrent would be generated by evanescent coupling from the guided mode, which responds to perturbations in the upper cladding refractive index. In practice, scattered light is absorbed by the underlying photodetector and contributes to the measured photocurrent. As demonstrated by Bauters *et al.*, single mode, $Si0_2/SiN_x$ optical waveguides can be fabricated with scattering losses of less the 0.1 dB/cm. By taking into consideration Fresnel reflection over all angles, only about 30% (0.5*0.6) of isotropically scattered light is absorbed by the underlying detector. Thus for such a waveguide, which can fabricated using DUV lithography and high optical quality thermally-grown silicon dioxide and LPCVD silicon nitride, total scattering loss would be 0.03 dB/cm of less. Compared to the photodetector coupled optical power of ~10 dB/cm, this contribution of scattering to the total signal is negligible, as it would comprise less then 1/300 of the total measured photocurrent and would produce a fixed small photocurrent offset.

In contrast to single mode waveguide's used for optical interconnects on CMOS chips, the LEAC waveguide is used for biological sensing. As it is nearly impossible to form perfectly uniform antibody films, such films increase surface roughness and thereby cause additional scattering. Furthermore, even if one had the capability of producing a uniform film thickness, at low concentrations, it is conceivable that only a single probe molecule or just a few probe molecules would bind in the sensing region, thereby increasing surface roughness and hence scattering loss. Depending on the magnitude of scattering loss, it is conceivable that scattering could overwhelm the evanescent field shift effect. In the event that scattering increased photocurrent by an amount equal to the decrease in photocurrent caused by the local evanescent field shift effect, the presence of the particle would not be registered at all. In short, if the increase in photocurrent caused by scattering is similar in magnitude to the decrease in photocurrent cause by field shifting, the LEAC's entire Biosensing mechanism could be flawed.

Fortunately, analysis reveals that scattering due to antibody-molecules (~5-10 nm in diameter), is minimal and for a 10 dB/cm coupling signal only produces a negligible scattering contribution. This is due to the r^6 dependence of scattering for small radii particles in the Rayleigh regime. Such small particles have Mie size parameters ($2\pi r/\lambda<0.1$) and are largely transparent to longer optical wavelengths (λ=654 nm).

In the following analysis, the fraction of light scattered by *p* particles, which fully fill an entire sensing region is calculated. As a first step, the optical scattering efficiency is computed for spherical antibody body sized particles in an evanescent field[1]. The scattering efficiency gives the fraction of light scattered relative to the total amount of light incident on the particles geometric cross section. For comparison, results for scattering from a plane wave are included as a sanity check. The scattering efficiencies are plotted in Fig. 1 and provided for antibody size particles and slightly larger particles in Table 1. In the analysis, the particles are assumed to have a refractive index of 1.48 (a good estimate for antibodies[1]) and are assumed to be in an aqueous ambient medium (n=1.33). As expected, for small particles, where the evanescent field is nearly constant over the diameter of the particle, the evanescent and plane wave scattering efficiencies are found to be nearly identical. Also note the steep exponential dependence on particle size.

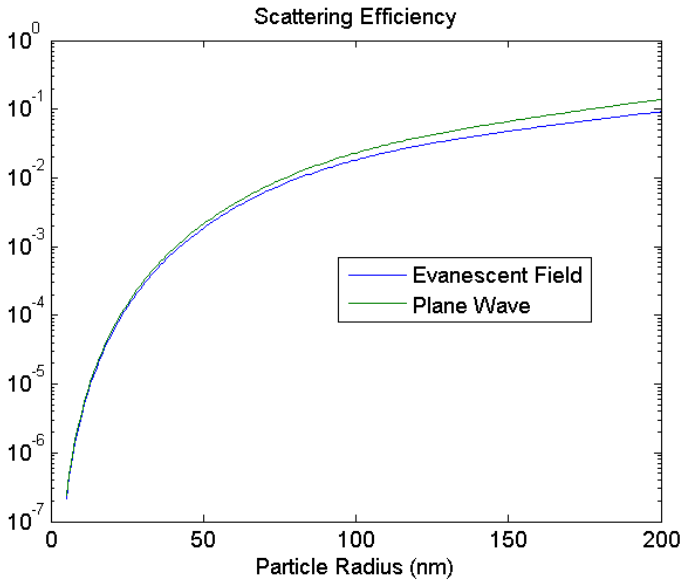

Fig. J1: Scattering efficiency vs. particle radius

Table J1: Scattering efficiency for various particle sizes

Particle Radius (nm)	Scattering Efficiency
4	8.90E-08
6	4.50E-07
8	1.40E-06
10	3.40E-06
12	7.20E-06
20	5.50E-05
30	2.70E-04
40	8.10E-04
60	3.60E-03

Assuming that the scattering events are independent (i.e. no coherent scattering leading to interference), then the total fraction of light scattered is the amount of light scattered by a single particle multiplied by the total number of particles. To calculate the fraction of light scattered in a single detector region, one

first assumes a line of particles placed on the surface of a cross section of waveguide as shown in Fig. 2, where the optical field is shown as contour plot lines. For clarity the particle size has been exaggerated to the point where the particles shown are approximately ~300 nm in diameter as about 14 fit on 4 micron wide waveguide).

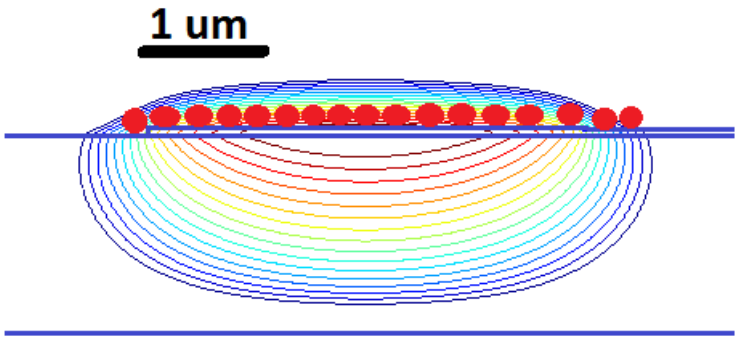

Figure J2: Particles in evanescent field

The fraction of light scattered by a line of particles *F* is given by the overlap integral of the normalized guided mode intensity $I_o(x,y)$ with the cross sectional area of the particles $A(x,y)$ multipled by the scattering efficiency *s*, such that:

$$F = \iint I_o(x,y)A(x,y)s \quad dxdy$$

The fraction of light scattered by a line of particles is shown below in Table 2 for various particle sizes.

Table J2: Scattered Fraction

Particle Radius (nm)	F (Scattered Fraction)
4	1.07E-09
6	7.65E-09
8	3.08E-08
10	7.48E-08
12	1.94E-07
20	2.15E-06
30	1.40E-05
40	5.10E-05
60	2.74E-04

Upon computing the fraction of light scattered by a line of particles. An upper bound for the total fraction of incident light scattered in a detector region is then computed by multiplying the fraction of light scattering by a line of particles by the number of lines *n* of such particles needed fill a 100 micron long sensing region. Assuming particle diameter *d* in nm, the number of lines of particles *n* in a 100 micron sensing section of the waveguide is $(100*10^{-6})/(d*10^{-9})=10^5/d$. The total loss fraction *L* is then then given

by $L=nF$. The equivalent loss in dB/cm $L_{dB/cm}$ is then given by $L_{dB/cm}$=-ln(1-L)*4.34*100. The end results are shown in Table 3.

Table J3: Estimated Scattering Loss Caused by Particle of Different Radii Filling a Detector Region

Particle Radius (nm)	Frac. Light Scat. in 100 microns	Total Scatter Loss (dB/cm)
4	0.00001335	0.005793939
6	0.00006375	0.027668382
8	0.0001925	0.083553042
10	0.000374	0.162346361
12	0.00081	0.351682451
20	0.0053625	2.333587539
30	0.0234	10.27630727
40	0.0637875	28.60615449
60	0.228	112.3064964

The results indicate the scattering loss for particles up to radii of 12 nm and diameters of 24 nm would introduce minimal scattering loss of less than 1 dB/cm. Even 40 nm diameter particles would only increase scattering loss by 2.33 dB/cm. As only about 30% of isotroptically scattered light is absorbed by the underlying photodetector, the total contribution to photocurrent would be less than 1 dB/cm even for 40 nm diameter spheres. Most antibodies complexes are less than 20 nm in length, which would put an upper bound on scattering loss at 0.16 dB/cm. This value is negligible compared to a 10 dB/cm coupled light signal.

As an example, simulation results indicate that modulation for a LEAC chip near cutoff in water to be ~1.6%/nm of protein coverage. Thus, a 20 nm layer would decrease modulation by roughly 24%. For a 10 dB/cm couple power signal, the protein binding would then reduce coupled from 10 dB/cm to about 7.6 dB/cm. With scattering these values would change to 10.16 dB/cm and 7.76 dB/cm, respectively. Thus the change in modulation is from 24% to 23.6%. The scattering from the relatively large antibody complex would only reduce the modulation signal by 1.6%. Thus, even for relatively large antibody complexes, the increase in photocurrent due to scattering is very small compared to the decrease in photocurrent caused by the evanescent field shift effect. It should be noted that in this example, all of the scattered light is assume to be absorbed by the underlying detector. When the isotropic nature of small particle scattering is taken into account, it can be shown that only 50% of the scattered light is incident on the underlying photodetector and off that 50%, only roughly 60% is absorbed due to Fresnel reflection, so

only about 30% of scattered light is absorbed by the underlying detector. Therefore scattering has an even smaller effect on device sensitivity than indicated in this simplified example.

J.1 Conclusion

This simplified scattering loss model provides theoretical justification that the LEAC chip's evanescent field shift mechanism should be not be overwhelmed by scattering losses when used for antibody sensing. The model does have several shortcomings including the fact that antibody complexes aren't spherical, that they may not be densely packed on the surface of the chip, and that modal mismatch due to poor antibody surface coverage could further increase scattering. Due to the inherent difficult in modeling scattering from complex antibody surface topographies on waveguide surfaces, experiment work is required to determine the ultimate sensitivity and performance of the LEAC chip from real-time antibody sensing in PBS, serum, blood, or other biofluid environments.

Appendix References

[1] Konuma, Mitsuharu. Film Deposition by Plasma Techniques. Springer-Verlag Berlin Heidelberg 1992.

[2] Poenar *et al.* "Optical Properties of Thin Film Silicon Compatible Materials." APPLIED OPTICS **36** (21) 5122-5128.

[3] Phillip, H.R. "Optical Properties of Non-crystalline Si, Si0, $Si0_x$ and $Si0_2$." J. Phys. Chem. Solids. 1971. Vol. 32. 1935-1945.

[4] B. Karunagaran *et al.* "Effect of rapid thermal annealing on the properties of PECVD SiN_x thin films." Materials Chemistry and Physics 106 (2007) 130-133.

[5] Gorin *et al. "*Fabrication of silicon nitride waveguides for visible-light using PECVD: a study of the effect of plasma frequency on optical properties." Optics Express. September 2008. Vol. 16. No. 18. 13509-13516.

[6] Batey and Tierney. "Low Temperature Deposition of High-Quality Oxide by PECVD." J. Applied Physics. 60, 3136 (1986).

[7] Batey *et* al. US Patent. 5,068,124. November. 26, 1991.

[8] Wang. *et al.* US Patent. 4,892,752. Jan. 9, 1990.

[9] Han. *et al.* "Modeling the Properties of PeCVD Silicon Dioxide Films Using Optimized Back-Propagation Neural Networks." IEEE Transaction on Components, Packaging, and Manufacturing Technology-Part A. Vol. 17. No. 2. June, 1994. 174-181.

[10] W. Stutius and W. Streifer, "Silicon nitride films on silicon for optical waveguides," Appl. Opt. **16**, 3218-3222 (1977)

[11] Mackenzie *et al.* "Characterization and Optimization of Low Stress PECVD Silicon Nitride for Prouduction GaAS Manufacturing." Unaxis USA, Inc. White Paper.

-End-